UNIVERSIDADE DE LISBOA

INSTITUTO SUPERIOR TÉCNICO

High-Temperature Non-Equilibrium CO_2 Kinetic and Radiation Processes

João Francisco da Cruz Vargas

Supervisor: Doctor Mário António Prazeres Lino da Silva
Co-Supervisor: Doctor Bruno Eduardo Lopez

Thesis approved in public session to obtain the PhD Degree in
Technological Physics Engineering

Jury final classification: Pass with distinction

2020

UNIVERSIDADE DE LISBOA

INSTITUTO SUPERIOR TÉCNICO

High-Temperature Non-Equilibrium CO_2 Kinetic and Radiation Processes

João Francisco da Cruz Vargas

Supervisor: Doctor Mário António Prazeres Lino da Silva
Co-Supervisor: Doctor Bruno Eduardo Lopez

Thesis approved in public session to obtain the PhD Degree in
Technological Physics Engineering
Jury final classification: Pass with distinction

Jury

Chairperson: Doctor Luís Paulo da Mota Capitão Lemos Alves, Instituto Superior Técnico, Universidade de Lisboa
Members of the committee:
Doctor Cristophe Laux, CentraleSupélec, Université Paris-Saclay
Doctor Elena Kustova, Saint Petersburg State University
Doctor Vasco António Dinis Leitão Guerra, Instituto Superior Técnico, Universidade de Lisboa
Doctor Mário António Prazeres Lino da Silva, Instituto Superior Técnico, Universidade de Lisboa
Doctor Brett Alexander Cruden, NASA - National Aeronautics and Space Administration

Funding Institution

Fundação para a Ciência e Tecnologia

2020

“*It’s like building medieval cathedrals. The guy who sets the first stone,*
will never see it done in his lifetime.”

Acknowledgments

I would like to acknowledge all the people who have contributed to making this work a reality. My girlfriend Eva, my parents, Luís and Cristina, my brothers, David and João Miguel, my step-mother Carla and of course my cat Curie. I would also like to thank António Rito Silva for proofreading and grammar checks. Besides those already mentioned, there is a host of extended family and friends too numerous to name, but to whom I would also like to express my sincerest thanks.

An acknowledgement to IPFN and its members in general, my fellow APPLAuSE cohort C3 students and the different programme directors, Luís Lemos Alves, João Pedro Bizarro and Vasco Guerra. A special thanks to members of the group where I worked, the N-PRiME Group, Jorge Loureiro, Carlos Pintassilgo, Nuno Pinhão, Tiago Silva, Polina Ogloblina, Loann Terraz, Duarte Gonçalves, Ricardo Ferreira and also the former members Luís Fernandes, Antonio Tejero-del-Caz, Maria Castela and Marija Grofulovć. The staff of IPFN is also not forgotten, specially Carla Reis and Carmo Nunes.

During my PhD I was also hosted in the University of Illinois at Urbana-Champaign (UIUC) as a visiting scholar. A heartfelt acknowledgment to Marco Panesi who hosted me in UIUC as well as members of the group where I was inserted and worked alongside for a year, Amal Sahai, Andrea Alberti, Robyn MacDonald, Simone Venturi, Vegnesh Jayaraman, Maitreyee Sharma, P.R., Alberto Messina and Alessandro Munafo.

Besides the ones I have already mentioned, I also had the opportunity to meet, by email or in person with several people who have helped me enhance my knowledge through discussions and lent me their expertise. These are, Pedro Caridade, Carlos Murilo Rocha, Brett Cruden, Xinchuan Huang, Aaron Brandis, Olivier Guaitella, Ana Sofia Morillo-Candas, Cristophe Laux, Erwan Pannier and Adrien Lemal.

Lastly, this work could not have been without my advisors Mário Lino da Silva and Bruno Lopez, to whom I owe very much.

Abstract

CO_2 kinetic and radiative vibrational state-to-state processes (STS) are explored in this work. Better insights into these processes may lead to more efficient spacecraft design for Mars atmospheric entries, and better understanding on the dynamics of physical-chemical processes for CO_2 plasma sources

The kinetic models developed in this work include an extension of the Forced Harmonic Oscillator (FHO) theory to the collisional dynamics of triatomic molecules. The FHO does not suffer from many shortcomings such as First Order Perturbation Theories such as SSH, while remaining computationally affordable, making it a very attractive theory at contemporary level. Other improvements to the state of the art include a better accounting of the dissociation pathways and the modelling of the excited $^3B_2$ state. Other important chemical processes in CO_2 gases and plasmas were accounted for, and in particular the reaction $CO_2 + O \longleftrightarrow CO + O_2$ was studied extensively, since it is found to significantly contribute to the decomposition of CO_2 and may as well play a key role in recombination processes through the inverse $CO+O_2$ reaction. Strong evidence of CO_2 dissociation being a two-step process through this exchange reaction is found, either from the bibliography research, and from the state-specific kinetic simulations carried out in this work. The obtained model was compared to available experimental shock-tube data, outperforming macroscopic chemistry models, and reproducing the observed experimental trends of decreasing characteristic dissociation times, while showing a reasonable agreement absolute values comparisons between experimental/synthetic decomposition times.

Contemporary radiative databases for carbon dioxide are not tailored for full spectrum calculations necessary for atmospheric entry spacecraft design. To this end, the well-known rovibrationally specific CDSD4000 database for CO_2 was refitted, using well known spectroscopic polynomial expressions, to obtain a vibrationally specific database. The presented method may be applied to databases for any arbitrary linear polyatomic molecule, yielding vibrationally specific data with the correspondingly compact data size, more performance friendly than detailed databases such as CDSD. The refitting procedure introduces some loss of detail since fitted polynomials cannot reproduce data with full accuracy. Once alternative methods for computing broadening effects are accounted for, the refitted database, dubbed CDSDv, is able to reasonably reproduce calculated and experimental spectra found in literature, particularly in the 4.3 μm spectral region the most significant contributor to the radiative features of CO_2 Infrared radiation.

In the last chapter of this work, several venues for improvement of both the kinetic and radiative model are discussed at length.

Keywords: CO_2, non-equilibrium, databases, radiation, kinetics

Contents

1 Introduction **1**

1.1 Motivation 1

1.2 Scope 2

1.3 Output 3

2 State-of-the-Art **6**

2.1 Structure of CO_2 6

2.1.1 The meaning of T_{v_2} 9

2.2 Kinetics 11

2.2.1 Thermal dissociation 11

2.2.2 Low-temperature non-equilibrium processes 15

2.2.3 Brief Outline of the FHO Theory 19

2.3 Aerothermal and Radiative Databases for Mars Exploration Missions 21

2.3.1 USSR/Russia Mars Missions 21

2.3.2 US Mars Missions (pre-2012) 22

2.3.3 Acknowledging the Impact of CO_2 Radiation 23

2.3.4 Mars Exploration Missions Planning (post-2012) 26

3 Kinetics Modelling **28**

3.1 Theory 28

3.1.1 Internal modes of gas species 28

3.1.2 Boltzmann distribution 30

3.1.3 Partition functions 32

3.1.4 Continuity and conservation equations 33
3.1.5 Classification of Equilibria 35
3.1.6 Detailed balance 38
3.1.7 State-to-state 40
3.1.8 Governing Equations 41
3.2 Models 43
3.2.1 Forced Harmonic Oscillator 44
3.2.2 Vibronic Transitions 46
3.2.3 Redistribution of exchange rates 47
3.2.4 Constant number of collisions approximation 48
3.3 Kinetic Scheme Development 49
3.3.1 Carbon Dioxide kinetics characterization 49
3.3.2 Rate generation 57
3.3.3 Macroscopic Chemistry 61
3.3.4 Final dataset 67
3.3.5 Underlying assumptions and restrictions 67
3.4 Results 70
3.4.1 Rates Dataset 71
3.4.2 Theoretical test cases 73
3.4.3 Comparison with experiments 76
3.5 Recap 79

4 Radiation **81**

4.1 Theory 81
4.1.1 Elementary Radiative Processes 81
4.1.2 Line Parameters 83
4.1.3 Diatomic molecules 84
4.1.4 Triatomic molecules 88
4.1.5 Refitting of ro-vibrational data 91
4.1.6 Broadening 97

4.1.7 Lineshape treatment 100
4.2 Applications 102
4.2.1 Comparison with other databases 102
4.2.2 Comparison with experimental results 108
4.3 Recap 126

5 Conclusions 128

5.1 STELLAR CO_2 kinetic model 129
5.1.1 Inclusion of different collision partners and state-to-state kinetics for diatomic molecules 129
5.1.2 Improved modeling of intermode vibrational transitions 129
5.1.3 Accounting for resonant processes 130
5.1.4 Inclusion of radiative processes 130
5.1.5 Uncertainty in the $CO_2 + O \longleftrightarrow CO + O_2$ process 131
5.1.6 Reduced order methods 133
5.1.7 Further steps beyond the state-of-the-art 135
5.1.8 The need for further experimental data 140
5.2 CDSDv radiative model 143
5.2.1 Future Developments 145

A Fluid governing equations 172

A.1 Time and Space Marching governing equations 172

B Reduced mass for each vibrational mode 176

B.1 Ground state 176
B.1.1 Symmetric stretch 176
B.1.2 Asymmetric stretch 177
B.1.3 Bending 177

C Determination of FHO parameters 179

C.1 Morse Potential 179

C.2 Bending mode V–T rates determination 181
    C.2.1 Symmetric and Asymmetric V–T rates determination 181
    C.2.2 v_1, v_2, and v_3 V–V–T rates determination 189

List of Abbreviations

ARAS - Atomic Resonance Absorption Spectroscopy

CDSD - Carbon Dioxide Spectral Databank, optimized for 4000, 1000 or 296 K

CDSDv - The vibrationally specific database refitted from CDSD4000

CFD - Computational Fluid Dynamics

CFRD - Computational Fluid Radiative Dynamics

EAST - Electric Arc Shock Tube

ESA - European Space Agency

ESTHER - European Shock-Tube for High Enthalpy Research

EXOMOL - Radiation database for exoplanets and hot atmospheres

FHO - Forced Harmonic Oscillator

FTIR - Fourier Transform Infrared Spectroscopy

FOPT - First Order Perturbation Theory

FWHM - Full Width Half Maximum

GASPAR - Radiation database, also known as GDPR

HITEMP - Radiation database inspired on HITRAN but calibrated for higher-temperatures

HITRAN - Radiation database for low-temperatures

HWHM - Half Width Half Maximum

IVT - Intermode Vibrational-Translational (processes)

IR - Infrared

JAXA - Japanese Aerospace Exploration Agency

LHS - Left Hand Side

LPP - Laboratóire de Physique des Plasmas

MIPT - Moscow Institute of Physics and Technology

MSL - Mars Science Laboratory

MWIR - Midwave Infrared

NASA - National Aeronautics and Space Administration

NIST - National Institute of Standards and Technology

NPRIME - The research group inside IPFN where this work was mainly developed

PES - Potential Energy Surface

QCT - Quasi-Classical Trajectory

RADIS - Radiation code

RHS - Right Hand Side

RKR - Rydberg-Klein-Rees

SPARK - Software Platform for Aerothermodynamics, Radiation and Kinetics

SPARK line-by-line - The line-by-line in-house code at NPRIME

SPECTRA - Online portal for the surveying and simulation of radiative data with several databases

SSH - Schwartz, Slawsky and Herzfeld

STELLAR - A kinetic state to state database

STS - State-to-State

TPS - Thermal Protection System

UV - Ultraviolet

VD - Vibrational-Dissociation (processes)

VT - Vibrational Translational (processes)

VUT - Combustion-Driven Shock Tube at MIPT

VVT - Vibrational-Vibrational Translational (processes)

List of Symbols

A_{ij} - Einstein A coefficient of transition $i \rightarrow j$

A_v - Vibrational part of the Einstein coefficient

$A^{J'}_{J''}$ Rotational part of the Einstein coefficient

B_{ij} - Einstein B coefficient of transition $i \rightarrow j$

B_v - Coefficient of polynomial expansion $F(J)$

c - Speed of light

c_2 - Second radiation constant hc/k_B

c_i - Mass fraction of mode, level or species i

C_V - Heat capacity of the gas at constant volume

C_p - Heat capacity of the gas at constant pressure

D_v - Coefficient of polynomial expansion $F(J)$

e - Internal energy of the gas in chapter 3

E_m - Well depth in a Morse potential

E_n - Energy of mode n or energy of the gas

f - Distribution function

$f_{\mathrm{CO_2}}$ - number density fraction of $\mathrm{CO_2}$

f_{CO} - number density fraction of CO

$F(J)$ - Polynomial expansion to obtain rotational energy levels of vibrational level v

$F(m)$ - Herman-Wallis polynomial, $m = -J$, $J(J+1)$ and $(J+1)$ for P, Q and R branches respectively

$F(\overline{\nu})$ - Line profile at spectral position $\overline{\nu}$

$\boldsymbol{F}$ - Force vector

g_n - Degeneracy of mode or level n

$G(v)$ - Energy coefficient dependent on vibrational level v

h - Planck's constant

$\hbar$ - Planck constant divided by 4π

H - Enthalpy of the gas

H_v - Coefficient of polynomial expansion $F(J)$

J - Rotational number

J_s - Bessel functions of the first kind and order s

k, K - Reaction rate coefficients

k_B - Boltzmann's constant

l_2 - Vibrational angular momentum

L_{ij} - Radiance of transition $i \to j$

M - Mach number

M_i - Molar mass of species i

$\tilde{m}$ - reduced mass of the two molecules involved in a collision

n_m - Number density of mode, species, level m

N_a - Avogadro's number

N_m - Number of particles or particle density where m is a mode, level or species

p - Pressure

P - Probability of transition or process to occur or a Polyad number

P_{ij} - Line profile of transition $i \to j$

Q_n - Partition function of mode, level or species n

r - Radius or distance

$\boldsymbol{r}$ - Position vector

$S_{l'J'}^{l'J'}$ - Hönl-London coefficient for transition defined by $l'J' \leftrightarrow l'J'$

S_V and S_{VV} - Steric factors

R - Universal gas constant

R_i - Specific gas constant, R/M_i where M_i is the molar mass of species i

t - Time

T - Temperature

$T(e)$ - Energy coefficient dependent on electronic level e

u - Blackbody radiation function or energy

v_n - Vibrational number where n corresponds to a number assigned to a mode

v - Velocity

$\boldsymbol{v}$ - Velocity vector

x_i - Molar fraction of mode, species, level i

$Y_{n,m}$ - Dunham matrix coefficient of row n, column m

Z - Classical Collisional Frequency

Other symbols

α - Absorption coefficient, conversion factor of CO_2 or the repulsive term of a potential

α' - Correction to the absorption coefficient due to self-absorption

β - Inverse of k_BT

γ - Mass parameter

$\Delta\overline{\nu}_P$ - Broadening due to collisional effects or Doppler effect

ε - FHO parameter

ε_k - Internal energy of mode, level or species k

$\varepsilon_{\overline{\nu}}$ - Emission coefficient at spectral position $\overline{\nu}$

Θ - Molecule specific constant, equal to c_2B_v

Λ_{ij} - Escape factor of transition $i \rightarrow j$

μ - Reduced mass of the internal oscillatory movement

ν_{ij} - Frequency of transition $i \rightarrow j$ or the stoichiometric coefficient of species i in reaction j

ν - Line position of a transition in frequency Hz

$\overline{\nu}$ - Line position of a transition in cm^{-1}

ρ - Mass density or FHO parameter

$\rho_{\overline{\nu}}$ - Radiation density in the spectral position $\overline{\nu}$

σ - Collision cross section

τ - Transmittance

τ_n - Characteristic time scale of process n

$\boldsymbol{\tau}$ - Stress tensor

ϕ_n - Fractions of partition function of mode n or FHO parameter

ω - Angular frequency of an oscillator

$\dot{\omega}_k$ - Mass source/sink term of mode, level or species k

$\dot{\Omega}_k$ - Energy source/sink term of mode, level or species k

Chapter 1

Introduction

1.1 Motivation

It is the stated goal of the world's leading space agencies to further the exploration of Mars, including manned missions in the next few decades. Spaceships suitable for manned missions to Mars deal with an assortment of challenges all of which require dedicated works to deal with. Particularly, the radiative heating experienced by spacecraft upon atmospheric entry is proportional to the dimension and shape of the spacecraft. A manned mission, with all the risks and rewards at stake, requires detailed knowledge of the heating experienced while descending. This becomes even more crucial when dealing with manned missions to Mars. The atmosphere on Mars is thin requiring a blunt shape to take advantage of what little drag there is to brake the spacecraft. However, the main component of Mars atmosphere is CO_2 with residual presence of N_2 and other species which creates the ideal environment for heating a spacecraft by radiation. A low ballistic coefficient spacecraft would be ideal to counteract radiative heating but it would not allow sufficient deceleration. Thus, Mars spacecraft tend to have blunt bodies and deal with surface heating by allowing greater than usual safety margins on thermal protection systems (TPS) (nowadays about 40–50%). As such, detailed knowledge on CO_2 kinetic and radiative processes is the main driver for this work, which might contribute for the improvement of safety margins and more efficient spacecraft design.

The most specific way of detailing kinetic processes is to build state-to-state (STS) models. In such models, interactions are specified on an internal state basis which can greatly escalate the amount of equations to be solved for any given problem. As such, it shares the promise for better detail in the description of molecular physical-chemical processes with the burden of increased complexity and computational overhead. There are tools which reduce the computational cost of state-specific models, so called reduced order models. However these still require STS data as input for calibration and will only be as good as the data that is fed onto them. Given the bottleneck nature of STS modelling, improving the state of the art becomes a desirable outcome of CO_2 research. This must generally be carried out in two fronts, radiation and kinetics as in a Martian atmosphere the dissociation degree and radiative heating by CO_2 are important quantities that will influence TPS design.

1.2 Scope

CO_2 is a linear triatomic molecule with three vibrational modes. A rotational-vibrational STS model would quickly become computationally intractable due to the excessive number of individual ro-vibrational states. As such, models developed in this work are solely vibrational state specific. Therefore, this work will be focused on the development of new vibrational STS kinetic and radiative models for CO_2.

Kinetic STS models for CO_2 belong to one of two categories: a) Analytical models, including First Order Perturbation Theory (FOPT) methods such as the Schwartz, Slawsky and Herzfeld (SSH); and b) more sophisticated trajectory methods such as the Quasi-Classical Trajectory (QCT). The former is currently the go-to model for CO_2 STS kinetics in the aerothermal and plasma communities while the latter has yet to be applied in large scales due to it's computational expense. The SSH theory may only account for single quantum jumps and relies on the scaling of known experimental low-level rates to obtain higher-level rates. This procedure may lead to non-physical values for collision probabilities in high-temperature regimes in which multi-quantum jumps are non-negligible. As such, the SSH theory is not adequate for atmospheric entry flows where high-temperature and non-equilibrium conditions are pervasive. An alternative to SSH and QCT models is the application of the Forced Harmonic Oscillator (FHO) theory to the CO_2 molecule. FHO is able to model multi-quantum jumps and does not yield non-physical probabilities in high-temperature regimes. However some adaptation of the existing theory, originally derived for diatomic molecules, must be made. This is performed in this work along with an analysis of the qualitative behaviour of this model and the role of the $CO_2+O \longleftrightarrow CO+O_2$ reaction in the decomposition of CO_2.

Current state-of-the-art IR radiation databases for CO_2 such as CDSD4000 are ro-vibrationally specific and, with such an amount of data, these databases are correspondingly large taking up to several GBs of hard-drive space. Furthermore, these databases are spectrally organized, built by defining local cut-off criteria for single line strengths at an optimized temperature (in the case of CDSD4000, 4000 K) and additionally, the broadening coefficients in such databases assume only self-broadening or air-broadening, meaning that detailed simulated spectra with other mixtures may not be well matched to experimental data. These characteristics make databases such as CDSD4000 less than optimal for use in spacecraft radiative heating calculations where the inclusion of the overall spectral range of CO_2 transitions is mandatory. To create a database better suited for atmospheric entry flow, there must be a reduction of database size, independence of the temperature optimization and still allow the reproduction of ro-vibrational levels of detail. In this work,the refitting of CDSD4000 for this purpose is performed and the result is a vibrationally specific database: CDSDv. This resulting database is more compact, fitting in an email attachment, and allows the separation of rotation and vibrational modes and is able to obtain a reasonable agreement with experimental and simulated high-temperature spectra.

The layout of this thesis is as follows: Chapter 2 will review the state of the art for kinetic and radiative data on CO_2, and includes a brief segment on the development of the FHO theory. Chapter 3 deals with the theory and development of the FHO model for CO_2, as well as the results obtained from the kinetic scheme. Chapter 4 deals with the theory and creation of the CDSDv database, as well as all the test cases the database has been applied insofar. Finally chapter 5 deals with the major conclusions of this work as well as a discussion on future work to improve the developed databases.

1.3 Output

This work has yielded the following peer-reviewed articles

1. "Heavy-Impact Vibrational Excitation and Dissociation Processes in CO_2" - ***J. Vargas***, *B. Lopez, M. Lino da Silva* June 2020 (*under peer review*)

2. "CDSDv: A Compact Database For The Modeling of High-Temperature CO2 Radiation" - ***J. Vargas***, *B. Lopez, M. Lino da Silva*, Journal of Quantitative Spectroscopy and Radiative Transfer, 245, April 2020.

Furthermore, this work has been presented in the following conferences

1. "" - ***J. Vargas***, *B. Lopez, M. Lino da Silva* - Design for Demise Workshop - 09/2020
2. "High Temperature Applications Of New Vibrationally Specific Kinetics and Radiation Models For CO_2" - ***J. Vargas***, *B. Lopez, M. Lino da Silva* - AIAA SciTech Forum and Exposition - 01/2020
3. "STELLAR CO2: A database for vibrationally-specific excitation and dissociation rates for Carbon Dioxide" - ***J. Vargas***, *B. Lopez, J. Loureiro, M. Lino da Silva* - 8th Workshop on High-Temperature Gases in Atmospheric Entry (RHTGAE) - 03/2019
4. "CDSD-vib: A vibrationally specific database refitted from ro-vibrational specific data" - ***J. Vargas***, *B. Lopez, M. Panesi, M. Lino da Silva* - 8th Workshop on High-Temperature Gases in Atmospheric Entry (RHTGAE) - 03/2019
5. "Refitting of Ro-Vibrational Specific CO2 Radiation Database to Vibrationally Specific" - ***J. Vargas***, *B. Lopez, M. Panesi, M. Lino da Silva* - AIAA SciTech Forum and Exposition - 01/2019
6. "Refitting of detailed CO2 IR databases to vibrationally specific databases tailored for aerothermodynamic flows" - ***J. Vargas***, *B. Lopez, M. Panesi, M. Lino da Silva* - AIAA Aviation Forum - 06/2018

and the following posters:

1. "Heavy Impact Dissociation of Carbon Dioxide" - ***J. Vargas***, *B. Lopez, M. Lino da Silva* Cold Plasmas: Fundamentals and Applications - 09/2019
2. "New Models For High-Temperature CO2: Gateway to Mars" - ***J. Vargas*** - FCT Science Meeting ("Encontros da ciência") - 07/2019
3. "Simulation of CO2 Shock Tube Experiments" - ***J. Vargas*** - PhD Open Days - 04/2019
4. "Refitting of CDSD to a vibrationally specific database" - ***J. Vargas***, *B. Lopez, M. Lino da Silva* - School on Hyper Meteroid Entry Physics (HyMEP) - 10/2017

5. “A reinvestigation on the energy levels of CO2 up to the dissociation limit” - ***J. Vargas***, *B. Lopez, M. Lino da Silva* - International Conference on Partially Ionized Gases (ICPIG) - 07/2017
6. “Non-Equilibrium High-Temperature CO_2” - ***J. Vargas*** - APPLAuSE Workshop - 01/2017

Chapter 2

State-of-the-Art

This chapter deals with the state-of-the-art of Carbon Dioxide modelling in kinetics and radiation. Firstly, a description of CO_2 is made, the vibrational modes, notations and other things relevant to understand this work. Secondly, a review of the vibrational state-to-state kinetic modelling of CO_2 is carried out and in the third section the same is carried out for radiation.

2.1 Structure of CO_2

Carbon Dioxide is a triatomic linear molecule with 3 so-called vibrational modes: symmetric stretch, bending and asymmetric stretch. Symmetric stretch is usually denoted as v_1, *ss* or just *s* and corresponds to the symmetrical change in bond length between the C=O bonds. The asymmetric stretch is denoted v_3, *as* or *a* and corresponds to a stretching of one of the bonds with simultaneous compression of the other. The bending mode is denoted v_2, *be* or just *b* and corresponds to the deviation from linearity of the molecule by the two C=O bonds. As the bonds can bend in two directions, the bending mode is doubly degenerate if there is any vibrational angular momentum l_2, associated with the bending motion. The possible l_2 values are v_2, $\mathrm{v}_2 - 2$, v_2-4, ..., 1 or 0 and the degeneracy is 2 except when $l_2 = 0$ for which degeneracy is 1. The vibrational angular momentum is usually represented as $\mathrm{v}_2^{l_2}$. Some authors do not represent l_2, choosing to only deal with the vibrational modes $\mathrm{v}_1\mathrm{v}_2\mathrm{v}_3$ for a complete assignment of a CO_2 vibrational state. In this case, the degeneracy of bending is $\mathrm{v}_2 + 1$. A true complete vibrational assignment of CO_2 makes use of l_2 and is denoted as $\mathrm{v}_1\mathrm{v}_2^{l_2}\mathrm{v}_3$. This notation is the so-called Herzberg notation [1]. However, it is often seen and is useful to keep $\mathrm{v}_2 = l_2$ and as such, another vibrational assignment is needed to denote cases where $v_2 \neq l_2$. This assignment is usually denoted r, the so-called ranking number and as such, the complete vibrational assignment of CO_2 state is usually written as $v_1v_2l_2v_3r$ where the numbers $v_2 = l_2$. This notation is the one introduced by the Air Force Geophysics Lab [1]. Increasing by one the ranking number, with all other assignments remaining the same, correspond to decreasing v_1 by 1 and increasing v_2 by 2. This is connected to the Fermi resonance phenomenon where levels which are close in energy and share the same molecular symmetry are shifted in respect to their expected values. In CO_2 such a resonance is observed in the low-lying levels of symmetric and bending with the vibrational frequencies $\omega_1 \approx 2\omega_2$. The number of possible r numbers for a given combination of $v_1v_2l_2v_3$ is v_1+1 and all possible r values have the same molecular symmetry. This is so, since the symmetric stretch does not change molecular symmetry (and as such is IR inactive) and the bending mode only changes the symmetry through l_2. Another possible notation for CO_2 levels is the Amat notation [2] which for non-coupled levels is written in the same shape as Rothman's notation. The difference is when denoting levels which share the same molecular symmetry and as such are prone to be perturbed by Fermi resonance. When dealing with a group of N levels the Amat notation is written $(v_{1,\mathrm{max}}v_{2,\mathrm{min}}^{l_2}v_3,v_{1,\mathrm{min}}v_{2,\mathrm{max}}^{l_2}v_3)_X$ where X is a number written in Roman numbering. The assignments inside the parenthesis correspond to the true vibrational numbers for the lowest and greatest ranking numbers. The vibrational angular momentum is then allowed to be different from v_2. X is then the ranking number written in Roman numbering. Table 2.1 contains examples of the notations of vibrational levels of CO_2 discussed in this work.

Table 2.1: Possible notations for vibrational level assignment of CO_2.

Herzberg	Amat	AFGL
00^01	$(00^01)_\mathrm{I}$	00011
12^20	$(12^20,04^20)_\mathrm{I}$	12201
04^20	$(12^20,04^20)_\mathrm{II}$	12202
05^50	$(05^50)_\mathrm{I}$	05501
05^30	$(13^30,05^30)_\mathrm{II}$	13302
05^10	$(21^10,13^10,05^10)_\mathrm{III}$	21103

In the scope of this work, a definition of the ro-vibrational assignment of CO_2 is also required. Given a combination of $\mathrm{v}_1\mathrm{v}_2 l_2 \mathrm{v}_3 r$, there is an absolute minimum for rotational numbers J of the vibrational state which is equal to l_2. This does not mean that $J_{\min} = l_2$ but rather $J_{\min} \geq l_2$. In the cases where $l_2 = 0$, the possible J numbers are even or odd and, as such, $J_{\min}$ might be 1 or 0. In cases where $l_2 > 0$, $J_{\min} = l_2$. Then, the possible rotational numbers for $l_2 = 0$ are $J = J_{\min}, J_{\min} + 2, ..., J_{\max}$ where $J_{\max}$ is the last bound rotational state for a given combination of $\mathrm{v}_1\mathrm{v}_2 l_2 \mathrm{v}_3 r$. In cases where $l_2 > 0$, $J = l_2, l_2 + 1, ..., J_{\max}$. One of the things that also distinguish CO_2 ro-vibrational states from one another are the e/f symmetries. These symmetries are important when ro-vibrational radiative processes are modeled. A ro-vibrational assignment $\mathrm{v}_1\mathrm{v}_2 l_2 \mathrm{v}_3 r J$ can only have either e or f symmetry. If $l_2 > 0$, odd J numbers have a single symmetry while even J numbers have the other. In the cases where $l_2 = 0$ and only odd or even J numbers are possible, only one symmetry exists either e or f.

Fermi resonance is an effect in which vibrational levels with the same molecular symmetry and a small energy gap are observed shifted in the spectrum, with a bigger energy gap and with line intensities different than those expected. This is usually interpreted as a coupling between the symmetric and bending modes of CO_2 [3]. While it is not a specific effect of CO_2, it is used to justify the widespread approximation of a single temperature to characterize the symmetric and bending modes. In this work, no *a priori* coupling between the symmetric and bending mode can be admitted. As will be seen ahead in section 3.3.1 the included bending levels are considered to be $\mathrm{v}_2 = l_2$ and as such, there are no symmetric levels with the same molecular symmetry and therefore, no mode coupling is considered in this work. Furthermore, it cannot be reasonably assumed that the small energy gap condition for Fermi Resonance to occur is maintained higher in the vibrational ladder where anharmonicity leads to a wider gap between the "would-be" resonant states. As such, resonances between levels higher in the vibrational ladder are accidental which ties in to the concept of *vibrational chaos*. These concepts and other possible approaches for the modelling of higher levels of CO_2 are discussed more in depth in chapter 5. It is also worth mentioning that Fermi resonances in the level energies, depending on gas conditions, do not always translate to symmetric and bending levels populations in equilibrum [4, 5, 6, 7, 8], and that the fitting of high-resolution FTIR spectra in the 4.3μm region (as discussed in section 4.2.2) may be relatively insensitive to the v_1 and v_2 level populations (as defined in each respective work), which means that the error bars in the fits allow for a great latitude of interpretation of the level populations for symmetric and bending states, which may be considered with separate temperatures ($T_{\mathrm{v}_1} \neq T_{\mathrm{v}_2}$) [9] or with equivalent temperatures ($T_{\mathrm{v}_1} = T_{\mathrm{v}_2}$) [10] indistinguishably [11]. The next section will present a discussion on what references [4, 5, 6, 7, 8] actually contain as well as what it means to have $T_{\mathrm{v}_1} = T_{\mathrm{v}_2}$.

A final note on Fermi resonance: the unperturbed energies of CO_2 levels 10001 and 10002 are approximately 1332 and 1334 cm^{-1} respectively but the observed energies for these levels are 1285 and 1388 cm^{-1}. The work of Amat [2] suggests that the lower energy value should be assigned to the symmetric stretch mode $(10^00{,}02^00)_{\mathrm{I}}$ and the higher value to the bending mode $(10^00{,}02^00)_{\mathrm{II}}$, the same was pointed out in the report by McClatchey *et al.* [12]. However this does not bear any practical consequences in this work as the aforementioned report [12]: “It seems vastly preferable always to label the upper level 10001 and the lower 10002”. In this work the perturbed values are only used in the context of chapter 4, which follows the convention set by McClatchey *et al.* and references [13, 14, 15] (as well as others), the higher energy level is labeled with the lower r number and the lower energy level is labeled with the higher r number. This means that the second and third lines of the last column in table 2.1 should be switched according to the work of Amat [2].

2.1.1 The meaning of T_{v_2}

Several works on the topic of CO_2 usually reference the temperature of the bending mode with a 2 in the subscript: T_{v_2} or T_2. The question is which levels define or are defined by T_{v_2}? In the context of chapter 3, this temperature is defined as a fit to a Boltzmann distribution of the population of the energy levels with bending excitation which, in this work, are all of the form $0\mathrm{v}_2^{\mathrm{v}_2}0$. In chapter 4 and in the context of CO_2 infrared radiation, T_{v_2} can only be defined by assuming an internal partition function as done in [16]. Since the vibrational part of the partition function is determined by direct summation, only a general vibrational temperature T_{v} is defined. In works such as [17, 3] the bending modes are lumped together with the corresponding symmetric modes which are Fermi resonant, henceforth resulting in a CO_2 model with only two vibrational modes. In the work of Silva *et al.* [18] the bending mode temperature is defined as in this work (chapter 3), and the other bending levels are considered to be part of the symmetric stretch mode through Fermi resonance, and it is additionally stated that T_{v_1} and T_{v_2} “are very close”. Indeed, the work of Grufolović *et al.* [19] explains the assumption of a common temperature for the symmetric and bending mode (both defined as in [18]). This is justified through the Fermi resonance effect between symmetric and bending levels, lumped together in a single mode and “the similarity of energy levels and rate coefficients involving Fermi and non-Fermi bending levels”. This assumption may lead to a good match between experiments and simulations, however it cannot be guaranteed to stand in the general case of a gas containing CO_2, leading to the assertion in the previous section: “Fermi resonances in the level energies, depending on gas conditions, do not always translate to symmetric and bending levels populations in equilibrium” whatever the definition of T_{v_2} that includes bending levels. Note that this is an extremely low bar to set, as this statement only requires a single example where symmetric and bending populations are not defined by the same temperature to be true. Whether T_{v_2} is defined by all bending levels or by non-Fermi resonant bending levels and $T_{\mathrm{v}_1} \neq T_{\mathrm{v}_2}$ then it is insufficient to simply invoke the Fermi resonance phenomenon to assume equality in the generality of cases. To explore this further, it is worthwhile to examine what the works cited in this context mean [4, 5, 6, 7, 8]. The work of Rosser *et al.* [4] studies the relaxation of symmetric CO_2 level 10^00 in several gas mixtures using a CO_2 laser system, injecting excess populations in the mixture and monitoring the return to equilibrium. The general assumption was that the v_1 and v_2 levels were believed to be “tightly–coupled”. The authors state in the conclusion that “the mechanism of relaxation is more involved than implied by a ’tight-coupling’ model” and “during relaxation the population distribution within v_1–v_2 is not describable using a single vibrational temperature”. At the end Rosser *et al.* also state that if one assumes a strong Fermi coupling between 10^00 and 02^00, the remainder of the v_2 ladder (01^10 and 02^20) should also be included in the coupling. It can be speculated from this that the kinetic coupling between the symetric stretch is stronger with the levels of the form $0\mathrm{v}_2^{\mathrm{v}_2}0$ than the coupling through Fermi resonance. This is also suggested by the works of Brodnikovskii *et al.* [5] and Millot & Roche [6]. Brodnikovskii *et al.* [5] uses two-photon Raman excitation combined with coherent active Raman-scattering spectroscopy (TRE-CARS) to probe (separately) the relaxation of an out of equilibrium 10^00 and 02^00 levels in CO_2. The authors found that these levels interacted preferably with others including 01^10, 02^20 and 11^10 for 10^00 and 01^10, 02^20 and 03^10 for 02^00 but not with each other. Millot & Roche [6] used a laser to excite selected ro-vibrational states of CO_2 and monitored the relaxation of the vibrationally excited states to equilibrium. Like in [5], Millot & Roche concluded that the quenching of the level 10^00 goes preferentially through the bending mode levels 01^10 and 02^20 rather than through the Fermi resonant state 02^00, even providing reaction rate coefficients for some of these processes, suggesting non-equilibrium coupling between these states. Together with the work of Rosser *et al.* [4], the works of Brodnikovskii *et al.* [5] and Millot & Roche [6] sugest two things: Not only can Fermi resonant levels be uncoupled, the bending levels of the form $0\mathrm{v}_2^{\mathrm{v}_2}0$ may also be uncoupled from the symmetric states. The work of Losev [7] contains a discussion on the $10^00 \longleftrightarrow 02^00$ reaction. Besides considering several estimations and experimental values, it states that if the rate of this process is below a certain threshold the equality $T_{\mathrm{v}_1} = T_{\mathrm{v}_2}$ must be renounced. Losev continues by stating that when "high-degree of accuracy is required, the breakdown of the equality of T_{v_1} and T_{v_2} [...], can be found to be very important" and that "For rather rough evaluations, it is generally assumed that $T_{\mathrm{v}_1} = T_{\mathrm{v}_2}$", henceforth assuming $T_{\mathrm{v}_1} = T_{\mathrm{v}_2}$ for the rest of the work [1]. Finally, the work of Allen *et al.* [8] experimentally measures the rate constants of the v_1–v_2 (considered to be the collection of 10^00, 02^00, 01^10 and 02^20 levels) in the low temperature range (170–300 K), for a variety of mixtures. The relevant part of this discussion is the acknowledgment by the authors that not all mixtures will ensure the coupling of the 10^00, 02^00, 01^10 and 02^20 levels: "Thus by a careful choice of mixture composition it is possible to ensure that the (bs) levels are maintained in equilibrium even for mixtures containing a low percentage of CO_2"[2]. Thus, it is fair to say that the assumption of $T_{\mathrm{v}_1} = T_{\mathrm{v}_2}$ should not be considered the general case and should not be justified solely by Fermi resonance.

2.2 Kinetics

2.2.1 Thermal dissociation

Shock-tube investigations of thermal dissociation rates for CO_2 were initiated in the mid-60's of the past Century, in support of Mars/Venus exploration missions.

Brabbs [21] carried out shock-tube experiments for a highly diluted CO_2/Ar mixture around 2,500-2,700 K, using two complementary techniques: 1) a single pulse technique where the gas is shocked and successively quenched by a rarefaction wave, freezing the

---

[1] An interesting comment found in [7] is the reference to the work of Likal'ter [20] where for low anharmonicity of the vibrational ladders and in conditions where VV processes dominate over VT processes, the symmetric and bending modes may be considered as a single mode. Once again this is not a general case, but probably a useful reference for low-temperature plasmas.

[2] (bs) levels means the 10^00, 02^00, 01^10 and 02^20.

chemistry and allowing chemical analysis; 2) measurement of CO_2 near-UV chemiluminescence bands[3]. Both measurement techniques provided similar results. Davies carried out shock-tube experiments in high dilution CO_2/Ar mixtures, with post-shock temperatures in the range of 3,500-6,000 K [22] and 6,000-11,000 K [23]. The first work probed the emission of the IR vibrational bands of CO_2 at 2.7/4.3 μm whereas the high-temperature study additionally measured the CO_2 chemiluminescence bands. The comparison between both measurements showed an order of magnitude difference, providing evidence that dissociation/recombination processes of CO_2 might be a multi-step process. Michel [24] measured reflected shockwaves IR radiation at 4.3 μm in diluted CO_2/Ar and CO_2/N_2 mixtures, in the range T=2,800-4,400 K. These studies were followed through by Fishburne [25] and Dean [26] who measured IR radiation (at 2.7/4.3 μm for Fishburne, 4.3 μm for Davis) in 3,000-5,000 K shock-tube flows, for CO_2/Ar mixtures (and CO_2/N_2 mixtures for Fishburne), again with a high dilution ratio. Generalov and Losev [27] measured the rate of dissociation for CO_2 without dilution from other mixtures, probing the CO_2 near-UV chemiluminescence bands through absorption spectroscopy, in the 3,000-5,500 K range. Kiefer [28] carried out shock-tube experiments for a highly diluted CO_2/Kr mixture in the 3,600-6,500 K range using a laser Schlieren technique. Hardy [29] and Wagner [30] measured reflected shockwaves IR radiation at 4.3 μm and CO + O chemiluminescence in the near-UV in un-diluted CO_2 mixtures, in the T=2,700-4,300 K and T=3,000-4,000 K ranges respectively. Finally, Ebrahim [31] complemented the work of Generalov and Losev, determining the rate of dissociation of pure CO_2 in the 2,500-7,000 K range, using a Mach–Zender interferometry technique[4].

These initial measurements showed a significant scattering between the different dissociation rate values, but also in the dissociation activation energy, which ranged from 2.9 to 4.6 eV [31] [5]. Potential explanations for these large uncertainties were attributed to the effects of impurities in the gas [32, 33], or to a failure in reducing the systematic errors in the measured quantities [33]. Another potential source of uncertainty [34, 35] stems from the fact that dissociation products (atomic oxygen) may react with CO_2, further dissoci-

---

[3] $CO + O + M \longleftrightarrow CO_2{}^* + M$ followed by $CO_2{}^* \longrightarrow CO_2 + h\nu$.

[4] A common characteristic of most of these early studies is the presence of CO_2 in a highly diluted gas bath of either Ar, Kr, or N_2 so as to avoid the establishment of significant endothermic reactions as, for example, Ar has a rather large ionization energy of 15.76 eV and N_2 a rather large dissociation energy of 9.79 eV, hence keeping a high post-shock-temperature.

[5] The bond dissociation energy of CO_2 to $CO(^1\Sigma) + CO(^3P)$ being 5.52 eV.

ating it (reaction $O+CO_2 \longleftrightarrow CO+O_2$). This means that the measured dissociation rate of CO_2 (assessed through the measurement of CO_2 concentrations) is in fact an effective rate resulting from a two-step process (dissociation of CO_2 and dissociative recombination of O and CO_2). Clark further studied the dynamics of $O+CO_2$ interactions using different isotopes of atomic oxygen [36].

Another proposed explanation was that dissociation proceeded through a two step mechanism[6] consisting of the collisional excitation of CO_2 to an upper electronic state, followed by dissociation:

$$\mathrm{CO_2(^1\Sigma) + M \rightarrow CO_2^* + M} \tag{2.1}$$

$$\mathrm{CO_2^* \rightarrow CO(^1\Sigma) + O(^3P)} \tag{2.2}$$

with Brabbs proposing that ${CO_2}^*$ corresponds to $CO_2(^3\Pi)$ [21], and Fishburne proposing that ${CO_2}^*$ corresponds to either $CO_2(^3B_2)$ or $CO_2(^1B_2)$ [25]. However, such propositions were not entirely satisfactory, since this implied potential curve crossings below the dissociation limit, and that further energy was still required for dissociation [37]. This led to the understanding that detailed knowledge on the potential energy surfaces for the excited electronic states of CO_2 was needed.

To allow improved insights on the dynamics of thermal CO_2 dissociation, later studies focused on measuring the concentrations of atomic oxygen through Atomic Resonance Absorption Spectroscopy (ARAS) at 130 nm. This allowed avoiding ambiguities derived from the measurement of CO_2 concentrations, such as having additional processes that lead to the depletion of CO_2 (e.g. the aforementioned $O + CO_2 \longleftrightarrow CO + O_2$ reaction). Fuji [37] used an ARAS technique for reflected shockwaves in diluted CO_2/Ar mixtures, in the 2,300-3,400 K range. The determined rate had an activation energy of 3.74 eV. Burmeister [38] used the same technique to determine CO_2 dissociation rates in diluted CO_2/Ar mixtures, in the temperature range 2,400–4,400 K. The activation energy was found to be 4.53 eV. Eremin [39] investigated the chemiluminescence radiation in pure CO_2 shocked flows and developed a simplified kinetic model that allowed concluding that above 3,000 K, part of the dissociation products were composed of excited oxygen $O(^1D)$, and not only $O(^3P)$. In a later experiment, Eremin [40] carried out ARAS measurements in shocked CO_2/Ar diluted mixtures in the 4,100-6,400 K temperature range to determine the fraction

---

[6] Since the dissociation of the ground electronic state of CO_2 to the ground states of CO and O is spin-forbidden.

of excited oxygen O(^{1}D) produced during CO_2 dissociation. He found out that O(^{1}D) amounted to 0-10% of the dissociation products. Park [41], in the scope of the development of his Mars entry kinetic model, considered the results from Davies [22, 23], fitting them to an Arrhenius expression where the activation energy was constrained to the accepted CO_2 dissociation energy, and the pre-exponential factor set to $n = 1.5$. Ibragimova [42] carried out a critical review of past works, proposing a CO_2 dissociation rate valid in the 300-40,000 K temperature range, for different colliding partners (Ar, diatomic molecules, CO_2, C, N, and O). She also proposed a dissociation coupling factor $Z(T, T_v)$ for accounting for thermal non-equilibrium conditions during dissociation. Saxena [43] claimed that the anomalous low activation rates were the result of rapid secondary loss of CO_2 via the reaction $\mathrm{O} + \mathrm{CO_2} \longleftrightarrow \mathrm{CO} + \mathrm{O_2}$. Activation rates of more recent experiments, discarding this effect, are systematically above 4.3 eV. A pressure dependence on the dissociation rate, noticeable at higher pressures, was also found. Jaffe [44] claimed that the explanation for the low activation energy laid in the transition from the ^{1}X to ^{3}B$_2$ state, being the rate-determining step for CO_2 dissociation. In a follow-up work, Xu et al. [45] reviewed the past works and proposed an effective rate in the range 2,000-10,000 K.

Vibrational relaxation and dissociation incubation times

Vibrational relaxation and dissociation incubation times for the dissociation of CO_2 have been derived by some authors from the aforementioned shock-tube dissociation measurements. These imply firstly developing analytical master equation models and then applying them to the measurements of time-dependent data from shock-tube experiments.

Weaner [46] compared the density relaxation times τ_E through Mach–Zender interferometry and the v_3 mode relaxation time through measurement of the 4.3 μm bands, Weaner considered that the energy in the v_3 mode is less than 8% of the other v_1 and v_2 modes and even less at lower temperatures, and that as such $\tau_E = \tau_{\mathrm{v}_{1,2}}$. The obtained values for τ_E and τ_{v_3} were equivalent in the temperature range 450–1,000K, leading to the conclusion that all the vibrational modes of CO_2 relax at the same rate.

Simpson [47] studied vibration relaxation in shocked flows in the range T=360-1,500K, for pure CO_2 gases, and for CO_2 diluted in nitrogen, deuterium and hydrogen, with an emphasis on the deactivation of the bending mode. The obtained results put into evidence different behaviours at low and high temperatures, wherein a strong dependence from the collisional partner reduced mass exists at high temperatures, but not at low temperatures.

Oehlschlaeger [48, 49] carried out several shock-tube experiments, investigating the dissociation of CO_2 behind reflected shock waves at temperatures in the 3,200–4,600 K range and pressures in the 45–100 kPa range. This has been done probing the CO_2 UV bands (B→X transition) in absorption using an UV laser, with a sampling rate in the millisecond range. Oehlschlaeger also carried out an extensive review of previous works regarding dissociation incubation times and reproduced his experiments through a simplified one-dimensional energy-grained master equation model. The obtained results highlight the importance for knowing the average energy $\langle \Delta E \rangle$ transferred through a collision, for the whole, p, T range. Unfortunately, no shock speed values are reported, preventing the selection of his experimental work as a suitable test-case.

The incubation times obtained by Oehlschlaeger were deemed too high by Saxena [43], who carried similar experiments using a laser Schlieren experimental technique, and found much lower incubation times in the temperature range T=4,000-6,600K, for CO_2−Kr mixtures. Saxena found that full vibrational equilibrium was reached before the onset of dissociation.

2.2.2 Low-temperature non-equilibrium processes

Room-temperature non-equilibrium processes in CO_2 were the subject of a large amount of research studies at about the same time, in the wake of the development of the first CO_2 lasers [50]. Namely, the vibrationally-specific resonant reaction

$$\mathrm{CO_2(001) + N_2(0) \longleftrightarrow CO_2(000) + N_2(1) + 18\ cm^{-1}} \tag{2.3}$$

was acknowledged as key to the inversion of the upper populations in CO_2-N_2 lasers [51, 52, 53, 54, 55, 56]. Interestingly, several measurements evidenced that a minimum of the rate for this process was reached at around 1,000 K, with a rate increase both at lower and higher temperatures. This behavior could not be expected to be explained by standard kinetic models like the Landau-Teller theory, which predicts increasing rates with increasing temperature, no matter the temperature range. To account for this low-temperature behavior, Sharma and Brau suggested [57] that the rate increase at lower temperatures could be attributed to long-range attractive forces between the dipole moment of $CO_2(v_3)$ and the quadrupole moment of N_2. On this basis, they proposed the Sharma–Brau perturbation theory that has been very successful at reproducing this class of kinetic processes, predicting a temperature dependence of the order $T^{-1/2}$ in the low-temperature region, as opposed to the $T^{3/2}$ temperature dependence in the high-temperature range, attributable to short-range (nonadiabatic) repulsive forces. Fig. 2.1 presents a list of the measured rates for process 2.3, alongside with predicted rates from the SSH, FHO, and Sharma–Brau theory.

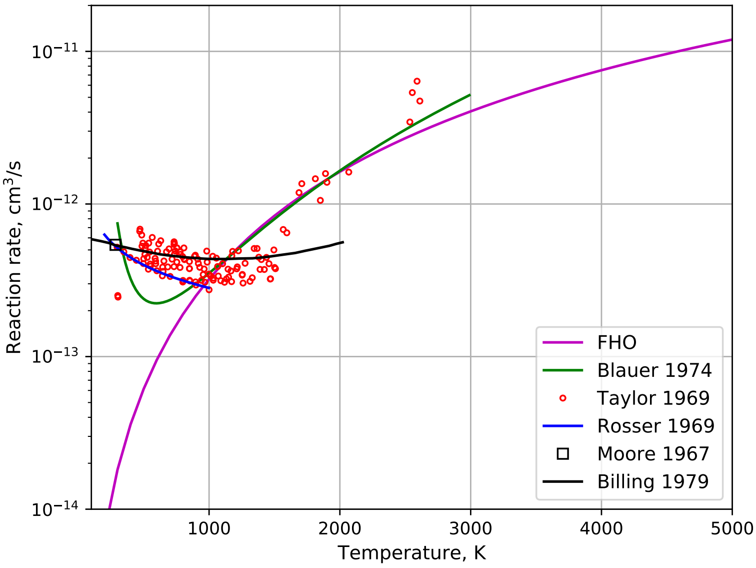

Figure 2.1: Comparisons of rate coefficients [56, 58, 59, 51, 60] for the reaction $CO_2(001) + N_2(0) \longleftrightarrow CO_2(000) + N_2(1)$.

In the wake of these experimental and theoretical developments, a significant number of vibrationally-specific exchange rates have been measured for the three vibrational modes of CO_2 and a great deal of collisional partners (both atomic and polyatomic [7, 61]).

In the late 70's of the last Century, a new venue for the investigation of low-temperature vibrational non-equilibrium processes in CO_2 was opened by the investigation of the key vibrational excitation processes:

$$CO_2(000) + O \rightarrow CO_2(0n0) + O \tag{2.4}$$

$$CO_2(0n0) \rightarrow CO_2(000) + h\nu \tag{2.5}$$

which have been recognized [62, 63] to be the main contributor to the cooling of upper planetary atmospheres (Venus, Earth, Mars) trough the removal of translation energy from oxygen atoms by the bending mode of CO_2 (eq. 2.4), and the subsequent radiation of energy away from the atmospheric layer (either towards the ground or towards Space eq. 2.5). This has led to an extensive number of theoretical and experimental works that have put a strong emphasis on the improvement of low-temperature, neutral kinetic models for

CO_2.

More recently, plasma reforming of CO_2 into Syngas has been proposed as a potentially viable option for producing CO_2-neutral fuels [64, 65, 66, 67]. This is achieved in microwave plasma sources, through the electron-impact excitation of the vibrations of CO_2. This has led to renewed studies on the modeling of low-temperature CO_2 plasmas, with the development of detailed kinetic models for this specific application [17, 68, 69, 18], the investigation of alternative high-power microwave [70], or gliding arc [71] plasma sources, the modeling of complex hydrodynamic effects [72], or the investigation on improving the efficiencies of this technique [73]. Last but not least, the spectroscopic analysis of high-resolution spectra in plasma sources alongside the reconstruction of emission/absorption spectra using synthetic line by line codes is a powerful technique that has been pioneered, among others, by C. Laux [74, 75, 76]. This allows obtaining time dependent internal level populations which then can be used for calibration of kinetic model. Recent experimental works have measured the lower-vibrational levels of CO_2 in the discharge and post-discharge regions through Fourier Transform Infrared Spectroscopy (FTIR) [16, 9, 10].

As it can be inferred from these recent works, mostly published in the last decade, the modeling of CO_2 non-equilibrium processes appears to be a contemporary “hot-topic”. One may trace this to the seminal book by Fridman [65] which extensively reported and discussed past topical theoretical and experimental works, mostly of USSR origin. The theoretical methodologies discussed in this book were all but adopted by the contemporary plasma chemistry community, working as a *de-facto* standard approach. In parallel, much effort was put into reproducing the experimental work discussed in this work, with an emphasis on reaching energy efficiencies for CO_2 dissociation as high as reported therein. It is relevant to review both of these aspects, in an effort for understanding the current *status-quo* on this topic.

The proposed pathways for CO_2 dissociation by means of vibrational excitation in nonequilibrium plasmas start with an electron energy input in the range 1–2 eV. This provides excitation of low vibrational levels of CO_2 which then excite higher levels through V–V ladder-climbing processes. Finally a non-adiabatic transition to the excited electronic state $X^1\Sigma \rightarrow ^3B_2$ takes place, followed by dissociation. Based on the works by Rusanov et al.[77] and Rusanov, Fridman, & Sholin, [78], Fridman considers that only the assymetric mode v_3 contributes for this up-pumping process, as the other mode (lumped bending and symmetric bs) has small enough energy spacings that V–T de-excitation processes dominate over V–V up-pumping processes, since typically $T < T_v$.

The CO_2 conversion efficiencies of several classes of experiments in achieving such dissociation processes are extensively reviewed by Fridman. The maximum thermodynamical efficiency for dissociation in thermal plasmas is claimed not to exceed 43–48%[79, 80, 81, 82], with quasi-equilibrium arc discharges achieving efficiencies of no more than 15%[83]. Fridman points out that increased efficiency may be achieved for non-thermal plasmas, with efficiencies up to as 30% for electron impact dissociation, achieved through plasma radiolysis using high-current relativistic electron beams at atmospheric pressure[84, 85, 86, 87, 88, 89]. If the pressure is reduced, the combination of electronic and vibrational excitation allows conversion efficiencies in the range of 20–50% for plasma-beam experiments[90, 91]. Fridman concludes that even higher efficiencies may be achieved in nonequilibrium discharges at moderate pressures, with conversion efficiencies of 60% for a pulsed microwave/radiofrequency discharges in a magnetic field n the conditions of electron cyclotron resonance[92, 93]. Finally, for flowing plasmas, conversion efficiencies as high as 80% and 90% are reported for subsonic[84, 85, 86, 87] and supersonic[94, 95, 96] flows respectively. These high efficiencies are claimed to be reached for input energies in the range 0.8–1.0 eV/molecule, and may be explained by the decrease of the gas translational temperature through the subsonic and supersonic expansions, hindering the V–T de-excitation processes. In particular, the maximum efficiency of 90% is achieved for near-hypersonic plasma flows with Mach numbers in the range $M = 3 - 5$.

All the sources cited by Fridman correspond to works carried out in the later 70's/early 80's USSR. Such high efficiencies have to date not been reproduced, with a review by Ozkan [97] finding that no atmospheric plasma sources achieve a energy efficiency above 15%. Also of importance is the fact that no atmospheric plasma source can reach a fraction of converted CO_2 higher than 25%, meaning that plasma reforming of CO_2 in large quantities is not yet a viable economic endeavor. More recently, Bongers [98] carried out a set of experiments on a vortex-stabilized, supersonic 915MHz microwave plasma reactor, achieving CO_2 conversion efficiencies in the range of 47–80% and energy efficiency in the range of 35–24% for an energy input in the range 10.3–3.9 eV/molecule. Upon increasing the mass flow of CO_2 (from 11slm to 75slm), the energy input may be reduced to the range 1.9–0.6 eV/molecule, which is deemed as optimal by the Fridman review. In this case the energy efficiency increases, showcasing a range of 51–40%, however the

CO_2 conversion output decreases significantly, to the range 11–23%. Further analysis were carried out for a subsonic 2.45GHz microwave plasma reactor, wherein a maximum energy efficiency of 46% was achieved. Of particular interest is a comparison of these results with the ones presented by Fridman, wherein the obtained efficiencies stayed well below the ones reported by Fridman, even for similar experience conditions.

Recent modeling works have further laid the theoretical foundations [17, 99] to which most of the subsequent published numerical models for CO_2 adhere. Reference transitions are considered for the first vibrational levels of CO_2 [59, 100, 101], and SSH scaling laws are applied for determining transition rates for higher vibrational levels. A few sample rates include[102, 99]

$$k^{\mathrm{CO_2}}_{\mathrm{v_2+1\to v_2}} = k^{\mathrm{CO_2}}_{010\to 000}(\mathrm{v_2}+1) \tag{2.6}$$

for V–T processes;

$$k^{\mathrm{CO_2}}_{\mathrm{v_1+1,v_2+1,v_3\to v_1,v_2,v_3+1}} = k^{\mathrm{CO_2}}_{110\to 001}(\mathrm{v_1}+1)(\mathrm{v_2}+1)(\mathrm{v_3}+1) \tag{2.7}$$

for V–V–T processes, among others.

Energy levels are approximated by a simple anharmonic oscillator [103], up to the dissociation limit, which is considered to lie in the crossing to the $^3B_2$ state at about 5.5 eV. Dissociation occurs when a molecule in the $\mathrm{v_3}$ level jumps to a $\mathrm{v_3}+1$ level above this energy limit, dissociating with a probability of one. Typically the maximum quantum number for $\mathrm{v_3}$ is considered to lie at 21 [17].

2.2.3 Brief Outline of the FHO Theory

Here a brief discussion on the development of the FHO model is made. This is intended as a reference recap and not a extensive review. A more in depth review for atmospheric entry studies may be found on [104]. The SSH theory was proposed in 1952 [105] and has been continually developed and improved since the 50's/60's. Shortly thereafter, Rapp & Sharp [106] in 1955 computed transition probabilities in the high-velocity regime using both SSH theory and a more exact quantum calculation. The results showed the SSH method could not yield adequate results in the high-temperature regime. Treanor in 1965 [107] firstly applied what would henceforth be known as the Forced Harmonic Oscillator, using the derivations from Kerner in 1958 [108]. Treanor's method consisted of constraining the wavefunctions of molecules to a harmonic oscillator, effectively forcing the wavefunction to behave as one of Kerner's solutions, in a 1D collision with an atom. The semi-classical solution of Treanor showed the correct asymptotic behavior in the high-velocity regime. In 1968 Zelechow, Rapp and Sharp [109] extended the treatment put forward by Treanor to collisions of two molecules, thus opening the way to the calculation of V–V–T probabilities. The theory then was somewhat left dormant for the next decades, before more powerful computational resources were made available, allowing to tackle the increased computational complexity for this theory. Additional improvements to the theory would come only in the 90's, where the work of Adamovich, Macheret, Rich and Treanor [110, 111] further advanced the theory by introducing the simmetrization of collision velocities and the so-called steric factors to account for isotropy of collisions. Additionally, they validated the FHO theory against three dimensional quasi-classical trajectory (QCT) calculations for N_2 and found remarkable agreement in the $200 - 8,000$ K range. This work was performed with the traditional polynomial extrapolation for Nitrogen levels, v$= 0 - 40$. We note that a more adequate calculation for the manifold of N_2 levels was proposed by Lino da Silva et al. one decade later [112]. Further advances were made by Adamovich and Rich [113] to include the effects of rotation in a collision between a diatomic and an atomic species, Adamovich made the generalization for the inclusion of rotation in two colliding diatomics [114]. Macheret also introduced later corrections, most notably the correction for the anharmonicity of levels [115]. In the late 2000's and early 2010's, the FHO theory was extensively deployed in several works by Lino da Silva, Guerra, Loureiro and Lopez [116, 117, 118, 119, 120], culminating in a vibrational STS model for five species air, N_2, NO, O_2, N and O [121]. The most recent work [120] used FHO rates for molecule to molecule interactions and QCT rates for molecular-atomic interactions. While not as sophisticated as complex quantum calculations, the FHO theory was also shown to be on par with aforementioned complex methods on simple cases of vibrational excitation and de-excitation. Indeed, in [104], FHO is considered to be accurate compared to QCT methods when calculating non-reactive rates, while representing a fraction of the computational overhead. Additionally, it can compute arbitrarily small probabilities in contrast with QCT which requires a minimum threshold for the determination of transition probabilities [104]. These are some advantages which complement more accurate calculations made by other authors and with it comes the acknowledgment that the FHO theory has a place in modern non-equilibrium works.

2.3 Aerothermal and Radiative Databases for Mars Exploration Missions

It is somehow surprising that the issue of CO_2 radiation influence on Martian entries has been discarded up until so recently. It may further seem surprising that this did not preclude many spacecraft from successfully reaching Mars. However this can in part be attributed to the engineering margins considered in these spacecraft designs, and the fact that radiative heating typically remains inferior to convective heating. The exception is in the base region where it doesn't lead to excessively high heat fluxes owing to the low densities encountered in this recirculation region.

The first efforts to correctly account for CO_2 IR heating may be traced to the Mars PREMIER program [122, 123] sponsored by the French Space Agency CNES[7] and the AURORA program [124] sponsored by the European Space Agency (ESA) which took over once the Mars PREMIER program was terminated. These took place in the beginning of the 21st Century, and gathered several European and Russian research teams, which undertook some early works outlining the importance of these effects. Later on, the importance of these radiative heating effects was also acknowledged by several research teams in the US which provided additional key contributions, namely at the experimental level. Here, the different US and Russian missions that were launched towards Mars without accounting for any radiative heating effects will be outlined (all the Russian Mars exploration missions, and all the US Mars exploration missions up to Mars Science Laboratory in 2012). This is followed by an historical account of the different efforts that led to this phenomena being nowadays recognized as an important design driver for Mars missions.

2.3.1 USSR/Russia Mars Missions

All USSR/Russian missions to Mars have failed to achieve a successful landing. Mars 2 crashed, Mars 3 successfully landed but stopped transmitting after 20s, Mars 6 lost contact prior to landing, Mars 7 missed Mars, and Mars 8 (Mars 96) suffered a failure during the injection to a trajectory towards Mars and reentered the atmosphere.

---

[7] in collaboration with NASA, as a staging for a Mars Sample Return mission

2.3.2 US Mars Missions (pre-2012)

US Mars exploration missions have historically neglected CO_2 IR radiative heating until very recently.

The second lander to touch down the surface of Mars, Viking 1 in 1976, was developed without any previous test carried out in a ground test facility simulating a Martian-like CO_2 atmosphere [125]. It nevertheless was the first lander to successfully touch down the surface of Mars[8], following an atmospheric entry at a velocity of 4.5 km/s and an entry angle of 11° [126, 127]. The Viking probe was instrumented with stagnation pressure and temperature sensors, as well as four additional pressure transducers and a mass spectrometer in the forebody. The backshell had an additional pressure transducer and two thermocouples. This entry data has since been extensively reviewed and rebuilt by several authors, since it constituted for many years the only available post-flight data for a Martian entry [125].

Pre-flight analysis predicted that afterbody heating would account for 3% of stagnation-line heating, and that radiation would be totally negligible owing to the low entry velocity [125]. However, 5% heating relative to stagnation-line heating reference was measured instead. Recent reinvestigations accounting for CO_2 radiative heating showed that this difference might indeed be due to neglecting these heating effects in the original analysis [128, 129].

The subsequent 1996 Mars pathfinder mission considered a faster entry at a velocity of around 7.5km/s. Pre-flight analysis had to consider ablation effects in the CFD analysis, however radiation heating effects were once more neglected [125], with Gupta's pre-flight analysis predicting that radiative heating would account for less than 4.5% of total heating [130]. The probe was instrumented with accelerometers, 9 thermocouples, and 3 platinum resistance thermometers. The latter did not perform well due to calibration problems, with only the thermocouple data being valid [125]. Pre-flight experimental campaigns were carried in the HYPULSE shock-expansion tube with different gas mixtures including CO_2, with negligible dissociation in the free-stream flow [131], and the NASA LaRC 31 Mach 10 wind-tunnel for estimating the probe wake flow. These last experiments were carried solely on air [132].

Other NASA missions like the Mars Polar Lander (6.9 km/s; failure during entry), Mars Exploration Rovers (5.4 km/s; success; for MER-A and 5.55 km/s; success; for

---

[8] following the failure of the USSR Mars 3 mission

MER-B), and Phoenix (5.7km/s; success) missions, made use of the same assumptions regarding radiation (see Reynier [125] and references therein). These probes were not instrumented as regarding their entry phases, and as such, no post-flight data is available for these.

The following mission, Mars Science Laboratory, is the largest space vehicle to ever have entered Mars, having done it successfully. The probe has a 4.5 m diameter, and entered Mars at 5.6km/s in 2012. Owing to the increased risks for this mission, it underwent an extensive pre-flight test campaign, namely in which pertains to transition to turbulence effects. Several tests were carried out in the CUBRC LENS and Caltech T5 shock tunnels [125]. The probe itself had an extensive instrumentation package named MEDLI, which monitored temperature, pressure and TPS (Thermal Protection System) performance in the probe forebody. No radiative heating sensors were included, as radiation was again considered negligible [133] [125]. Ref. [134] provides a synthesis of all the experimental and numerical activities carried out in preparation of this mission.

2.3.3 Acknowledging the Impact of CO_2 Radiation

As mentioned before, European efforts regarding Mars exploration may be traced back to the Mars PREMIER/Mars Sample Return project, a joint CNES/NASA venture aiming at a return of Samples from Mars surface to Earth. The early mission definition considered the direct insertion in Mars of the Mars Sample Return Orbiter (MSRO) designed by CNES [135, 136, 137]. The challenges for performing such a maneuver[9] (requiring precise guidance as the orbiter descends significantly in Mars atmosphere), and the high thermal loads involved (mandating an heat shield), fostered several European research activities related to Mars entry aerothermodynamics. For example two Ph.D. thesis were funded by this program, one related to the modelling of free-molecular CO_2-N_2 flows [138], and the other related to CO_2-N_2 plasmas radiation [139].

Ultimately, difficulties in enabling such an ambitious programme, funding difficulties, as well as a shifting political climate, led to the cancellation of such programme. In the meanwhile, ESA had launched the AURORA programme, chiefly aimed at the robotic exploration of Mars, as a stepping stone to a Mars Sample Return mission and ultimately a manned Mars exploration mission. A workshop titled “Radiation of High-Temperature

---

[9] Which only has been partially achieved by the Russian Zond 6 and Zond 7 probes during their Lunar return trajectories

Gases in Atmospheric Entry" (RHTGAE) has been held biannually since 2003, which has been chiefly focused on the radiative heating effects of atmospheric entry flows [140, 141, 142, 143, 144, 145, 146, 147, 148]. The workshop defined a set of testcases tailored for the examination of radiative properties for gases of different compositions and different levels of thermodynamic equilibrium (ranging from thermochemical equilibrium to strong non-equilibrium of the species internal modes). Among these, the TC3 testcase focused on a 70° sphere-cone geometry which is a simplified configuration of the MSRO vehicle [149, 150]. Reference CFD solutions were proposed to the teams who wished to only simulate the radiative proper, but nevertheless, a significant number of CFD simulations were carried out by different teams. An INTAS project [151] was also devoted to the TC3 configuration, including CFD, radiative transfer and ground-test experiments of a scale model [152]. This work was carried out by five Russian (ICAD, IPM, NIIMech, SPU, TsAGI), and two European institutions (Office national d'études et de recherches aérospatiales, ONERA and Von Karman Institute, VKI).

Radiative heating for this spacecraft configuration has been modelled considering different numerical approaches and using different radiative databases: The EM2C team at École Centrale de Paris used their in-house HITELOR radiative database [153, 154], based on a statistical narrow-band model, and developed from a set of CO_2 and CO spectral coefficients valid at high temperature, obtained both in-house and adapted from the HITEMP database [155]. The databank has been successfully applied to the reproduction of medium-resolution spectra at temperatures up to 2850 K [156]. Radiative transfer on the backcover of TC3 was carried out using a Ray-Tracing model, considering both line-by-line and statistical narrowband models. The agreement of the obtained results for both the reference (line-by-line) and the approximate (statistical narrowband) models validated the later approach, for the one-temperature case, allowing fast and efficient simulations of CO_2 IR radiation in this configuration. These results were presented at the 1st. RHTGAE workshop [157].

Surzhikov used increasingly refined CFD and radiative approaches since 2001 [158], where a one-temperature, chemical non-equilibrium CFD model was used coupled to a multigroup radiative database based on HITRAN. Radiative transfer was modeled using a modified discrete ordinates method. Further works used improved physical models, namely in what pertains to CFD simulations, where multitemperature models, including the influence of thermal non-equilibrium on chemistry were considered [159, 160]. A coupling between flow and radiation was ensured by injecting divergence of radiative flux in the energy equation for the CFD model. The model was applied to the TC3 testcase, with the determination of a CFD solution and the subsequent calculation of radiative heating [161]. The computed heat fluxes were in agreement with the previous solutions from EM2C. Surzhikov also carried CFRD (Computational Fluid Radiative Dynamics) simulations on other US Mars entry vehicles, namely Pathfinder [162, 163] and Mars Science Laboratory [163]. As for TC3, it was found that radiative heating from the IR region was not negligible, even exceeding convective heating in some regions of the leeward flow.

In 2002, ONERA started developing the PHARAON computing chain, comprised of the CelHyo2D CFD solver [164, 165], coupled to the radiative heat transfer solver ASTRE, which is a Monte Carlo solver enabling the treatment of 3-D geometries using unstructured meshes [166, 167, 168]. The ASTRE code was initially developed for the study of turbulent flames in the presence of soot. The EM2C radiative database is utilized by this platform. The simulation results for the TC3 test-case were presented in Ref. [169], with again the same results than the previous authors.

Finally, IPFN-IST (Instituto de Plasmas e Fusão Nuclear - Instituto Superior Técnico) relied on the CO_2-N_2 radiative database developed by Lino da Silva [139], implemented in the SPARTAN Line-by-Line code [170, 171]. The CO_2 line-by-line database was developed from the 1992 HITRAN database [172], using the same theoretical approach than the one used for developing the HITELOR database [155]. Radiative transfer for the TC3 configuration was computed using a ray-tracing approach, both for the forebody and the backshell, considering the reference two-temperature solution from the workshop booklet [173]. This work found essentially the same results than the previous ones, and further found that the influence of thermal non-equilibrium did not have a significant impact on the computed radiative heat fluxes. Further applications of this radiative database were carried out in the scope of the unsuccessful tracking of the PHOENIX entry by the Mars Express orbiter, as it was not capable of switching its IR thermal detectors. CFD simulations were carried with a Direct Simulation Monte Carlo (DSMC) code, and a simplified radiative transfer model showed that the IR radiative signal would be several orders of magnitude above the VUV signal (from the CO 4th Positive system). The outcome of this work was published in Ref. [104, 174]

These different results obtained for TC3 showed good agreement regarding the radiative heating trends and absolute values. Radiative heating in the forebody remained within the margins of convective heating, however in the backcover it exceeded significantly the convective heating values, due to the radiation from the spacecraft wake. Namely, the radiative heating values (of the order of W/cm^2) were deemed too large, requiring for the backshell to have a certain amount of thermal protections.

2.3.4 Mars Exploration Missions Planning (post-2012)

The ESA EXOMARS mission was the first Mars Exploration mission that was designed considering the effects of CO_2 and CO IR radiative heating. Initial plans accounted for a single mission of a large entry vehicle carrying a rover. However, this required a heavy launcher (PROTON-M/Ariane-5). Further, it was found that the radiative fluxes would mandate a backshell TPS of about 12 kg. Eventually, these uncertainties, as well as the necessity of testing Mars entry technologies for what was an European first, led to a redefinition of the program into a two-stage mission: A first launch of an orbiter (Mars Trace Gas Orbiter) and a fully instrumented lander in 2016, followed by a second launch of a larger lander including the rover in 2018 (since then postponed to 2020). The Phase B of the mission was managed by Fluid Gravity Eng., who performed the CFD simulations. IPFN-IST performed radiative transfer calculations using the same ray-tracing model than for TC3. A further code-to-code comparison was carried out with Surzhikov, who simulated the same spacecraft configurations [175]. As for the TC3 test case, the simulation results showed that over 99.95% of radiative heating would come from CO_2 and CO IR radiation [176]. Another interesting feature of the probe was its instrumentation package, who was capable of determining static pressure, surface temperatures, radiative heat flux rates and total heat flux rates, both in the forebody and backshell.

Schiaparelli entered Mars atmosphere on the 19th October 2016, at a velocity of about 5.8km/s, and collected data from its sensor package throughout all of its entry phase. This data was relayed to the orbiter and retrieved in its entirety, except for the blackout phase data that was stored for a later post-landing transmission. Unfortunately the probe was lost due to a software malfunction which led to the premature stopping of the descent engines and the discarding of the descent parachute. As such, the data for the blackout phase, including the peak radiative heating, was lost. Nevertheless the retrieve of data still contains an interesting amount of information which makes it useful for a test-case. The details on the post-processing for this data may be found in reference [177].

Further developments in the US, roughly after the Mars Science Laboratory mission, started looking into the issue of IR radiation with more detail. For example, teams from NASA Ames participated in the later issues of the ESA radiation workshop, and this fostered an interest in trying to measure experimentally IR radiation from CO_2 flows in shock-tubes and shock-tunnels, which provided the more realistic ground-test conditions. Around that time, the EAST shock-tube was in the process of being refurbished, alongside with its instrumentation, therefore efforts were put into achieving a capability for carrying measurements in this spectral region [178]. A first batch of CO_2 IR measurements was carried out in EAST around 2010 [179], which confirmed the presence of a strong radiative signal. Around the same time the numerical tools for radiative prediction were being overhauled. Although some works had been carried out in the 90's regarding IR radiation in wake flows [180], there had been no follow-up since, and radiative tools like NEQAIR were lacking the appropriate spectral models. As the CDSD4000 database was published around this time [14], it was integrated to the NEQAIR code, using a simplified pseudo-continuum approach [181]. Since then, more detailed experimental campaigns were carried out on EAST, focusing on Mars entries [182]. These works further cemented the relevance of CO_2 IR heating in the scope of NASA missions for Mars exploration [183]. Lastly, the Mars Science Laboratory flight data was reinterpreted in view of the presence from CO_2 radiation [184], and the available Schiaparelli flight data was also reproduced recently to a good agreement with these new improved radiative models [185].

Nowadays, no question remains about the necessity to account for IR radiative heating in Mars entry flows, and all aerothermal databases account for these effects in one way or another, which allows reducing the uncertainties in TPS design, leading to lighter TPS, more room for payloads, and more confidence in designing ever larger entry spacecrafts in preparation of a Manned Mars mission.

Chapter 3

Kinetics Modelling

> “*These are my rates, if you don’t like them I have others.*”
>
> - NPRIME Cientist

The results in this chapter will be published in “Heavy-Impact Vibrational Excitation and Dissociation Processes in CO_2” by ***J. Vargas***, *B. Lopez, M. Lino da Silva* currently under review.

3.1 Theory

3.1.1 Internal modes of gas species

In general, a gas in composed of atomic and molecular species. If the gas is sufficiently heated, ionization also occurs and this generates atomic and molecular ions and electrons. Within the Born–Openheimer approximation [186, 187], the energy of a molecule may be computed as the sum of translational and internal energy:

$$E_{\text{tot}} = E_{\text{tra}} + E_{\text{int}} \tag{3.1}$$

and in turn, the internal energy is separated into the internal modes of a species:

$$E_{\text{int}} = E_{\text{ele}} + E_{\text{vib}} + E_{\text{rot}}. \tag{3.2}$$

For the sake of completeness, we may note that this approximation brings several theoretical challenges, namely at the statistical physics level [188], nevertheless, for most of practical applications, this approximation holds reasonably well.

In the equation above, the first term on the right-hand side (RHS) is the electronic energy, corresponding to the different ways electrons can be arranged in the orbitals of molecules. The second term on the RHS is the vibrational energy corresponding to the changes in length and angle of the bonds of atoms that make up a molecule. The third term is the rotational energy, corresponding to the energy of rotation of a molecule. In the case of atomic species, where bonds are non-existent and the nucleus is considered symmetrical, there is no vibrational or rotational energy. Free electrons have no discrete internal structure and as such only have translational energy. The contribution of each mode to the total energy is also not a continuous function but rather a set of discrete values. Additionally, the typical spacing in energy of each mode is varied, with the inequality $E_{\text{ele}} > E_{\text{vib}} > E_{\text{rot}} > E_{\text{tra}}$ usually holding true. Figure 3.1 is a representation of the spacing between energy levels of each mode. The collection of a modes energy levels becomes a so-called energy ladder which molecules climb provided some energy input from the outside the system or stored in another mode. The spacing of the translational energy ladder is very regular and short, it is often approximated as a continuum of energy. The rotational mode has a very regular spacing initially but levels grow apart as the ladder is climbed. Vibrational levels also have a regular spacing initially but contrary to rotation levels become closer together. Electronic levels are considered to have a much larger spacing between levels than any other mode and like vibrational levels they bunch together the higher they go. Just as a question of reference, the energy of a molecule at 0K should be 0 and as such the energy of each mode is defined as:

$$E = (E_{\text{tra}} - E'_{\text{tra}}) + E_{\text{rot}} + (E_{\text{vib}} - E'_{\text{vib}}) + (E_{\text{ele}} - E'_{\text{ele}}) \tag{3.3}$$

where E' means the zero point energy of each mode. The rotational mode does not require this offset since the energy of rotation at 0K is already 0. Intuitively, we may guess which kind of processes can occur the fastest. If some external energy is deposited within a molecular gases, the time scale at which this occurs is important. The lowest energy a molecule may absorb should be on the order of the translational energy ladder and as such, this should be the fastest process occurring since it needs the smaller time scale. The same reasoning implies the ordering of other molecular internal processes. If chemical processes are also included as well as ionization and recombination, the ordering of the typical time scales for each process (assuming heavy-particle collisions and not electron-neutral collisions) is [189]:

$$\tau_0 \sim \tau_{\text{tra}} \leq \tau_{\text{rot}} \ll \tau_{\text{vib}} \ll \tau_{\text{che}} \ll \tau_{\text{ele}} \ll \tau_{\text{ion}} \tag{3.4}$$

where τ_0 is the mean time between consecutive collisions, τ_{che} is the time scale for chemical

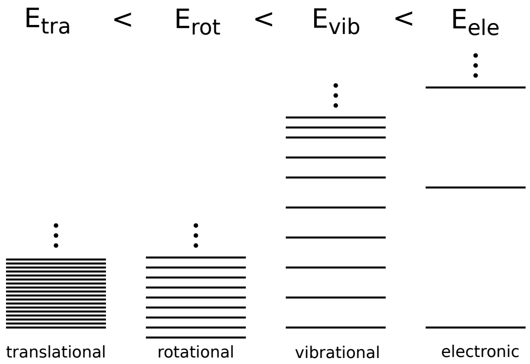

Figure 3.1: Representation of energy modes of a molecule

reactions and τ_{ion} is the time scale for ionization and recombination reactions to occur. This hierarchy is not static as the temperature dependence on each process is different. In high temperatures for example, it can happen that $\tau_{\text{vib}} \sim \tau_{\text{che}}$.

The concept of energy levels is now well defined. A molecule has a discrete energy from the sum of its modes. Lets consider a molecule rotating in the same manner with different orientations of its angular momentum. In the macroscopic scale the energy level is the same but the state of the molecule is not the same. In the microscopic scale, for the same energy level, different states are possible. These are called degenerate states and a degeneracy or statistical weight can be assigned equal to the number of states with the same energy. Besides rotation, the electronic and vibrational angular momentum, electron and nuclear spin are also distinguishable in the microscopic scale while having the same energy. To relate the microscopic and macroscopic state of a gas, the macrostates and microstates of the gas must be defined, which will be done in the next section.

3.1.2 Boltzmann distribution

A mixture of non-reactive chemical species has a finite number of particles in an enclosed volume. These may be counted as:

$$N = \sum_{\text{spe}} \sum_{j} N_j^{\text{spe}} \tag{3.5}$$

where the first sum on the RHS is a sum on all species present in the gas and the second sum is a sum on all levels of a particular species. N_j^{spe} is the total number of particles in each energy level j of a species also called population. For now the summation over all species present in a gas will be dropped for simplicity. If the number of particles in each energy level of a species versus the energy of the levels were plotted, it would be the distribution function of that species. The total distribution of each species is known as a macrostate. If one level has a different population after some time, this is a new macrostate. Each macrostate also has a well defined energy:

$$E = \sum_j E_j N_j \tag{3.6}$$

where E_j is the energy of level j. Considering now two copies of the same gas that has been considered so far with the same number of particles, energy and distributions of chemical species. The only difference between the two gases is that one contains only positive angular momentum of rotating molecules and the other only contains negative angular momentum however the positive and negative angular momentum are defined. Microscopically the two gases are not the same, even if macroscopically they are. The two gases are in the same macrostate but are in two different microstates. A microstate and a macrostate can share the same macroscopic properties, populations and energy but microstates care about the specific arrangement of degenerate states. As such, a macrostate is composed by a number of microstates.

Assuming now a gas in full equilibrium *ie*, the macroscopic properties of the gas do not change, the macrostate corresponding to equilibrium is the one with the greatest prabability of occurring. If all microstates are considered to be equally likely, then the likeliest macrostate is the one with the greatest number of microstates. Indeed, one fundamental assumption of statistical physics is the equal likelihood of each microstate. As long as the number of microstates can be counted, the most likely macrostate can be found and thus the most likely system can too. In the "high-temperature" limit the most probable macrostate can be derived as the Boltzmann distribution:

$$N_j = N \frac{g_j \exp{(-E_j \beta)}}{\sum_j g_j \exp{(-E_j \beta)}} \tag{3.7}$$

where g_j is the degeneracy of level j and $\beta = 1/k_B T$ where $k_B T$ is Boltzmann's constant multiplied by the temperature. The "high-temperature" limit must be taken in one of the steps of the derivation of Boltzmann's distribution. This should not be any source of concern as any temperature above 5 K should be "high-temperature" enough for any real system. The denominator in equation 3.7 is defined as the partition function with symbol Q:

$$Q = \sum_j g_j \exp{(-E_j \beta)}. \tag{3.8}$$

The partition function is a very useful quantity which for a given species depends on temperature and volume.

3.1.3 Partition functions

The population fraction of level j is given by equation 3.7. Specifically, j is a combination of electronic, vibrational, rotational and translational levels. Combining equations 3.1 and 3.7 the total partition function of a molecule is:

$$Q = \left[\sum_{\text{tra}} g_{\text{t}} \exp\left(-\frac{E_{\text{t}}}{k_B T}\right)\right] \times \left[\sum_{\text{ele}} g_{\text{e}} \exp\left(-\frac{E_{\text{e}}}{k_B T}\right)\right] \times \left[\sum_{\text{vib}} g_{\text{v}} \exp\left(-\frac{E_{\text{e,v}}}{k_B T}\right)\right] \times \left[\sum_{\text{rot}} g_{\text{r}} \exp\left(-\frac{E_{\text{e,v,r}}}{k_B T}\right)\right]. \tag{3.9}$$

Each term in the square brackets is considered as the partition function of each mode, meaning the total partition function is the multiplication of each partition function individually. This is useful as each term can be evaluated individually and then multiplied for the total value. The translational partition function can be approximated to a multiplication of integrals which are evaluated to:

$$Q_{\text{tra}} = \left(\frac{2\pi m k_B T}{h^2}\right)^{3/2} V \tag{3.10}$$

where m is the mass of the species, h is Planck's constant and V the volume occupied by the gas which yields the dependence of the partition function on volume. The rotational partition function can also be approximated to a continuous integral instead of a discrete summation. With $g_{\text{rot}} = 2J+1$, where J is the rotational number. The rotational partition function becomes for diatomics:

$$Q_{\text{rot}} \approx \frac{T}{\sigma\Theta} \tag{3.11}$$

where $\Theta = c_2 B_v$, c_2 being the second radiation constant hc/k_B and B_v a spectroscopic constant which is molecule dependent. σ is a symmetry dependent constant, 1 for non-symmetric molecules and 2 for symmetric molecules. The approximation in this case is the better as long as $T \gg \Theta$. For linear polyatomic molecules the rotational partition function can be approximated to:

$$Q_{\text{rot}} \approx \frac{T}{\sigma\Theta} \exp\left[\frac{1}{3}\left(\frac{\Theta}{T}\right) + \frac{1}{90}\left(\frac{\Theta}{T}\right)^2\right]. \tag{3.12}$$

The electronic and vibrational partition functions should be evaluated by their sums. If the electronic level ladder is sufficiently sparse and the first excited electronic level is much higher than the ground electronic level, the partition function could be approximated to g_e^0, as it would be safe to consider only the ground electronic level in many applications. A usual assumption for the calculation of the vibrational partition function is the harmonic oscillator, wherein the vibrational energy levels are approximated to an harmonic oscillator, $E = h\omega(v + 1/2)$. Taking the vibrational degeneracy to be 1, the sum of the partition function can be approximated to

$$Q_\mathrm{vib} \approx \frac{1}{1 - \exp\left(-\frac{h\omega}{k_B T}\right)}. \tag{3.13}$$

This approximation is very acceptable for low temperature applications, but as the real energy of vibrational levels starts deviating from the harmonic oscillator, this approximation becomes less acceptable. As such it is not used in this work.

To obtain the population fraction of level j, equation 3.7 must be used. Level j corresponds to a combination of electronic, vibrational and rotational levels. Since the translational levels have been approximated to a continuum, they are no longer quantized and the translational energy is only described by the temperature. If level j is a combination of numbers e, v and J which stand for the electronic, vibrational and rotational numbers, the fraction is

$$\frac{N_{e,v,J}}{N} = \frac{N_e}{N}\frac{N_{e,v}}{N_e}\frac{N_{e,v,J}}{N_{e,v}} \tag{3.14}$$

where N_e, $N_{e,v}$ and $N_{e,v,J}$ are the populations of electronic level e, vibronic level e, v and rovibronic level e, v, J, respectively. The fractions of these populations are computed as:

$$\frac{N_e}{N} = \frac{Q^e_\mathrm{ele}\sum_{v,J} Q^{e,v}_\mathrm{vib} Q^{e,v,J}_\mathrm{rot}}{\sum_{e,v,J} Q^e_\mathrm{ele} Q^{e,v}_\mathrm{vib} Q^{e,v,J}_\mathrm{rot}} \tag{3.15}$$

$$\frac{N_{e,v}}{N_e} = \frac{Q^{e,v}_\mathrm{vib}\sum_J Q^{e,v,J}_\mathrm{rot}}{\sum_{v,J} Q^{e,v}_\mathrm{vib} Q^{e,v,J}_\mathrm{rot}} \tag{3.16}$$

$$\frac{N_{e,v,J}}{N_{e,v}} = \frac{Q^{e,v,J}_\mathrm{rot}}{\sum_J Q^{e,v,J}_\mathrm{rot}} \tag{3.17}$$

where Q^x is the contribution to the partition function of level x.

3.1.4 Continuity and conservation equations

In spatial and velocity space, the statistical distribution of the gas is given by the distribution function denoted $f(\boldsymbol{r}, \boldsymbol{v}, t)$ where $\boldsymbol{r}$ and $\boldsymbol{v}$ are the position and velocity vectors and t being the time. The distribution function is normalized in such a way that

$$\sum_j \int_{\boldsymbol{r}} \int_{\boldsymbol{v}} f_j(\boldsymbol{r}, \boldsymbol{v}, t) d\boldsymbol{r} d\boldsymbol{v} = N \tag{3.18}$$

with N being the total number of molecules in the gas and j being the species contained in the gas. The physical meaning of f is the number of particles at instant t which have positions in the space-volume element $\mathrm{d}\boldsymbol{r}$ at the end of vector $\boldsymbol{r}$ and velocities in the velocity-volume element $\mathrm{d}\boldsymbol{v}$ at the end of vector $\boldsymbol{v}$. The volume elements $\mathrm{d}\boldsymbol{r}\mathrm{d}\boldsymbol{v}$ are small compared with the macroscopic dimensions of the system. In the double volume element $\mathrm{d}\boldsymbol{r}\mathrm{d}\boldsymbol{v}$ Boltzmann's equation is valid

$$\frac{\partial f_j}{\partial t} + \nabla_{\boldsymbol{r}} \cdot (f_j \boldsymbol{v}) + \left(\frac{\boldsymbol{F}}{m} \nabla_{\boldsymbol{v}} \cdot f_j\right) = \left(\frac{\partial f_j}{\partial t}\right)_{\text{coll}} . \tag{3.19}$$

In this equation $\boldsymbol{F}$ is the vector of resulting force acting on particles in the double volume element $\mathrm{d}\boldsymbol{r}\mathrm{d}\boldsymbol{v}$. Equation 3.19 is written assuming a single species, for a multi-species gas an equation for each species might be required. The RHS term in equation 3.19 is the collision term which contains the physics of all collisions occurring in the double volume element $\mathrm{d}\boldsymbol{r}\mathrm{d}\boldsymbol{v}$.

So far the discussion in this chapter has avoided specifics about the problems this work is tackling. The only consideration so far has been a gas with a mixture of species, some or all of them are molecules. To solve the problems considered in this work there is no need for the Boltzmann equation in its current form. The Knudsen number is the ratio of the mean free path of a particle over the typical dimension of the system. This number determines if the statistical mechanics or the continuum mechanics description of fluid dynamics applies to a certain system. If the Knudsen number is close to 1 or greater, the problem is better treated by statistical mechanics, otherwise continuum mechanics provides a better treatment. Generally, in hypersonics, the Knudsen number should always be checked as the low density environment of the upper atmosphere may lead to a high Knudsen number, however in the systems under consideration in this work, the assumption for a continuum flow may be considered as more adequate. From Boltzmann's equation the Navier–Stokes equations can be derived by taking moments of Boltzmann's equation. The traditional Navier–Stokes equations in the case of a non-reactive ideal gas are continuity/conservation equations describing a viscous flow. In this work there is no need for the Navier–Stokes equations as transport and viscous effects are neglected. Thus the Euler equations for fluid dynamics are obtained without effects such as radiation and chemistry, which are for now ommited in favour of a step-by-step introduction at a later section. The governing equations are then, the mass continuity equation,

$$\frac{\partial \rho}{\partial t} + \nabla \cdot (\rho \boldsymbol{v}) = 0 \tag{3.20}$$

which fundamentally is the constraint that there is no creation or destruction of mass in the system. The moment conservation equation,

$$\frac{\partial \rho \boldsymbol{v}}{\partial t} + \nabla \cdot (\rho \boldsymbol{v}\boldsymbol{v}) = -\nabla p \tag{3.21}$$

which in this specific form was written assuming compressible flow. An even more complete form of this equation would include the acceleration acting on the whole system, such as gravity. As such the RHS of the equation above contains only the pressure gradient. The term $\boldsymbol{v}\boldsymbol{v}$ represents the outer product of the velocity vector with itself. The energy continuity equation,

$$\frac{\partial \rho E}{\partial t} + \nabla \cdot (\rho H \boldsymbol{v}) = 0 \tag{3.22}$$

with the variable E representing the total volume energy density and H the total volume enthalpy. It is important to note that E contains internal and kinetic energy of the system and thus can be written $e + v^2/2$ where v is the magnitude of the velocity vector. The system of equations above should be closed by the state function of the gas, often assumed to be the ideal gas state equation:

$$p = \rho R T \tag{3.23}$$

where p is the pressure, R the gas constant and T the temperature. In the next section the phenomena compatible with multi-component, reactive flow in the presence of radiation is introduced. These phenomena will change the dynamics of the problem allowing for different properties of the equilibria state of the system.

3.1.5 Classification of Equilibria

The first equilibrium that is usually discussed is the Maxwell balance. In equilibrium, the particle energy distribution function is given by Maxwell's distribution:

$$f(u) = \frac{2}{\sqrt{\pi}\,(k_B T)^{3/2}} \exp\left(-\frac{u}{k_B T}\right) \tag{3.24}$$

where u is the energy of the particle. The fraction of particles with u energy is always defined for a temperature T. As seen in section 3.1.1 the translational time scale is the fastest and when using Navier–Stokes equations it should be considered to be always valid and nothing needs to be changed in the formulation so far. In situations where the gas is not Maxwell balanced, Boltzmann's equation should be solved instead of Navier–Stokes.

As was seen in section 3.1.2, the internal modes of a species follows a Boltzmann distribution in equilibrium. If all modes of all species are in equilibrium this is Boltzmann's balance. A common way to deal with Boltzmann non-equilibrium is to force individual modes to follow different temperatures. Depending on the application, the separation might be two or more temperatures. Such models are called multi-temperature models due to their use of more than one temperature and are sometimes denoted 2T or 3T for two and three temperature models, respectively. This is such that equation 3.14 is still valid, but each partition function may be calculated with a different temperature. As an example, in shock tubes it is a popular approach to consider that important molecules have $T_{\text{tra}} = T_{\text{rot}} = T$ and that $T_{\text{vib}} = T_{\text{ele}} = T_{\text{int}}$. By separating the temperatures a new energy equation must be solved for tracking the changes in the internal energy of the species

$$\frac{\partial \rho \varepsilon_k}{\partial t} + \nabla \cdot (\rho \boldsymbol{v} \varepsilon_k) = \dot{\Omega}_k \tag{3.25}$$

where ε_k is the internal energy corresponding to mode k, which can be any internal mode of a molecule. $\dot{\Omega}_k$ is the source term for the internal energy and contains a term for the creation of excited species and a term for the k to translational energy exchanges. Considering as an example the vibrational energy exchange equation,

$$\dot{\Omega}_{\text{vib}} = \sum_i \varepsilon_{\text{vib},i} \dot{\omega}_i + \sum_i \rho c_i \frac{\varepsilon_{\text{vib},i}(T) - \varepsilon_{\text{vib},i}(T_{\text{vib}})}{\tau_i^{VT}} \tag{3.26}$$

where $\dot{\omega}_i$ is the rate of production of excited species i, the numerator of the second term is the difference in internal energy evaluated at the gas temperature and at the vibrational temperature, and the denominator is the Millikan and White coefficient, which is the typical time for vibrational and translational to be in equilibrium. The form of the second term on the RHS of the previous equation is the Landau-Teller rate model [190]. In this scheme $\dot{\omega}_i$ could be computed from equation 3.14 with temperatures T and T_{vib}. Other ways to compute $\dot{\omega}_i$ will be discussed later in sections 3.1.6 and 3.1.7.

The ionization and recombination balance is given by Saha's equation

$$\frac{N_e N_{i+1}}{N_i} = \frac{2Q_{i+1}(T)}{Q_i(T) a_0^3} \left(\frac{k_B T}{4\pi E_H} \right)^{3/2} \exp\left(-\frac{E_\infty}{k_B T} \right) \tag{3.27}$$

where N_e, N_i and N_{i+1} are the number of electrons and the number of ions in the i-th state of ionization. $Q_i(T)$ and $Q(T)$ are the ion partition function and the total partition function, a_0 is the Bohr radius and E_H the ionization energy of the Hydrogen atom. The E_∞ term is the ionization energy of the neutral species from where the ions are being formed. The equation above is valid for low ionization gases, if enough charges builds up in the gas there will be a reduction of the ionization energy required. More details can be found in [191]. In this work, the gas is assumed to not build up significant charges, in some sense it does not become a plasma.

The balance between matter and radiation is called Boltzmann's balance and is given by Planck's law for blackbody radiation

$$u_\nu \left(T\right) = \frac{8\pi h\nu^3}{c^3}\left[\exp\left(\frac{h\nu}{k_B T}\right) - 1\right]^{-1} \tag{3.28}$$

where u_ν is the spectral radiance with units W/sr/Hz. Dealing with radiation coupled to the flow of a gas is a complex endeavour. Radiation is a local and omnidirectional phenomenon which creates complications for coupling with gas dynamics. A common approach is the definition of escape factors Λ_{ij} for specific transition ij and line profiles P_{ij}:

$$\Lambda_{ij} = \frac{\int_\nu \int_l P_{ij} I_{ij} d\nu dl}{\int_\nu P_{ij} d\nu} \tag{3.29}$$

where I_{ij} is the radiative intensity of transition ij. Although the numerator contains an integral dependent on the path l, an expression for Λ_{ij} may be derived which will not depend on l under certain circumstances, an example of this may be found in [192]. In most circumstances, the escape factors are computed on the fly in a region of interest for specific paths. The local escape factor may be written as:

$$\Lambda ij = 1 - \frac{1}{N_i A_{ij}} \int\limits_0^{+\infty} \int\limits_0^{4\pi} \frac{\alpha(\nu)}{h\nu} \frac{L_\nu}{4\pi} d\Omega d\nu \tag{3.30}$$

where the integration is done over the whole spectrum and the whole solid angle. The quantity α is the absorption coefficient and L_ν is the radiance of transition ij. These quantities will be further discussed in chapter 4. The escape factors can be thought of as the mean probability of a photon escaping the plasma directly. The energy escaping the gas may be written in mass density terms

$$\dot{\Omega}^{\text{rad}} = \sum_i \frac{M_i}{N_a} \sum_t \nu_t A_t \Lambda_t n_t \tag{3.31}$$

where M_i is the molar mass of species i, N_a is Avogadro's number, the sum over t means the sum over all transitions in the gas with n_t the number density of the upper level of transition t. $\dot{\Omega}^{\text{rad}}$ is a term that may be added to the RHS of an energy continuity equation for accounting the escaped energy. The source/sink term for the mass continuity equation may be written:

$$\dot{\omega}_i = \frac{M_i}{N_a} n_i \sum_t A_t \Lambda_t. \tag{3.32}$$

The equation above contains a sum over all transitions t pertinent to species i and contains an omitted plus or minus sign which depends if species i is on the lower or upper level of transition t, respectively. Besides the escape factors, the other possibility is to assume a completely thin gas with no absorption or stimulated emission where radiation only leads to losses. In this case, Λ_t becomes 1 for the equations above, everything else remaining the same.

For the Navier–Stokes equations shown in the previous section it was assumed that the flow is non-reactive. This is certainly not the case in hypersonics, plasmas or combustion. If the flow is reactive, a continuity equation must be solved for each species present in the gas:

$$\frac{\partial \rho c_i}{\partial t} + \nabla \cdot (\rho c_i \boldsymbol{v}) = \dot{\omega}_i \tag{3.33}$$

where c_i is the mass fraction of species i in the gas and $\dot{\omega}_i$ is the source term. The total number of particles might not be constant in this case, but the overall conservation of mass must hold. For now, no details on the calculation of $\dot{\omega}_i$ will be given. Reactions consume energy that is available in the gas, in the form of internal species energy. As such, the internal energy of the gas will be dependant on the reactions occurring in the system, but the total energy of the system should not change. One way to deal with this is to add an internal energy equation to be solved in the system:

$$\frac{\partial \rho \varepsilon}{\partial t} + \nabla \cdot (\rho \boldsymbol{v} \varepsilon) = \dot{\Omega} \tag{3.34}$$

where ε is the internal energy of the gas, and $\dot{\Omega}$ is the sink/source term for the internal energy. When all $\dot{\omega}_i = 0$ and $\dot{\Omega} = 0$ the gas is said to be in chemical equilibrium. The difference of this equation from 3.25 is that the former tracks only changes in vibrational energy while the latter accounts for internal energy as a whole. Other than that, they serve the same purpose and using both equations leads to an over-determined system. Chemical equilibrium is directly related to the principle of detailed balance which is introduced in the next section.

3.1.6 Detailed balance

For every chemical reaction, $\mathrm{aA} + \mathrm{bB} \longrightarrow \mathrm{cC} + \mathrm{dD}$, there is a correspondent inverse reaction, $\mathrm{aA}+\mathrm{bB} \longleftarrow \mathrm{cC}+\mathrm{dD}$. In these reactions, A, B, C and D are chemical species and a, b, c and d are the stoichiometric coefficients. Reactions are usually written, $\mathrm{aA}+\mathrm{bB} \longleftrightarrow \mathrm{cC}+\mathrm{dD}$ and when aA+bB forms cC+dD the reaction is in the forward direction/reaction.

The other way around it is called the backward direction/reaction. In a chemical system with just the reaction above, the change in concentration of the species are:

$$\begin{aligned}
\frac{\mathrm{d}[A]}{\mathrm{d}t} &= -aK_{fr}[A]^a[B]^b + aK_{br}[C]^c[D]^d \\
\frac{\mathrm{d}[B]}{\mathrm{d}t} &= -bK_{fr}[A]^a[B]^b + bK_{br}[C]^c[D]^d \\
\frac{\mathrm{d}[C]}{\mathrm{d}t} &= cK_{fr}[A]^a[B]^b - cK_{br}[C]^c[D]^d \\
\frac{\mathrm{d}[D]}{\mathrm{d}t} &= dK_{fr}[A]^a[B]^b - dK_{br}[C]^c[D]^d
\end{aligned}$$

where quantities in square brackets are concentrations, K_{fr} and K_{br} are the forward and backwards reaction rate coefficient, respectively. Generalizing from the production and consumption rates above, the source term for a species i is given by

$$\dot{\omega}_i = M_i \sum_r \Delta\nu_{ir} \left(K_{fr} \prod_i^{\text{prod}} x_i^{\nu_i'} - K_{br} \prod_i^{\text{reac}} x_i^{\nu_i''} \right) \tag{3.35}$$

where $x_i = \rho c_i / M_i$ and $\Delta\nu_{ir} = \nu_i'' - \nu_i'$, where ν_i are the stoichiometric coefficients for species i in reaction r. The reaction rate coefficients are often written through the so-called Arrhenius form:

$$K_{fr} = AT^{\theta} \exp\left(-\frac{T_a}{T}\right) \tag{3.36}$$

where A, θ and T_a, also called activation temperature, are the Arrhenius coefficients. The activation temperature is interpreted as the temperature for which the reaction is significant and is thus "activated" in the flow. A more detailed expression for the reaction rate coefficient is the function:

$$K_{fr} = \exp\left(\frac{a}{\overline{T}^3} + \frac{b}{\overline{T}^2} + \frac{c}{\overline{T}} + d\log(\overline{T}) + e + f\overline{T} + g\overline{T}^2 + h\overline{T}^3 + i\overline{T}^4\right) \tag{3.37}$$

where $\overline{T}$ is a reduced temperature $T/1000$ and the letters a to i are 9 numerical coefficients. The Arrhenius form is theoretically justified since it is the result of averaging the hard-sphere cross sections with a Maxwell distribution. However, the latter form is preferred in this work since fitting in a large temperature range it yields much smaller fitting errors, but in a lot of the literature the Arrhenius form is used.

In equilibrium, the concentration of chemical species should not change, and as such the production and consumption rate of a chemical species must be the same. This is the principle of detailed balance. As such, taking equation 3.35 and for each reaction

$$K_{fr} \prod_i^{\text{prod}} x_i^{\nu_i'} = K_{br} \prod_i^{\text{reac}} x_i^{\nu_i''} \tag{3.38}$$

which can be rewritten as

$$\frac{K_{fr}}{K_{br}} = \frac{\prod_i^{\text{reac}} x_i^{\nu_i''}}{\prod_i^{\text{prod}} x_i^{\nu_i'}} = K_{eq} \tag{3.39}$$

which is defined as the equilibrium constant of reaction r. It is more useful to write the equilibrium constant as

$$K_{eq} = \prod_i Q_i^{\nu_i} \tag{3.40}$$

where ν_i is the stoichiometric coefficient of species i in reaction r and is negative if i is in the reactants and positive if i is in the products of reaction r. The partition function becomes an even more important quantity as not only allows the calculation of the population of the internal modes of molecules and atoms, it also provides critical information about the balance of reactions occurring in the flow.

3.1.7 State-to-state

Section 3.1.5 has focused on the distributions and properties of a gas in and out of equilibrium. One of the solutions to model the gas out of equilibrium is to assume that distributions are still valid but are characterized by different temperatures. This leads to the multi-temperature approaches that are widely used in scientific communities such as plasma, combustion, hypersonics and so on. This effectively forces non-equilibrium effects to be manifested by temperatures characterizing different effects which may not be a sufficient description of non-equilibrium phenomena. In particular, the internal structure of molecules does not follow a Boltzmann distribution. A solution for a better description of the internal population of molecules may be found in the state-to-state framework. In state-to-state, instead of assuming an internal distribution of modes, the changes in populations are tracked as the name suggests in a state-to-state basis. This effectively means that the number of mass continuity equations increases by the number of internal states of a molecule that the modeler wants to capture. Each internal level becomes effectively a pseudo-species. Depending on the molecule and level of detail this might be an untenable problem for current computational structures. For instance, in the work [193, 194] the N_2 molecule in the ground state contains 9390 ro-vibrational levels. The number of continuity equations is on the order of ~ 9000 and the number of processes will be around $\sim 9000^2$. A 2D ro-vibrational state-to-state simulation of N_2 is too computationally expensive. Using the same scheme in a 0D or 1D simulation is more appropriate. Binning models such as the ones in [195] bridge the gap between state-to-state and more complex, higher dimension simulations by reducing the complexity of the kinetic schemes. Binning methods and algorithms are outside the scope of this work, examples of binning can be found in [195].

3.1.8 Governing Equations

In sections 3.1.4 to 3.1.7 the more general equations and subsequent modifications were briefly introduced and discussed. Here these equations are introduced again, modified with some assumptions of non-equilibrium. The equations are:

$$\frac{\partial \rho c_i}{\partial t} + \nabla \cdot (\rho \boldsymbol{v} c_i) = \dot{\omega}_i \tag{3.41}$$

$$\frac{\partial \rho \boldsymbol{v}}{\partial t} + \nabla \cdot (\rho \boldsymbol{v}\boldsymbol{v}) = -\nabla p \tag{3.42}$$

$$\frac{\partial \rho E}{\partial t} + \nabla \cdot (\rho E \boldsymbol{v}) = -\nabla \cdot (p\boldsymbol{v}) \tag{3.43}$$

the mass continuity equation, the momentum conservation equation and the energy conservation equation. No internal energy equation is solved as in state-to-state there is no assumption of an internal temperature. In the equations above, chemical non-equilibrium has been assumed, by the presence of $\dot{\omega}_i$ in the mass continuity equations and assumed a non-Boltzmann distribution by solving mass continuity equations for each state of the species under study. If the RHS of the energy equation is passed to the LHS, the inside of the spatial derivative becomes $\nabla \cdot (\rho \boldsymbol{v} H)$ where H is the enthalpy of the gas. To obtain the time relaxation equations of the flow, the spatial terms are neglected and the evolution of primitive variables c_i and T are obtained:

$$\frac{\partial c_i}{\partial t} = \frac{\dot{\omega}_i}{\rho} \tag{3.44}$$

$$\frac{\partial T}{\partial t} = -\frac{\sum\limits_i \varepsilon_i \dot{\omega}_i}{\rho C_V^f} \tag{3.45}$$

where the energy of the flow is described by a calorically perfect gas in a constant volume $E = C_V^f T$ where the heat capacity of the gas is $C_V^f = \sum_i c_i C_{V,i}$. Like in equation 3.3, the $C_{V,i}$ of a species is separable into translational, rotational, vibration and electronic contributions. In the STS formulation, the heat capacity of the gas may not be determined by a simple sum over all species, it is required to consider the distribution function over the specified internal modes. For vibrational state specific species the translational and rotational contributions are analitically defined by the temperature while the vibronic contributions are defined by their respective populations. As such the expression is still valid if it is assumed that the sum over i is for all species and all the individual vibronic states considered in the gas. By neglecting the temporal derivatives the spatial relaxation equations are found:

$$\frac{\partial c_i}{\partial x} = \frac{\dot{\omega}_i}{\rho v} \tag{3.46}$$

$$\frac{\partial v}{\partial x} = \frac{c_1 b_2 - c_2 b_1}{a_1 b_2 - a_2 b_1} \tag{3.47}$$

$$\frac{\partial T}{\partial x} = \frac{c_1 a_2 - c_2 a_1}{a_1 b_2 - b_1 a_2} \tag{3.48}$$

where the coefficients a_1, a_2, b_1, b_2, c_1 and c_2 are

$$a_1 = \frac{\rho v^2}{p} - 1 \tag{3.49}$$

$$a_2 = \rho v^2 \tag{3.50}$$

$$b_1 = \frac{v}{T} \tag{3.51}$$

$$b_2 = \rho v C_p^f \tag{3.52}$$

$$c_1 = -\frac{M}{\rho} \sum_i \frac{\dot{\omega}_i}{M_i} \tag{3.53}$$

$$c_2 = -\sum_i h_i \dot{\omega}_i \tag{3.54}$$

where h_i is the specific enthalpy of species i and M is the molar mass of the gas averaged by the molar fraction of each species. In the spatial relaxation system of equations the gas is assumed to be at constant pressure, instead of constant volume. As the models presented in this work have been developed with the aim of modelling CO_2 in hypersonic regimes the shock wave jump relations are needed to bridge the macroscopic quantities of the gas before to post-shock. The Rankine-Hugoniot jump relations are obtained by assuming a frozen gas composition after the shock and a frozen vibrational energy term while other quantities are treated as a discontinuity of the gas properties:

$$\frac{\rho_2}{\rho_1} = \frac{M_1^2(\gamma+1)}{2 + M_1^2(\gamma-1)} \tag{3.55}$$

$$\frac{v_2}{v_1} = \frac{\rho_1}{\rho_2} \tag{3.56}$$

$$\frac{p_2}{p_1} = 1 + \frac{2\gamma(M_1^2 - 1)}{\gamma+1} \tag{3.57}$$

$$\frac{T_2}{T_1} = \frac{(2\gamma M_1^2 - (\gamma-1))(2 + (\gamma-1)M_1^2)}{M_1^2(\gamma+1)^2} \tag{3.58}$$

where the 2 subscript refers to post-shock properties and the 1 subscript to the pre-shock properties and γ is the ratio of specific heats of the mixture C_p^f/C_v^f. A more detailed derivation of the governing equations can be found in appendix A.

3.2 Models

This section details on how general modelling tools are employed in calculating or extrapolating reaction rate coefficients in this work. Firstly, the FHO model is detailed in how to compute the VT and VVT transitions with an overall look on the mathematical formulation of the theory. Secondly, the Rosen-Zener theory is discussed, which will be used to compute the spin-forbidden interactions of the CO_2 ground state and $^3B_2$ state. Thirdly, a redistribution method will be laid out, as discussed in [196], which will allow the division of a macroscopic reaction rate to a manifold of STS levels. Finally, the approximation of constant number of collisions is introduced. All these tools will be used in the following section 3.3.

Just as a matter for reference and completeness, some general formulas between probability, cross section and reaction rates are laid out here. Converting a probability to a reaction rate coefficient is done through the relation:

$$K_{fr}(T) = \int_{-\infty}^{+\infty} Z(T)P(v)f(v)dv \tag{3.59}$$

where $P(v)$ is a velocity dependent probability, $f(v)$ is the Maxwell distribution function written in terms of velocity v and $Z(T)$ is the classical collisional frequency given by

$$Z(T) = n_a n_b \pi \left(r_a + r_b\right)^2 \sqrt{\left(\frac{8k_B T}{\pi \mu_{ab}}\right)} \tag{3.60}$$

where a and b are the species involved in the collision, n is the number density, r the radius of the species and μ_{ab} the reduced mass of the ab system. The $\pi \left(r_a + r_b\right)^2$ is the hard-sphere cross section and as such should be treated as the maximum cross section allowed for the collisions between species a and b. Transforming a cross section to a reaction rate coefficient yields:

$$K_{fr}(T) = \int_{0}^{+\infty} \frac{Z(T)}{\pi \left(r_a + r_b\right)^2} \sigma(u)f(u)du \tag{3.61}$$

where $\sigma(u)$ is the collision cross section in units of energy.

3.2.1 Forced Harmonic Oscillator

Here the fundamental equations of the FHO model are summarized, which yield V−T and V−V−T transition probabilities for any arbitrary collinear, nonreactive collisions for triatomic-triatomic, triatomic-diatomic, and triatomic-atomic pairs.

– V–T transition probabilities [108, 107]:

$$P(i \rightarrow f, \varepsilon) = \quad i!f!\varepsilon^{i+f} \exp\left(-\varepsilon\right) \left| \sum_{r=0}^{n} \frac{(-1)^r}{r!(i-r)!(f-r)!\varepsilon^r} \right|^2 \tag{3.62}$$

with $n = min(i, f)$.

– V–V–T transition probabilities [109]:

$$\begin{aligned} P(i_1, i_2 \rightarrow f_1, f_2, \varepsilon, \rho) = & \left| \sum_{g=1}^{n} (-1)^{(i_{12}-g+1)} \right. \\ & \times C^{i_{12}}_{g,i_2+1} C^{f_{12}}_{g,f_2+1} \varepsilon^{\frac{1}{2}(i_{12}+f_{12}-2g+2)} \exp\left(-\varepsilon/2\right) \\ & \times \sqrt{(i_{12}-g+1)!(f_{12}-g+1)!} \exp\left[-i(f_{12}-g+1)\rho\right] \\ & \left. \times \sum_{l=0}^{n-g} \frac{(-1)^l}{(i_{12}-g+1-l)!(f_{12}-g+1-l)!l!\varepsilon^l} \right|^2 \end{aligned} \tag{3.63}$$

with $i_{12} = i_1 + i_2,\ f_{12} = f_1 + f_2$ and $n = min(i_1 + i_2 + 1, f_1 + f_2 + 1)$. ε and ρ are related to the two-state First-Order Perturbation Theory (FOPT) transition probabilities, with $\varepsilon = P_{\text{FOPT}}(1 \rightarrow 0)$, $\rho = [4 \cdot P_{\text{FOPT}}(1, 0 \rightarrow 0, 1)]^{1/2}$, and C^k_{ij} is a transformation matrix calculated according to:

$$\begin{aligned} C^k_{ij} = & 2^{-n/2} \binom{k}{i-1}^{-1/2} \binom{k}{j-1}^{1/2} \\ & \times \sum_{v=0}^{j-1} (-1)^v \binom{k-i+1}{j-v-1} \binom{i-1}{v}. \end{aligned} \tag{3.64}$$

For a Morse intermolecular potential $V(r) \sim E_m(1 - \exp(-\alpha r))^2$, the expression for ε is given by Cottrell [197], the expression for ρ being identical to the one obtained for a purely repulsive potential [109].

$$\varepsilon = \frac{8\pi^3 \omega \left(\tilde{m}^2/\mu\right) \gamma^2}{\alpha^2 h} \frac{\cosh^2\left[\frac{(1+\phi)\pi\omega}{\alpha\bar{v}}\right]}{\sinh^2\left(\frac{2\pi\omega}{\alpha\bar{v}}\right)} \tag{3.65}$$

$$\phi = (2/\pi) \tan^{-1} \sqrt{(2E_m/\tilde{m}\bar{v}^2)} \tag{3.66}$$

$$\rho = 2\left(\tilde{m}^2/\mu\right) \gamma^2 \alpha \bar{v}/\omega. \tag{3.67}$$

In these expressions, ω is the frequency of the oscillation, $\tilde{m}$ is the reduced mass of the two molecules involved in the collision, γ and μ are collision parameters to be discussed in 3.3.1. Expressions 3.62 and 3.63 have been shown [117] to be cumbersome at high quantum numbers, where limitations with the application of large factorial numbers in the denominator and numerator of the probabilities expressions lead to overflows and underflows that depend on the precision of the floating point operations of the calculating algorithm. These issues may be solved by either a careful tailoring of the simulations with variable precision arithmetics techniques, or resorting to the corresponding asymptotic Bessel functions [198] may be used without any noticeable loss of accuracy:

$$P(i \to f, \varepsilon) = J_s^2 \left(2\sqrt{n_s \varepsilon}\right) \tag{3.68}$$

for $i, f \gg s = |i - f|$, and $n_s = [\max(i, f)!\min(i, f)!]^{-s}$, and

$$P(i_1, i_2 \to f_1, f_2, \varepsilon, \rho) = J_s^2 \left[2\left(n_s^{(1)} n_s^{(2)} \rho_\xi^2 / 4\right)^{1/2}\right] \tag{3.69}$$

for $i_1 + i_2 = f_1 + f_2$, and $i_1 + i_2 + f_1 + f_2 \gg s = |i_1 - f_1|$. Here J_s stands for the Bessel function of the first species and s^{th} order.

The generalizations of the FHO model [199, 110, 113, 117] that allow it to be applied to practical rates calculations are shortly summarized below:

1. Symmetrization of the collision velocity to enforce detailed balance ($\bar{v} = (v_i + v_f)/2$);

2. Accounting for the anharmonicity of the oscillator potential curve using an average frequency $\omega = |(E_i - E_f)/(i - f)|$ if $i \neq f$, and $\omega = |E_{i+1} - E_i|$ if $i = f$;

3. Generalization of the model for nonresonant V–V–T transitions and V–V–T transitions between different species, by replacing $\rho \to \rho \times \xi / \sinh(\xi)$, with $\xi = \pi^2(\omega_1 - \omega_2)/4\alpha\bar{v}$;

4. Generalization of the FHO model to non-collinear collisions (general case) through the multiplication of the parameters ϵ and ρ by steric factors such that $\varepsilon = \varepsilon \times S_{VT}$ and $\rho = \rho \times \sqrt{S_{VV}}$, using the values $S_{VT} = 4/9$ and $S_{VV} = 1/27$, as proposed by Adamovich [110, 113];

5. Modeling vibration-dissociation V–D processes as a transition to a quasi-bound level above the dissociation limit, followed by a decay into the dissociation products [115, 117]: $P(i \to, \varepsilon) = P(i \to v_{qbound}, \varepsilon) \cdot P_{decay}$.[1]

---

[1] with $P_{decay} \sim 1$

One last modification that is proposed in this work is a simple semi-empirical correction for the better modeling of near-resonant V–V–T transitions. It is very well-known [199, 118] that the FHO theory fails at predicting these transitions, since it considers a V–V–T process as the product of several V–T processes (e.g. a (0;1)→(1;0) V–V–T transition will be treated as a sequence of two V–T transitions: (0;1)→(0;0)→(1;0)), which implies artificially larger energy jumps and in consequence an underestimation for the transition probability. The simple semi-empirical correction of figure 3.2 is carried out. A more adequate transition probability is obtained if for the purposes of calculating the transition probability, if a transition of both initial states to a fictitious state such that $|\Delta E_{(i_1-f_1')}| = |\Delta E_{(i_2-f_2')}| = |\Delta E_{VVT}|/2$ is considered. An example of this correction can be seen in figure 2.1 where the V–V–T reaction $CO_2(001)+N_2(0) \longleftrightarrow CO_2(000)+N_2(1)$ is correctly modeled using this semi-empirical correction.

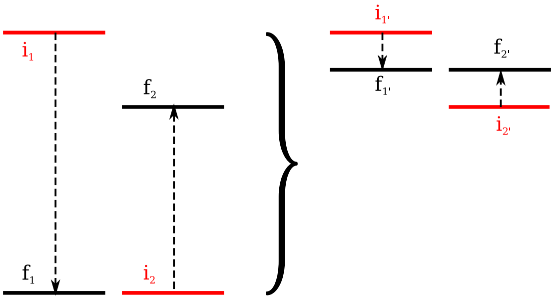

Figure 3.2: Forced Harmonic Oscillator correction for near-resonant V–V–T transitions

3.2.2 Vibronic Transitions

In order to study spin-forbidden transitions, occurring between vibronic states of CO_2, the FHO framework cannot be used. Other works [44, 45] studying the interaction between CO_2 ground and electronically excited state proposed to use the Landau-Zener theory. In principle, this would not be possible since spin-forbidden processes have a negligible contribution to the diagonal of the Hamiltonian of the system. As such, using the Landau-Zener theory on these cases relies on using the off-diagonal terms of the Hamiltonian. The difficulty would then lie in determining the off diagonal term which coincides with the spin-orbit coupling term. Though this is mathematically sound, the Landau-Zener theory was developed assuming a constant off-diagonal term [200]. The Rosen-Zener theory is more appropriate in the case of spin-forbidden interactions, although the region of applicability of this theory has not been verified in this case. The preference of this theory over the Landau-Zener theory can be justified thus: "*The Rosen-Zener model, [...] can be associated with the one-dimensional motion of a system featuring the exponential off-diagonal coupling between the zero-order states of constant spacing [...].*" as can be read in the review of Nikitin [200]. It continues: "*In a way, this model [Rosen-Zener] is the opposite to the avoided crossing Landau-Zener model, for which the spacing between the zero order states features the crossing while the off-diagonal term is constant*". In other words, the crossing of singlet-triplet interactions is described by the off-diagonal terms in the Hamiltonian of the system. The Landau-Zener theory assumes a description of the crossing contained in the diagonal terms, while the Rosen-Zener theory assumes this description to be featured in the off-diagonal term. This is the case in the crossings that are dealt with in this work.

The Rosen-Zener probability can be written as a function of velocity v,

$$P(v) = \left[1 + \exp\left(\frac{\pi \Delta E}{\hbar \alpha v}\right)\right]^{-1}. \tag{3.70}$$

The probability then is dependent on the difference in energy of the interacting levels ΔE, and the repulsive term of the interaction potential α. With the current expression and with no data to calibrate the rate coefficients for this kind of reactions, the values for the probability are used as calculated. The expression above tends to 1/2 in the high velocity limit. In high-temperature regimes, this might lead to a somewhat higher than expected rate coefficient, comparable (but still lower) to the collisional rate coefficient. Thus spin-forbidden vibronic interactions are modelled.

3.2.3 Redistribution of exchange rates

Exchange and chemical reactions are usually given as Arrhenius global rate coefficients, *i.e.* as non-STS. In order to include the process, a redistribution of the global reaction must occur, whereby from a global reaction a set of STS rates are obtained. The redistribution employed in this work is almost identical to the one found in [196]. A brief description is warranted here. Redistributing a macroscopic reaction rate to a manifold of state to state reaction rates relies on the balance of energy of a reaction. If the reagents have energy above the activation energy E_a, then the reaction is exothermic, if not the reaction is endothermic. E_a is taken as the balance of the enthalpies of formation between the products and reagents of the reaction or alternatively with the third Arrhenius coefficient θk_B converted to a suitable unit. The form of the exothermic state to state reactions is assumed to be:

$$K_v(T) = A_v T^n \exp\left(-\frac{\theta}{T}\right) \tag{3.71}$$

and the endothermic state to state reactions to be:

$$K_v(T) = B_v T^n. \tag{3.72}$$

where A_v and B_v are vibrational-state specific coefficients. It is further assumed that A_v has the form,

$$A_v = b\frac{E_a - E_v}{E_a - E_-} \tag{3.73}$$

and B_v has the form,

$$B_v = b\frac{E_+ - E_a}{E_v - E_a}, \tag{3.74}$$

where b is some coefficient dependent on temperature, E_v is the energy of level v and E_- is the last level where the reaction is endothermic and E_+ the first level in which the reaction is exothermic. The macroscopic reaction rate K_{macro} is then made equal to:

$$K_{\text{macro}}(T) = \sum_v K_v(T)\frac{g_v \exp\left[-E_v/(k_B T)\right]}{Q_v} \tag{3.75}$$

where g_v is the degeneracy of level v, E_v the energy of level v and Q_v the vibrational partition function of the considered levels for redistribution. Following the above equation, the assumed forms for the state to state reaction rates are substituted in and the functions of A_v and B_v to solve for b,

$$b = \frac{K_{\text{macro}} Q_v}{\sum\limits_{E=0}^{E_-} \frac{E_a - E_v}{E_a - E_-} g_v \exp\left(-T_a/T\right) + \sum\limits_{E_+}^{E_{\text{max}}} \frac{E_+ - E_a}{E_v - E_a} \exp\left(-E_v/(k_B T)\right)}. \tag{3.76}$$

This yields a state to state reaction rate set that is self-consistent with the initial macroscopic reaction rate. In this work only the vibrational manifold of the ground state of CO_2 is considered for redistribution, assuming that the triplet CO_2 effects on exchange reactions are negligible.

3.2.4 Constant number of collisions approximation

When an estimation of a process is provided only for a single temperature, as a probability or a rate coefficient, an extrapolation in temperature is required. The given probability or rate coefficient might be considered of as the average number of collisions required for the process to occur. A way to extrapolate the given data point is to assume the ratio between the average number of collisions and the total number of collisions of the relevant species is constant for all temperatures. This leads to an extrapolation of the sort:

$$K_{fr}(T) = \frac{K_{fr}(T_{\text{given}})}{Z(T_{\text{given}})} Z(T) \tag{3.77}$$

where $K_{fr}(T)$ is the extrapolated reaction rate coefficient, $K_{fr}(T_{\text{given}})$ is the given reaction rate coefficient at temperature T_{given} and $Z(T)$ is the classical collisional frequency.

3.3 Kinetic Scheme Development

At this point all the theory and model groundwork has been laid for the development of a vibrational STS kinetic scheme. Moving forward, the assumptions and specificities of developing a vibrational STS scheme for CO_2 will be discussed. The dataset obtained in this work is part of the STELLAR database which is publicly available [201]. The objective here is to build a vibrational specific STS model of CO_2 including the ground electronic state and the first excited triplet state $^3B_2$ of CO_2.

3.3.1 Carbon Dioxide kinetics characterization

Collision parameters

Before starting with the development of the kinetic scheme, an adaptation of the existing theory must be performed for the CO_2 molecule. Of the parameters presented in section 3.2.1 all are accounted for except γ and μ which are parameters in equations 3.65 and 3.67. These parameters are molecule dependent and could be called the “Mass parameters” of CO_2. First, γ named the mass parameter, relates the center of mass distance of the colliding particles to the distance between the colliding atoms of both molecules [202]. Secondly, μ is the reduced mass of the internal oscillatory movement of the molecule. This is determined by considering the individual bonds vibrations and conservation of the center of mass during the oscillatory motion. Thus, μ is not only species dependent but also mode dependent since each vibration displaces the C and O atoms differently.

The dynamics and amplitude of the displacement coordinates for each of the CO_2 vibrational modes may be determined from a normal modes analysis [203]. The interest here lies only in the determination of the average motion of the center of mass, to determine γ and the reduced mass of each vibration for μ. For γ it is rather straightforward to reason that it is 1/2 for all modes. In the case of the symmetric stretch the two O atoms equally push and pull the C atom between them and as such the C atom is always half-way between them and as such $\gamma = 1/2$. For the asymmetric stretch each bond will compress and consequently stretch in the same way, the C atom motion will be a sinusoidal centered half-way between the two O atoms and thus, $\gamma = 1/2$. In the case of bending the angle between the two CO bonds varies between $180° + \alpha$ and $180° - \alpha$, meaning the average angle will be 180°, where the C atom is halfway between the O atoms, and as such $\gamma = 1/2$. Figure 3.3 presents a schematic of the three CO_2 vibrational modes in the ground state where the above reasoning may be checked. The derivation of the μ parameter may be consulted in appendix B. In table 3.1 the mass parameter and the reduced mass for the vibrational modes of ground state CO_2 are shown. For the excited $^3B_2$ state, also an object of this work, has the same μ and γ parameter as the corresponding modes of the ground state.

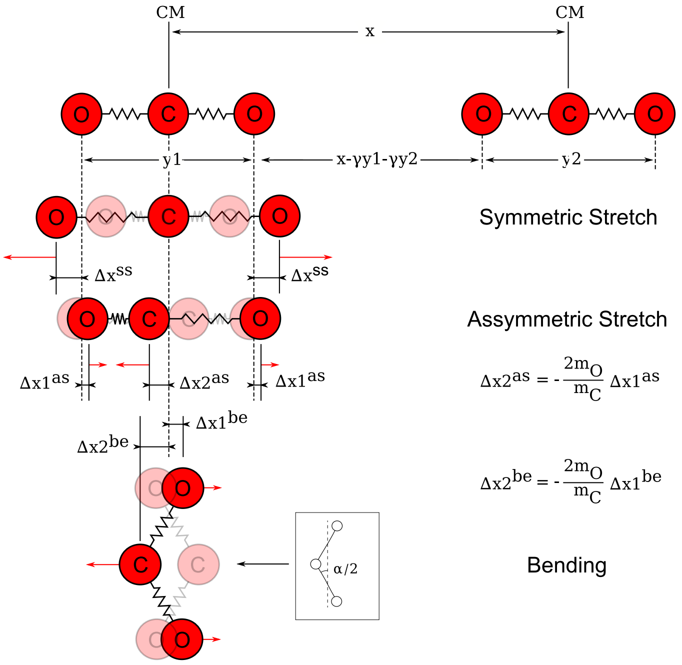

Figure 3.3: CO_2 mass coordinates for the symmetric stretch, asymmetric stretch and bending modes

Energy levels

The first step in the development of a kinetic scheme is to define a manifold of level energies. In this work, this is performed for the ground state and the electronically excited

Table 3.1: Mass parameters for the three vibrational modes of ground state CO_2

Mode	μ	γ
sym. stretch	m_O	1/2
asym. stretch	$\frac{m_C m_O}{m_C + 2m_O}$	1/2
bending	$\frac{m_C m_O}{2(2m_O + m_C)}$	1/2

state ${}^3B_2$ of CO_2. Starting with the ground state of CO_2, since there are no ground state Potential Energy Surfaces (PES) that are accurate up to the dissociation energy, the asymptotic limits of dissociation must first be established. These must be different for each mode, as each breaks apart in a different configuration, the dissociation energy can be computed by the balance of the enthalpy of formation of the products of dissociation. These are as follows:

- Symmetric stretch: $CO_2(X^1\Sigma)$ + 18.53 eV → $C(^3P)$ + $O(^3P)$ + $O(^1D)$,
- Bending: $CO_2(X^1\Sigma)$ + 11.45 eV → $C(^3P)$ + $O_2(X^3\Sigma)$,
- Asymmetric stretch: $CO_2(X^1\Sigma)$ + 7.42 eV → $CO(X^1\Sigma)$ + $O(^1D)$.

Having the asymptotic behaviour of each mode allows the extension of a PES to the near-dissociation limit and thus, a well behaved 1D potential curve for each mode is obtained. This process is the known Rydberg–Klein–Rees (RKR) method which is detailed in [112]. Upon obtaining a well-behaved potential curve, the radial Schrödinger's equation may be solved and a manifold of levels can be determined. The NASA–Ames–2 PES by [204] (kindly shared by Dr. Huang) is used up to $25,500\ \text{cm}^{-1}$ and extended to the respective dissociation limit in the long range for the symmetric and asymmetric stretch modes by Hulburth [205] and Rydberg [112] potentials, respectively. In the short range, the potential is extended by a repulsive term of the form (a/x^b). Thus, the 1D potentials of the symmetric and asymmetric stretch modes are obtained and are reported in fig. 3.4. The dotted line in each figure represents the limit to which the NASA–Ames–2 PES is used, above which the potentials are extrapolated. The eigenvalues obtained from the radial Schrödinger's equation are also plotted along the potential curve. A full line at 18.53 and 7.42 eV represents the asymptotic limit for the potential curve of each mode, along with the last bound solution of Schrödinger's equation. The bending mode requires a different treatment. The symmetry of the bending mode potential excludes the possibility of using the same treatment described above as there is no expectation for the shape of the potential near the asymptotic limit. Furthermore, it is of no benefit to model such extreme states close to the dissociation limit of "pure" bending of the molecule. Nevertheless, due to the symmetry of the bending mode, the potential may be fitted to a polynomial expression $ax^2 + bx^4$ as described in [206] [2]. As for the energy levels, and once more acknowledging the symmetry of the potential, these may be extrapolated from a polynomial expression with a greater degree of confidence. In this work, the Chédin polynomial fit [207] is used for this purpose. Figure 3.5 shows the symmetry of the bending mode along with the energy levels obtained from the Chédin fit. In the same figure the dashed line represents the threshold above which the potential is extrapolated from the NASA-Ames-2 PES. A solid line represents the asymptotic limit which cannot be captured by the extrapolation of the employed $ax^2 + bx^4$ polynomial. Note that there is no problem in assigning the obtained level energies. The symmetric and asymmetric levels were obtained from solving Schrödinger's equation and can be simply ordered in value for a correct assignment while the bending levels were computed from a polynomial fit [207] which described the unperturbed (by Fermi resonance) levels. Given the choice to consider the full manifold of l_2 levels or a single l_2 for a specific v_2, the latter is preferred with $\mathrm{v}_2 = l_2$. This is done in order to simplify the model since accounting for the full l_2 manifold implies a more than double the amount of considered levels and the number of rates grows with the square of number of levels.

Electronically excited CO_2 in the $^3B_2$ state is a bent molecule in its equilibrium configuration with the same vibrational modes as the ground state CO_2. Although there are some available PES of this excited state, not having the symmetry of a linear molecule precludes the use of the same methods as in the fundamental state. Solutions to Schrödinger's equation could possibly be found but the assignment of each solution to a state would be made a complex endeavour which requires a work of its own. Instead the values found and assigned in the work of Grebenshchikov [208] will be used. These may be used to fit a polynomial based on the same expression as the Chédin fit [207]. The resulting polynomial takes the form:

$$E(\mathrm{v}_1, \mathrm{v}_2, \mathrm{v}_3) = \sum_{i=1,2,3} \omega_i \mathrm{v}_i + \sum_{i=1,2,3} x_{ii} \mathrm{v}_i^2 + x_{12}\mathrm{v}_1\mathrm{v}_2 + x_{13}\mathrm{v}_1\mathrm{v}_3 + x_{23}\mathrm{v}_2\mathrm{v}_3. \tag{3.78}$$

---

[2] excluding perturbations from other states

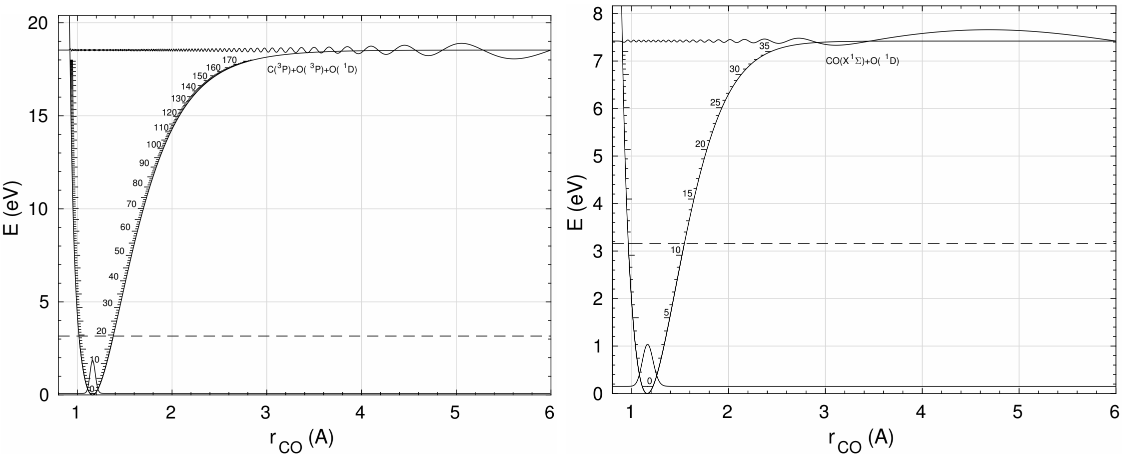

Figure 3.4: Symmetric (left) and asymmetric (right) 1D potentials of the CO_2 ground state with extrapolation to correct asymptotic limit of potential by the RKR method. The extrapolation is done above the dashed line, below which the data belongs to the NASA-Ames-2 PES.

The coefficients found by fitting this polynomial are in table 3.2. The obtained values for ω_i are very close to the ones obtained by Grebenshchikov which is not surprising since the level energy values were also obtained in the same work. Other works that have listed the mode frequencies for the excited state are Spielfiedel et al. [209] and Hwang & Mebel [210]. The values obtained by Spielfiedel for the symmetric and bending mode are relatively close to the ones obtained in this work while Hwang & Mebel have obtained similar values to the bending and asymmetric mode however, their values have not been assigned to any mode. The asymmetric mode value obtained by Spielfiedel and the third value obtained by Hwang & Mebel are not close to each other. Figure 3.6 presents the levels found by fitting the values in [208] to equation 3.78. The circles with a cross inscribed are the values found in [208] and the other are energy levels found from extrapolating the fit. The fine dotted line, labeled MSX1 is the seam of crossing between the ground state of CO_2 and the $^3B_2$ state. The line labeled as TS3 is the dissociation energy of the $^3B_2$ state. Usually, the spacing of levels will be lowered as the dissociation limit is approached. This is not the case in the asymmetric stretch mode of the $^3B_2$ state as the extrapolation of a polynomial expression does not allow replicating this behaviour. However as a first approximation it is a reasonable enough estimation. The line labeled as TS3 is the dissociation limit of the $^3B_2$ state. It is assumed that as in the case of the ground state, the asymptotic limit for each mode will be different and as such the symmetric and bending modes are not

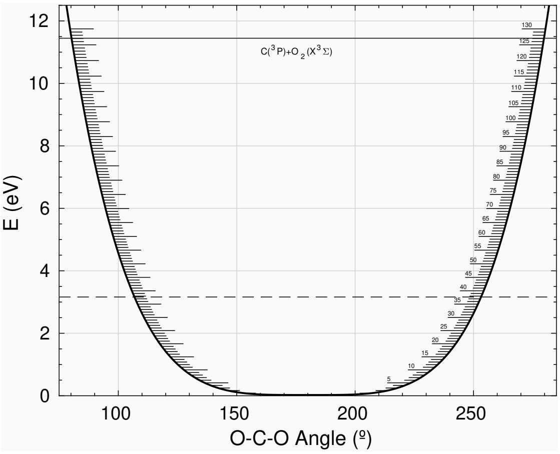

Figure 3.5: Bending angular potential of the CO_2 ground state. Above the dashed line extrapolation of the potential is performed by the expression $ax^2 + bx^4$. Below the dashed line is the data extracted from the NASA-Ames-2 PES.

asymptotically limited by TS3.

This concludes the determination of the level manifold used in this work. The number of levels used in this work is summarized in tab. 3.3. The number of levels in the v_3 mode for both electronic states is fixed since dissociation occurs through this mode. A v_3 level above the dissociation limit is considered to be quasi-bound (q.b.) and dissociates with probability 1 [116, 110]. The number of levels in the other modes may differ. We have elected to use 59 and 100 levels since these correspond to the same energy chosen arbitrarily, roughly ≈ 9 eV. No study was conducted to verify the sensitivity of the number of levels in the other modes. However, it was verified that using a smaller amount of levels in the ground state would lead to greater numerical instability in the code. With the levels included in tab. 3.3 and the ground state of each electronic level there is a total of 245 vibrational levels in the model.

Table 3.2: Coefficients obtained from fitting the expression in equation 3.78 to the energy levels found in [208] in units of cm^{-1}.

ω_1	ω_2	ω_3	x_{11}	x_{22}
1.387E+3	6.031E+2	1.092E+3	-8.254E+0	2.311E-1
x_{33}	x_{12}	x_{13}	x_{23}	
1.501E+0	-1.358E+1	-6.422E+1	-1.808E+1	

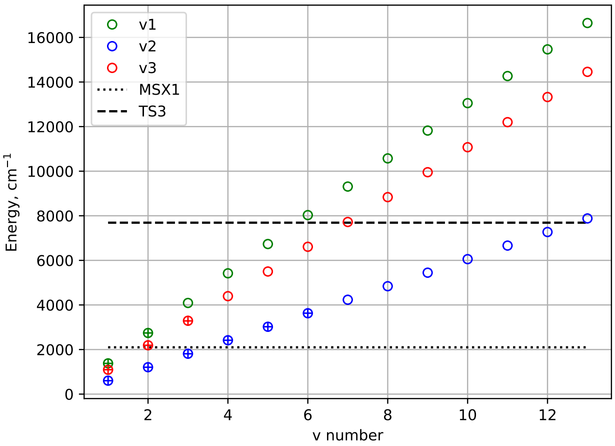

Figure 3.6: Manifold of vibrational levels of $CO_2(^3B_2)$ used in this work. These levels were determined with expression 3.78 and with the coefficients in table 3.2. MSX1 refers to the seam of crossing energy of the $CO_2(^3B_2)$ with the ground state, TS3 refers to the dissociation energy of $CO_2(^3B_2)$.

Table 3.3: Number of levels in the manifold used in this work for each mode of vibration and each electronic mode of CO_2.

CO_2	v_1	v_2	v_3
$X^1\Sigma$	59	100	41
$^3B_2$	12	25	6

PES Crossings

This work aims to account for the different pathways to dissociation of CO_2. For this, the configuration of the interactions between the ground state and electronically excited states of CO_2 needs to be defined. The work of Hwang & Mebel [210] provides a basis for the configuration of these interactions. There are two seams of crossings between the ground and $^3B_2$ states of CO_2. The first takes place at approximately 4.99 eV when the CO_2 molecule is bent close to the equilibrium configuration of the $^3B_2$ state. The exact configuration of the crossing will depend on the calculation method of calculation used. Looking at the range of values proposed in [210] an approximate region of the exact configuration is defined, between 1.22–1.30 Å and 105.0–110.4º, assuming the C–O bonds to be the same length. This region is plotted in fig. 3.7 as a black box. Fig. 3.7 also presents a 3D color map of the PES of the ground state of CO_2, considering both C–O bonds at the same length and varying the angle between them. The cyan line in the aforementioned figure is the position of minimum potential at each angle. The cyan line intersects the region where the exact configuration of the crossing is most likely to be. This indicates that the crossing may occur purely through the ground state with v_2 excitation, as this mode will play the main role interacting with the $^3B_2$ excited state. Only a few vibrational levels close to the crossing will interact with the bending levels of the ground state. The interacting $^3B_2$ levels have been defined as the ones within 2000 cm^{-1} of the crossing (MSX1). These coincide with the levels listed in the work of Grebenshchikov [208].

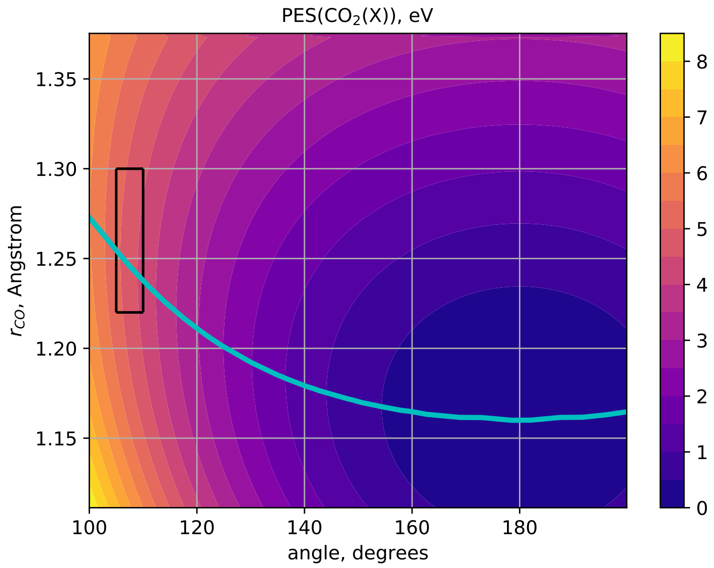

Figure 3.7: Color map of the PES of the ground state of CO_2 with $r_{1\text{CO}} = r_{2\text{CO}}$. The cyan line which crosses the color map is the equilibrium r_{CO} distance given a specific angle. The black box on the left side of the figure is the probable configuration space for the crossing between the CO_2 ground and triplet state to occur.

The second crossing takes place 5.85 eV in a linear configuration of CO_2 but with the bonds at very different lengths. In this crossing, the determined configuration in [210] has one bond length at approximately 1.9 Å and the other bond at 1.3 Å. This suggests that the mode which interacts the most in this crossing is the asymmetric stretch, v_3. The excited state in this crossing is in a repulsive configuration and being excited to this state will lead to immediate dissociation. As there is no access to the functional form of the triplet state there is no possibility to compute the energy levels of the quasi-bound states.

As such, it is assumed there is a level at the energy of the crossing of 5.85 eV to which the v_3 levels of the ground state of CO_2 will dissociate to.

The crossings considered in this work, where the Rosen-Zener theory will be applied, have been discussed. There are other singlet and triplet electronically excited states of CO_2 in a configuration alike to the $^3B_2$ level which was discussed in this section. These other states are not considered in this work due to the scarcity of published data on crossings between the ground state and other electronically excited states of CO_2. In the following section, the types CO_2 specific processes determined with FHO and Rosen-Zener are discussed.

3.3.2 Rate generation

The details of the FHO theory and how the probability of a collision is computed can be consulted in section 3.2.1. More examples of the application of this theory are found in [201, 116]. Here a description of what kind of collisions the model can compute is made. The FHO model computes Vibrational-Translational (VT) energy exchanges:

$$\mathrm{CO_2(i) + M \longleftrightarrow CO_2(f) + M} \tag{3.79}$$

where the i and f are vibrational levels of the same mode and M is a generic collision partner. In these reactions the electronic mode can be the ground state or the $^3B_2$ state. For transitions involving larger vibrational number changes and at higher-vibrational numbers, it is no longer possible to accurately compute transition probabilities. When such a computation is not possible it is instead replaced by the approximations suggested by Nikitin and Osipov [198] that make use of Bessel functions. Details of these approximations are found in section 3.2.1 and [201, 116]. Dissociation (Vibrational-Dissociation reactions, VD) can occur by the asymmetric stretch mode when the level in the products of the reaction is a quasi-bound (q.b.) level:

$$\mathrm{CO_2(v_3) + M \longleftrightarrow CO_2(q.b.) + M \xleftrightarrow{P=1} CO + O + M} \tag{3.80}$$

where the dissociation products are $CO(X^1\Sigma)$ and $O(^1D)$ in the case the reactant is the ground state and $CO(X^1\Sigma)$ and $O(^3P)$ in the case the reactant is the $^3B_2$ state. Dissociation is considered to be a certainty in a quasi-bound state and the recombination reaction is computed through detailed balance. A VT reaction can also occur when the initial and final level are not of the same mode (Intermode Vibrational-Translational, IVT). In that case the VT reaction is considered to be two VT reactions and the total probability is considered to be the product of these two collisions:

$$CO_2(\mathrm{i}) + \mathrm{M} \longleftrightarrow CO_2(0) + \mathrm{M} \longleftrightarrow CO_2(f) + \mathrm{M} \tag{3.81}$$

where $CO_2(0)$ is the fundamental vibrational state of either the ground electronic state or the $^3B_2$ state. Note that this classical approximation will lead to a vanishing small transition probabilities at higher v's[3]. This might not be necessarily the case since many "accidental resonances" may occur for these higher levels which means this approach will be underestimating IVT processes for these higher energy levels. Approaches to address this shortcoming will be discussed more ahead in chapter 5. A Vibrational-Vibrational-Translational (VVT) reaction can also be modeled. In these reactions, two molecules with the same vibrational level can collide in an almost resonant fashion such that at the end of the process, one has gained a quanta and the other lost one quanta:

$$CO_2(\mathrm{v}) + CO_2(\mathrm{v}) \longleftrightarrow CO_2(\mathrm{v}+1) + CO_2(\mathrm{v}-1). \tag{3.82}$$

In these reactions, a residual amount of energy is transferred to the translational movement of the molecules due to the anharmonicity of the vibrational ladder. Certain parameters in the model must be adjusted such that experimental measurements can be effectively reproduced by the calculations. As such, a so called semi-empirical adjustment of collision parameters takes place. Most notably, the inter-molecular potential, which is taken as a Morse potential $V = E\left[1 - \exp\left(-\alpha[r - r_{eq}]\right)\right]^2$, and the steric factors, which are corrective factors to account for the isotropy of collisions when these are computed in a 1D framework, will be adjusted such that calculations will match experimental rate coefficient measurements in the best possible way. Table 3.4 presents the semi-empirical coefficients obtained in the adjustment. The first two columns are for pure VT and VVT reactions as described in equations 3.79 and 3.82. The last three columns are specific for IVT reactions such as the ones in equation 3.81 and correspond to legacy calibrations of experimental rates. These coefficients have not been updated from a previous calculation method of IVT transitions since there was no major improvement without incurring into an unplausible parameter space for the parameters. Additionally, the current calculation method will be dominated by the Δv between initial and final vibrational numbers of the different modes corresponding to a rapid decline in transition probabilities as the vibrational number is

---

[3] unless the translational temperature is very high

increased. All experimental measurements are made for the ground state of CO_2, and it is assumed they are the same for $CO_2(^3B_2)$ since there is no experimental data available for calibrating the FHO model.

Table 3.4: Collision parameters used in the FHO rate calculation processes in this work.

	$VT_{s,b,a}$	$VVT_{s,b,a}$	$IVT_{s,b}$	$IVT_{s,a}$	$IVT_{b,a}$
S_{VT} (10^{-4})	6	-	2	1	6
S_{VVT} (10^{-3})	-	6.5	-	-	-
α (Å^{-1})	4.3	4.3	3.0	4.3	4.3
E (K)	650	650	300	650	650

Some of the adjustment results can be found in fig. 3.8 where examples of the VT and VVT reactions found in the literature can be recovered after adjusting the semi-empirical coefficients. In fig. 3.8 on the left some SSH VT rates of the bending mode are superimposed on FHO calculated rates of the same kind and on the right some experimentally determined VVT rates are compared against the same rates determined with FHO. The SSH rates which were proposed by Blauer & Nickerson in [59] are the extrapolation from the first rate which is experimental and obtained from [56]. Lacking other usable data the rates proposed by Blauer & Nickerson are suitable for adjusting FHO parameters. Furthermore, these rates have been used successfully to model low-temperature plasmas by a range of authors, see for example [17, 211], which suggests reasonability at least in the low-temperature regimes. More examples can be found in [201] and in the appendix C.

Finally, spin-forbidden reactions are modeled through the Rosen-Zener theory as described in section 3.2.2. This theory will be used to describe two crossings, the first one is the linear crossing at 5.85 eV described in section 3.3.1

$$CO_2(X,v_3) + M \longleftrightarrow CO_2(\text{rep.}) + M \xleftrightarrow{P=1} CO(X) + O(^1D) + M \tag{3.83}$$

where any level in the asymmetric stretch vibrational ladder can cross to the repulsive electronic state which rapidly dissociates into CO+O. The backwards reaction is computed through detailed balance. The difference between the reaction in equation 3.80 and this one is that the former requires a climb up the vibrational ladder up to 7.42 eV, above which only *quasi-bound* states are found, before dissociating. Also, as the former does

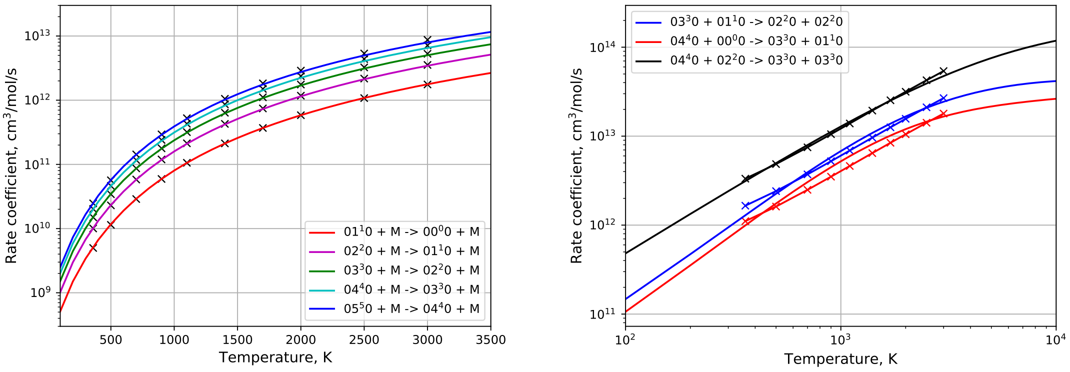

Figure 3.8: Examples of adjustment of FHO computed rates to SSH obtained VT rates (left) and experimentally determined VVT rates (right). The used collision parameters can be found in table 3.4. More examples of these adjustments are found in [201] and in the appendix C.

not involve a potential crossing, the interactions are described by the FHO theory. The latter reaction involves a smaller climb of 5.85 eV or a decay from a higher level to 5.85 eV and since it involves a potential crossing the interaction is described by the Rosen-Zener theory. In the Rosen-Zener formulation the difference in energy between the initial and final level ΔE is the fundamental parameter required to model the transition. In this case, no final level is known and ΔE is computed as the difference in energy between the initial vibrational level and the crossing energy of 5.85 eV. The second interaction described by the Rosen-Zener theory in this model is the crossing between the $\mathrm{CO_2}$ ground and $^3\mathrm{B}_2$ states

$$\mathrm{CO_2}(X, \mathrm{v}_2) + \mathrm{M} \longleftrightarrow \mathrm{CO_2}(B, \mathrm{v}_f) + \mathrm{M} \tag{3.84}$$

where v_f is the final vibrational level, which can be any of the modes of the $^3\mathrm{B}_2$ state. This is so since the crossing is very close to the bottom of the potential well of the excited state and as such the low lying levels of all modes are assumed to be very close to the crossing configuration between the ground and excited state. The interacting mode of the ground state can only be the bending mode as discussed in figure 3.7. In this case ΔE is defined between the initial and final levels. However, ΔE only makes sense as a parameter for the collision as long as the crossing is between the initial and final state. As Rosen-Zener is a "single-passage" theory, meaning the colliding species only "meet" once, in contrast with the Landau-Zener theory, in which they "meet" twice, hence "double-passage", only one energy exchange is permitted. This means that internal energy of $\mathrm{CO_2}$ only goes up or down, it cannot do both. As such, rate generation must take the configuration between initial, intermediate and final steps of the process into account. Within the Rosen-Zener formulation that is done ensuring that

$$E_i < E_{\text{crossing}} < E_f,$$

where i and f means the initial and final state, or the reverse must be true. In contrast with the FHO generated rates, the Rosen-Zener rates cannot be calibrated with literature data, since there is no known data for the processes to be calibrated to. Figure 3.9 schematically represents the model constructed so far. The levels are realistically aligned in the figure and the arrows represent the processes by which each ladder interacts with each other and itself. The slashed magenta lines represent CO_2 decomposition limits.

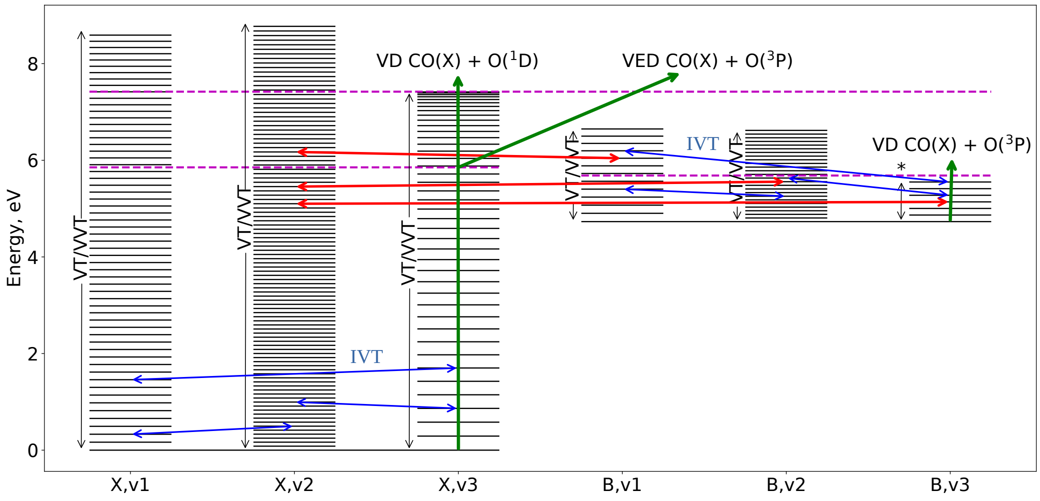

Figure 3.9: Schematic of kinetic model with included levels and types of interactions between levels. Dissociation reactions indicate the products of dissociation and the dashed lines represent crossings or dissociation limits for certain configurations of CO_2.

3.3.3 Macroscopic Chemistry

At this point, some simulations were conducted to test if the model with its current dissociation pathways is consistent with typical dissociation time and degree of CO_2. A 1D shock wave at 3690 m/s was simulated passing a CO_2 gas at 1 Torr and 300K. In these conditions dissociation was expected to be noticeable on the micro-second scale and the gas would be nearly in equilibrium under a second. In these conditions dissociation was expected to be noticeable on the 10^{-4} seconds scale and the gas would be nearly in equilibrium under a second. These are general expectations based on simulations using the macroscopic models of Park *et al.* [41] and Cruden *et al* [212]. Figure 3.10 presents in black the CO_2 mole fraction of this first simulation with the model described so far. This result fails to meet the expected macroscopic physical behaviour for these conditions as the flow has not arrived to equilibrium after 1 second. As such, in this section the model will be enriched by other processes that will make an impact on the overall decomposition of CO_2.

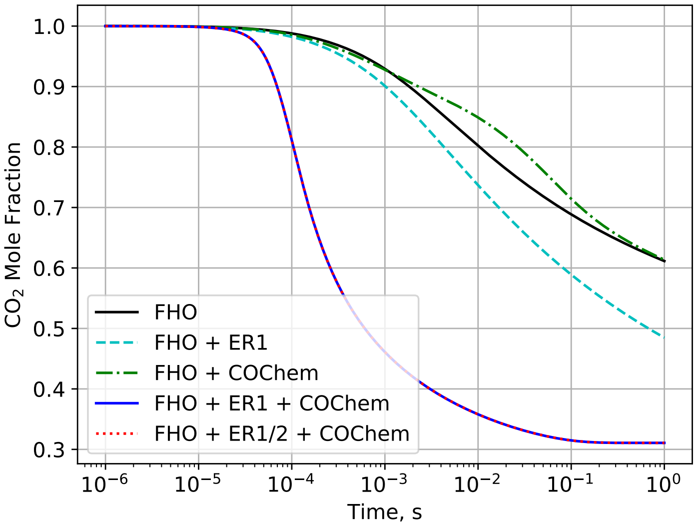

Figure 3.10: CO_2 simulated mole fraction in a 3690 m/s shock at 133 Pa in pure CO_2. The different lines correspond to the inclusion or exclusion of certain reactions. FHO corresponds to the model schematized in fig. 3.9. The inclusion of the exchange reaction $CO_2 + O \longleftrightarrow CO + O_2$ (Sharipov), the $CO_2 + C \longleftrightarrow CO + CO$ and the CO chemistry to the aforementioned FHO model are labeled ER1, ER2 and COChem, respectively.

It has been experimentally observed that the addition of O atoms to the gas composition increases the dissociation rate of CO_2 [36]. This is usually attributed to the exchange reaction $CO_2 + O \longleftrightarrow CO + O_2$. Table 3.5 presents some of the different exchange reaction rates found in literature and considered for this work. Reactions 1 and 2 are taken from experimental studies [213, 214] of the inverse reaction $CO + O_2 \longleftrightarrow CO_2 + O$. The first source presented is the original experiment and the second source is where the rate coefficient for the $CO_2 + O \longleftrightarrow CO + O_2$ reaction was reported. Reaction rate 3 from [70] is mentioned as an adaptation from [215] but it is not made clear how this adaptation was performed. Rate 4 was originally reported in [216]. The original document could not be found and as such it is not know whether this rate is experimental or calculated by other means. Rates 5, 6, and 7 are presented as Arrhenius fit coefficients valid in the $800 - 5,000$ K region from QCT calculations carried out by Sharipov and Starik [217] on the $CO + O_2$ collision. Rate 5 assumes a Boltzmann distribution of the internal states of all intervening chemical species. Rates 6 and 7 are state to state rates corresponding to different seams of crossing between the $CO+O_2$ ground states intermolecular potential and $CO_2 + O$ intermolecular potential. The first crossing allows only the production of ground state oxygen, $O(^3P)$ while the second crossing also produces $O(^1D)$. The authors of [217] decided not to branch the production of different O levels as this reaction is negligible compared to others presented in the same work. An additional reaction is presented in [217] where $CO + O_2(a)$ produces $CO_2 + O$ but the contribution of $O_2(a)$ will be neglected in this work and considered only for future developments of this model. Finally, rate 8 coefficients were obtained from sensitivity analysis of combustion experiments in Varga PhD Thesis [218] and reported to have low uncertainty. In this work, an inversion of rates 5 to 8 was performed using an in-house code by computing the partition functions of intervening molecules and the equilibrium constant of the $CO + O_2 \longleftrightarrow CO_2 + O$ reaction. The coefficients in table 3.6 correspond to the coefficients in equation 3.37 for the forward reactions of rates 5 to 8. Reaction rates 1 to 5 and 8 were assumed to involve only the ground state of each chemical species. Reactions 6 and 7 were used to derive a reaction rate coefficient for the $CO_2 + O(^3P) \longleftrightarrow CO + O_2$ and $CO_2 + O(^1D) \longleftrightarrow CO + O_2$ reactions, by assuming a $50 : 50$ branching for O atoms in rate 7. The addition of k_6 and half of k_7 are labeled as 'Sharipov StS 1' and half of k_7 is labeled as 'Sharipov StS 2' in figure 3.11 where these rate coefficients are plotted along with k_1 to k_5 and k_8 of table 3.5. The collisional rate coefficient of the $CO_2 + O$ collision is also plotted in black in the same figure. Back to fig. 3.10, the curve with the redistributed (see 3.2.3) $CO_2 + O$ exchange reaction reported by Sharipov [217] and denoted k_5 in table 3.5, is plotted with the label 'FHO + ER'. An improvement to the previous model is obtained but still far from an equilibrium state at the second time scale.

An important reaction in industrial processes is the Boudouard reaction $2\,CO \longleftrightarrow CO_2 + C$. In the aforementioned processes this usually involves a phase change of the product carbon and is one of the responsible reactions in the creation of soot. Therefore, most available data does not consider all chemical species in the gaseous phase. The NIST Chemical Kinetics Database contains two estimates for the reaction rate coefficient at

Table 3.5: List of $CO_2 + O \longleftrightarrow CO + O_2$ reaction rates found in literature and considered for this work.

#	A ($cm^3/mol/s$)	n	θ (K)	Notes	Source
k_1	2.11E+13	0.0	6,651	2,400-3,000 K	[213, 215]
k_2	2.10E+13	0.0	27,800	1,700-3,500 K at 1.8 bar	[214, 41]
k_3	2.14E+12	0.0	22,848	Adapted from k_1	[70]
k_4	2.71E+14	0.0	33,800	-	[216, 212]
k_5	4.32E+7	1.618	25,018	inv. reac., 800-5,000 K	[217]
k_6	7.63E+6	1.670	26,950	$O(^3P)$, see k_5	[217]
k_7	5.18E+6	1.728	33,470	$O(^1D)$ and $O(^3P)$, see k_5	[217]
k_8	2.88E+12	0.0	24,005	inv. reac., set of exp.	[218]

300 K of the reaction $CO_2 + C \longleftrightarrow 2\,CO$. The lowest estimate, which is also the most recent, is taken from [219] as $k_f = 6.022 \times 10^8$ cm^3/mole/s and expanded as in section 3.2.4. After the expansion, a redistribution as in section 3.2.3 is performed. Despite being an important industrial process in the gaseous phase this reaction is not expected to be important since C atoms are very reactive and disappear fast in gaseous environments to form other compounds. It is included just for the sake of completeness.

Quenching of atomic O is also introduced in the model. Specifically, the reaction $O(^1D) + M \longleftrightarrow O(^3P) + M$ is addressed with data from the literature. Before that, a brief discussion on the importance of this mechanism is carried here. The appendix of the work of Fox and Hać [220] provides an extensive review of cooling mechanisms of hot O atoms. These hot atoms need not be electronically excited O, even translationally excited $O(^3P)$ atoms can redistribute their energy to the ro-vibrational modes of molecules. Important collision partners are CO, O_2 and CO_2. One contribution [221] has even reported an efficient deposition of translational energy into the ro-vibrational modes of CO_2. Additionally, the importance of the excited $O(^1D)$ atom cannot be understated as its excess energy can be redistributed to vibrationally excited O_2 and CO_2 molecules by the reactions: $O(^1D) + CO_2 \longleftrightarrow O_2(v,J) + CO + 1.63$ eV and $O(^1D) + CO_2 \longleftrightarrow O(^3P) + CO_2(v,J) + 1.97$ eV. However, this work only deals with quenching reactions like $O(^1D) + M \longleftrightarrow O(^3P) + M$. Some measurements of the reaction rate coefficients at 300 K are summarized in table 3.7.

Table 3.6: Coefficients for the $CO_2 + O \longleftrightarrow CO + O_2$ reactions 5 to 8 of table 3.5 using equation 3.37 for fitting. Units are in $cm^3/mol/s$.

	k_5	k_6	k_7	k_8
a	-4.071E-1	2.643E-5	2.377E-5	-4.071E-1
b	2.888E+0	2.072E+2	2.073E+2	2.888E+0
c	-3.693E+1	-3.115E+1	-3.767E+1	-1.194E+1
d	-1.716E+0	1.678E+0	1.736E+0	-3.334E+0
e	3.578E+1	2.969E+1	2.970E+1	3.571E+1
f	4.620E-1	-5.880E-4	-5.871E-4	4.619E-1
g	-7.840E-3	9.232E-6	9.217E-6	-7.840E-3
h	6.734E-5	-8.196E-8	-8.182E-8	6.734E-5
i	-2.220E-7	2.877E-10	2.872E-10	-2.219E-7

These reactions are given a temperature dependence according to equation 3.77 and fitted to Arrhenius rates

$$k_f = AT^n \exp\left(-\frac{\theta}{T}\right). \tag{3.85}$$

A reaction rate coefficient with partner $O(^3P)$ is also available from [222] but with no temperature validity range, with the form:

$$k_f = A + B\sqrt{T} + CT \tag{3.86}$$

and coefficients $A = 7.66 \times 10^{-12}$, $B = 2.13 \times 10^{-13}$ and $C = -1.84 \times 10^{-15}$ in units of $cm^3/part./s$. An Arrhenius fit was performed on this reaction from 300 up to 2500 K and checked for consistency up to $100,000$ K. The Arrhenius coefficients of the fitted O quenching reactions are found in table 3.8. This concludes the construction and preparation of the STS model. The main mechanisms for this model are summarized in table 3.10 with the type of reaction and the number of state-to-state reactions which are included. However, other processes not directly related to CO_2, could still make an impact on the concentration of CO_2. As such the thermochemistry for CO reported in the work of Cruden *et al.* [212] has been included in the kinetic model. In these reactions it has been assumed that O is in its ground state. The included rates can be found in table 3.9. In fig. 3.10 the label 'COChem' indicates the inclusion of the reactions in table 3.9 of the

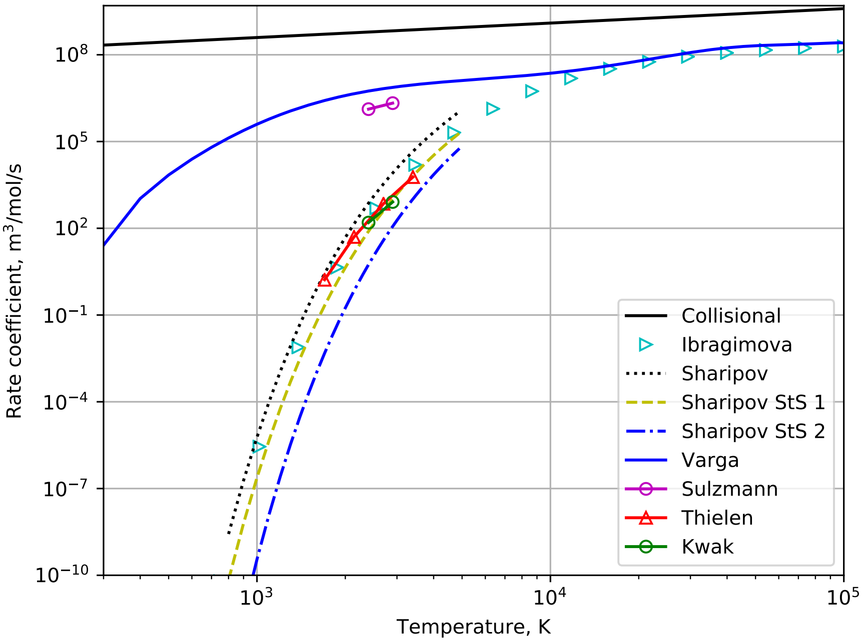

Figure 3.11: Exchange reactions $CO_2 + O \longleftrightarrow CO + O_2$ found in some works in literature plotted with the collisional $CO_2 + O$ rate coefficient.

simulation. In the curve with label 'FHO + COChem' the CO_2 mole fraction of the model without the exchange reaction of $CO_2 + O \longleftrightarrow CO + O_2$. This suggests a major role of the exchange reaction in the decomposition of CO_2.

Table 3.7: Quenching reaction rates of $O(^1D) + M \longleftrightarrow O(^3P) + M$ at 300 K. Units are 10^{-10}cm^3/part/s.

M	CO_2	CO	O_2
k_f	1.03	0.3	0.41
Source	[223]	[224]	[225]

To recap, figure 3.10 presents some typical conditions where a pure CO_2 flow is expected to be at equilibrium before 1 second has elapsed. Several simulations with different versions of the model are checked for consistency against this benchmark. In figure 3.10 the label 'FHO' contains all rates determined in section 3.3.2 while all other labels refer to enhancements to the model detailed in this section. The label 'FHO + ER1' pertains to the 'FHO' model plus the $CO_2 + O$ exchange reaction. The label 'FHO + COChem' refers to the 'FHO' model plus the CO reactions included in Cruden2018. The label 'FHO

Table 3.8: Quenching reaction rates of $O(^1D) + M \longleftrightarrow O(^3P) + M$ fitted by Arrhenius reaction rates.

M	CO_2	CO	O_2	$O(^1D)$
A (10^{12}cm^3/mol/s)	3.58	1.04	1.43	4.21
n	0.50	0.50	0.50	0.088
θ (K)	0.00	0.00	0.00	21.91

+ ER1/2 + COChem' refers to the base STS model, the redistribution of the $CO_2 + O$ and $CO_2 + C$ exchange reactions and the CO reactions in [212].

3.3.4 Final dataset

To summarize the model developed in this work, reaction names and number of reactions are in table 3.10. This table excludes the macroscopic reactions from [212], since these are presented in table 3.9. There are 11 species in the model: CO_2, CO, O_2, C_2, C, O, CO^+, ${O_2}^+$, C^+, O^+, e^-, two of which are state specific, CO_2 with 201 vibronic levels and O with 2 electronic levels. The model contains a total of $22,569$ reactions, only 14 of which are not STS.

3.3.5 Underlying assumptions and restrictions

CO_2 is a triatomic molecule and consequently it has more degrees of freedom than a diatomic molecule. This induces complexities in the sense that modeling for such molecules needs to be tractable with a reasonable number of levels and rates, compatible with current-day computational resources. In this sense, much more restrictions and assumptions than in the case of diatomic molecules need to be brought. For example, diatomic molecules state-to-state models customarily assume a Boltzmann equilibrium for the rotational levels, solely modeling a reasonable number of vibrational and electronic states (in order of the hundred). For CO_2 not only this has to be assumed, but furthermore additional restrictions have to be brought regarding the different vibrational degrees of freedom. These include:

- Full separation of the three vibrational modes of CO_2, only considering its so-called *extreme states*. An *extreme* state is a state which is only part of a single mode, in our

Table 3.9: Reactions and Arrhenius coefficients proposed in [212].

Reaction	A ($cm^3/mol/s$)	n	θ (K)	Source
$CO + M \longleftrightarrow C + O + M$	7.99×10^{38}	-5.5	129,000	[226]
$C_2 + O \longleftrightarrow CO + C$	3.61×10^{14}	0.0	0.0	[227]
$C_2 + M \longleftrightarrow C + C + M$	1.82×10^{15}	0.0	64,000	[227]
$CO + O \longleftrightarrow C + O_2$	3.9×10^{13}	-0.18	69,200	[41]
$O_2 + M \longleftrightarrow O + O + M$	1.2×10^{14}	0.0	54,246	[228]
$C + e^- \longleftrightarrow C^+ + e^- + e^-$	3.7×10^{31}	-3.0	130,700	[41]
$O + e^- \longleftrightarrow O^+ + e^- + e^-$	3.9×10^{33}	-3.78	158,500	[229]
$CO + e^- \longleftrightarrow CO^+ + e^- + e^-$	4.5×10^{14}	0.275	163,500	[230]
${O_2} + e^- \longleftrightarrow {O_2}^+ + e^- + e^-$	2.19×10^{10}	1.16	130,000	[230]
$C + O \longleftrightarrow CO^+ + e^-$	8.8×10^{8}	1.0	33,100	[41]
$CO + C^+ \longleftrightarrow CO^+ + C$	1.1×10^{13}	0.0	31,400	[41]
$O + O \longleftrightarrow {O_2}^+ + e^-$	7.1×10^{2}	2.7	80,600	[231]
$O_2 + C^+ \longleftrightarrow {O_2}^+ + C$	1.0×10^{13}	0.0	9,400	[41]
${O_2}^+ + O \longleftrightarrow O_2 + O^+$	2.19×10^{10}	1.16	130,000	[231]

model it implies that no mixed-mode states are treated. This is perhaps the most significant limitation of this model, with implications on the modeling of higher, near-dissociation levels, which will be discussed ahead. Nevertheless, this allows us to achieve a computationally tractable model with about $N \approx 250$ levels instead of the $N \approx 10,000+$ real ground state levels of CO_2.

- For the same reasons, there is no specific accounting of the l_2 bending quantum numbers. Billing calculations from ref. [232] predict differences ranging from a factor of 5 to one order of magnitude in transitions from the same v_2 level, depending on the l_2 quantum number.

- The CO_2 PES is extrapolated in its 3 modes limit (*ss*, *be*, *as*) by a representative repulsive and near-dissociation potential. While this is not as accurate as defining a proper PES near-dissociation potential (which is not carried out in the NASA-

Table 3.10: List of reactions included in the CO_2 kinetic model. Not listed are the reactions taken from the kinetic scheme in [212] which describes CO thermochemistry. These reactions can be found in table 3.9.

	Name	Type	#Reac.
R1	$CO_2(X,v'_1) + M \leftrightarrow CO_2(X,v''_1) + M$	VT	1770
R2	$CO_2(X,v'_2) + M \leftrightarrow CO_2(X,v''_2) + M$	VT	5050
R3	$CO_2(X,v'_3) + M \leftrightarrow CO_2(X,v''_3) + M$	VT	861
R4	$CO_2(X,v'_1) + CO_2(X,v'_1) \leftrightarrow CO_2(X,v'_1+1) + CO_2(X,v'_1-1)$	VVT	58
R5	$CO_2(X,v'_2) + CO_2(X,v'_2) \leftrightarrow CO_2(X,v'_2+1) + CO_2(X,v'_2-1)$	VVT	99
R6	$CO_2(X,v'_3) + CO_2(X,v'_3) \leftrightarrow CO_2(X,v'_3+1) + CO_2(X,v'_3-1)$	VVT	41
R7	$CO_2(X,v'_1) + M \leftrightarrow CO_2(X,v''_2) + M$	IVT	5900
R8	$CO_2(X,v'_1) + M \leftrightarrow CO_2(X,v''_3) + M$	IVT	2478
R9	$CO_2(X,v'_2) + M \leftrightarrow CO_2(X,v''_3) + M$	IVT	4200
R10	$CO_2(B,v'_1) + M \leftrightarrow CO_2(B,v''_1) + M$	VT	78
R11	$CO_2(B,v'_2) + M \leftrightarrow CO_2(B,v''_2) + M$	VT	325
R12	$CO_2(B,v'_3) + M \leftrightarrow CO_2(B,v''_3) + M$	VT	21
R13	$CO_2(B,v'_1) + CO_2(B,v'_1) \leftrightarrow CO_2(B,v'_1+1) + CO_2(B,v'_1-1)$	VVT	11
R14	$CO_2(B,v'_2) + CO_2(B,v'_2) \leftrightarrow CO_2(B,v'_2+1) + CO_2(B,v'_2-1)$	VVT	24
R15	$CO_2(B,v'_3) + CO_2(B,v'_3) \leftrightarrow CO_2(B,v'_3+1) + CO_2(B,v'_3-1)$	VVT	6
R16	$CO_2(B,v'_1) + M \leftrightarrow CO_2(B,v''_2) + M$	IVT	300
R17	$CO_2(B,v'_1) + M \leftrightarrow CO_2(B,v''_3) + M$	IVT	84
R18	$CO_2(B,v'_2) + M \leftrightarrow CO_2(B,v''_3) + M$	IVT	175
R19	$CO_2(X,v'_2) + M \leftrightarrow CO_2(B,v''_1) + M$	VE	103
R20	$CO_2(X,v'_2) + M \leftrightarrow CO_2(B,v''_2) + M$	VE	311
R21	$CO_2(X,v'_2) + M \leftrightarrow CO_2(B,v''_3) + M$	VE	163
R22	$CO_2(X,v'_3) + M \leftrightarrow CO + O(^1D) + M$	VD	42
R23	$CO_2(X,v'_3) + M \leftrightarrow CO + O(^3P) + M$	VD	42
R24	$CO_2(B,v'_3) + M \leftrightarrow CO + O(^3P) + M$	VD	7
R25	$CO_2(X,v'_{1,2,3}) + O(^3P) \leftrightarrow CO + O_2$	Exchange	201
R26	$CO_2(X,v'_{1,2,3}) + C \leftrightarrow CO + CO$	Exchange	201
R27	$O(^1D) + M \leftrightarrow O(^3P) + M$	Quench.	4

Ames-2 PES), the extrapolation should still be capable of providing correct near-dissociation trends, as compared with the usual extrapolation of polynomial expansions. Past similar approaches for diatomic molecules have provided quite accurate results [112].

In addition to those, other limitations currently exist, but could easily be waived in future works:

- Considering an isotropic Morse-like intermolecular potential, and assuming the collision as 1D with the application of a steric factor. Comparisons carried out with the FHO model against PES-based methods show that rates with the same order of magnitude are predicted. However the temperature dependence at low-temperatures is poorly reproduced by the FHO model, and attractive low-temperature effects should be modeled resorting to the Sharma-Brau [57] theory, and added to the rate provided by the FHO theory. Results in the higher temperature limit have a better agreement with PES results, as would be expected in the Landau-Teller limit (increasing $\log(K_f)$ over $T^{-1/3}$). Regarding the scaling of rates to higher vibrational quantum levels, there is not enough PES-based data to provide a meaningful comparison. Nevertheless, since this work is mostly concerned with mid to high-temperature regimes, the low-temperature limits below room temperature may be safely neglected.
- The rates of collision are the same independently of the collisional partner, which is assumed to be CO_2. This assumption is temporarily used as a matter of convenience, since the examples in this work are applied to pure CO_2 flows. This assumption will need to be revisited for increasing the accuracy of the database or allowing for simulations of highly diluted CO_2 flows (typically in Helium or Argon baths).

3.4 Results

The results of the developed model are shown and discussed in this section. Firstly some of the calculated rates in table 3.10 are shown and discussed. Then, simulations of an isothermal gas with no dissociation, a CO_2 gas excitation and relaxation with dissociation and a recombination simulation are shown and discussed with an emphasis on the behaviour of the modes of CO_2 and mechanisms for the decomposition of CO_2. Secondly, a comparison to available shock-tube data is performed.

3.4.1 Rates Dataset

This subsection will present some of the calculated rates presented in table 3.10. Notably, mechanisms R2, R7 and R23. Mechanisms R1-R3 and R10-R12 share the same functional form. The same can be said for mechanisms R7-R9 and R16-R18. Reactions that involve a spin-forbidden interaction such as R19, R20, R21 and R23 also share some similarities.

Firstly, in fig. 3.12 the $\log_{10}(K_{\mathrm{VT}})$ rate coefficients of the bending levels of ground electronic state of CO_2 are shown at 5000 K. These correspond to the rate coefficients of mechanism R2 in table 3.10. It is expected that transitions with small differences in the vibrational number should be stronger than transitions with greater Δv. This is observed as the rate coefficients tend to a maximum value around the plane where $\mathrm{v}_2' = \mathrm{v}_2''$. The reactions with no change in vibrational number are not depicted as these correspond to no energy exchange taking place. Two oblique surfaces corresponding to exothermic and endothermic reactions are observed. The exothermic reactions are slightly more likely than endothermic reactions and this is also observed by comparing the inclination of the surfaces against the z axis scale in the planes $v_2' = 100$ and $v_2'' = 100$. Reaction mechanisms R1-R3 and R10-R12 are functionally the same as R2 with some deformations that might occur when the Bessel approximation [198] is used.

Secondly, in fig. 3.13 the $\log_{10}(K_{\mathrm{IVT}})$ rate coefficients between the bending and symmetric stretch levels of ground CO_2 are shown at 5000 K. These processes correspond to mechanism R7 in table 3.10. As these transition probabilities are modeled as VT transitions with large changes in vibrational number, the rate coefficients drop very fast as the vibrational numbers increase. Reaction mechanisms R8, R9 and R16-R18 share the same functional form as mechanism R7.

Finally, in fig. 3.14 the rate coefficients of mechanism R23 in table 3.10 are plotted at 1000, 3000 and 5000 K. A maximum of the rate coefficient is observed at the vibrational number which is closest to the crossing between the ground state of CO_2 and the repulsive triplet state of CO_2. This is expected by the simple formulation of the Rosen-Zener probability formula in eq. 3.70. Mechanisms R19, R20 and R21 are also computed through the same formula and may have different crossings which will correspond to horizontal shifts in the peak of the rate coefficients plotted in fig. 3.14. Otherwise, the aforementioned mechanisms share the same functional form as R23.

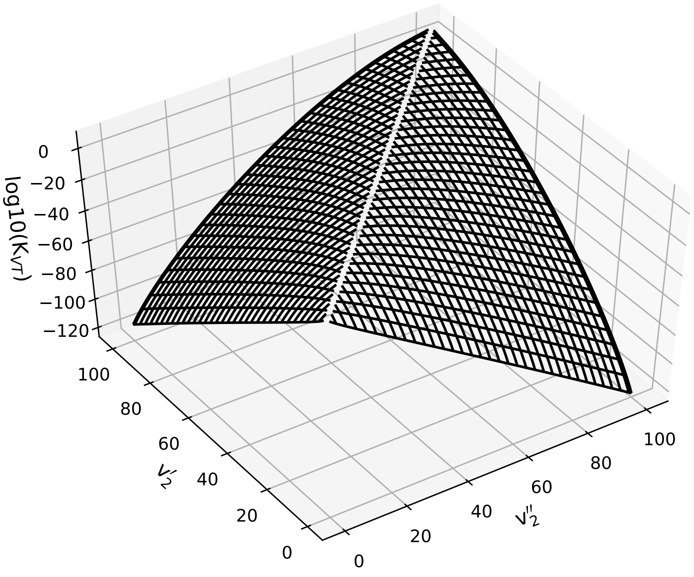

Figure 3.12: Logarithm 10 of VT rate coefficients (in m^3/mol/s) at 5000 K between bending levels of CO_2. As expected, large quantum jumps have lower probability than smaller jumps. VT rate coefficients of other modes have the same functional shape.

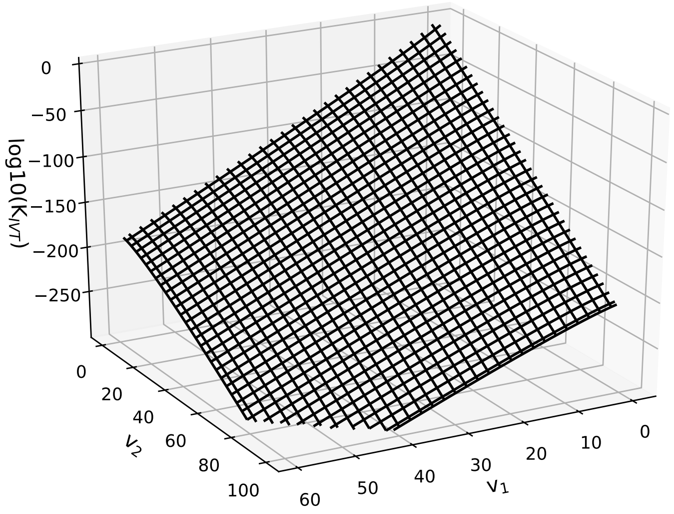

Figure 3.13: Logarithm 10 of IVT rate coefficients (in m^3/mol/s) at 5000 K between the symmetric and bending modes of CO_2. As expected, the probability of intermode energy exchange is lowest when the vibrational numbers are high and highest when the vibrational numbers are low. Other IVT rate coefficient sets have the same functional shape.

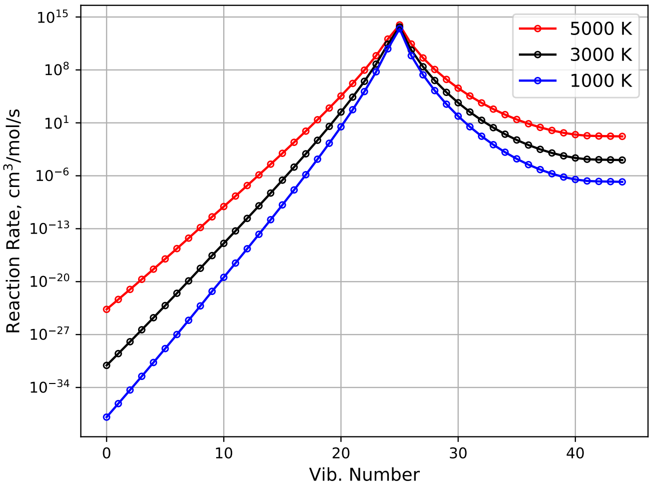

Figure 3.14: Rate coefficients computed using the Rosen-Zener probability formula (eq. 3.70) for mechanism R23 in table 3.10. The rate coefficients are computed at 1000, 3000 and 5000 K and as expected, the greater transition probabilities lie close to the crossing point between the singlet and triplet CO_2.

3.4.2 Theoretical test cases

Results in this section were obtained using the in-house code SPARK (Simulation Platform for Aerodynamics, Radiation, and Kinetics), which is an object-oriented multiphysics code written in Fortran and capable of solving a set of Ordinary Differential Equations (ODE) for 0D/1D geometries, or a set of Partial Differential Equations (PDE) for 2D axyssimetric geometries, solving the Navier–Stokes equations with macroscopic and/or state-to-state chemistry, high-temperature thermodynamic models, multicomponent transport, and plasma effects (ambipolar diffusion, etc...) [233]. The code has been primarily applied to the simulation of atmospheric entry flows [120, 234], but is also being recently tailored for the simulation of atmospheric pressure plasma jets (APPJ's) [235]. The governing equations implemented in this code were already described in section 3.1.8.

CO_2 isothermal

An isothermal 0D simulation was performed for a pure CO_2 gas, initially at 300 K and 2000 Pa with the thermal temperature suddenly raised to 5000 K. For this particular simulation it was decided not to use dissociation processes and consider only CO_2 internal processes. Time snapshots of the mass fractions of CO_2 are plotted in fig. 3.15. In the top left figure, at $t = 8.52 \times 10^{-7}$ seconds the bending mode is excited much faster than the

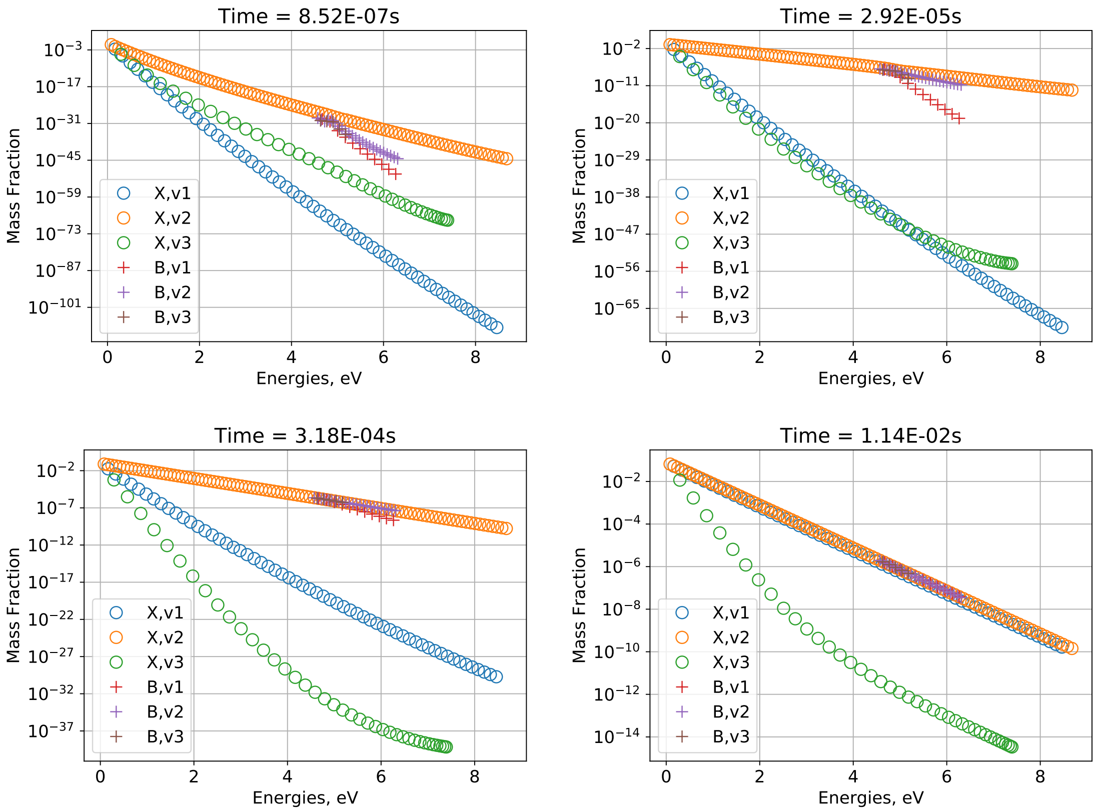

Figure 3.15: Time snapshots of the CO_2 vibrational distribution in a 0D Isothermal simulation of a pure CO_2 gas at 2000 Pa initially at 300 K and a final temperature of 5000 K.

other modes. This is expected since the spacing between consecutive vibrational levels is smaller. The electronically excited CO_2 accompanies the excitation of the bending which gets more populated than the levels at the same energy of the asymmetric and symmetric stretch modes of the ground state of CO_2. Contrary to expectations the asymmetric mode is more populated than the symmetric stretch mode. That changes at $t = 2.92 \times 10^{-5}$ seconds in the top right of figure 3.15. At this time, the symmetric stretch mode overtakes the asymmetric stretch mode of CO_2 ground state, except in the higher energy levels of the asymmetric stretch mode. At $t = 3.18 \times 10^{-4}$ seconds the bending mode and the CO_2 triplet state are almost in their equilibrium populations. At $t = 1.14 \times 10^{-2}$ seconds all CO_2 subpopulations are in equilibrium except the asymmetric stretch mode. From these simulations and considering the possible pathways for CO_2 dissociation, it is expectable that the greatest contributor to CO_2 dissociation is the pathway through the excited triplet state of CO_2.

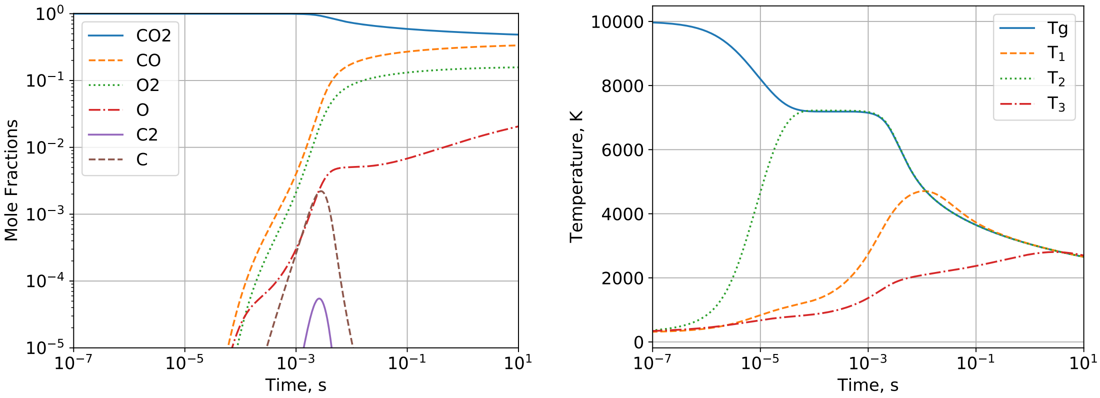

Figure 3.16: Mole fractions (right) and temperatures (left) of CO_2 gas initially at 300 K and 2000 Pa suddenly heated to $10,000$ K in a 0D simulation.

CO_2 Dissociating flow

Another 0D simulation was performed again in a pure CO_2 gas initially at 300 K and 2000 Pa is suddenly heated to $10,000$ K and allowed to relax and dissociate. The mole fractions are plotted on the left in fig. 3.16. On the right, the gas temperature and the internal temperature obtained from fitting a Boltzmann distribution on the vibrational distribution of each mode of ground CO_2 are presented. There are several features that should already be expected from previous discussion in this work. Firstly, the relative distribution of vibrational modes of CO_2 is in agreement with the distributions in fig. 3.15, except in this case the gas is not isothermal and as such the temperature continuously drops and the thermal equilibrium is achieved later. Secondly, as has been seen in fig. 3.10 the exchange reaction $CO_2 + O \longleftrightarrow CO + O_2$ dominates the decomposition of CO_2 as the creation of CO and O_2 far outpaces the production of O atoms which are created mostly through the VD reactions calculated through the FHO or the Rosen-Zener model. Additionally, the initial temperature decay from 10^{-7} to 10^{-5} seconds stems mostly from the excitation of the bending mode and the exchange reaction $CO_2 + O \longleftrightarrow CO + O_2$ is very efficient energy-wise as the gas temperature is mostly constant between 10^{-4} to 10^{-3} when the aforementioned reaction is most active. Beyond 10^{-3} seconds, chemistry becomes most active with the dissociation of C_2 molecules into C atoms and around 10^{-2} seconds CO_2 vibrational modes are in equilibrium with each other.

$\mathbf{CO_2}$ Recombining flow

A third and final 0D simulation attempts to capture the recombination dynamics of CO_2. The equilibrium composition of a $CO_2COO_2C_2CO$ gas and their respective ions and electrons was determined at 5000 K through an in-house code. A very similar mixture, to round the sum of all molar fractions to 1, is determined and left at 1000 K and 1 bar with the isothermal condition enforced. This simulation is performed with the $CO_2 + O \longleftrightarrow CO + O_2$ determined by Sharipov [217] and Varga [218]. This is thus since at 1000 K these reactions are over nine orders of magnitude different as can be seen in figure 3.11. It is also worth to remind that although most rate coefficients in figure 3.11 agree with the rate from Sharipov [217], the rate from Varga is obtained from a sensitivity analysis of experimental data of combustion experiments. As such, it is not a whimsical comparison but a demonstration of the disparity of the $CO_2 + O$ reaction rate estimate at low temperatures. The mole fractions of this simulation are plotted in fig. 3.17 with the simple lines using the Sharipov rate and the lines with circles using the Varga rate. Very quickly, C atoms and C_2 molecules disappear from the gas and as such are not displayed in the figure. C^+ atoms recombine somewhat slower, O^+ and e^- take somewhat longer to recombine and their temporal variation is very similar. For the simulation using Sharipov, O atoms start recombining into O_2 molecules at around 10^{-8} seconds and further combine with CO to form CO_2 at 10^4 seconds. At around 10^1 CO_2 starts to recombine and is fully recombined around 10^6 seconds. In contrast, the simulation using the Varga rate starts the recombination of O atoms into O_2 molecules and at the same time CO_2 has also started recombination. O_2 molecules diverge from the Sharipov simulation after 10^{-7} seconds to react with CO to create more CO_2. The O atoms are consumed more rapidly, either recombining into O_2 or into CO_2, than CO and O_2 molecules recombining into CO_2 which becomes close to fully recombined by 10^{-2} seconds. It is clear that the exchange reaction $CO_2 + O \longleftrightarrow CO + O_2$ is an essential mechanism in the recombination of CO_2. Its importance and the need to obtain accurate estimates of the reaction rate of this process at low temperatures should not be understated.

3.4.3 Comparison with experiments

In 2008, a shock tube campaign was carried out in the Moscow Institute of Physics and Technology (MIPT) under a contract from the European Space Agency (ESA) [236, 237, 238, 239, 240, 241]. The objective of the study was to validate the existing CFD tools

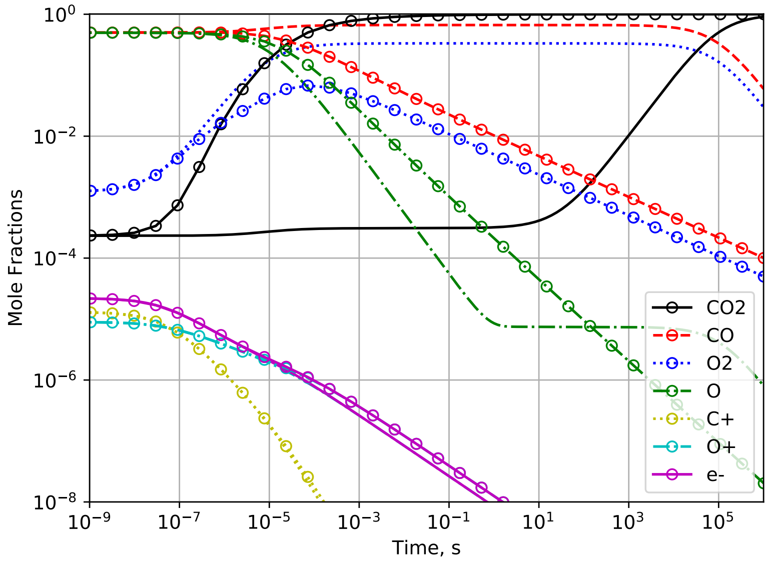

Figure 3.17: Mole fractions of C and O atoms compounds and ions in a recombining isothermal gas kept at 1000 K and 1 bar in a 0D simulation.

employed in the design of the EXOMARS mission. Among the employed diagnostics, a mercury lamp was used to measure the absorbance of the flow in the hot $CO_2(B \longrightarrow X)$ band around 253.7 nm. This allows the measurement of the evolution of concentration of CO_2 in the ground state and an estimation of the time of decomposition of the shock. Seven shots were performed using this diagnostic as per table 3.11 with initial temperatures of $T = 300$ K and the test gas fully composed of CO_2. 1D simulations, using the CO_2 STS model described in this work, were carried out using the conditions in table 3.11 as the upstream conditions. Variations were performed by using the reaction rate sets of the different macroscopic coefficients for $CO_2 + O$. In a simulated profile, it is not straightforward to define the incubation time, as it is in an experimental signal. In this work a criterion for computing the incubation time has been defined: The dissociation time is the time at which the derivative of the molar fraction of CO_2 is at its lowest. In other words, the time of decomposition is when the molar fraction changes curvature, which represents the moment where the flow is in a quasi-steady-state. In contrast, an example of the experimental measurements performed at MIPT is shown in figure 3.18 with an estimation of the time of decomposition. Initially, the decaying signal depicted in the aforementioned figure does not represent an immediate decay of CO_2 but rather the dropping pressure after the initial passage of the shockwave. At 60 μs, the arrival of the contact wave marks the end of the useful flow.

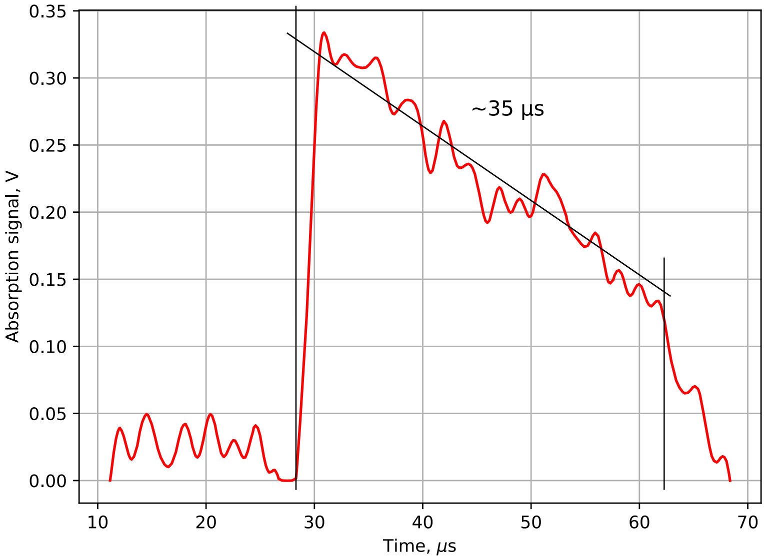

Figure 3.18: Experimental measurement of CO_2 absorbance in a shock tube. The shock velocity was 3020 m/s and the pressure in the tube 8.8 Torr corresponding to the first shot in table 3.11 and the left-most point in figure 3.19. Here the useful test time lies between 30μs with the arrival of the shockwave, and 60 μs with the arrival of the contact wave. The black lines show how the time of decomposition can be estimated in these measurements.

The results of the simulations can be found in figure 3.19 with experimental points reported against the results of the FHO model with the exchange reactions described in section 3.3.3. The lowest velocity point, near 3000 m/s is overestimated by all exchange rate coefficients except by Thielen. In fact, the simulations at this point do not have any physical significance as the model does not capture any significant dissociation at this velocity. Therefore, this point will be ignored in the remainder of this analysis. As the shock velocity increases the time of decomposition decreases in a linear fashion indepedently of pressure. This trend is observed with whatever exchange reaction is used with the model, the inclination of the trend is what changes with the exchange reaction used. The best results are achieved with the redistributed reactions obtained from Varga [218], good estimates are also achieved with the rates obtained from Sulzmann, Ibragimova and Sharipov [213, 216, 217]. The results obtained from Thielen and Kwak [214, 70] do not provide a good estimate but also obtain a linear trend. Also plotted with these models is the macroscopic model presented by Cruden *et al.* in [212]. This macroscopic model underestimates the time of decomposition and does not determine the same linear trend that is expected from the experiments and other models. This may be due more to the

Table 3.11: Shock characteristics of the experimental campaign carried out in MIPT.

Shot #	1	2	3	4	5	6	7
Pressure (Torr)	8.8	9.0	6.5	8.0	5.9	6.2	5.6
Velocity (m/s)	3020	3340	3370	3370	3450	3470	3620
Incubation Time (μs)	35	17	12	14	9	13	2

underlying assumption of a Boltzmann distribution for the internal states, rather than any inherent inadequacy of the proposed macroscopic kinetic rates.

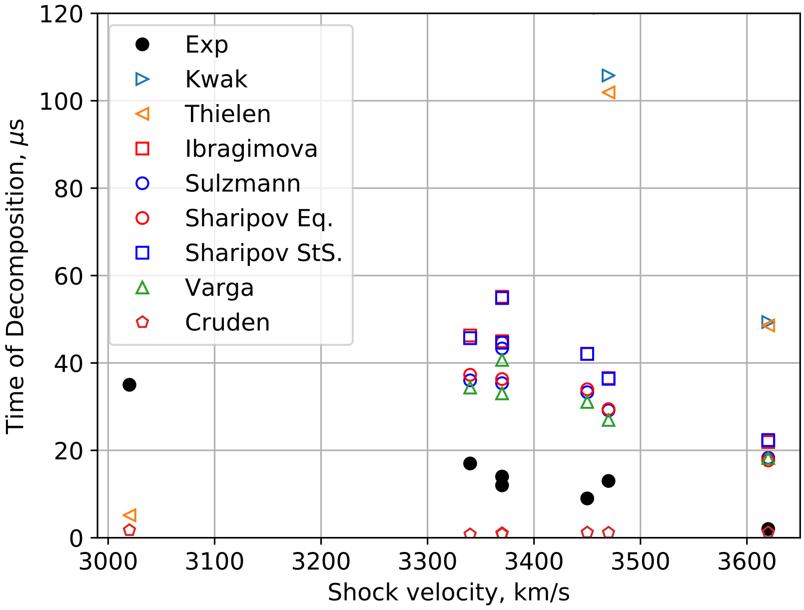

Figure 3.19: Time of decomposition of several shocks in pure CO_2. Experimental points are plotted in circles and calculated points in other symbols. A linear relationship between increasing shock speed and decreasing time of decomposition is observed in experimental and calculated points.

3.5 Recap

We have presented a vibrational state to state kinetic model for CO_2 with a number of improvements over current state of the art models. Firstly, the Forced Harmonic Oscillator theory has been for the first time extended to linear triatomic molecules such as

CO_2 and deployed in a complete and self-contained state-to-state kinetic model tailored for heavy-impact reactions. This is a significant improvement compared to the traditional SSH scaling laws (discussed in section 2.2.2). Instead of carrying a scaling of experimental rates, we estimate the different intermolecular potentials that approximates such experimentally-determined rates and then applied it over the whole vibrational level energies manifold. Furthermore, by using the general FHO theory instead of First Order Perturbation Theories such as the SSH model, we avoid obtaining transition probabilities above one in the high-temperature regime, and in the near-dissociation limit, where energy spacings become ever smaller. These are well known shortcomings of the SSH theory [116]. More importantly, we may now account for multiquantum transitions, which are well known to become important in higher temperature regimes [116].

A second improvement against the current status-quo is provided by the detailed discussion on the crossings between the ground and electronic states of CO_2 which is treated in a much more consistent fashion that in past works, which make the more naïve assumption of an assymetric mode crossing from the linear ground-state configuration of CO_2 to a near-dissociative vibrational level 70° bent excited state configuration around 5.52 eV. Instead, from the analysis of published PES, we find that PES crossings may instead arise from the bent v_2 mode at 4.99 eV, or trough the assymetric stretch mode v_3 at 5.85 eV. In this last case the excited state is repulsive and the CO_2 molecule is allowed to dissociate immediately after the crossing.

Ultimately these two improvements are overshadowed by the findings that the $CO_2 + O \longleftrightarrow CO + O_2$ reaction is quintessential to both the dissociation and recombination dynamics of CO_2. Indeed, it has been found that without the inclusion of this rate, direct dissociation and recombination processes of CO_2 become unrealistically slow, hinting that dissociation for CO_2 is likely to follow a two-step process where direct dissociation of CO_2 create a first batch of atomic oxygen atoms O which then induce further decomposition of CO_2 into CO and O_2 products. This is consistent with the findings of our literature review in section 2.2.1. Flaws, other short-term improvements and a proposed roadmap for future CO_2 experiments are discussed in section 5.1. The data generated in this section is available as part of the STELLAR database [201].

Chapter 4

Radiation

> “*Man must shape his tools lest they shape him.*”
>
> - Arthur Miller

The modelling and results in this chapter can be mostly found in “CDSDv: A Compact Database For The Modeling of High-Temperature CO_2 Radiation” [242] by ***J. Vargas***, *B. Lopez, M. Lino da Silva* and published in the Journal of Quantitative Spectroscopy and Radiative Transfer.

4.1 Theory

4.1.1 Elementary Radiative Processes

At the end of the 19th century, Planck was studying the problem of the Black Body radiation. Published in 1900 with the English title of “On the Law of Distribution of Energy in the Normal Spectrum”, his work introduced a proportionality of energy E and frequency ν in the spectrum:

$$E = h\nu \tag{4.1}$$

with h being the proportionality constant, the aptly called Planck’s constant. Since in this work, the use of reciprocal centimeters, or wavenumber is preferred, the previous equation may be written as

$$E = 100hc\overline{\nu} \tag{4.2}$$

where the c is the speed of light, $\overline{\nu}$ is the wavenumber in units of cm^{-1}, and the 100 factor is for conversion of m to cm. There are only three radiative processes that can change the internal energy of an atom or molecule. Emission, by which an atom or molecule in

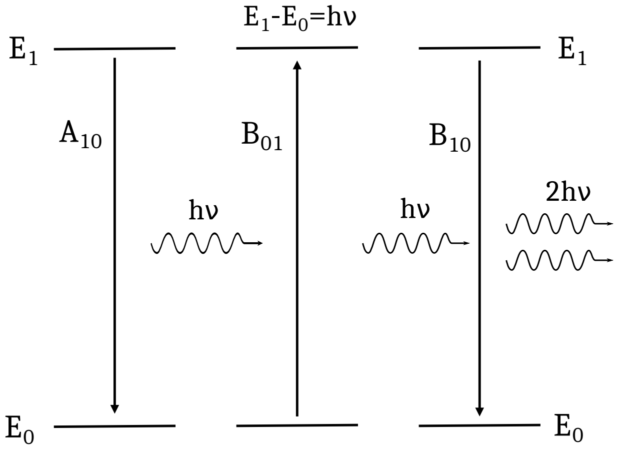

Figure 4.1: Elementary radiative processes, from left to right: emission, absorption and stimulated emission.

an excited state radiates energy and lowers its internal energy by the same amount that it radiated. Absorption, by which radiation with energy between two states, is absorbed to excite an atom or molecule from the lower to the higher state. Finally, stimulated emission, by which some radiation with a resonant frequency stimulates the emission of more radiation by an excited atom or molecule. In figure 4.1 the aforementioned processes are schematically depicted with a two level system.

Considering a two level system, with lower level “0” and higher level “1” the rate equations can be written for each process. Considering emission only, the population of excited states N_1 rate equation is:

$$\frac{\mathrm{d}N_1}{\mathrm{d}t} = -A_{10}N_1 \tag{4.3}$$

where A_{10} is the Einstein A coefficient with units s^{-1} for transition $1 \rightarrow 0$. This coefficient represents the rate at which an excited state decays to a lower state. Considering only absorption, the rate equation is,

$$\frac{\mathrm{d}N_1}{\mathrm{d}t} = B_{01}\rho_{\overline{\nu}}\left(\overline{\nu}_{10}\right)N_0 \tag{4.4}$$

where B_{01} is the Einstein B coefficient with units $\mathrm{J}^{-1}\mathrm{m}^3\mathrm{s}^{-2}$. Notice that the order in which the subscripts of the variables are written also indicates the order of the process which the variables describe. $\rho_{\overline{\nu}}\left(\overline{\nu}_{10}\right)$ is the radiation density in the spectral position $\overline{\nu}_{10}$ which corresponds to the line of emission of the transition $1 \rightarrow 0$. And finally, considering only stimulated emission,

$$\frac{\mathrm{d}N_1}{\mathrm{d}t} = -B_{10}\rho_{\overline{\nu}}\left(\overline{\nu}_{10}\right)N_1 \tag{4.5}$$

where B_{10} is the coefficient for stimulated emission. Considering this system in equilibrium, equations 4.3, 4.4 and 4.5 can be used to obtain:

$$\frac{N_1}{N_0} = \frac{g_1}{g_0}\frac{B_{01}\rho_{\overline{\nu}}}{A_{10} + B_{10}\rho_{\overline{\nu}}} = \frac{g_1}{g_0}\exp\left(-\frac{c_2\overline{\nu}_{10}}{T}\right) \tag{4.6}$$

where the right-most equality is given by Boltzmann's equilibrium equation, c_2 is the second radiation constant $c_2 = hc/k_\mathrm{B}$ in units of cm K and T the temperature of the system. The radiation density at equilibrium must be:

$$\rho_{\overline{\nu}} = \frac{A_{10}}{B_{10}\exp\left(-c_2\overline{\nu}_{10}/T\right) - B_{10}}. \tag{4.7}$$

The radiation density can also be obtained from Planck's blackbody function:

$$\rho_{\overline{\nu}} = 8\pi hc\overline{\nu}^3\frac{1}{\exp\left(c_2\overline{\nu}/T\right) - 1} \tag{4.8}$$

written in energy density form. For the equality of equations 4.7 and 4.8 to hold, it is necessary that:

$$g_1B_{10} = g_0B_{01} \tag{4.9}$$

$$A_{10} = 8\pi hc\overline{\nu}^3B_{10}. \tag{4.10}$$

These relationships still hold outside equilibrium conditions since the A and B coefficients only depend on the characteristics of the radiating system and are a constant for a specific transition.

4.1.2 Line Parameters

For line-by-line calculations, such as the ones presented in this work, five parameters must be known about a line that fully characterize it:

1. Position, $\overline{\nu}$
2. Emission coefficient, $\varepsilon_{\overline{\nu}} = N_uA_{ul}\overline{\nu}_{ul}$
3. Absorption coefficient, α
4. Profile, $F(\overline{\nu})$.

The line profile is characterized by the FWHM given a lineshape. Generally speaking, the lineshape is the convolution of a Gaussian and a Doppler profile. The convolution of these profiles is a Voigt profile which has no analytical solution. As such, the line profile in this work is determined instead by two parameters, a Lorentz broadening FWHM, $\Delta\overline{\nu}_L$ and a Doppler broadening FWHM, $\Delta\overline{\nu}_D$. The initial list of variables is in fact a list of 5 parameters.

The general Kirchhoff-Planck law can be written thus:

$$\frac{\varepsilon_{\overline{\nu}}}{\alpha\left(\overline{\nu}\right)} = 2hc^2\overline{\nu}^3\left(\frac{g_u N_l}{g_l N_u} - 1\right)^{-1}. \tag{4.11}$$

As such, the absorption of a line can be calculated from the emission coefficient of that line:

$$\alpha(\overline{\nu}) = \frac{\varepsilon_{\overline{\nu}}}{2hc^2\overline{\nu}^3}\left(\frac{g_u N_l}{g_l N_u} - 1\right). \tag{4.12}$$

To obtain the emission coefficient and the absorption coefficient of a line, only its position $\overline{\nu}$, Einstein A coefficient and the populations of the upper and lower levels N_u and N_l need to be known. The position and Einstein coefficients of diatomic and triatomic molecules must be extracted from databases. The necessary treatment of vibrational specific databases will be detailed in section 4.1.3 and 4.1.4 respectively. If the database is ro-vibrational, this treatment is already "pre-applied" to the data within a database. The extraction of this data from a ro-vibrational database to a vibrationally specific database is dealt with in section 4.1.5. The broadening parameters $\Delta\overline{\nu}_L$ and $\Delta\overline{\nu}_D$ is dealt with in section 4.1.6.

The one-dimensional radiative transfer equation is

$$\frac{dL_{\overline{\nu}}}{dx} = \varepsilon_{\overline{\nu}} - \alpha'_{\overline{\nu}}L_{\overline{\nu}} \tag{4.13}$$

where α' corresponds to the correction to the absorption coefficient due to self-absorption and stimulated emission

$$\alpha' = \alpha\left(1 - \exp\left[-\frac{c_2\overline{\nu}}{T}\right]\right). \tag{4.14}$$

The discrete form of this equation is written thus

$$L^n_{\overline{\nu}} = \frac{\epsilon_n}{\alpha'_n}\left(1 - \exp\left(-\alpha'_n d\right)\right) + L^{n-1}_{\overline{\nu}}\exp\left(-\alpha'_n d\right) \tag{4.15}$$

where ϵ_n is the emission coefficient and α_n the absorption coefficient in the n-th cell and d is the length of the cell.

4.1.3 Diatomic molecules

Modelling of CO_2 radiation in the 4.3μm spectral region would not be complete with out adding CO IR radiation present in the same region. In this work only the electric dipole transitions of the IR spectrum of the ground electronic state of CO are considered. This greatly simplifies the analysis of the selection rules involved for this kind of transitions as the only rule is $\Delta J = \pm 1$ for any Δv, assuming only the ground electronic state which is a $^1\Sigma^+$ state. If any other state is considered, more general rules are required. The symbols v and J represent the vibrational and rotational number of CO. Each vibrational transition is split between rotational branches. In general, three main branches are considered, P branch if $\Delta J = -1$, Q branch if $\Delta J = 0$ and P branch if $\Delta R = 1$. Any exchange of Δv is possible, v being the vibrational number, however the intensities of transitions drop with increasing Δv.

Energy levels are calculated with an electronic, vibrational and rotational components:

$$E_{e,v,J} = E_{ele} + E_{vib} + E_{rot} \tag{4.16}$$

where each term is much larger than the next one $E_{ele} \gg E_{vib} \gg E_{rot}$. These level energies are usually represented through polynomial expansions that will depend on their e, v, J assignment:

$$E_{e,v,J} = T(e) + G(v) + F(J). \tag{4.17}$$

One compact way to represent the rovibronic energy level information is replacing these expressions by a Dunham matrix such that:

$$E_{e,v,J} = \sum_{m,n} Y_{n,m}(v + 1/2)^m \left[J(J+1)\right]^n . \tag{4.18}$$

where $Y_{n,m}$ are the Dunham matrix coefficients. The correspondence between between Dunham matrices and the polynomial expressions $T(e)$, $G(v)$ and $F(J)$ are:

$$T(e) + G(v) = \sum_m Y_{0,m} \left(v + \frac{1}{2}\right)^m \tag{4.19}$$

$$F(J) = B_v(J(J+1)) - D_v(J(J+1))^2 + H_v(J(J+1))^3 + ... \tag{4.20}$$

$$B_v = \sum_m Y_{1,m} \left(v + \frac{1}{2}\right)^m \tag{4.21}$$

$$D_v = -\sum_m Y_{2,m} \left(v + \frac{1}{2}\right)^m \tag{4.22}$$

$$H_v = \sum_m Y_{3,m} \left(v + \frac{1}{2}\right)^m . \tag{4.23}$$

Notice that the electronic level information is contained in the first line of the Dunham matrix together with the vibrational polynomial. In practice, a Dunham matrix must be constructed for each electronic level. A Dunham matrix might be several rows and columns long and as such, there is always the possibility of adding higher-order terms in the polynomial expansion.

The Einstein A coefficient of a transition can be split into three components:

$$A_{ul} = A_v \times A^{J'}_{J''} \times F(m) \tag{4.24}$$

the first component is A_v considered to be the "vibrational" Einstein coefficient. The second component $A^{J'}_{J''}$ is a normalization factor that separates the vibronic component into the rotational branches. Then, the rotational component is:

$$A^{J'}_{J''} = \frac{S^{l',J'}_{l'',J''}}{2J'+1} \tag{4.25}$$

where $S^{l',J'}_{l'',J''}$ are the Hönl-London factors, a set of analytical expressions that depend on the upper and lower states vibrational angular momentum l and rotational number J. The Hönl-London factors obey the summation rule:

$$\sum_{l',l'',J',J''} S^{l',J'}_{l'',J''} = 2J'+1 \tag{4.26}$$

and can be found in table 4.1. The third component of equation 4.24 is the Herman-Wallis coefficients with symbol $F(m)$. This term accounts for a vibration-rotation interaction which is termed the Herman-Wallis effect. This effect might appear as a strengthening of the R branch and a weakening of the P branch (or vice versa) relative to the expected intensity if equation 4.24 had $F(m) = 1$. In many cases, the Herman-Wallis effect is small but in this work it should not be ignored. There is no definitive expression for $F(m)$ and it is usually modeled as a polynomial expansion:

$$F(m) = 1 + Cm + Dm^2 + ... \tag{4.27}$$

with $m = -J$ for P branches and $m = J + 1$ for R branches. In this work these forms are used:

$$F^P_{J',J''} = \left[1 - A_1 J'' + A_2 J''^2 - A_3 J''^3\right]^2 \tag{4.28}$$

$$F^R_{J',J''} = \left[1 + A_1(J''+1) + A_2(J''+1)^2 + A_3(J''+1)^3\right]^2 . \tag{4.29}$$

The coefficients $A_{1,2,3}$ are the Herman-Wallis coefficients which are the same for P and R branches. Notice that the form of equation 4.27 is slightly different from the one used in equations 4.28 and 4.29. In the former, the polynomial expression is simply the sum of terms while in the latter it is a square of the sum.

Several databases for CO IR radiation exist such as EXOMOL [243], HITEMP [244], HITRAN [15] and GASPAR [245]. Several of these follow the HITRAN format [15], the exception being GASPAR which follows a vibrational state-specific matrix format. The former specifies the ro-vibrational information for each line, to obtain a simulated spectrum the convolution of the Lorentzian and Gaussian lines would have to be taken into consideration. As such, most of the treatment detailed in this section is not necessary for these types of databases. The latter specifies vibrational information which coupled with the Dunham matrices can be used to compute the full ro-vibrational line positions and Einstein coefficients. The Doppler and Lorentzian broadening can then be computed as described in section 4.1.6 and the convolution of the lineshapes would be the last step to obtain a simulated spectrum. The first approach is technically simpler but requires the maintenance of extensive and detailed databases. The latter can be used with simplified and smaller databases but requires more complex algorithmical treatment. In this work the latter approach is adopted as the algorithmical structure for CO_2 radiation can be slightly modified to include CO radiation.

The GASPAR database consists of vibrationally specific line positions and Einstein coefficients matrices which are expanded with equation 4.24 with $F(m) = 1$. Some issues arose when comparing the vibrational band $\Delta v = 1$ to HITRAN. Firstly, the line positions were off by less than 1 cm^{-1} and secondly, the line peaks were not matching well. The Dunham coefficients for the ground state of CO were updated with the coefficients found in [246] and the line positions were reproduced. Matching the line peaks requires that $F(m) \neq 1$ in equation 4.24 and the multiplication of the Einstein coefficients by a 11/8 constant. The multiplication by a constant is a correction for a probable unit or conversion error that has been introduced in the database generation. The form of $F(m)$ is determined comparing with HITRAN data. Using the data, it can be determined that $A_1 \approx 2.7 \times 10^{-3}$ and $A_2 \approx -7.5 \times 10^{-6}$ for equations 4.28 and 4.29 for bands where $\Delta v = 1$. The Einstein coefficients of bands $1-0$ and $2-1$ are plotted in figures 4.2 and 4.3 with the values for the Einstein coefficient found in HITRAN. This solution to modelling the CO IR radiation is a simple and fast way to model the 4.3 μm spectral region where the CO and CO_2 lines overlap. This is also the region where the CO bands with $\Delta v = 1$ will be located. For a more general solution to the Herman-Wallis effect in CO a more general database would have to be generated which includes the Herman-Wallis coefficients for all bands. Since the purpose of adding CO radiation is to obtain simulated spectra that can be compared

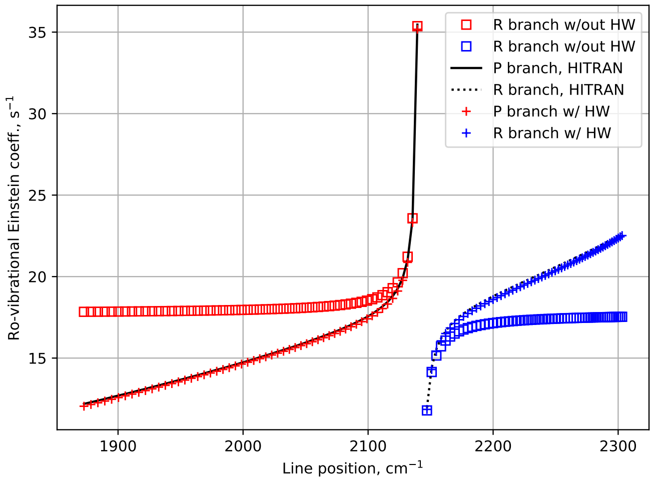

Figure 4.2: Ro-vibrational Einstein coefficients of the 1-0 vibrational band of CO. The P and R branches of the HITRAN database are displayed along with their projected Einstein coefficients using equation 4.24 with and without the Herman-Wallis effect term using the GASPAR database.

with experimental measurements of CO_2−CO radiation, the simple adaptation of using the same coefficients for all bands is sufficient.

4.1.4 Triatomic molecules

In linear polyatomic molecules, calculating line positions is no different from diatomic molecules. The only difference is with respect to how the data is stored. In the case of CO the Dunham matrices are used to obtain the spectroscopic coefficients and line positions and intensities can be computed according to the existing transitions and their selection rules. For CO_2 the spectroscopic coefficients, namely G_v, B_v, D_v and H_v of equations 4.19 and 4.20 have been refitted from CDSD4000 database [14]. This process is detailed in section 4.1.5.

Linear polyatomic molecules have one more set of selection rules. These selection rules allow for three different cases depending on the upper and lower vibrational angular momentum, which in the case of CO_2 is labeled l_2. These cases are [247]:

1. $\Delta l = l_2' - l_2'' = 0$ and $l = 0$, only has P and R branches.

2. $\Delta l = l_2' - l_2'' = \pm 1$, has P and R branches with a strong Q branch.

3. $\Delta l = l_2' - l_2'' = 0$ and $l \neq 0$, has P and R branches with a weak Q branch which is

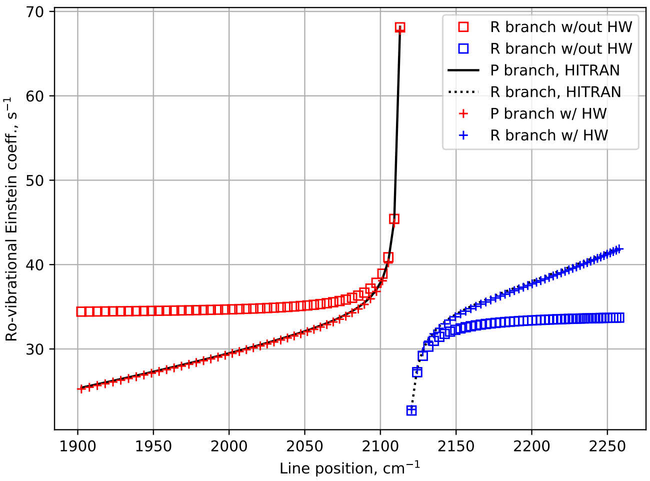

Figure 4.3: Ro-vibrational Einstein coefficients of the 2-1 vibrational band of CO. The P and R branches of the HITRAN database are displayed along with their projected Einstein coefficients using equation 4.24 with and without the Herman-Wallis effect term using the GASPAR database.

not always observed experimentally.

The branches P and R have been discussed previously. The Q branch is the rotational transition when $\Delta J = 0$. Additionally the selection rules for e/f parity apply: for P and R branches parity must be conserved (e $\leftrightarrow$ e or f $\leftrightarrow$ f) and for Q branch parity must be changed (e $\leftrightarrow$ f). The possible ro-vibrational transitions between two vibrational levels is illustrated in fig 4.4 assuming that all rotational levels exist, i.e. that both v' and v'' have $l_2 > 0$. Care must be taken when dealing with cases 2 and 3 as the alternating parity of rotational numbers can create two different transition groups, one group with P, R branches ending in e levels and Q branches ending in f levels and another group with P, R branches ending in f levels with Q branches ending in e levels. Separate treatment of the same transition is necessary especially for higher rotational numbers as the separation between e and f levels becomes irregular and the two groups become distinct in their spectral position.

Line intensities of linear polyatomic molecules are also affected by the rotational branch separation calculated with the Hönl-London coefficients and the Herman-Wallis effect. Due to the possibility of having a Q branch a form must be assumed for $F(m)$:

$$F^{Q}_{J',J''} = \left[1 + A_Q J''(J''+1)\right]^2 \tag{4.30}$$

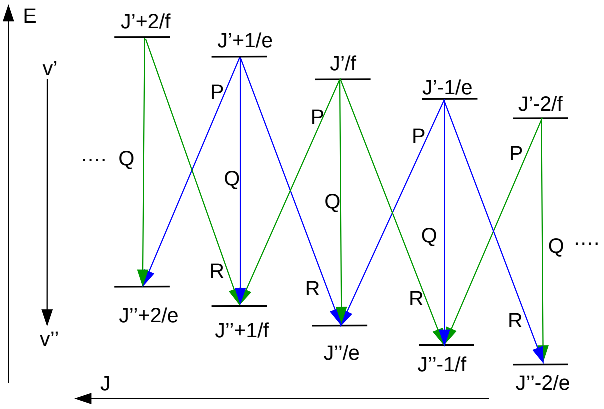

Figure 4.4: Possible ro-vibrational transitions between upper and lower ro-vibrational levels.

where A_Q is the Herman-Wallis coefficient exclusively for the Q branch. The Hönl-London factors considered in this work are found in table 4.1 for diatomics and triatomic molecules.

Table 4.1: Hönl-London factors from [247]. These factors are only valid for $\Delta l = -1, 0, 1$.

Branch	$\Delta l = 0$	$\Delta l \neq 0$
P	$\frac{(J''+l_2'')(J''-l_2'')}{J''}$	$\frac{(J''-1-l_2''\Delta l)(J''-l_2''\Delta l)}{2J''}$
Q	$\frac{(2J'')l_2''^2}{J''(J''+1)}$	$\frac{(J''+1+l_2''\Delta l)(J''-l_2''\Delta l)(2J''+1)}{2J''(J''+1)}$
R	$\frac{(J''+1+l_2'')(J''+1-l_2'')}{J''+1}$	$\frac{(J''+2+l_2''\Delta l)(J''+1+l_2''\Delta l)}{2(J''+1)}$

There are also several databases for CO_2 IR radiation such as, HITRAN [15], HITEMP [244], CDSD4000 [14]. All these databases share a common structure and in most cases fundamental data. These databases employ a line strength cut-off on included transitions. The cut-off will depend on the required accuracy of the database. For a given temperature, an experimental spectrum is used for calibration. As such, not only the aforementioned databases are carefully tailored to the temperature for which they were calibrated, they are also extensive for higher temperatures. CDSD4000 for instance, takes over 72 GB of hard-drive space. Straightforwardly using these types of databases in the context of atmospheric entry is not efficient as a more compact database is desirable which can be efficiently used at higher or lower temperatures. As such, the data in CDSD4000 will be used to refit the ro-vibrational data into a vibrationally specific database. This is described in the next section.

4.1.5 Refitting of ro-vibrational data

Part of this thesis is to refit the ro-vibrational specific CDSD4000 database into a vibrational specific one. This part of the work was published [242]. The resulting data was dubbed CDSDv and made publicly available in the GASPAR database. Ro-vibrational databases such as HITRAN [15] and CDSD [13, 14] adopt a similar format. Each data entry in CDSD contains all the parameters in table 4.2 spectrally organized. A refitting process will involve reorganizing the database by spectroscopic assignment instead of line position. Besides featuring the four main isotopes of CO_2 by terrestrial abundance, CDSD also features transitions in which the upper, lower or both levels could not be spectroscopically assigned reliably. Partially or totally unassigned transitions are excluded from the treatment presented in the scope of this work. Also excluded are isotopes other than 626, the most abundant one. In the case of CDSD4000 there are 2769 different files which represent over 72 GB when in a uncompressed format. Not all the parameters in table 4.3 are necessary for the processing done in this work. The first half of the table contains the parameters that are needed for refitting while the parameters on the second half can be discarded. Table 4.2 does not present the data ordered as it is in CDSD.

The energy E_{vJ} of a level with vibrational quantum state v and rotational state J have been fitted using the least squares procedure to the following expression:

$$E_{vJ} = G_v + B_v[J(J+1)] - D_v[J(J+1)]^2 + H_v[J(J+1)]^3 \tag{4.31}$$

with a least squares fitting procedure. This expression is the sum of equations 4.19 and 4.20. Inevitably several fits will be performed on the same level v', most of which are discarded as only the fit with the smaller squared norm of the residual is kept. Some extrapolation may be required as the fit was performed between a $J_{\min}$ and $J_{\max}$. If $J_{\min}$ is higher than l_2, the rotational numbers in between will be missing. For every level, $J_{\min}$ is replaced by $\max(l_2,1)$ if $J_{\max}$ is odd, or $\max(l_2,2)$ if $J_{\max}$ is even. The differentiated treatment ensures that $J_{\min}$ is consistent with the rotational numbers parity. $J_{\max}$ also needs to be extrapolated, as usually the highest rotational level is not enough to cover the regions where the transition is not negligible. As such all fitted polynomials are considered to be valid up to $J_{\max} + 100$. This ensures that most of the relevant levels are covered and the partition function is recovered. As validation of this method, fig. 4.5 presents

Table 4.2: Description of parameters format of CDSD4000. The parameters in the first half of the table are the ones used in the refitting. Some parameters of the lower half of the table are saved for possible future reference but are not used in the refitting. The data is not ordered as represented in this table. [13, 14]

Symbol	Parameter	Comment
I	Isotope index	Ordered by abundance
$\overline{\nu}$	Line position	cm^{-1}
A	Einstein A-coefficient	s^{-1}
E''	Lower state energy	cm^{-1}
$v_1'v_2'l_2'v_3'r'$	Upper state vibrational numbers	
$v_1''v_2''l_2''v_3''r''$	Lower state vibrational numbers	
b	Branch	P, Q or R
J''	Lower state J	
w”	Lower state Wang symmetry	e or f
M	Molecule	$M = 2$ for $\mathrm{CO_2}$
S	Intensity	$\mathrm{cm}^{-1}/(\mathrm{part.cm}^{-2})$ at 296K
γ_{air}	Air-broadened half-width	$\mathrm{cm}^{-1}\mathrm{atm}^{-1}$ at 296 K
γ_{self}	Self-broadened half-width	$\mathrm{cm}^{-1}\mathrm{atm}^{-1}$ at 296 K
n_{air}	Temperature-dependence exponent for γ_{air}	
δ_{air}	Air pressure-induced line shift	$\mathrm{cm}^{-1}\mathrm{atm}^{-1}$ at 296 K
n_{self}	Temperature-dependence exponent for γ_{self}	
$p'\ c'\ n'$	Upper polyad, Wang sym. and rank. num.	$c = 1$(e) or $c = 2$(f), n'=r'
$p''\ c''\ n''$	Lower polyad, Wang sym. and rank. num.	$c = 1$(e) or $c = 2$(f), n''=r''

the internal partition function calculated by direct summation compared with values from literature [248], CDSD1000 [13] and of CDSD4000 [14]. The partition function computed through this method is overlapped with the values from literature, thus validating this approach.

Vibrational transitions are related to ro-vibrational transitions through equation 4.24. There are four terms to this equation where $A^{v'}_{v''}$ are the vibrational Einstein-A coefficients, $S^{l'J'}_{l''J''}$ the Hönl-London factors, $F_{J',J''}$ the Herman-Wallis factors and $A^{v'J'}_{v''J''}$ the ro-vibrational Einstein-A coefficients. The Hönl-London factors account for the rotational

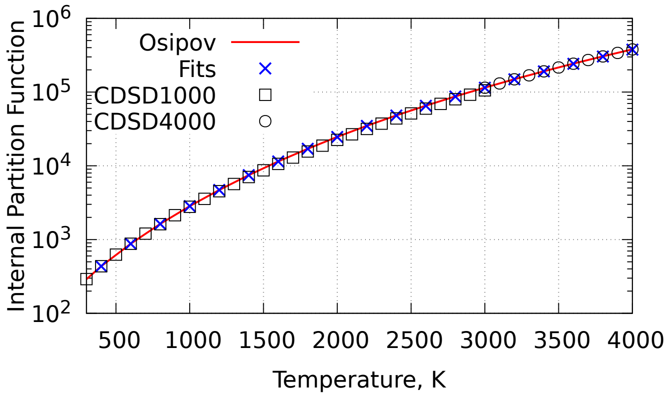

Figure 4.5: Total internal partition function obtained through direct summation versus values from Osipov [248] and CDSD1000 [13] and CDSD4000 [14].

separation of a vibrational transition into P, Q and R branches and are normalized by the factor $(2J'+1)$. These factors are summarized in table 4.1. The Herman-Wallis term is reproduced here for all branches for convenience:

$$
\begin{aligned}
F^P_{J',J''} &= \left[1 - A_1 J'' + A_2 J''^2 - A_3 J''^3\right]^2 \\
F^Q_{J',J''} &= \left[1 + A_Q J''(J''+1)\right]^2 \\
F^R_{J',J''} &= \left[1 + A_1(J''+1) + A_2(J''+1)^2 + A_3(J''+1)^3\right]^2 .
\end{aligned}
$$

The Hönl-London factors and the ro-vibrational Einstein coefficients are fully determined through databases. However, the vibrational Einstein coefficients and the Herman-Wallis coefficients A_1, A_2, A_3 and A_Q are not included and need to be computed. It is worth mentioning that since the P and R branches share the same coefficients, the fitting should be done simultaneously for the two branches. Thus the least square fitting procedure is applied to the following equation:

$$
A^{v'}_{v''} \times F_{J',J''} - \frac{A^{v'J'}_{v''J''}}{S^{l'J'}_{l''J''}} = 0. \tag{4.32}
$$

Figures. 4.6 and 4.7 present examples of transition fitting using equation 4.32. Figure 4.6 presents the fitting of transition 00011 → 00001 which has a P and R branch while Fig. 4.7 presents the fittings of transition 01111 → 01101. In both cases the fitting is able to match very well the data contained in CDSD4000. The reconstruction of these fits can be seen in fig. 4.8 where data from these fits is used to reconstruct the ro-vibrational information contained in CDSD4000 and HITRAN. This reconstruction provides some validation as to the fitting procedure ability to reconstruct the ro-vibrational information from vibrational specific data as transitions 00011 → 00001 and 01111 → 01101 are reconstructed

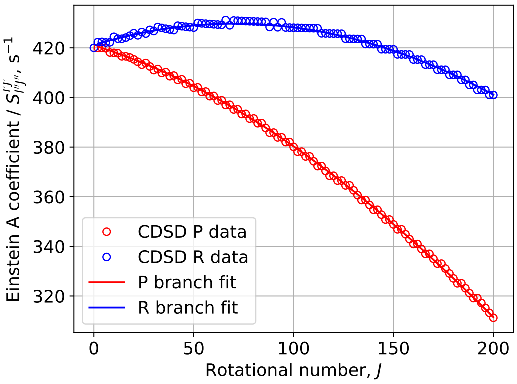

Figure 4.6: Fitting example of transition 00011 → 00001.

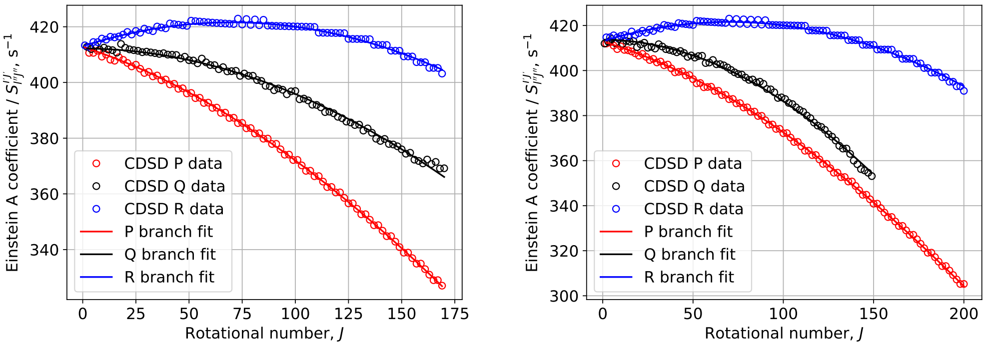

Figure 4.7: Fitting example of transition 01111 → 01101. On the left, P and R branches with lower symmetry of e and Q branch with symmetry of f. On the right, P and R branches with lower symmetry of f and Q branch with symmetry of e.

without any obvious flaws. The perturbations at the high rotational levels in the P and R branches are not reconstructed and when J_{max} is extrapolated these perturbations are not reproduced.

Transitions in CDSD4000 are organized by their vibrational assignment excluding all the isotopes except the main one. The data associated to these transitions is used in the fit according to equation 4.32. Regarding the possible electric dipole transitions in CO_2 the ideal case would be the following procedure:

1. First case is only fitted once for P and R branches since no Q branch exists.

2. Second case is fitted once for P and R branches and another time for Q branch if l_2' or l_2'' are equal to zero. If this is not the case, four fits must be performed: one for P and R with e symmetry, another for P and R with f symmetry, one Q with e and

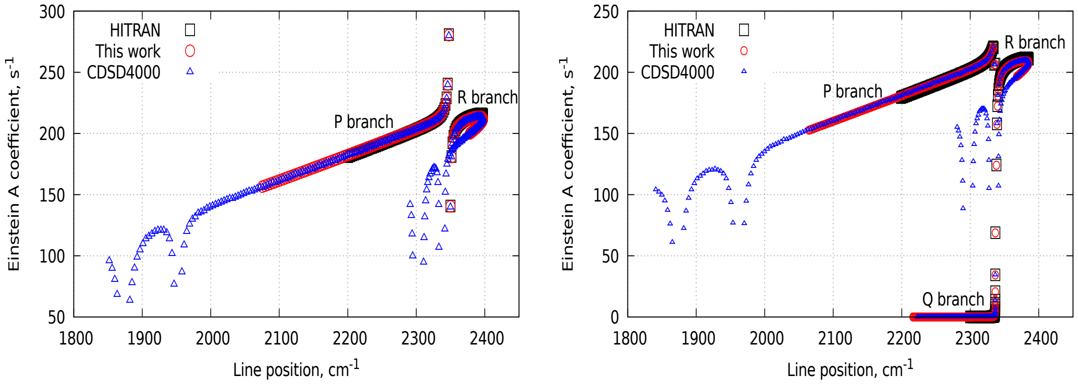

Figure 4.8: Reconstruction examples of fitted quantities of transitions 00011 → 00001 (left) and 01111 → 01101 (right) compared against values from HITRAN and CDSD4000.

Table 4.3: Total number of cases considered for re-fitting divided by fit case and category.

Category	Case 1	Case 2	Case 3
Total	4146	111843	88863
Usable	761	1720	1772
Not Usable	2206	42054	40208
Too small	1179	68070	46883
Usable/Total(%)	18.0	1.5	2.0

another Q with f.

3. Third case is always fitted four times as in the second case when both l_2 are greater than zero.

Some transitions have missing data or exhibit perturbations. Due to this missing/perturbed data, not all transitions can be successfully fitted. In a previous work [249], an attempt was done to develop a universal fitting approach. In this work, a different approach is considered where the data associated to transitions is analyzed and then classified into different categories. Thus, transitions are classified into a "usable" or "non-usable" categories depending whether how much missing/perturbed data has been identified. Subjective merits, such as the smoothness of the branches and the shape of the curves, are used when classifying transitions as well. Additionally, a category for transitions, which do not have more than 20 points for P and R branches separately, is used to ensure a

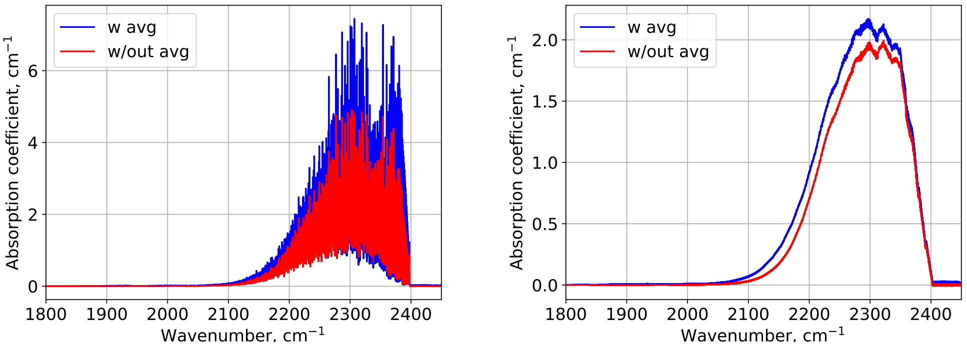

Figure 4.9: Absorption coefficient of 1 atmosphere of pure CO_2 at 2000K with and without the Einstein coefficient averaging.

minimum amount of data is available for the fit.

The number of vibrationally specific transitions, excluding unidentified transitions is approximately 2.5 million in the 4.3 μm spectral region. In order to reduce the considered dataset, and as a first approach, only transitions with $v_1' < 4$ are considered. Table 4.3 presents the total number of transitions that meet the criterion $0 \leq v_1' \leq 4$. The number of transitions in each category ("usable", "non-usable") after classification as well as the percentage of usable transitions for each case are listed in table 4.3. Each column represents one of the cases for the possible electric dipole transitions for linear polyatomic molecules. The resulting database is composed by the upper and lower level assignments, Einstein coefficients, Herman-Wallis coefficients and the lower level Wang symmetry.

For some transitions the Q branch data is missing. If this is the case the coefficient A_Q is considered to be zero. Convergence issues have been observed if A_3 is considered in the equations to be fitted. As such A_3 was neglected and fitting only occurred with A_1, A_2 and A_Q. It was also found that filtering out perturbations and/or neglecting high rotational levels was required to obtain a good quality of the fits.

There is a way of reconsidering previously discarded transitions as well as including transitions outside the scope of the first classification process. A script was developed to compute the absorption for every ro-vibrational transition inside a specified spectral range in CDSD4000. By specifying a temperature and number density it returns a list of transitions which are above a specified threshold of absorption. This list can then be compared against the transitions in CDSDv and missing transitions can be (re-) considered for classification. This process may be iterated over different temperatures and spectral ranges to improve accuracy. It also includes transitions outside the previous criterion $0 \leq v_1' \leq 4$.

Transitions that are reconsidered for classification will be classified again. In many cases it is impossible to fit these as the data does not have internal structure when seen through eq. 4.32. In these cases it is not possible to find fit any expression. These transitions can still be considered by averaging the RHS of eq. 4.32, after removal of outliers by the interquartile range method, while neglecting the influence of the Herman-Wallis factor:

$$A_{v''}^{v'} = \overline{\frac{A_{v''J''}^{v'J'}}{S_{l''J''}^{l'J'}}}. \tag{4.33}$$

With this averaging method, a list of vibrational Einstein A coefficients is obtained. Databases such as CDSD and HITRAN use a cut-off criteria for ro-vibrational transitions, deciding which are included or discarded. Due to this cut-off criterion, the proposed averaging will overestimate the average of Einstein coefficients of a given transition. For now, only electric dipole transitions are included in the averaging process. Later on, transitions with $|\Delta l_2| > 1$ may be added to CDSDv but this falls outside the scope of this work. Figure 4.9 presents the difference in the absorption coefficient between a simulation with and without Einstein coefficient averaging for 1 atm of pure CO_2 at 2,000K with the lineshape on the left and the convolution with a 10 cm^{-1} wide square apparatus function on the right. There is a noticeable impact by including the averaged transitions in the database. The inclusion of averaged transitions is necessary for better accuracy at higher temperature regimes. The results in this work are obtained by retaining the averaged transitions in CDSDv.

4.1.6 Broadening

Broadening mechanisms belong to one of two categories:

- Collisional or pressure broadening, which has a Lorentzian profile and as such is also called Lorentz broadening
- Broadening by Doppler effects, described by a Gaussian profile.

The Lorentzian line has profile described by the expression:

$$l(\overline{\nu}) = \frac{1}{1 + 4\left(\frac{\overline{\nu} - \overline{\nu}_0}{\Delta \nu_L}\right)^2} \tag{4.34}$$

where $\overline{\nu_0}$ is the line position and $\Delta\overline{\nu_L}$ is the Lorentzian FWHM. When considering the effect of several lines, the lineshapes must be convoluted. The convolution of Lorentz lineshapes is a Lorentzian profile such that $(\Delta\overline{\nu_L})_{TOT} = \sum(\overline{\nu_L})_i$. The Doppler line is described by a Gaussian:

$$g(\overline{\nu}) = \exp\left[-4\log(2)\left(\frac{\overline{\nu}-\overline{\nu}_0}{\Delta\overline{\nu}_D}\right)^2\right] \tag{4.35}$$

where the log is the natural logarithm and $\Delta\overline{\nu}_D$ is the Doppler FWHM. The convolution of Doppler lines is a Gaussian profile such that $(\Delta\overline{\nu_D})_{TOT} = \sum(\overline{\nu_D})_i^2$. The Voigt profile is the convolution of a Lorentzian and Gaussian lineshapes:

$$v(x) = l(x) \otimes g(x) = \frac{\Delta\overline{\nu}_L}{\Delta\overline{\nu}_G}\sqrt{\frac{\log 2}{\pi^3}}\int_{-\infty}^{+\infty}\frac{\exp\left(-\left[(\xi-x)^2\log 2\right]/\Delta\overline{\nu}_G^2\right)}{\xi^2+\Delta\overline{\nu}_L^2}\mathrm{d}\xi \tag{4.36}$$

where $x = \overline{\nu}-\overline{\nu}_0$. This profile has no analytical solution and even a numerical one is more complex than it needs to be. Whiting [250] proposed an approximated expression:

$$v(\overline{\nu}) = C_1\exp\left(-4\log(2)D^2\right) + \frac{C_2}{1+4D^2} + C_3\left(\exp\left(-0.4D^{2.25}\right) - \frac{10}{10+D^{2.25}}\right) \tag{4.37}$$

where $D = \frac{\overline{\nu}-\overline{\nu}_0}{\Delta\overline{\nu}_V}$ and the Voigt FWHM, $\Delta\overline{\nu}_V$ is given by

$$\Delta\overline{\nu}_V = \frac{1}{2}\left(\Delta\overline{\nu}_L + \sqrt{\overline{\nu}_L^2 + 4\overline{\nu}_D^2}\right). \tag{4.38}$$

The constants in equation 4.37 are given by:

$$C_1 = \left(1-\frac{\Delta\overline{\nu}_L}{\Delta\overline{\nu}_V}\right)(n.f.), \tag{4.39}$$

$$C_2 = \left(\frac{\Delta\overline{\nu}_L}{\Delta\overline{\nu}_V}\right)(n.f.), \tag{4.40}$$

$$C_3 = 0.016\left(\frac{\Delta\overline{\nu}_L}{\Delta\overline{\nu}_V}\right)\left(1-\frac{\Delta\overline{\nu}_L}{\Delta\overline{\nu}_V}\right)(n.f.). \tag{4.41}$$

where $n.f.$ is the normalization factor,

$$n.f. = \frac{1}{\Delta\overline{\nu}_V\left(1.065 + 0.0447\frac{\Delta\overline{\nu}_L}{\Delta\overline{\nu}_V} + 0.058\left(\frac{\Delta\overline{\nu}_L}{\Delta\overline{\nu}_V}\right)^2\right)}. \tag{4.42}$$

Olivero [251] critically assessed the proposed expression by Whiting and estimated that it was accurate with a minimum of 1%. Olivero then proposed a modification to the Voigt FWHM calculation which improved the accuracy of the expression to 0.02%:

$$\Delta\overline{\nu}_V = \frac{1}{2}\left(1.0692\Delta\overline{\nu}_L + \sqrt{0.86639\overline{\nu}_L^2 + 4\overline{\nu}_D^2}\right). \tag{4.43}$$

Databases such as CDSD and HITRAN choose to compute pressure broadening by a semi-empirical expression that accounts, with fitted coefficients, for the broadening of ro-vibrational lines caused by self-broadening and air-broadening for any pressure and temperature conditions from a reference value at standard pressure and temperature. This approach, while straightforward, neglects the effect of other species in the calculation of the FWHM of Lorentz broadening. In this work a more complex approach was adopted, that accounts for the different broadening effects by generalized and specific expressions for each effect. While these general expressions are often approximations and not valid universally, they do offer a more flexible approach to different conditions and gas mixtures that ro-vibrational state of the art databases do not possess. These statements are not meant as a final judgement on the approaches that should be used but more of a comment on the relative merits and disadvantages of both methods. While both approaches will be close in value at low temperature, enough for a relatively fair comparison of lineshape calculation, the values will diverge for other conditions, which will not yield a fair comparison between lineshape calculations using different methods. This is mitigated by the fact that Lorentz broadening is only expected to be significant at high pressures and low temperatures, while Doppler broadening, which can be computed through an analytical expression, will be dominant at higher temperatures. The theoretical expressions for the different broadening mechanisms are summarized below. Resonance broadening adapted from [171]:

$$\Delta\overline{\nu} = K_1 \sqrt{\frac{g_u}{g_l}} A_{ul} \frac{N_l}{\overline{\nu}^3} \tag{4.44}$$

where $K_1 = 1.2893 \times 10^{-19}$, g_u and g_l the upper and lower degeneracies, A_{ul} the Einstein coefficient, N_l the lower level number density in m^{-3} and $\overline{\nu}$ the line position in cm^{-1}. Van der Waals broadening adapted from [252]:

$$\Delta\overline{\nu} = K_2 \frac{2}{c_0} \sqrt{\frac{2T_{\mathrm{gas}}}{M_{\mathrm{avg}}}} N_{\mathrm{tot}} \overline{\nu}^2 \tag{4.45}$$

where $K_2 = 1.95 \times 10^{-28}$, c_0 the speed of light in m/s, T_{gas} the gas temperature, M_{avg} the average molar mass of the mixture in kg/mol, N_{tot} the total number density in m^{-3} and $\overline{\nu}$ the line position in cm^{-1}. Collisional broadening adapted from [171]:

$$\Delta\overline{\nu} = \frac{2}{c_0} \sqrt{8 k_B \pi T_{\mathrm{gas}}} \sum_i \frac{N_i}{\sqrt{\mu_{\mathrm{red}}}} (r_i + R)^2 \tag{4.46}$$

where c_0 the speed of light in m/s, k_B the Boltzmann constant, T_{gas} the gas temperature, N_i the number density of perturbing species i in m^{-3}, μ_{red} the reduced mass of the radiative and perturbing species system, r_i the radius of perturbing species i in meters and R the radius of the radiative species. Additionally, Doppler broadening is also considered:

$$\Delta\overline{\nu} = \overline{\nu_0}\sqrt{8\log{(2)}\frac{k_B T}{mc^2}} \tag{4.47}$$

where log is the natural logarithm, m the mass of the emitting particle and $\overline{\nu_0}$ the center of the line of the broadened transition.

4.1.7 Lineshape treatment

When dealing with spectral calculations in the IR spectrum in the high temperature regime it is normal to have millions of individual lines in a relatively small spectral region. One of the most computationally intensive tasks when calculating spectra is to determine the overlap of several million lineshapes, a lot of which might be orders of magnitude below the main features of the spectrum. To this end, an algorithm was applied to reduce the number of lines to be processed as well as reduce the computational effort required to fully compute the spectrum. This algorithm was originally developed by Lino da Silva [170] and is deployed in line-by-line open code SPARTAN [171]. A summarized version is presented here.

Given the parameters of a radiative line discussed in section 4.1.2, the first step is to sort lines into categories. These categories define the algorithmical treatment each line gets, with stronger lines being well reproduced and weaker ones being stored in a pseudo-continuum spectrum. The maximum emission and absorption coefficients are found in the spectrum and compared to the emission and absorption coefficients of all lines, like so:

$$\text{Weak Line} < \frac{I_{\text{max}}}{T_2} \leq \text{Strong-Weak Line} < \frac{I_{\text{max}}}{T_1} \leq \text{Strong Line} \tag{4.48}$$

where $T_2 \geq T_1 > 0$ are some numerical factors, I is the emission coefficient or the absorption coefficient and I_{max} the maximum value of I in the spectrum under consideration. A Strong Line which will have $I_{\text{max}}/T_1 < I$ will have its lineshape calculated explicitly. A Strong-Weak Line with $I_{\text{max}}/T_2 < I < I_{\text{max}}/T_1$ will be calculated explicitly if they are uncovered, otherwise, if they are covered they will be part of the pseudo-continuum. Weak Lines with $I < I_{\text{max}}/T_1$ will always be part of the pseudo-continuum. To check if a line is covered the position of the Strong-Weak line is checked against the strong lines position $|\overline{\nu}_{\text{s-w}} - \overline{\nu}_{\text{s}}| \leq C \times \Delta\overline{\nu}_V$ where C is a constant dependent on the factors T_1 and T_2. If this criterion is met, the line is considered covered, otherwise it is considered uncovered. For a ratio of 1000 between T_2/T_1, C is considered 20.

In the work of Lino da Silva [170] high and low resolution methods are proposed for calculating a Voigt profile. In this thesis the low-resolution method is ignored. A high-resolution Voigt profile can be calculated by defining two regions of a line. This is accomplished by defining two parameters whose values define the boundaries between the core and the wings region W and the wings and the negligible contribution region of the line FW. The expressions for these parameters is proposed by Zhou [253]:

$$[W,FW] = \frac{2}{\pi}\left(1+\xi\right)\Delta\overline{\nu}_L + \beta\Delta\overline{\nu}_D. \tag{4.49}$$

The parameters ξ and β are taken as 1 and 1.18 respectively for the calculation of W as proposed by Smith [254] and 2.6 and 5.8 for the calculation of FW [170]. Notice that this numerical definition generates two wings region and a core region for each line. It is considered that one wing region is symmetrical to the other and is such that only one of the extreme regions needs to be considered since the second is a copy of the first. Two more parameters, par_c and par_w, related to the core and wings of the profile must be calculated. The line center is independent of the profile, Voigt, Doppler or Gaussian. The wing parameter will therefore have a strong dependence on the Lorentz and Doppler FWHM. This is acknowledged by the separation into wing parameters for Lorentz and Doppler shapes:

$$par_w = par_{wL} + \frac{\Delta\overline{\nu}_D}{\Delta\overline{\nu}_D + \Delta\overline{\nu}_L} par_{wD}. \tag{4.50}$$

This is such that when Doppler broadening dominates over Lorentz, $par_w = par_{wL} + par_{wD}$ and when Lorentz dominates, $par_w = par_{wL}$. A monotonous grid, i_0 is then defined and geometrically transformed through the relation:

$$i = \frac{1-\exp\left(par \times i_0\right)/\exp\left(par \times i_0(\max)\right)}{1-\exp\left(par \times i_0(1)\right)/\exp\left(par \times i_0(\max)\right)} \tag{4.51}$$

where par is either par_c or par_w if the grid is being transformed for the core or the wing region respectively. Practically speaking, expression 4.51 makes a grid between 0 and 1 with points clustered closer to 1. The core region is then defined as $i_c = i$ and the wings region is $i_w = 1 - i$ which makes the points clustered around 0. The points of the core region i_c are applied to the core region, defined in equation 4.49, according to the following normalisation:

$$i_c = \frac{v''(\overline{\nu})_c}{\max\left[v''(\overline{\nu})_c\right]} \tag{4.52}$$

where v'' is the second derivative of the Voigt lineshape expression. This ensures that the most points will be distributed to regions where the second derivative is highest. The wings region of the line, also defined in equation 4.49 are distributed according to:

$$i_w = \frac{v(\overline{\nu})_w}{\max\left[v(\overline{\nu})_w\right]}. \tag{4.53}$$

Then, the only thing that needs to be defined is the number of points in the core and wings region of the line. A higher number of points in each region will incur a higher computational overhead. The default number for the calculations seen ahead are 12 points in the core region with 24 points in the wings region.

4.2 Applications

4.2.1 Comparison with other databases

The absorption coefficient of one atmosphere of pure CO_2 was computed using CDSDv in the spectral range of 145 to 5500 cm^{-1} at 296, 1000, 2000 and 3000K and compared with the results of SPECTRA [255] using HITEMP. The results are plotted in fig 4.10. The figures on the top present the results for the 296 and 1000K cases. In both figures, the peaks for the represented bands (left to right, 15, 4.3, 2.7 and 2.3 μm) are well matched as well as the wings of these bands, especially in the case of 1000K. The figures on the bottom present the results for the 2000 and 3000K cases in which the absorption peaks are relatively well matched but CDSDv overestimates the inter-band region by several orders of magnitude. This is the consequence of transition averaging that was introduced in section 4.1.5. Despite the overestimation in these regions, the relative magnitude of the radiative peaks in these regions is low when compared to the peaks located inside the spectral bands. At 2000K, this difference is up to 2 to 3 orders of magnitude in the worst case and is considered to be negligible. At 3000K the wings and peaks of the bands may be separated by less than one order of magnitude and the effects of the wings can no longer considered to be negligible in some spectral regions. As a future update to the database, steps may be taken to ensure the averaging procedure does not overestimate the "global" radiative intensity of the averaged transitions.

The total radiative power of CDSDv is assessed by comparing the contribution of CO_2 IR radiation of an equilibrium Martian-like 97%CO_2- 4%N_2 mixture to other authors. This comparison is shown in figure 4.11. The full lines are the contribution of CO_2 IR radiation to the total radiative power by Lino da Silva [139] in grey, by Perrin *et al* [156] in red and CDSDv in blue. The dashed lines in black and red are the contribution of

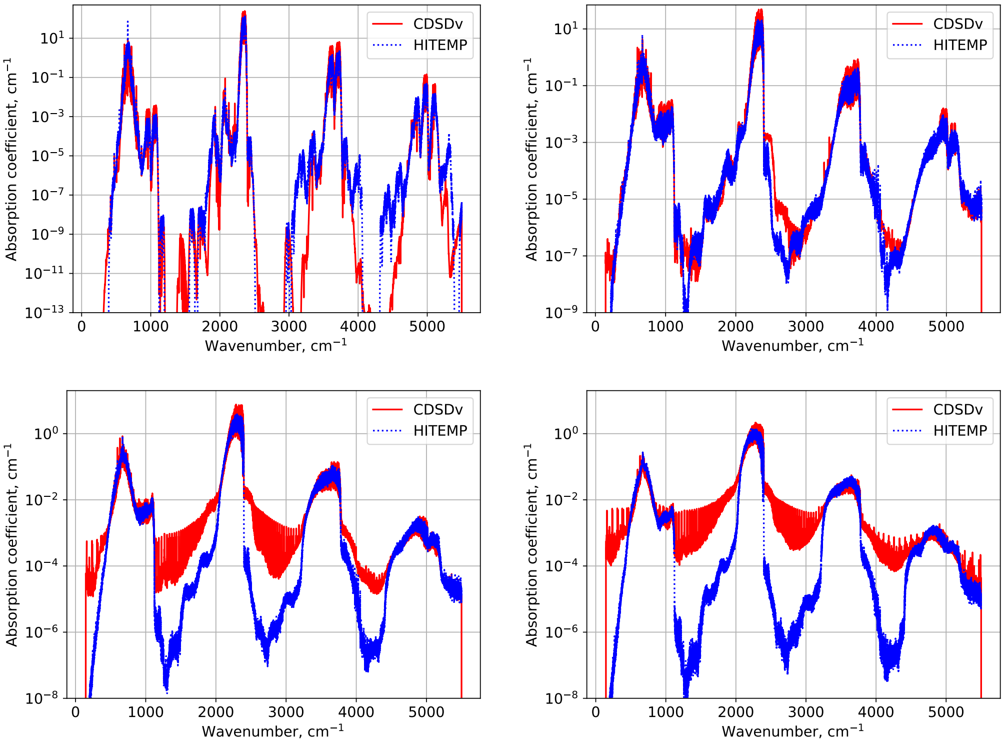

Figure 4.10: Absorption coefficient of one atmosphere of pure CO_2 between 145 to 5500 cm^{-1} at 296 (top left), 1000 (top right), 2000 (bottom left) and 3000K (bottom right) using databases and the tools for interpreting CDSDv and online tool SPECTRA using HITEMP.

other systems relevant to the CO_2-N_2 mixture. The three calculations of the contribution of CO_2 radiative power are in reasonable agreement at low temperatures. Lino da Silva's calculation will underpredict at higher temperatures since it lacks several hot bands included in CDSD. Perrin *et al* predicts higher values for the overall radiative power but CDSDv does not underpredict by very much.

The performance of the CDSDv database was assessed by using an in-house tool for the calculation of the emission and absorption spectra from the Dirac properties of radiative lines as described in [170] and in section 4.1.7. The same calculation was also performed using the CDSD4000 database. In summary the process in [170] sorts lines into "strong" and "weak" categories. Strong lines are checked for coverage of other strong lines and processed by explicitly computing the Voigt lineshape (if they are uncovered by other lines). Weak lines are treated as pseudo-continuum. Performance largely depends on the distribution and number of strong lines. Results of this calculation are summarized in

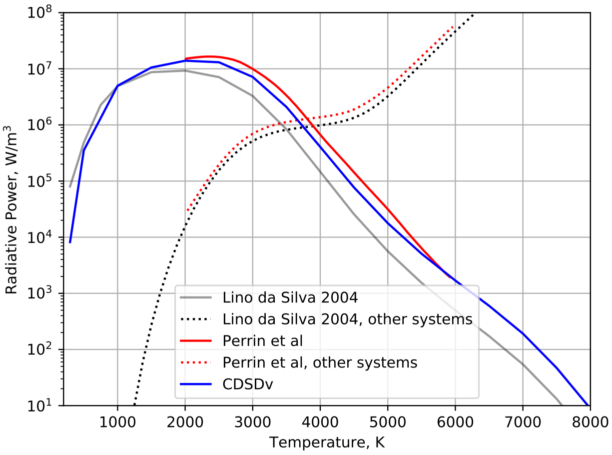

Figure 4.11: Radiative Power for an equilibrium Martian-like 97% CO_2- 4% N_2 mixture. The full lines present the radiative power attributted to IR CO_2 while the dashed lines present the radiative power from other radiative systems relevant to the CO_2-N_2 mixture. Data from Lino da Silva in [139], data of EM2C from [156].

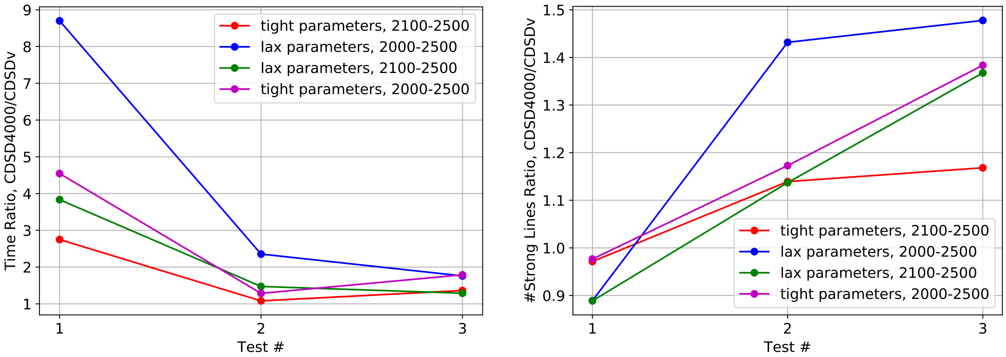

Figure 4.12: Ratio of simulation times (on the left) and ratio of number of strong lines between CDSD4000 and CDSDv for each case in table 4.4.

table 4.4. Each set of results is one of four possible combinations between tight and lax numerical parameters and a spectral range of 2000-2500 or 2100-2500 cm^{-1}. Tight and lax parameters refer only to the threshold below which lines are considered weak and above are considered strong. In each combination of parameters and spectral range the radiation of one atmosphere of pure CO_2 is simulated at 1000, 2000 and 3000K corresponding to Time 1, 2 and 3 respectively. Also presented are the maximum RAM (Random-access Memory) used in each simulation and the input file size. In fig. 4.12 the ratios of calculation times and the ratio of strong lines between CDSD4000 and CDSDv is plotted. Although this is

Table 4.4: Performance of CDSD4000 and CDSDv using the method described in [170] using tight or lax numerical parameters in a spectral range of 2100-2500 or 2000-2500 cm^{-1}.

#	1		2	
Parameters	Tight		Lax	
Range	2100-2500		2000-2500	
Database	CDSDv	CDSD4000	CDSDv	CDSD4000
Time 1 (s)	30.98	85.18	20.11	174.95
Time 2 (s)	329.58	356.25	145.11	341.63
Time 3 (s)	2855.43	3891.64	1007.92	1773.45
Max RAM	446.3 MiB	3.830 GiB	607.75 MiB	7.985 GiB
# Lines	4,266,280	37,497,133	5,867,324	81,963,950
#	3		4	
Parameters	Lax		Tight	
Range	2100-2500		2000-2500	
Database	CDSDv	CDSD4000	CDSDv	CDSD4000
Time 1 (s)	17.09	65.53	39.95	181.62
Time 2 (s)	124.82	183.89	574.38	738.41
Time 3 (s)	613.40	791.06	6846.50	12253.16
Max RAM	442.7 MiB	3.660 GiB	608.14 MiB	7.963 GiB
# Lines	4,266,280	37,497,133	5,867,324	81,963,950

not an extensive performance test there are some trends that might be suggestive of the general relative behaviour of both databases. The first trend is that increasing temperature decreases relative performance but always maintains it above one. At low temperatures the performance difference is mostly impacted by the calculation of the pseudo-continuum. CDSD4000 with approximately 81 million lines will underperform when compared to the 5 million lines in CDSDv. At higher temperatures the calculation time is dominated by the number of strong lines that need to be treated. In tests 2 and 3 the ratio of strong lines can be between 1.1 and 1.5 as shown in fig 4.12 which leads to performances usually below a factor of 2 better between CDSD4000 and CDSDv. The second trend is that increasing the spectral range and retaining lax numerical parameters leads to better performance of CDSDv. In a small spectral range the number of strong lines in CDSD4000 and CDSDv will be approximately the same. With a greater spectral range and sufficiently relaxed numerical parameters, while maintaining safe margins for faithful reproduction of the exact spectrum, a better global performance might be achieved. Something worth mentioning and not shown by this performance check is that it would be impossible to simulate a full spectrum of CDSD4000 with the available computational resources as is done in fig. 4.10. This can be done with CDSDv and at least in a smaller spectral range, CDSDv is always faster than CDSD4000.

Table 4.5: Performance comparison between CDSDv and CDSD4000 for the calculation of one atmosphere of pure CO_2 at 1000, 2000 and 3000K. The computational time is proportional to the number of lines considered for the calculation.

	Time (s)		Number of Lines	
Temperature	CDSDv	CDSD4000	CDSDv	CDSD4000
1000K	23	63	35,314	35,832
2000K	445	504	565,066	662,118
3000K	1,997	2,873	2,230,224	3,416,204

One last comparison was performed where the pseudo-continuum method is not used. The purpose of this test is to make a direct comparison of the number of lines used in CDSD4000 and CDSDv and the computational times using the same thresholds but without any numerical shortcut. In these simulations any line with absorption and emission 10^5 times smaller than the highest absorption and emission of the entire ensemble of lines is discarded. The temperatures 1000, 2000 and 3000K are again considered in the spectral range of 2000-2500 cm^{-1}. The results for this calculation are presented in table 4.5. The total number of lines in this spectral region are 5,823,586 for CDSDv and 81,963,950 for CDSD4000. Only a fraction of the total number of lines are used in these calculations. At 1000K both databases use a similar number of lines. CDSD4000 takes 63 seconds compared with the 23 seconds of CDSDv due to the time it takes to read the input file

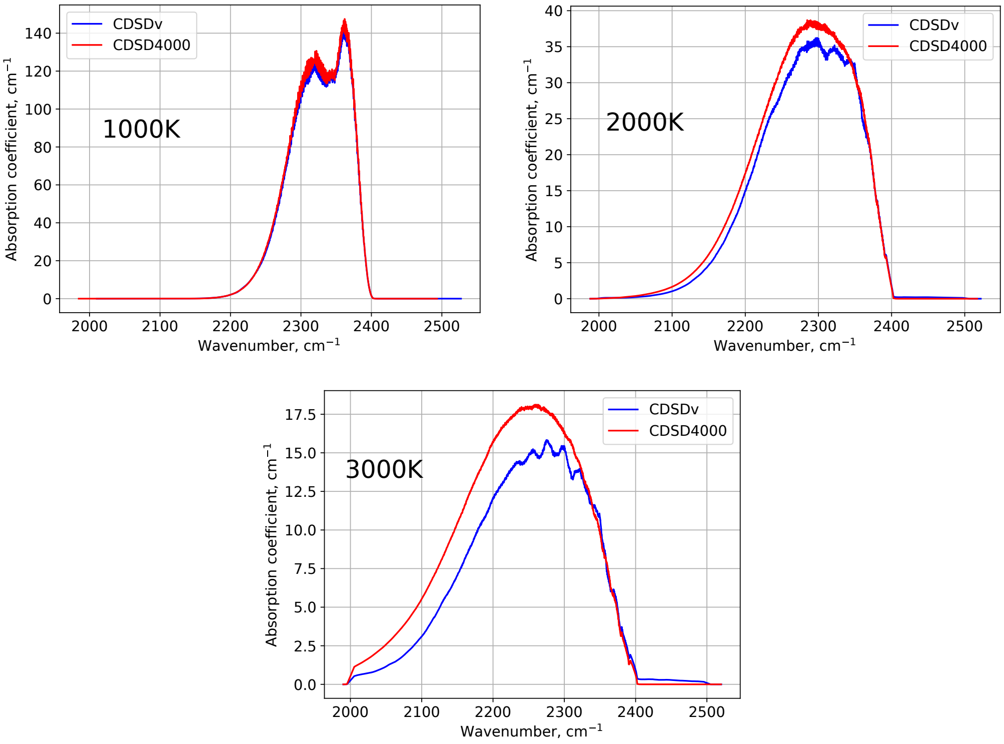

Figure 4.13: Absorption coefficients of one atmosphere of pure CO_2 at 1000, 2000 and 3000K computed with CDSD4000 and CDSDv. These results were convoluted with a 10 cm^{-1} wide rectangular apparatus function.

of CDSD4000. At 2000K the calculation using CDSD4000 takes almost a minute longer than CDSDv due to the reading a much larger input file and handling 100,000 more lines in the calculation. At the highest temperature, CDSD4000 takes approximately 45 minutes compared against the 30 minutes that CDSDv takes. The difference in the number of lines is also very significant with 2.2M considered by CDSDv and 3.4M considered by CDSD4000. Obviously, this comparison is inconsequential if the obtained spectra are too different. Figure 4.13 presents the absorption coefficient obtained from the calculations of 1 atmosphere of pure CO_2 at 1000, 2000 and 3000K as in table 4.5. The absorption coefficients were convolved with a 10 cm^{-1} rectangular apparatus function. For the 1000 and 2000K cases, the obtained spectra are quite similar but in the 3000K case there are significant differences between the CDSD4000 and CDSDv absorption coefficients. This is not necessarily a deal breaker, as the pressure and the typical dimension of the system also come into play in determining how important radiative heating will be at this temperature.

4.2.2 Comparison with experimental results

Transmittance

The transmittance of CDSDv was computed according to the test cases presented in [256] which include simulations using CDSD4000 and experimental measurements. The conditions used for these simulations are summarized in table 4.6 where the lettered labels are the same as in [256]. The number density in each case may be determined by $N = xp/k_BT$ where x is the fraction of CO_2. The transmittance τ is computed through a length L through:

$$\tau_{\overline{\nu}} = \exp\left(-\alpha_{\overline{\nu}} L\right) \tag{4.54}$$

where $\alpha_{\overline{\nu}}$ is the absorption coefficient at position $\overline{\nu}$. The quantity Δ is defined in [256] as the spectral resolution, which by itself is poorly defined in this context. In this work it was taken as a moving average window for post-processing of the exact result. The results for these simulations can be seen in figs. 4.14, 4.15, 4.16 and 4.17 for the 2.3, 2.7, 4.3 and 15 μm regions, respectively. Most cases are well matched with experiments and/or calculations. Two cases stand out as almost or completely mismatched with either experiments or calculations, case b) and s).

Case b) is in the 2.3 μm region shown in fig. 4.14. In this region, CDSD4000 does not perform particularly well against experimental values. The region between 5000-5200 cm^{-1} for instance is completely missed. It is not surprising therefore to see a case where refitted transitions from CDSD4000 do not perform well. It is surprising that the 5000-5200 cm^{-1} region is captured relatively well by CDSDv in most cases. This might be purely coincidental as benefitial result of extrapolations of CDSDv beyond the cutoff parameter of CDSD4000 (since it is the lineshape routine which adoptively manages these, instead of the databases). The region between 4600-5000 cm^{-1} is also generally well captured, close to experiments and calculations except in case d) where it is close to calculations but far from the experimental points.

In the 2.7 μm region, in fig. 4.15 CDSDv performs very well against experiments and calculations except in case i) where the absorption coefficient is underestimated and thus, the transmittance is overestimated.

The 4.3 μm region, shown in fig. 4.16, displays also the other worst case, s). In this case, the gas temperature is already high enough (2850 K) and the gas dimension small enough that any initial discrepancy is enhanced as per equation 4.54. The absorption has

Table 4.6: Test cases in Lemal et al. [256].

Label	T (K)	p (atm)	x (%)	L (cm)	Δ (cm^{-1})
a	500	1	100	54	30
b	1000	1	100	50	30
c	1203	1	43	54	40
d	1300	1	100	50	35
e	1550	1	50	50	10
f	1770	1	18	54	30
g	298	1	100	95.3	10
h	500	1	100	53.3	15
i	1000	1	5	40	15
j	1300	1	100	40	10
k	1500	1	100	7.75	25
l	300	0.66	6	5.14	50
m	667	0.5	11	9.64	10
n	1000	1	100	50	12
o	1200	1	100	7.75	30
p	1300	1	100	50	50
q	1500	1	53	7.75	10
r	1771	1	17	54	54
s	2850	1	24	2.34	20
t	500	1	100	53.4	7
u	1000	1	100	50	6
v	1203	1	43	53.7	3
w	1473	1	1	50	5
x	1950	1	53	3.12	5
y	2300	1	49	1.67	5

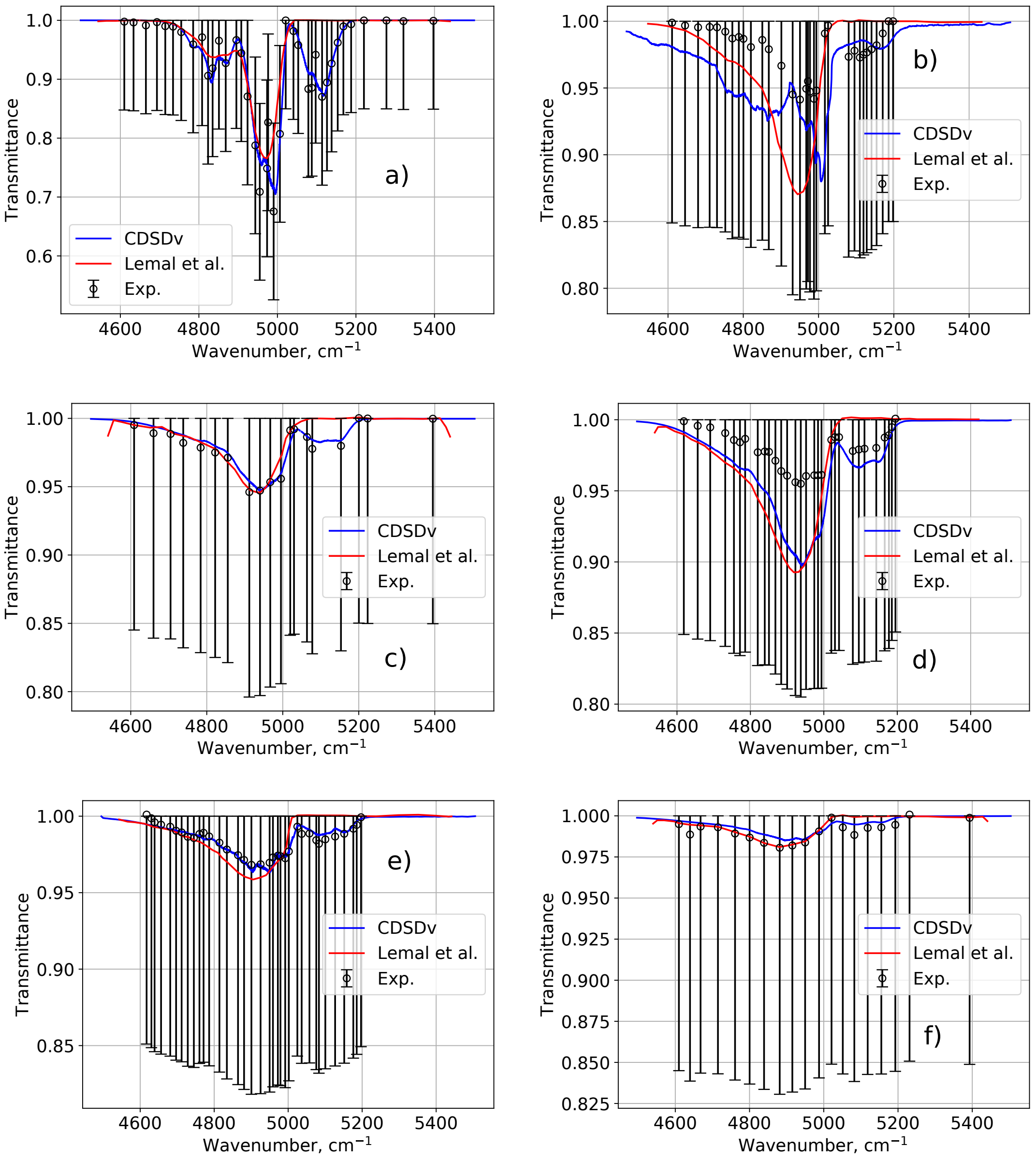

Figure 4.14: Transmittances of test cases listed in table 4.6 compared against the same that are listed in [256] of the 2.3μm region, cases a through f.

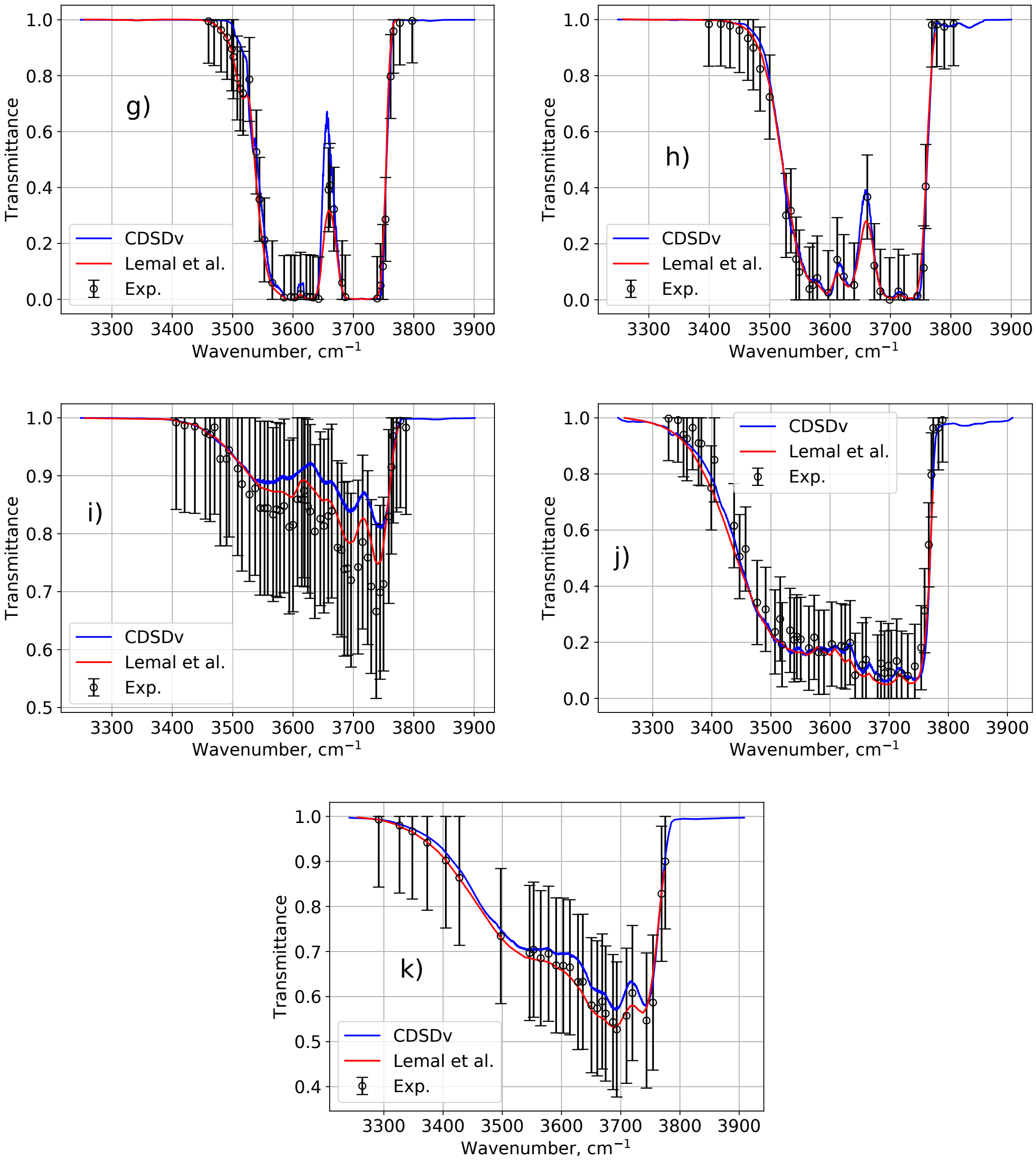

Figure 4.15: Transmittances of test cases listed in table 4.6 compared against the same that are listed in [256] of the 2.7μm region, cases g through k.

to be very well estimated to capture the region where $0 < \tau_{\overline{\nu}} < 1$ as it happens in case s) where transmittance is between 0.2 and 0.8 in the region of $2050 - 2375$ cm^{-1}. All other cases are close to experimental calculations and experimental measurements except case l) where most points between 2300-2475 cm^{-1} are closer to the CDSDv line than CDSD4000.

The last spectral region treated in this work, 15 μm is shown in fig. 4.17. In these cases CDSDv fares as well as, or better than CDSD4000, as in cases w), x) and y). The reason for this might be that calculations with CDSD4000 are usually performed with the Lorentzian HWHM coefficients present in the database. These coefficients only account for self-broadening and/or air-broadening. CDSDv does not assume any coefficients for Lorentz broadening, relying instead on general expressions that account for different collisional effects, including different mixtures than the ones used in CDSD4000. Cases w), x) and y) are cases where the gas mixture is not fully composed of CO_2 and therefore, Lorentz broadening cannot be fully accounted using self-broadening only as it is usually done in CDSD4000.

JAXA Mars Entry Conditions

Measurements of IR radiation of CO_2 were performed out in JAXA expansion and shock tube facilities and reported in [257]. Pannier and Laux carried out a numerical and radiative analysis using the code RADIS [258] and CDSD4000 database [259]. Fig. 4.18 displays the framework of the calculations carried out in [259]. The line of sight is composed of three cells. The first and the last have the same size and gas conditions.

Part of the work developed by Pannier and Laux was to assess which conditions in the three cells would make a better match for the experimental measurements. The first and last cells would be considered "freeflow" cells characterized by low pressure and non-equilibrium. The freeflow conditions were estimated by measurements performed with the line of sight blocked by the model in the expansion tube. The conditions in the freeflow were then determined to be: $T_{\mathrm{CO}} = T_{\mathrm{CO2}} = 2200$K and $T_{\mathrm{gas}} = T_{\mathrm{rot}} = 1690$K at a pressure of 17 mbar with the molar fraction of CO_2 being 0.606 and CO 0.257. The center cell would be the "forebody" region chracterized by a high-pressure shock wave, thermal equilibrium and strong dissociation of CO_2. With the free-stream conditions fixed, the center cell is considered to be at $T = 4000$K with a pressure of 1 bar. CO_2 is mostly dissociated, amounting to only 0.027 molar fraction, and CO corresponds to 0.520 molar fraction. The radiance is computed through equation 4.15. Fig 4.19 presents the best

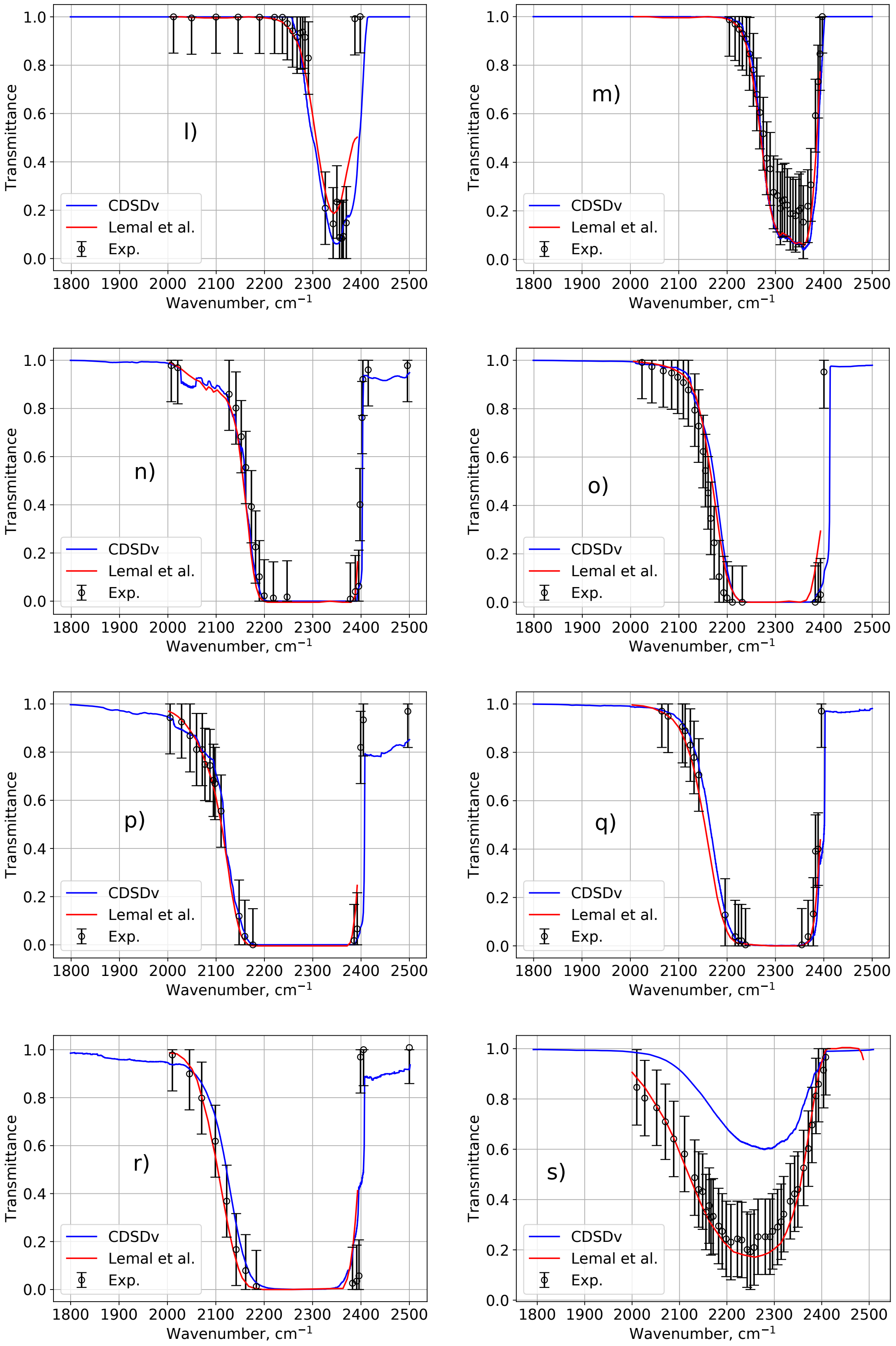

Figure 4.16: Transmittances of test cases listed in table 4.6 compared against the same that are listed in [256] of the 4.3μm region, cases l through s.

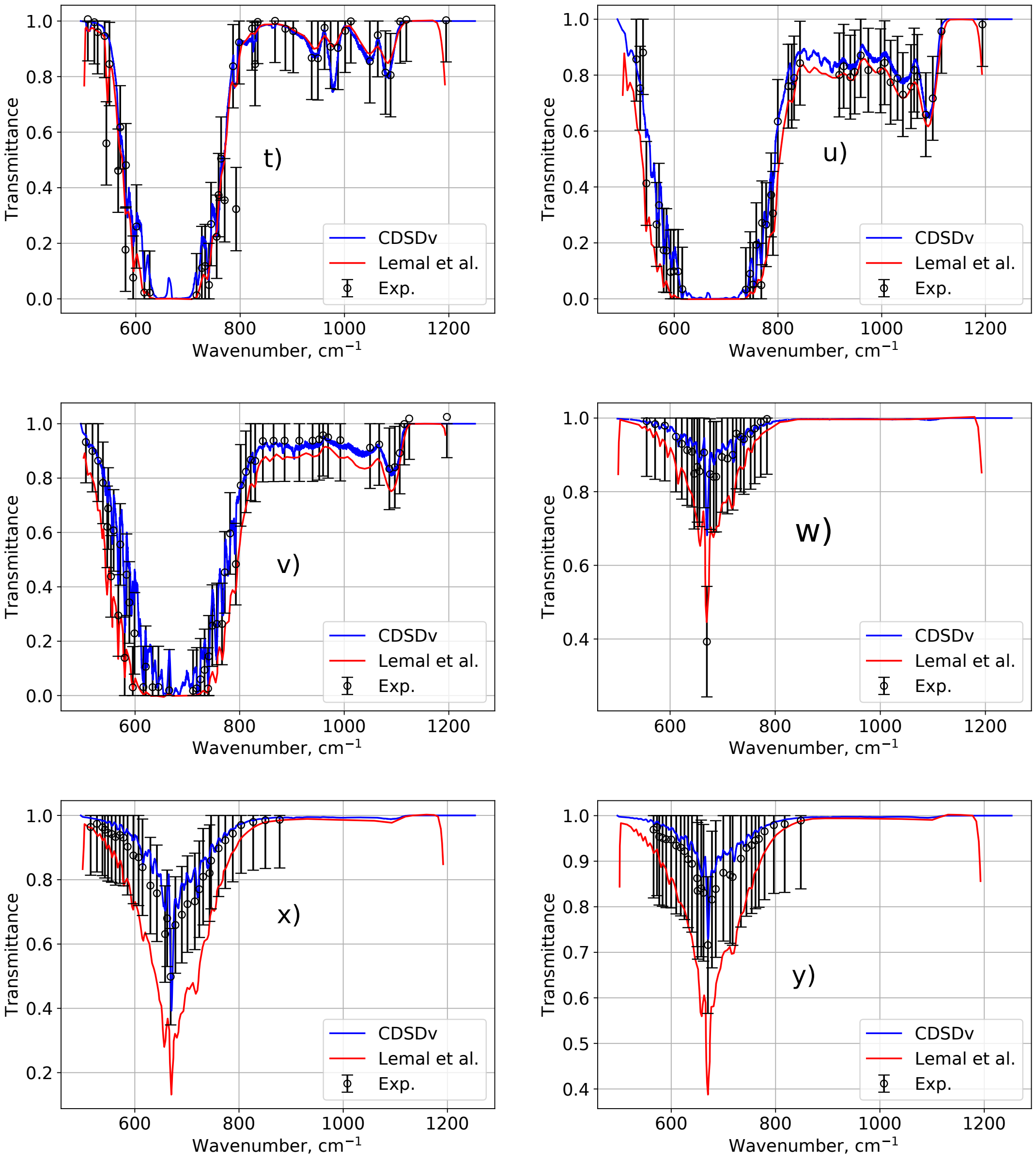

Figure 4.17: Transmittances of test cases listed in table 4.6 compared against the same that are listed in [256] of the 15μm region, cases t through y.

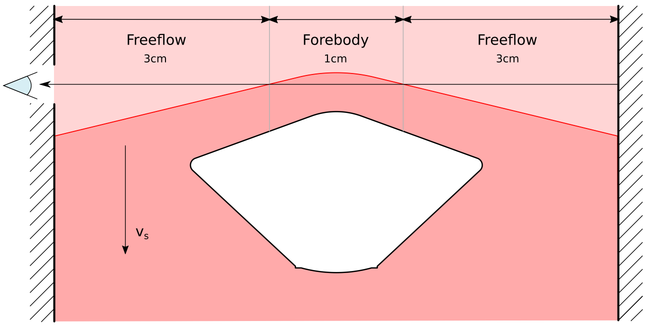

Figure 4.18: Schematic of the calculation performed in [259] to reproduce the results in [257].

case result presented in [259] and briefly described in this paragraph. It also displays the same case computed with CDSDv and the in-house radiation code (SPARK line-by-line). The experimental and numerical results are reproduced quite well by CDSDv. There is a small underprediction in the tail region between 4600-4900 nm. According to the analysis carried out in [259] CO is the main radiator in this region and a detailed comparison showed that our database describing CO IR radiation might need an update. In the cases described in this work however focus will be on CO_2 radiation and as such, an update on the CO database will be left for future work.

EAST Mars Entry Condition

A shock tube experimental campaign was performed in the Electric Arc Shock Tube (EAST) facility in NASA Ames Research Center to replicate the conditions experienced by the Mars Science Laboratory (MSL) which landed on Mars in 2012. These series of tests are known as as EAST test suite 55. A work analysing the radiative heating experienced by MSL during atmospheric entry was published by [260] which uses data from the aforementioned campaign to explain the measurements obtained by the MSL thermo-couples embedded in the heat-shield. Data was taken from this campaign in the conditions which most resemble the peak radiative heating. Shots 9 and shot 30 and additionally shot 19 is also considered in this work as a low pressure case the radiative signal of two different kinetic models. Table 4.7 presents the conditions inside the shock tube for each considered shot.

In the low pressure case (shot 19), using the in-house code SPARK, the 1D shock relaxation is solved using Park's kinetic scheme described in [261] or Cruden's kinetic

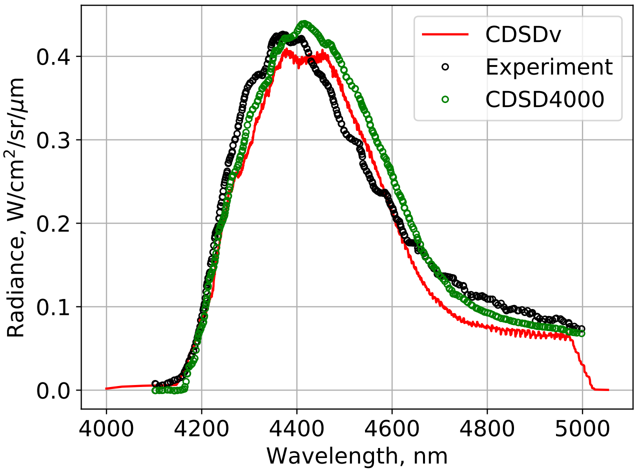

Figure 4.19: Measurement and calculation of radiance in expanded flow around a model of a spacecraft. Experiments were carried out by [257] and the calculation using CDSD4000 by [259]. The calculation using CDSDv was performed for this work.

Table 4.7: Conditions and measured spectral region in EAST shock tube for shots 9, 19 and 30 of test 55. The molar composition is the same for all shots and all were performed at ambient temperature.

Shot #	Pressure (Torr)	Speed (km/s)	Spectral Region (μm)	Molar Mixture
9	1.0	3.69	4.3	95.8% CO_2
19	0.1	5.52	4.3	2.7% N_2
30	1.0	3.64	2.7	1.5% Ar

scheme described in [212]. Park's kinetic scheme does not consider Ar and Cruden's kinetic scheme does not consider Ar and N_2 and as such these species were neglected in their respective simulations. From the 1D relaxation, the pressure, molar fractions, vibrational temperatures (shared by CO_2 and CO) and gas temperatures are obtained and the radiance of the flow is obtained considering a 10.16 cm tube (EAST dimensions). Equation 4.15 is used to compute the radiance without the additional term on the right hand side of the equation. Fig. 4.20 presents the measured and calculated radiance using Park and Cruden kinetic models. The measured radiance was smoothed out for aiding in visualization. The radiative signals from Park and Cruden models are very similar for this shot. Both peak at the same position and relax in comparable time scales. The

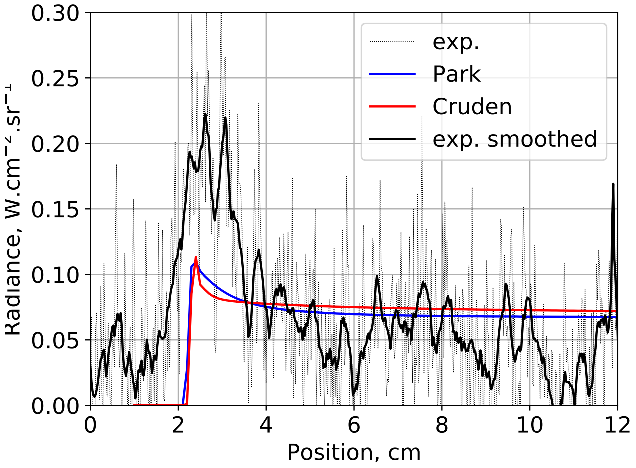

Figure 4.20: Measurements and calculations of the radiance of a shock-wave on 0.1 Torr gas with a composition of 0.958 CO_2, 0.027 N_2, 0.015 Ar at 5.52 km/s.

post-shock tail is also very close, two centimeters after the shock. While not completely in equilibrium in the measured distance after the shock, there is a small difference in the equilibrium parameters due to the inclusion of N_2 in Park's model. The experimental peak is approximately twice the calculated peaks.

In the high-pressure case, using an equivalent stagnation line for the flow profile, kindly ceded by B. Cruden, the aforementioned treatment is applied with equation 4.15. Instead of the ideal 1D postshock flow, the equivalent stagnation line accounts for diffusion effects across the shock-wave as described in [262]. In fig. 4.21, the measured and calculated radiance of shots 9 and 30 are plotted. Shot 9 was measured in the 4.3 μm region and shot 30 in the 2.7 μm region. The simulated shot 9 is in very good agreement with the experimental results, the abrupt end in calculated signal at the end is due to an early stop in the simulation. On the 2.7 μm region there is no agreement with the experimental values and the signal is not simulated fully along the test distance. The mismatch between experiments and simulations in this spectral region is attributed to missing transition data in the 2.7 μm region of CDSDv.

Atmospheric Plasma Torch

In the work of Depraz et al., published in two parts [263] and [264], an high-temperature CO_2 microwave plasma is studied and characterized. The radiance of the plasma was measured at a height h of 6 and 20 mm and also at different distances from the central chord

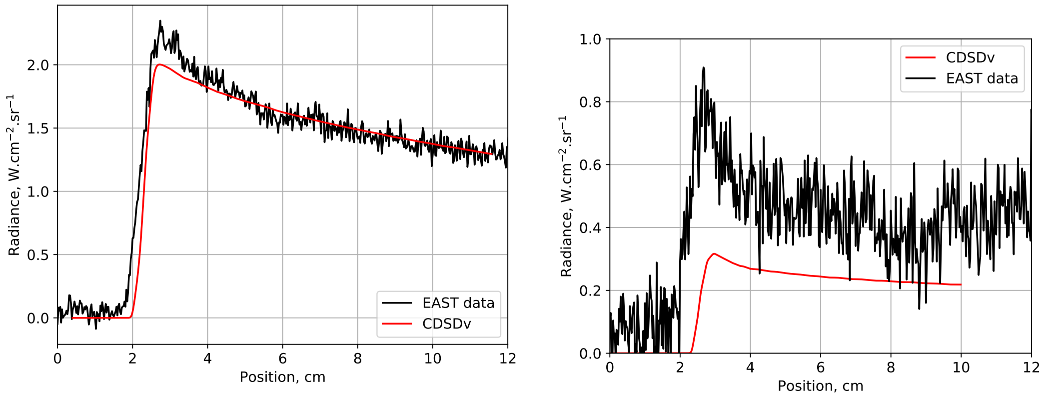

Figure 4.21: Measurements and calculations of the radiance of a shock-wave on 1 Torr gas with a composition of 0.958 CO_2, 0.027 N_2, 0.015 Ar at 3.69 km/s in the 4.3 μm region (left) and 3.64 km/s (right) in the 2.7 μm region.

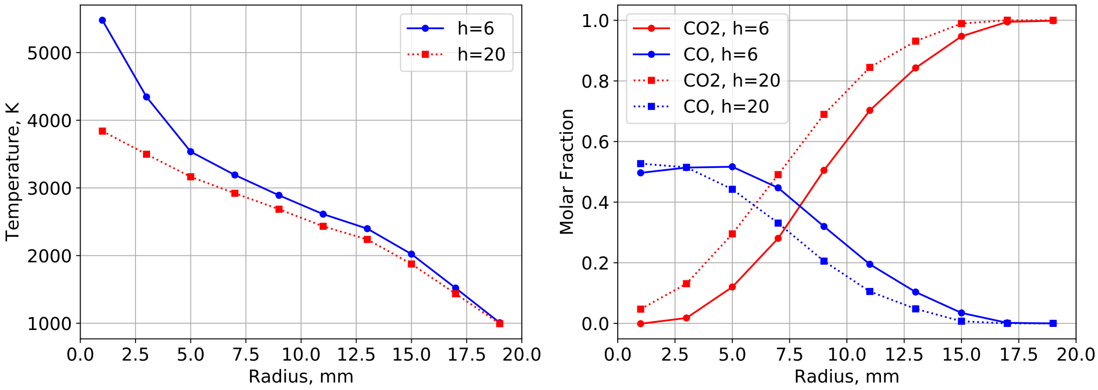

Figure 4.22: Temperature and molar fraction profiles for the cases where $h = 6$ mm and $h = 20$ mm in the atmospheric plasma torch studied in [263] and [264]

of the plasma. These measurements are compared with calculations using CDSD4000. In this work only the measurements taken at different heights at the central chord will be analyzed. Fig. 4.22 presents the radial profile of the plasma torch. The continuous profile was divided in ten cells and its conditions averaged to yield the discrete profile in fig. 4.22. For this calculation the full diameter profile is taken, with the two cells closest to the center merged, according to the line of sight. Again, equation 4.15 is used along the line of sight with the self-absorption correction.

Fig. 4.23 presents the results for the 4.3 μm region at the two heights, 6 (left) and 20 (right) mm. In this spectral region calculations were performed including and excluding the radiation of CO. By including CO there is a non-negligible effect in the region $1800 - 2250$

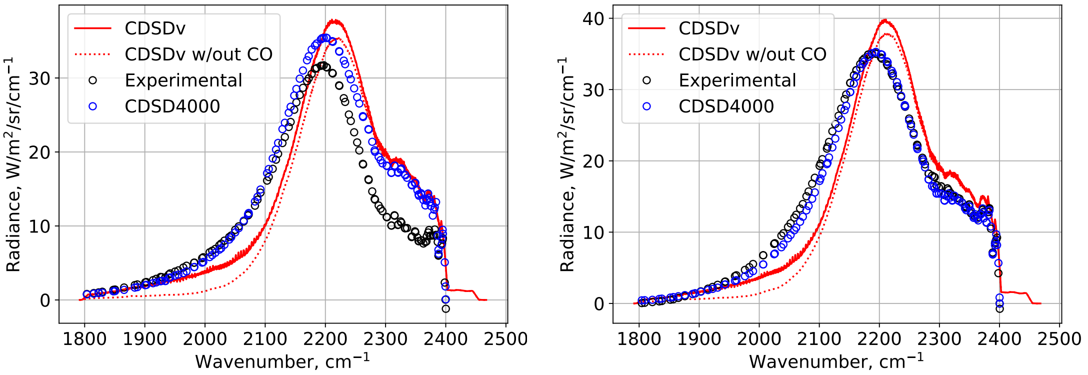

Figure 4.23: Measurements and calculations of the radiance of the atmospheric plasma torch in the 4.3 μm region at a $h = 6$ mm (left) and $h = 20$ mm (right). Calculations were performed using CDSD4000 and CDSDv.

cm^{-1}. Most notably, the radiative peak is higher and the region $1800 - 2050$ is closer to experimental lines than the calculation without CO. CDSDv curves in the $2250 - 2400$ cm^{-1} region are matching CDSD4000 quite well at $h = 6$ but fail otherwise. The radiative peak, while close in magnitude is blue shifted by a bit less than 20 cm^{-1}. Both databases overestimate the experimental measurements in the $2150 - 2400$ cm^{-1} region. At $h = 20$ mm, the analysis is similar, except the $2150 - 2400$ cm^{-1} region is well predicted by CDSD4000 and overestimated by CDSDv. The peak is still blue shifted by a similar value as in the $h = 6$ measurement.

Fig. 4.24 shows the results for the 2.7 μm spectral region. The figure on the left is the measurement and calculation corresponding to $h = 6$ mm and the figure on the right to $h = 20$ mm. In this region CDSDv underestimates the experimental and calculated results in the work of Depraz et al. The inclusion of CO in this region does not change the radiative profile significantly and is therefore deemed negligible.

The underestimation in the 2.7 μm region is attributed to transition data missing from CDSDv. A review of this spectral region might improve the results for a better match with experimental results. In the 4.3 μm region, where most time was devoted to the construction of CDSDv, the situation is more complex. Although there might be some missing information in the $1900 - 2150$ cm^{-1} region, there might also be an issue with the refitting procedure carried out during this work. A better translation of the data contained in CDSD4000 (in refitting and averaging procedures) is possible and it could improve results to the point where a better match with CDSD4000 calculations would be

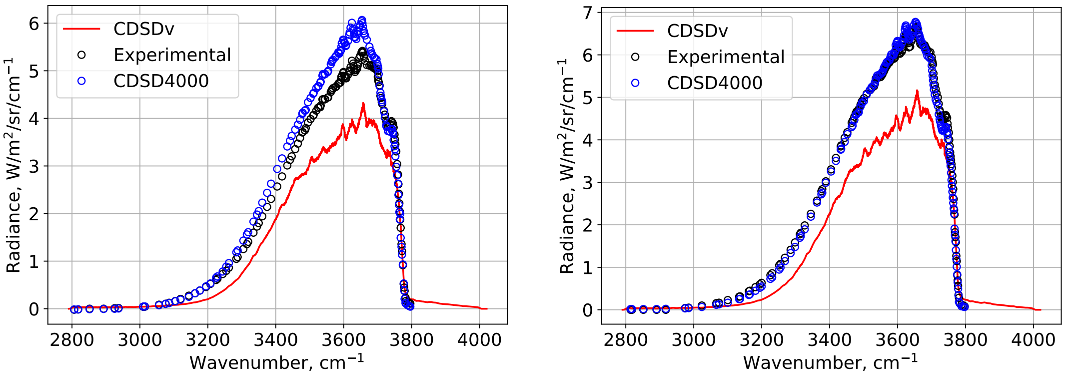

Figure 4.24: Measurements and calculations of the radiance of the atmospheric plasma torch in the 2.7 μm region at a $h = 6$ mm (left) and $h = 20$ mm (right). Calculations were performed using CDSD4000 and CDSDv.

achieved.

IR radiation of Glow Discharge

In recent works [16, 211, 19, 265], the CO_2 DC Glow Discharge has been used for the study of CO_2 fundamental processes. The simplicity of the discharge allows reproducibility of experimental results which is an advantage for both experimentalists and modellers. Notably, the work of Klareenar *et al.* has used spectral measurements of the 4.3 μm band taken at Laboraitoire de Physique des Plasmas (LPP) in Paris with a fitting algorithm to obtain time resolved translational, vibrational and rotational temperatures as well as the dissociation fraction α and pressure of the gas. In conversations with Olivier Guaitella and Ana Morillo-Candas, the two experimentalists who performed the measurements at LPP, the idea to apply CDSDv to model experimental data from the CO_2 Glow Discharge setup at LPP came to be. The fitting of absorption measurements must include the CO_2 isotopes $O^{16}C^{13}O^{16}$, $O^{16}C^{12}O^{18}$ and $O^{16}C^{12}O^{17}$. As such, absorption spectroscopy cannot be considered without the inclusion of these isotopes in CDSDv. The only option is then emission measurements, which had to be taken in a slightly modified setup. What follows in this section is a part of an on-going collaborative work on the analysis of the CO_2 glow discharge using CDSDv with Drs. Guaitella, and Morillo-Candas.

The setup of the experiment is schematically represented in figure 4.25. The discharge tube has a inner diameter of 2 cm and a length of 23 cm but the electrodes are only 17 cm apart in perpendicular side tubes. The apparatus function of the FTIR spectrometer

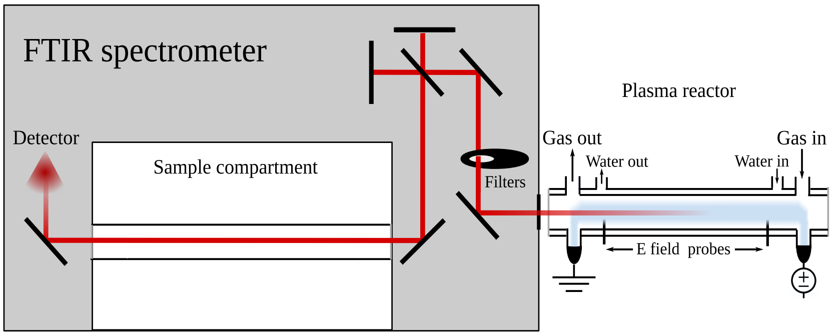

Figure 4.25: Schematic of experimental setup of the glow discharge by emission FTIR at LPP. Adapted from [266]

(Bruker V70) is a gaussian with FWHM of 0.2 cm^{-1}. Two measurements are performed at 20 and 40 mA at a pressure of 1 Torr. In these measurements the light is collected by a parabolic mirror and as such, the emitting region of the plasma is more of a punctual or circle source. The path length of emitted light cannot be exactly estimated but some preliminary testing puts it between 1-2 cm. Furthermore, without a well defined collection angle no unit calibration of the measurement is possible and as such, the measured radiance is in arbitrary units. The same experimental parameters were used to obtain the absorption spectra, schematically represented in figure 4.26. These measurements allowed the determination of the fitting parameters given by the algorithm described in [16] which are shown in table 4.8.

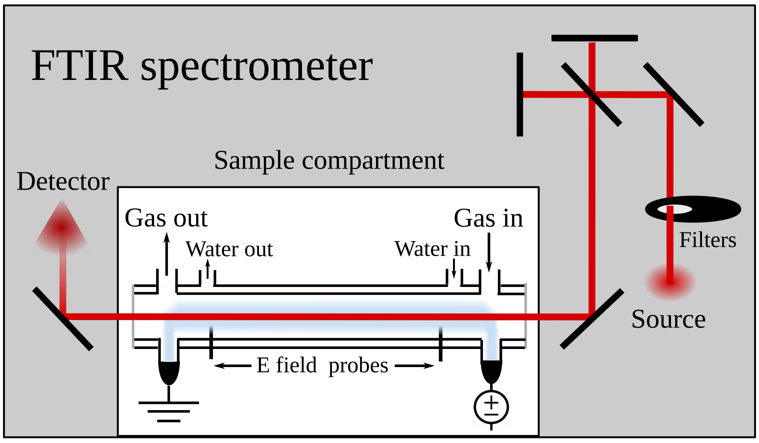

Figure 4.26: Schematic of experimental setup of the glow discharge by absorption FTIR at LPP. Adapted from [266]

The fitting algorithm in [16] assumes a population of the internal levels of this form

$$N_i = N\phi_{\mathrm{rot},J} \prod_v \phi_{\mathrm{vib},v} \tag{4.55}$$

where $\phi_{\mathrm{rot},J}$ is given by

$$\phi_{\mathrm{rot},J} = \frac{g_{\mathrm{rot},J}}{Q_{\mathrm{rot}}} \exp\left(-\frac{hcE_{\mathrm{rot},J}}{k_B T_{\mathrm{rot}}}\right) \tag{4.56}$$

and $\phi_{\mathrm{vib},v}$ is given by

$$\phi_{\mathrm{vib},v} = \frac{g_{\mathrm{vib},v}}{Q_{\mathrm{vib},v}} \exp\left(-\frac{hc}{k_B}\left[v\frac{G_v}{T_v} - v(v-1)\frac{\omega_e\chi_{e,v}}{T_{\mathrm{rot}}}\right]\right) \tag{4.57}$$

and must be computed for each vibrational mode of the species. The parameters G_v and $\omega_e\chi_{e,v}$ are displayed in table 4.9 for the main isotope of CO_2 and CO. The degeneracy of vibrational levels is 1, except for the bending mode of CO_2, which in this calculation, without considering l_2, should be $g_{v_2} = v_2 + 1$. The temperature of the symmetric stretch and bending mode is also considered to be the same, hence there is only one $T_{1,2}$. The rotational energy is computed as in equation 4.31 without the vibrational component G_v and with the coefficients in table 4.9 for all modes. The α parameter in table 4.8 is the CO_2 conversion factor and it relates to the mole and number density fractions of CO_2 and CO:

$$f_{\mathrm{CO_2}} = \frac{1-\alpha}{1+\alpha/2} \tag{4.58}$$

$$f_{\mathrm{CO}} = \frac{\alpha}{1+\alpha/2} \tag{4.59}$$

with $\alpha = f_{\mathrm{CO}}/(f_{\mathrm{CO2}} + f_{\mathrm{CO}})$. Finally, the gas temperature represents the thermal region after the discharge. The pressure, which is also fitted from the algorithm is the same inside and outside the plasma column. As such the number densities inside and outside the plasma is given by

$$n_{\mathrm{in}} = \frac{p}{k_B T_{\mathrm{rot}}} \tag{4.60}$$

$$n_{\mathrm{out}} = \frac{p}{k_B T_{\mathrm{gas}}}. \tag{4.61}$$

It is not certain what is the amount of CO_2 that recombines outside of the plasma. There are two possible assumptions, a full recombined and a non-recombining frozen gas. In this work it was assumed that outside the plasma chemistry is frozen and as such the mole fractions are kept constant in and outside the plasma.

The same internal level population calculation in [16] was adapted for use with CDSDv. One of the issues in CO_2 conversion is the energy efficiency. It is plausible that not enough

Table 4.8: Parameters obtained by fitting the absorption spectra obtained by FTIR of the CO_2 Glow Discharge at LPP. The fitting algorithm is described in [16]

Current (mA)	20	40
p (Torr)	1.150	1.149
α	0.159	0.228
T_{gas} (K)	326.9	316.5
T_{rot} (K)	429.4	496.4
$T_{1,2}$ (K)	450.7	532.8
T_3 (K)	896.9	1054.1
T_{CO} (K)	1014.9	1219.2

Table 4.9: Spectroscopic parameters of the main isotopes of CO_2 and CO used to compute the population of internal levels in [16]. The three modes of CO_2 share the same B_v, D_v and H_v parameters.

Vib. mode	$G_v(\mathrm{cm}^{-1})$	$\omega_e\chi_{e,v}(\mathrm{cm}^{-1})$	$B_v(\mathrm{cm}^{-1})$	$D_v(10^{-6}\mathrm{cm}^{-1})$	$H_v(10^{-12}\mathrm{cm}^{-1})$
$^{12}C^{16}O_2$ v$_1$	1333.93	2.93	0.39022	0.1333	0.0090
$^{12}C^{16}O_2$ v$_2$	667.47	-0.38			
$^{12}C^{16}O_2$ v$_3$	2349.16	12.47			
$^{12}C^{16}O$	2143.24	13.29	1.9225	6.121	5.7

energy is being contained in the plasma for a more efficient conversion. As such, assuming a homogeneous plasma column 17 cm long and diameter of 2 cm, the energy radiated by CO_2 and CO in the IR can be calculated using CDSDv. An average path length of $1cm$ is assumed in the homogeneous plasma column to compute the spectral radiance as

$$L_{\overline{\nu}} = \frac{\varepsilon_{\overline{\nu}}}{\alpha'_{\overline{\nu}}}\left(1 - \exp\left[-\alpha'_{\overline{\nu}} d\right]\right) \tag{4.62}$$

between 300 cm^{-1} and 5600 cm^{-1}. Integrating over the spectrum and multiplying by the surface area of the column the power lost by IR radiation is 0.597 W for the measurement at 20 mA and 1.245 W for the measurement at 40 mA. It is uncertain whether other radiative systems play a role in providing an escape for energy in the system and this should be part of future measurements.

To compare CDSDv with the spectral measurements, a radiative transfer equation was solved, assuming a 2 cm long column of plasma behind an equilibrium gas with the same molar fractions of CO_2 and CO at T_{gas}. The apparatus function of the FTIR spectrometer is applied to the results and another convolution with a 10 cm^{-1} wide square function is applied to the simulation and experimental results for better visualization. The results are also normalized to their maximum value for a fairer comparison since the experimental results are not calibrated. Figure 4.27 presents the simulated and experimental results for the 20 mA (left) and for the 40 mA (right). As this is a proportional visualization, there is no straightforward correspondence between the experimental (black) and simulated (blue) profiles. It can be seen right away however, that there is an underestimation of the ratio between the CO_2 part of the profile (in the region 2250-2400 cm^{-1}) and the CO part of the profile (in the 2000-2250 cm^{-1} region). The experimental profile presents a much broader profile in the CO region and the height is about 1/5th of the CO_2 profile. With a 1 cm long plasma column the results do not significantly change to justify the presentation of new figures. Assuming a fully recombined CO_2 gas in front of the plasma helps the comparison as more CO_2 molecules will absorb the incoming radiation thereby increasing the height of the CO part of the spectrum compared with the CO_2 region.

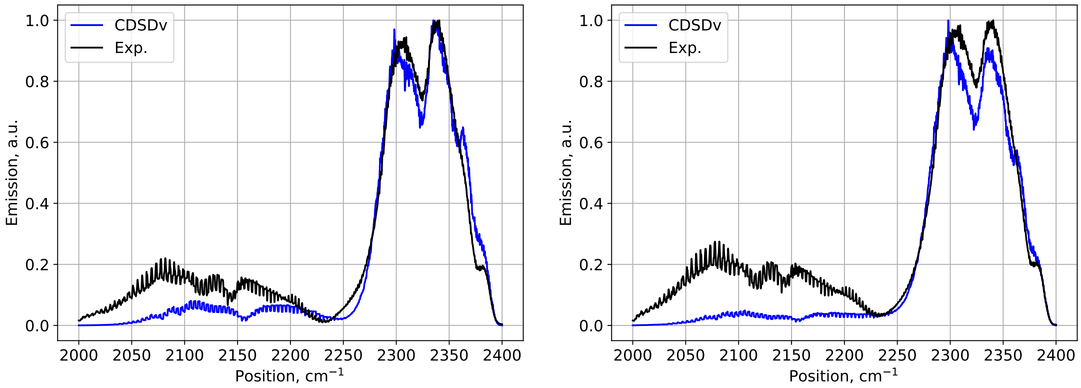

Figure 4.27: Emission from the glow discharge convoluted with a 10 cm^{-1} wide square function and normalized to the maximum value of the profile in this spectral range. Experimental and simulated results are presented here for the measurement at 20 mA in the left and 40 mA on the right.

Ideally, there would be time to implement a sort of fitting procedure to obtain the optimal parameters for CDSDv to compare with the experimental measurements. Such calculation would be of great interest to compare with the parameters obtained from the procedure in [16]. This has not been performed in this work but some particular trends may be checked. Since these comparisons are performed in the 4.3 μm region, the strongest transitions in this region are when $\Delta v_3 = 1$. In the work of Urbanietz *et al.* [9], the spectra of CO_2 is analyzed in a similar way as in [16]. In [9], the CO_2 is not in a glow discharge but in a helium atmospheric pressure plasma jet and the fitting algorithm admits different symmetric and bending mode temperatures. These temperatures are shown with a significant gap, about 200 to 300 K. The more recent work by the same authors [10] shows the lumping of the symmetric and bending mode into a single parameter $T_{1,2}$ as in [16]. The explanation is that [11], in the fits with separate temperatures the error of parameters T_1 and T_2 were big enough, such that there would be a region where the error bars would overlap. As such, a fit was attempted with the lumped parameter $T_{1,2}$ and showed no significant difference in the match between experimental and simulated profile. In the case of the work by Klarennar *et al.* [16], an earlier version of the same algorithm, would fit vibrational populations of levels instead of the vibrational temperatures. Both versions of the algorithm show that the population of symmetric and bending levels close in energy have similar populations within the experimental error and spectral resolution of the experiment[1]. As such a preliminary analysis was carried out by changing each temperature (except T_{gas}) and checking the variations on the mean absolute error for the 20 mA measurement. A similar analysis on the 40 mA measurement yields similar results. In figure 4.28, the mean absolute error is shown for a defect of -50 to 50 K for the T_{rot} (cyan, pentagon), $T_{1,2}$ (green, hexagon), T_{CO} (red, square) and T_3 (blue, triangle) parameters. The black star labeled T_0 is the absolute mean error of the measurement with the simulated spectrum calculated using the parameters on table 4.8. The mean absolute error is defined here as

$$E = \frac{\sum^{N} |Y - X|}{N} \tag{4.63}$$

where Y and X are the compared quantities and N is the number of observations. Based on the previous discussion it is expected that varying T_3 will lead to a greater error difference than varying $T_{1,2}$ which is verified in figure 4.28 but not so much a difference, as would be expected based on the large error bars verified by Urbanietz *et al.*. Varying T_{CO} does not lead to much change in the error and the only parameter that decreases the error by increasing is the T_{rot}. All this suggests that if a fitting algorithm was applied with

---

[1] private communication.

CDSDv to the measurements made at LPP all the analysed temperatures would decrease except T_{rot} which would increase. This might be due to the overestimation of CO_2 height in respect to the CO part of the spectrum. It has been previously shown in this work that calculations using CDSDv are in excellent agreement with experimental and calculated results in the range of temperatures that the fitting algorithm of Klarenaar *et al.* has determined for these experimental results. Although the calculations in this work still not match experimental measurements, improvements can be made, particularly on the CO database. After that, the next step will be to build an algorithm using CDSDv and the improved CO database to obtain a set of parameters to reproduce the measurements performed at LPP.

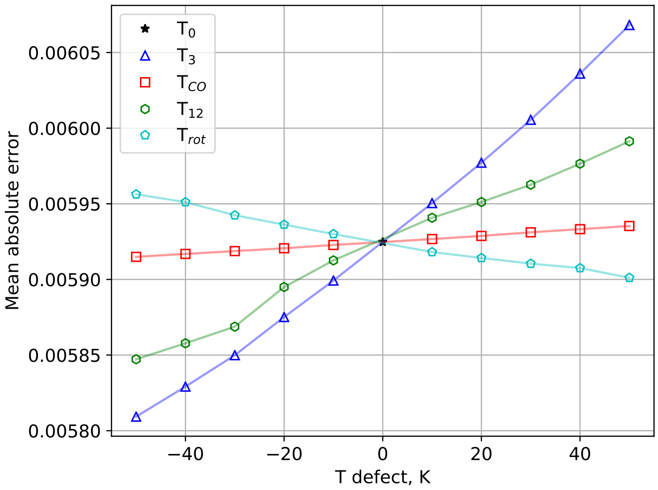

Figure 4.28: Mean absolute error versus temperature defect.

4.3 Recap

In this chapter the creation of a vibrationally-specific radiation database designated CDSDv, for CO_2 was presented. This database was refitted from a ro-vibrational specific database CDSD4000 and the general method for refitting is not specific to CO_2 and can be applied to other molecules. The refitting presents some advantages against ro-vibrational databases such as HITRAN, HITEMP and CDSD4000. Firstly, the reduction in size of the database, which is specially favorable for large databases like CDSD4000 which was reduced from several GB to a few MB in CDSDv. Secondly, the effective reduction of the number of ro-vibrational lines speeds up computations, is able to reproduce results using CDSD4000 or HITEMP and obtain estimates in high-temperature regimes. Thirdly, the vibrational specific nature of the database allows simplified separation of vibrational and rotational modes which is desirable for coupling radiation to kinetic calculations. Several test cases have been tested with CDSDv and yet more work has to be done. Sections 5.2 will detail the flaws and what remains to be done to improve CDSDv. The generated data is available in [245].

Chapter 5

Conclusions

> "*You shouldn't focus on this,*
> *in a few months time the CO_2 PES of <scientist> at <lab> will be ready...*
> *... and your work will be obsolete.*"
> - Several Researchers in several places,
> in 2016, 2017 and 2018

This chapter is discusses the impact of the models developed in the scope of this thesis. The main driver of this thesis is a somewhat niche application, spacecraft entering the atmosphere of Mars. Given the fickle nature of Space related activities funding and the ever sophistication of more complex models, it may be that this work will be obsolete in a shorter time than it took from start and finish. On the other hand, it may be that PES accurate, near-dissociation energies for CO_2 will only be feasible with vastly increased computational resources, and this work may remain at the cutting edge level for longer than anticipated. Still, it is the author's hope that this work might have contributed in some way, even if only as an inspiration to future works by other authors. Even so, a discussion on what needs to be done and on the possible pathways for improvement cannot be excluded from this work.

In fact, some approaches in this work are disruptive of the *status-quo* of CO_2 modelling, at least in some levels. In the kinetic model presented here, a more physically consistent approach to vibrational and dissociation processes of CO_2 has been introduced, with the use of the FHO theory and the explicit treatment of the excited $^3B_2$ state at the vibronic level. This more sophisticated dissociation modelling turns out to be overshadowed by the $CO_2 + O \longleftrightarrow CO + O_2$ exchange reaction, which by all evidence plays a key role in CO_2

dissociation. The inverse reaction might also have a significant effect on the recombination of CO_2, as will be discussed in section 5.1.5.

In CO_2 radiation, the calculation of broadening mechanisms by general expressions, instead of tabulated coefficients, allows greater flexibility and should be the standard when computing spectra from a mixture of gases. Furthermore, CDSDv has outperformed CDSD4000 in terms of size and memory, demonstrating the advantage of a smaller database at the cost of detail. The remainder of this chapter will be dedicated to the discussion of the two generated databases, flaws and work to come.

5.1 STELLAR CO_2 kinetic model

There are certainly shortcomings in the CO_2 FHO model, which may immediately be pointed out. Some inherent flaws originating from certain assumptions are also common to the models relying on simplified FOPT theories like SSH. Others should be addressed in future works or updates to this database and are summarized here.

5.1.1 Inclusion of different collision partners and state-to-state kinetics for diatomic molecules

The vibrational-translational effects in CO and O_2 atoms could be added for a further sophistication of the model. These rates have been reasonably well modeled in the past [111, 112]. Other simple improvements would be to account for collisional partners other than CO_2 in the model. This would require a straightforward review and calibration of the FHO model against further experimental rates, in the exact same fashion that was carried out in the development of the STELLAR-CO_2 database [201]. Nevertheless this will at most lead to a 5-fold increase of the number of rates in the model, so the real impact of these quality-of-life improvements in the model will have to be carefully weighted against its computational overhead.

5.1.2 Improved modeling of intermode vibrational transitions

The key shortcoming is undoubtedly the assumption for complete separability of the vibrational modes of CO_2. To include non-separated vibrational levels of CO_2 into this model several obstacles have to be lifted. Firstly, a manifold of mixed levels must be found. This has been done partially in [242] where a vibrationally specific level database for $CO_2(X)$ has been determined which reproduces the partition function of CO_2 by direct summation up to 4000 K within less than 1% error. For $CO_2(^3B_2)$ the same polynomial expression determined in this work will have to suffice while novel PES-based works are not made available. Secondly, the reduced masses of non-separated modes have to be determined. This difficulty could be overcome by writing the reactions in such a way that only a single mode is interacting $CO_2(v_1v_2v_3) + CO_2(v_1+1{,}0{,}0) \longleftrightarrow CO_2(v_1+1v_2v_3) + CO_2(v_10{,}0)$. While limiting, in the sense that only single quantum jumps can be modelled this way, it might become a first step in building a kinetic state to state model with no mode separability.

5.1.3 Accounting for resonant processes

By assuming full separability of the vibrational modes of CO_2 a series of so-called *accidental resonances* are neglected. These resonances arise in CO_2 and may effectively redistribute vibrational energy between the different modes. However, even considering the CO_2 *extreme states*, one may find out that a quite large number of these states might be near-resonant (with energy spacings below 100 cm^{-1}). One may apply a simplified Landau–Teller model to yield an additional set of near-resonant rates and deploy these in the model, according to the expression [267, 268, 201]:

$$\mathrm{K}'_{res}(T, \Delta E_v[\mathrm{cm}^{-1}]) = 1.57 \times 10^{-11} \exp\left\{\left[-\frac{(\Delta E_v)^2}{T}\right]^{1/3}\right\} [\mathrm{cm}^3/\mathrm{part./s}] \qquad (5.1)$$

While certainly not sufficient to account for the full effects of these accidental resonance effects, this may be a better approximation than neglecting those processes altogether. Another concept related to the redistribution of vibrational energy between different modes is the quasi-continuum of levels, where higher in the vibrational ladders levels can no longer be distinguished and form a practical energy continuum. This enables the application of the Fokker–Planck method as described briefly in section 5.1.6 and is also related to the concept of vibrational chaos discussed in section 5.1.7.

5.1.4 Inclusion of radiative processes

The inclusion of radiation of CO_2 may also be achieved by using the vibrationally-specific database developed in [242] and detailed in chapter 4 of this thesis. The database contains vibrational state-to-state Einstein coefficients which could be used by simply adding to the continuity equation the term $-A_{v'v''}N_{v'}$, which accounts for levels de-excitation through radiation losses. This would effectively model the escape of radiation from the gas. The addition of absorption and stimulated emission are also needed for full consistency. However it is easier to assume an optically thin medium than dealing with the spectral calculations required to account for the other radiative processes. This application however, is not so straightforward as one might think. The use of extreme states in this work implies some sort of adaptation for the published Einstein coefficients that could be achieved by some sort of binning. Even after binning and distribution of spontaneous emission effects on the vibrational ladder, important Einstein coefficients of IR radiation in CO_2 are in the order of $A_{v'v''} \approx 10^3$ s^{-1} as in fig. 5.1. The time-scale of interest for spontaneous emission effects is therefore higher than the vibrational kinetics time scale. As such, the inclusion of radiation might be moot for a lot of applications but significant in others. Appropriate methods for equating these general Einstein coefficients to the vibrational modes separability is currently underway.

5.1.5 Uncertainty in the $\mathbf{CO_2 + O \longleftrightarrow CO + O_2}$ process

As discussed in previously, the $CO_2 + O \longleftrightarrow CO + O_2$ reaction is essential for the decomposition of CO_2 and might as well also be critical in its recombination through the inverse process. The rates plotted in fig. 3.11 are in qualitative agreement over $8,000$ K but this agreement does not exist in lower temperature ranges. Most reactions surveyed in this work, both experimental and numerical are in qualitative agreement in the $1,000$ to $5,000$ K range. Only two rates estimate a much higher rate coefficient between $1,000$ to $5,000$ K, the Sulzmann [213] and Varga [218] rates both experimental. At first one might consider these rates as outliers and trust the cluster of results that are in agreement. However, the rate obtained by Varga was obtained by numerical optimization of 39 datapoints and is reported to have low uncertainty. As such, the relative agreement at lower temperatures for most of the reaction rates cannot be taken for granted. With a difference of over 9 orders of magnitude to other rates at $1,000$ K, it may be that this reaction has been underestimated by several authors in the low-temperature ranges. Given its importance to CO_2 chemical-kinetic processes, the emphasis on newer studies to obtain better estimates for this reaction should not be understated. Needless to say, a good quality PES-based quantum-chemistry analysis on this exchange process would significantly advance the insight on CO_2 dissociation processes.

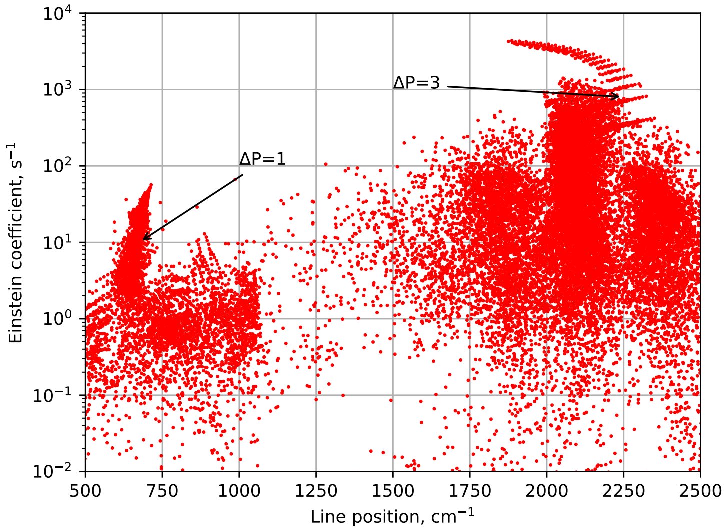

Figure 5.1: Line positions and respective Einstein coefficients of vibrational bands of CO_2 IR radiation. This figure focuses on the 15 and 4.3 μm regions of the CO_2 IR spectra located around 600 and 2400 cm^{-1} respectively. The arrows labeled ΔP= 1 and ΔP= 3 point towards the regions where polyad exchanges of that number are most common. The vibrational frequencies of CO_2 are related by $\omega_2 \approx \omega_3/3 \approx \omega_1/2$, and a pseudo-vibrational number may be written from the sum of the vibrational numbers from the so-called polyad, P= $2\mathrm{v}_1 + \mathrm{v}_2 + 3\mathrm{v}_3$. Vibrational bands can be organized in the spectrum by their polyad variation as in this figure. The ΔP= 1 and ΔP= 3 regions indicate a radiative decay of $\Delta \mathrm{v}_1$ and $\Delta \mathrm{v}_3$ respectively. Particularly the $\Delta \mathrm{v}_3$ decay might be an important inclusion in the continuity equation, owing to its high Einstein coefficients.

Furthermore, the inverse reaction $CO + O_2 \longleftrightarrow CO_2 + O$ might hold the key for the recombination of CO_2 at high-temperatures. In figure 5.2 the rate coefficients for the $CO + O_2 \longleftrightarrow CO_2 + O$ reaction are plotted. Reactions k_1, k_2 and k_{5-8} of table 3.5 are displayed along with the one reported by Baulch *et al.* [269] and a third STS reaction calculated by Sharipov [217]. The STS reactions by Sharipov are, ordered:

$$\mathrm{CO} + \mathrm{O_2}(\mathrm{X}^3\Sigma_g^-) \longleftrightarrow \mathrm{TS}_1 \longleftrightarrow \mathrm{CO_2} + \mathrm{O}(^3\mathrm{P}) \tag{5.2}$$

$$\mathrm{CO} + \mathrm{O_2}(\mathrm{X}^3\Sigma_g^-) \longleftrightarrow \mathrm{TS}_2 \longleftrightarrow \mathrm{CO_2} + \mathrm{O}(^1\mathrm{D}) \text{ or } \mathrm{O}(^3\mathrm{P}) \tag{5.3}$$

$$\mathrm{CO} + \mathrm{O_2}(\mathrm{a}^1\Delta\mathrm{g}) \longleftrightarrow \mathrm{CO_2} + \mathrm{O}(^1\mathrm{D}) \tag{5.4}$$

where the TS_1 and TS_2 are two pathways in the same collision, one leads to CO_2 + $\mathrm{O}(^3\mathrm{P})$ and the other has a 50:50 branching towards $CO_2 + \mathrm{O}(^3\mathrm{P})$ and $CO_2 + \mathrm{O}(^1\mathrm{D})$.

The third reaction was not considered for this work as it involved the metastable O_2(a) state, the inclusion of which would make the model even more intricate. Additionally, the T^n dependency on the provided rate would exceed the collisional rate violating physical consistency. But as may be seen in figure 5.2, the third Sharipov STS rate coefficient (eq. 5.4) is 6 orders magnitude greater than the other rates at $1,000$ K. Furthermore, between $2,000$ and $3,000$ K this rate is 3 to 2 orders of magnitude greater than the experimental rates measured by Baulch and Thielen and the rate determined by Varga[1], almost reaching a rate as high as Sulzmann's measurement. The metastability of the O_2(a) state and the greater reaction rate coefficient makes an compelling case for CO_2 recombination which occurs in the wakeflow of spacecraft entering Mars at a tipycal temperature of $2,000$ K. Additionally, the creation of excited O(^{1}D) atoms will redistribute the energy to the ro-vibrational modes of CO_2 as discussed in the review of Fox & Hác [220]. As such the study of the CO + O_2(a$^1\Delta$g) collision is a strong candidate for further studies. In the short term, a vibronically-specific O_2 description may be included in the current model [118], henceforth extending it to include the specific treatment to the (a$^1\Delta g$) state. This will undoubtedly increase the complexity of the model but not by too much, with at least $1,500+$ reactions added in.

5.1.6 Reduced order methods

Despite the inescapable assumption of full separability of the vibrational modes the fact still remains that this work's vibrationally-specific kinetic model yields an excess of 20,000 kinetic rates. This is simply not tractable for anything else than simplified 0D and 1D geometries. Therefore, the application of reduced order models appears as a natural next step for further deployments of this kinetic scheme. Interestingly, such numerical schemes have been actively discussed in recent years, with major strides advancing the theoretical state-of-the-art. Further, as these rely on a good quality set of kinetic data, the model in this work appears almost as tailor-made for the application of a reduced-order model as an additional layer. Two approaches are at the forefront of these reduced-order methods: Binning and Fokker–Planck methods

---

[1] The inversion of rates k_1, k_2 were made by other authors. k_1 was performed via an Arrhenius rate for the equilibrium constant [215]. Park [41] does not provide an inversion method for k_2. Rates k_{5-8} inversion were performed self-consistently through the partition function in the in-house code SPARK. As such it is strange that the Varga rate is now agreeing with the experimental rates measured by Baulch and Thielen. The inversion methods should be verified and checked for consistency in all cases.

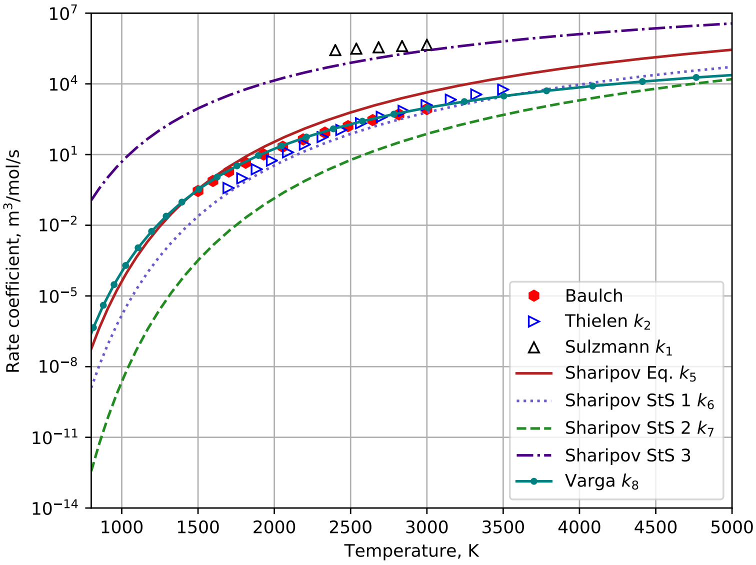

Figure 5.2: Reaction rate coefficients of the reaction $\mathrm{CO} + \mathrm{O}_2 \longleftrightarrow \mathrm{CO}_2 + \mathrm{O}$

- **Binning methods**: Binning is the process in which levels and processes are bundled together thereby reducing the number of de-facto individual states to be tracked in a state-to-state simulation making it more alike a macroscopic chemistry model. Some strategies and binning algorithms are described in [270, 271, 272, 195]. To build binned levels and processes, a state-to-state model has to be given as input. In Sahai's thesis [195] a CO_2 SSH based model with over $9,000$ levels (representing $9,000+$ ODEs to be solved) was reduced using a binning strategy to obtain a good match with state-to-state results using as few as 30 bins. The same methods have also been applied to N_2 system with over 9300 ro-vibrational levels with similar results as CO_2. Such a reduction of problem complexity is essential to the application of state-to-state databases to spatial problems of higher order such as 2D and 3D simulations.

- **Fokker–Planck methods**: Another method to obtain the vibrational distribution function of CO_2 is to replace the master equation by a drift-diffusion Fokker-Planck equation. This approach was already being developed in the 1970s and 80s [273, 274] and has been recently applied to CO_2 by a collaboration of authors [275, 276, 277, 278]. Instead of treating the levels of CO_2 as discrete, such as in the state-to-state approach, the states effectively become a continuum. This is a good approximation when levels may effectively be approximated to a continuum as is the case at the onset of *vibrational chaos* for CO_2. Again, this method does not preclude the estimation of state-to-state rates for higher-levels as these are still necessary in determining coefficients necessary to solve the Fokker-Planck equation. However once more this approximation is useful in reducing computational time, as it has been reported to be up to 1000 times faster than state-to-state simulations [278].

5.1.7 Further steps beyond the state-of-the-art

It should be apparent by now that the topic for this work is not considered closed by the improvements contained therein, no matter how meritorious these may be. Instead one may argue that this work exhausts the more simplified venues for modeling a complex polyatomic molecule such as CO_2. Although the expected theoretical trends are found for dissociative and recombinating flows, and although quite reasonable agreement is found against experimentally available shock-tube data, it may be well the case that further progress in the accuracy and predictability of vibrationally-specific CO_2 models may only be achieved if a *tabula-rasa* is made of the current approaches, and new theoretical descriptions for CO_2 are brought forward. This is particularly critical for a better understanding of high-vibrational levels and dissociation dynamics in triatomic molecules such as CO_2.

Insight may be found outside the more traditional views from the plasma chemistry community. A short review will follow on the recent quantum-chemistry works regarding the structure of higher-lying levels of polyatomic molecules.

Polyads and *quasi-continuum*

Before discussing the aforementioned short review, the concept of polyads should be introduced. The polyad is a useful concept when building spectroscopic Hamiltonians. There are several ways for defining the polyad but the most common (in CO_2) is the so-called "213" defined thus

$$P_{213} = 2\mathrm{v}_1 + \mathrm{v}_2 + 3\mathrm{v}_3. \tag{5.5}$$

The polyad number P may then be treated as a quantum number.

For higher polyad numbers P, a larger scattering of the energies for each individual $P + 1$ levels in the polyad is observed. This is shown in Fig. 5.3 where the energies of the different polyads are plotted against their quantum numbers, both for the perturbed (observed) levels of CO_2, and for the unperturbed levels (using Chedin's Hamiltonian [279]). As early as $P = 6 - 7$, overlapping between the vibrational energies of adjacent

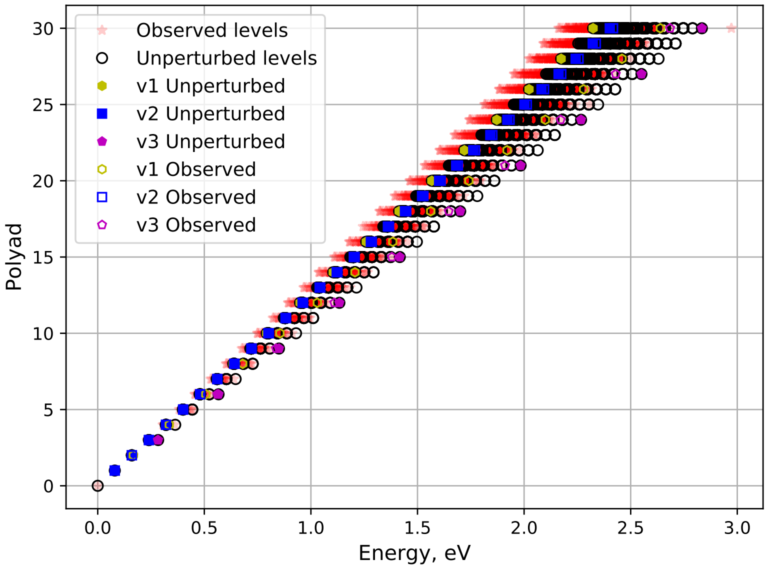

Figure 5.3: Energy levels of CO_2 in eV versus the polyad P for each level. Here the polyad of a level is computed as $P = 2\mathrm{v}_1 + \mathrm{v}_2 + 3\mathrm{v}_3$. This figure plots both observed levels in faded stars as well as the unperturbed levels of Chédin's polynomial [207]. Furthermore it highlights the extreme cases of pure v_1, v_2 and v_3 levels as used in this work, the perturbed and unperturbed values. This figure serves as an illustration of *vibrational quasi-continuum* whereas for a single high-enough energy, several polyads are crossed effectively meaning several combinations of v_1, v_2 and v_3 sharing the same symmetry or not have a similar energy. The energy need not be very high, at 1 eV polyads 11, 12 and 13 are crossed. The dissociation limit for the asymmetric mode of the ground electronic state of CO_2 is 7.42 eV and the chaos will only increase with higher energy up to dissociation.

polyads can be witnessed, up to overlapping from 4 different polyads for energies as low as 1.5 eV. This means that the grouping of levels in "lumped" resonant levels (polyads) starts failing [2] as soon as for about 10% of the effective dissociation of CO_2 (the $^3B_2$ level dissociation limit)[3].

In addition, the molecular dynamics for the different levels of a polyad might differ significantly, potentially affecting the transition probabilities in a collision. Kellman [280] carried out an analysis for the CO_2 molecule semiclassic dynamics up to $P = 8$, with an emphasis on the 2:1 Fermi resonance, using an algebraic resonance dynamics method. Trajectories for each individual quantum level were obtained in action-angle phase space, showing a varied structure. Although the strong Fermi resonance leads to the deviation of the molecule dynamics from its zero-order characteristics, as early as P=1, and up to P=8, it is also observed that different types of dynamics (so-called Type II, III, and IV) are observed for the internal quantum levels of a polyad. Then, it is not a big leap to question to which degree collisional dynamics may differ inside a polyad, and whether it is possible to lump the polyad levels for kinetic modeling applications. This highlights how much care should be brought into defining appropriate polyad conventions, capable of achieving more or less regular internal dyamics of the molecule.

For CO_2, different polyads have been proposed and successfully applied to the interpretation of CO_2 spectroscopic data. These include $P_{214} = 2\mathrm{v}_1+\mathrm{v}_2+4\mathrm{v}_3$, $P_{213} = 2\mathrm{v}_1+\mathrm{v}_2+3\mathrm{v}_3$, and $P_{212} = 2\mathrm{v}_1 + \mathrm{v}_2 + 2\mathrm{v}_3$. A recent analysis by Bermudez–Montaña et al. [281] shows that polyad-preserving Hamiltonians based on these three notations achieve an excellent fit of the available experimental data for the main isotopologue of CO_2 ($^{12}C^{16}O$), which goes up to 3.3 eV (26,550cm^{-1}). No clear distinction on the quality of the fit for each Hamiltonian was obtained, and hence no specific polyad scheme was recommended by the authors. In a later work, the same authors stated a preference for the "212" polyad with a similar upper limit on the fit, but did not make this preference a definitive conclusion [282].

The limits of validity for these fitted Hamiltonians corresponds to 56% for the crossing energy to the $^3B_2$ state, and 44% of the dissociation energy for the asymmetric stretch potential for the ground state. It is unlikely for these polyad-preserving Hamiltonians to faithfully reproduce highly, near-dissociative levels, where anharmonic terms increase sig-

---

[2] for this particular P_{213} polyad scheme

[3] The use of "fail" here is abusive: it should fail in the context of a state-to-state simulation where the polyad would soon cease to be a good quantum number.

nificantly. Yet, as no valid measurements or PES models exist for these energy regions of CO_2, this statement remains somewhat speculative. It might well be possible that the inclusion of polyad-breaking interactions, using Van Vleck perturbation theory [283] may be needed; or that phase-space Hamiltonians may prove more adequate in this energy region. Clearly, there is a strong necessity for more theoretical studies on the near-dissociative levels of CO_2.

Note that this concept has also been discussed by Fridman [65] in a simplified way, wherein he considers a transition to a *vibrational quasi-continuum* once the energy defect of the asymmetric mode, compared to the symmetric and bending modes, is "filled" due to anharmonicity effects, leading to additional resonance effects. This transition occurs in general for

$$x_{as} v_a v_s \geq \Delta\omega \tag{5.6}$$

where $x_{as} \simeq 12$ cm^{-1} is the asymmetric-symmetric anharmonicity coefficient; $v_a = \mathrm{v}_3$; $v_s = 2\mathrm{v}_1 + \mathrm{v}_2$; and $\Delta\omega = \Delta\omega_3 \simeq 300$ cm^{-1}. According to this expression, it is found that the energies corresponding to the critical v_a and v_s quantum numbers are in the 1.5-2.5 eV range. This is consistent with the observed results of figure 5.3 where different polyads start to mix energy-wise as soon as 1 eV. Fridman does note that the onset of vibrational *quasi-continuum* may be delayed up to higher energies, close to the dissociation limit, as long as the asymmetric vibrational temperature is higher than the symmetric/bending one ($T_{va} \gg T_{vs}$). However, in heavy-impact dominated flows such as shockwaves, with $T \gg T_v$, this is hardly the case, where the bending mode temperature increases the fastest, owing to the low energy spacings between adjacent v_2 levels, with v_1 lagging behind, and v_3 even lagging further behind, with no appreciable plateau observed in the *vdf* due to V–V–T transitions. The situation might be different for electron-impact dominated flows such as gas discharges, however this is outside the scope of this work. Still, as accidental resonances between the v_3 level and the other v_1 and v_2 modes may arise as early as 1–1.5 eV, the possibility for resonant transitions from v_3 towards the other modes counteracting the so-called *ladder-climbing* V–V–T processes, and therefore depleting the higher v_3 levels, make this a challenging proposition.

Vibrational chaos

In the last decades, polyad schemes in polyatomic molecules have been extensively discussed in relation to the concept of *vibrational chaos*, which has been brought forward for improving the description of high molecular vibrations, with some success stories, such as the modeling of higher vibrational motions of acetylene [284].

The theory of *vibrational chaos* starting point is the set of classical normal modes in the near-equilibrium configuration of polyatomic molecules (*ss*, *be*, and *as* modes of CO_2). The theory focuses on how new vibrational modes are born in bifurcations, or branchings, of these original low-energy normal modes. Original modes may still persist at these higher energies, but always in an altered form. Once a set of polyads for each energy space of CO_2 is agreed upon, a physically accurate kinetic model for CO_2 would necessarily proceed in a layered way: The departure point for the first electronvolt of energies would be based on the classical modes of CO_2, considering the extreme states in a similar way to the model proposed in this work (this model could even include the Fermi resonance, a preference in many works of CO_2 kinetics). Then, subsequent layers of kinetic models would follow the polyad schemes more adequate for each energy stage, with kinetic rates which allow energy flow inside a polyad, and block it among different polyads [284]. This work remains to be done, starting with a better description of the near-dissociative dynamics of CO_2, a challenge that can only be tackled by physical chemists.

An appropriate example can be found in the treatment of CS_2, which is a linear triatomic molecule such as CO_2. It is particularly suited to the study of *vibrational chaos* since it is molecule with heavy atoms (S) and as such has soft vibrational modes [285] ($v_1 =^{-1}$, $v_2 = 398$ cm^{-1}, $v_3 = 1559$ cm^{-1}, the CO_2 modes being, respectively 1334, 667 and 2349 cm^{-1}). Other characteristics that make CS_2 a very good candidate for studying *vibrational chaos* effects is the presence of strong Fermi resonances and anharmonicities, as well as the absence of low-lying excited electronic states that may interfere in the analysis [285]. The CS_2 molecule has a potential well of about 36,000 cm^{-1} [286], with regularly-spaced vibrational energy levels measured up to 18,000–20,000 cm^{-1} [285], which means levels up to about 50% of the dissociation energy of CS_2 are measured. This is in contrast with the more “chaotic” level structure of CO_2, which has been measured up to 25,000 cm^{-1}, 42% of the ground state asymmetric stretch dissociation limit (see section 3.3.1). The weaker Fermi 1:2 resonance of CS_2 allows showcasing a slow transition to chaotic behavior from the normal stretching and bending modes (the asymmetric stretch mode remaining unaffected) for increasing polyad numbers [286].

5.1.8 The need for further experimental data

This section is concluded by a short discussion on the possible new experiments that would allow better calibrating this theoretical model against experimental data. Since the chief concern is heavy-impact excitation and dissociation processes in CO_2, the best-suited facilities for such analyses are undoubtedly shock-tubes. Indeed, recent shock-tube experiments have already been considered for the calibration of this model [48, 49, 43, 237, 238, 239] and as an addition to this, an extensive amount of CO_2 broadband IR radiation measurements recently carried out in several test-campaigns related to Mars exploration missions in the NASA Ames EAST shock-tube [178, 179, 181, 182, 183, 184, 185]. These experiments yield datasets more tailored for the study of CO_2 radiation (not surprisingly since these are support campaigns for Martian planetary entry missions) rather than CO_2 dissociation. To the authors knowledge, the inherently high noise/signal ratio of shock-tubes (since these are impulsive facilities, with short acquisition times) precludes the acquisition of high-resolution spectra such as the one obtained in low-pressure, steady-state plasmas (e.g. FTIR spectra). Nevertheless, even broadband radiative signals without vibrational resolution may still be fitted spectroscopically, yielding meaningful results. A possibility that could be explored would be measuring the emission bands at 4.3 and 15 μm respectively, which yield information on the relative excitation of the asymmetric v_3 and symmetric v_1 modes, respectively. Although the former band has a strong signal in the aforementioned NASA Ames shock-tube experiments, to the author's knowledge no attempts have been made yet at measuring the 15 μm bands in CO_2, and owing to their low Einstein coefficients around 10^1–10^2 (see fig. 5.1), and these bands might be too diffuse to appear clearly over the background noise. On the other hand, the CO_2 4.3 μm has a certain amount of superposition with a CO band at 4.7 μm, which might hamper the interpretation of the measured experimental spectra, if it is carried out at low resolution (see fig. 5.4 and discussion ahead).

In the near-UV region, probing the CO_2 chemiluminescence (B→X) bands, yields information on the decomposition rate for CO_2. It is not possible to have absolute intensity measurements, as the transition is very diffuse and exact absorption coefficients for the transition are not known. Nevertheless, one may retrieve the rate for dissociation like in the VUT-1 experiments [236, 237, 238, 239, 240, 241], or the dissociation incubation times like in the works of Oehlschlaeger and Saxena [48, 49, 43].

Finally, other molecular radiative systems may further be considered. Further ARAS measurements (such as in Refs. [37, 38, 39, 40]) could be carried out in conditions properly tailored from numerical test-cases, allowing the experimental determination of O(^{3}P)/O(^{1}D) ratios, as an indication of the relative ratios for direct dissociation from the asymmetric stretch mode of the ground state (X$^1\Sigma$) of CO_2 versus transitions to the $^3B_2$ excited state and subsequent dissociation. Of particular interest would be the evolution of this ratio versus the shock speed (which induces higher translational excitation). The O_2 Schumann–Runge bands can be strong emitters and absorbers in the near-UV region, providing insight on atomic oxygen recombination into O_2 processes (through emission spectroscopy on the Schumann–Runge continuum), or insight on the time evolution of O_2 populations (through absorption spectroscopy on the Schumann–Runge discrete bands). The probing of the CO IR bands would also yield relevant information on the populations of one of the CO_2 dissociation products. For CO there is the fundamental band (Δv=-1) which emits around 4.7 μm, the first overtone band (Δv=-2) which emits around 2.35 μm, and the second overtone band (Δv=-3) which emits around 1.6 μm. The first band is often covered by the CO_2 asymmetric v_3 band at 4.3 μm, and the second overtone band is seldom observed due to its low intensity. This leaves us with the first overtone band, which may be observed without interference from CO_2 radiation. Since this band has a regular structure, high-resolution measurements might allow fitting the rotational bands with a synthetic line-by-line code, if the signal/noise ratio is high enough. Then, one would be able to determine the translational-rotational temperatures of the flow through fitting techniques. Fig. 5.4 presents a synthetic spectra of CO_2 and CO in equilibrium conditions at 3,000 K and 1 mbar pressure. A detail of the first overtone band of CO at 4300 cm^{-1} is also presented. It is also worth mentioning that microwave experiments can also achieve relevant conditions for the study of CO_2 kinetics as the ones mentioned in this paragraph. The work of Wolf *et al.* [287], for example, makes measurements on conditions not very unlike the ones suggested for the recombination case in section 3.4.2.

One key aspect of any experimental campaign is to have a more diversified array of shot conditions that allow reproducing slow to fast dissociation trends (with typical post-shock temperatures between 3,000 and 10,000 K) and near-equilibrium to strong non-equilibrium conditions (from 10 to 0.1 mbar pre-shock pressures). In terms of chemical compositions, the favoured approach would include the analysis of pure CO_2 shocked flows versus CO_2 flows highly diluted in an Ar carrier gas. The advantage for selecting Ar lies in its reduced mass which is quite close to CO_2. If similar aerothermodynamic conditions are achieved

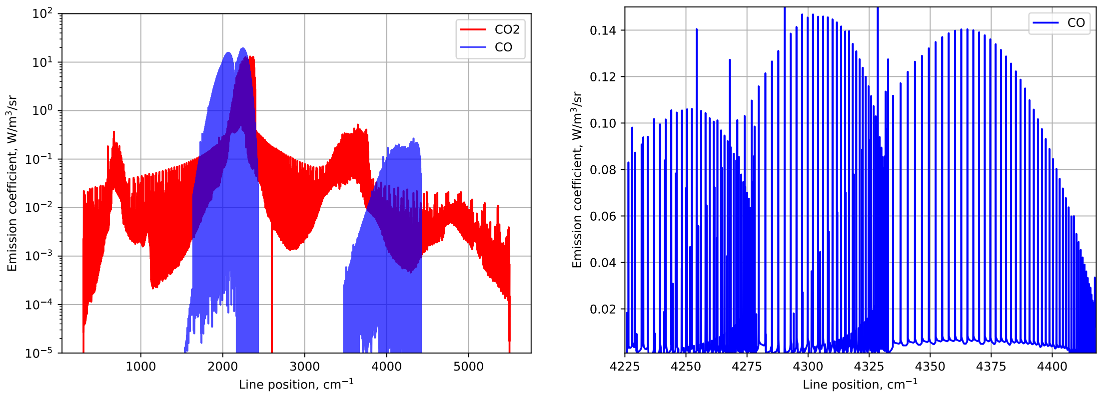

Figure 5.4: Left: Equilibrium CO_2 spectrum at 3000 K and 1 mbar, convolved with a 0.125 FWHM Gaussian Apparatus Function. The emission spectrum from CO_2 is reported in red, the one from CO is reported in blue. One may note the superposition of the fundamental band of CO and the CO_2 band in the 4.3–4.7 μm/2200–2500 cm^{-1}. The other CO_2 and CO bands are well enough separated. Right: Detail for the CO first overtone band (Δv=-2) where the rotational structure is well defined, making this a good candidate for monitoring the translational-rotational temperature in shocked flows.

(similar post-shock pressure p and temperature T) this will allow a comparison of the predictability of the kinetic model in this work with and without reactive transitions such as $CO_2 + O \longleftrightarrow CO + O_2$, since these last ones do not occur for a CO_2–Ar mixture, provided that CO_2 is present in residual concentrations only ($\sim$ 1%). Other lighter (He) or heavier (KrXe) dilution gases could be considered, but with a lower priority since the influence of the collisional partner of CO_2 in direct dissociation reactions has already been extensively studied in the past (see ref.[201] and references therein for a more detailed discussion).

The N-PRiME research group hosts a new generation shock-tube that has been developed in the past 10 years under funding by the European Space Agency, with the specific aim of providing Europe with a facility capable of carrying extensive investigations on non-equilibrium kinetic processes of shocked flows, for arbitrary chemical compositions. The performance mapping for the European Shock-Tube for High Enthalpy Research (ESTHER) has been recently carried out for all the Solar System planetary atmospheres [288], including Venus and Mars CO_2-N_2 atmospheres. The conditions of a Venus and a Mars entry, which are of interest for planetary exploration missions nicely dovetail with the objectives of this work, as these roughly correspond to the high-temperature and low-

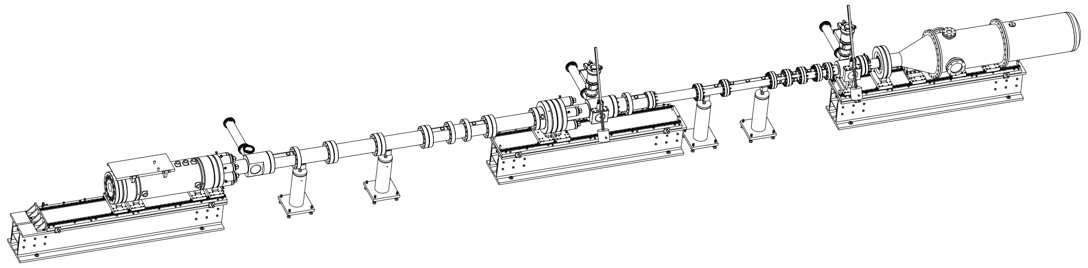

Figure 5.5: View of the European Shock-Tube for High Enthalpy Research. ESTHER is a two-stage, combustion driven shock-tube capable of reaching shock velocities in excess of 10km/s, deploying high-speed emission and absorption diagnostics (streak-cameras+spectrometers) in the VUV, Visible, near-IR, and MWIR spectral regions

temperature regimes of CO_2 (around 10,000 and 3000 K respectively). A research program on the kinetics of CO_2 shocked flows with interest for atmospheric entry applications is currently underway under funding from the European Space Agency [289], and some of the recommendations for novel experiments discussed here will be deployed in ESTHER (see fig. 5.5).

5.2 CDSDv radiative model

In regards to the radiation model, a method for refitting ro-vibrationally specific radiative databases in the format of HITRAN, HITEMP, and CDSD to a vibrationally specific format has been presented. This method has been applied to the refitting of CDSD4000 and the resulting database has been branded CDSDv. The use of these compact databases carries several advantages over the original ones:

- Both level and transition databases fit in an email attachment, two binary files 10.6 MB in total, 16.6 MB in ASCII format.
- The total number of ro-vibrational lines is greatly reduced in the main spectral regions of interest. For example, in the 4.3 μm region, the 81 million lines from CDSD4000 are reduced to 5 million lines in CDSDv.
- Possibility to separate vibrational and rotational modes with individual temperatures.

- This reduced number of lines leads to lesser computational overheads, namely regarding memory an processing power. While a full spectrum comparison could not be carried out in this work, due to the large size of CDSD4000, a standard laptop is able to simulate a full high-temperature CO_2 infrared spectra in a reasonable time using CDSDv.

- Several experimental and calculated results were adequately reproduced by CDSDv which may therefore be considered experimentally validated.

Naturally, a few disadvantages also exist:

- The reordering of the CDSD database from frequency-based to quantum transition based may in some cases be a disadvantage, such as in atmospheric sensing applications, where only a specific spectral window is of importance

- In addition to the loss of accuracy already mentioned, it is not possible to account for perturbations in the spectra using the presented method.

Owing to the aforementioned points, CDSDv is a database appropriate for the calculation of high-temperature, broadband CO_2 radiation, such as in the case of Mars atmospheric entries. In some cases it exceeds the performance of CDSD4000, which can be attributed to the more generic methods applied for the calculation of Lorentz broadening, whereas CDSD4000 is more limited in the gas mixtures selection, as regarding broadening mechanisms. In trying to reproduce other results, CDSDv sometimes failed to achieve an excellent match. Most notably, cases where CO_2 can be found at a relatively high-temperature are not always well reproduced by CDSDv. These results may be improved by reworking the averaging procedure, the refitting procedure in some circumstances and by including more transition data in regions where these might be lacking. As an example, preliminary tests have shown that extending the expressions for the Hermann–Wallis coefficients, namely adding a reciprocal term in equations 4.28-4.29 (in the form of C/J or $C/(J+1)$ where C is a fit parameter), may bring a non-negligible bands currently considered to be unfitable back to the fitable category. All of these changes will be postponed to a future version of CDSDv. The current version of CDSDv, is nevertheless considered mature enough to be of use to the community.

CDSDv is part of the libre code SPARK line-by-line. Both can be handed upon request [290].

5.2.1 Future Developments

The most ambitious outcome of this work would be a unified model for kinetics and radiation. This is only possible in simplified cases and using assumptions which restrict the analysis to more partial conclusions. However, there are still some venues which may provide additional insights or simply improve what has been done. The recombination of CO_2 is particularly important for the IR heating on the wakeflow of a spacecraft entering Mars. Therefore, the modelling of O_2 ground and the $(a^1\Delta_g)$ metastable states should be considered a priority for this application. This, combined with a reduced-order modelling approach, could be deployed into a higher-order simulation, and it would be relevant to check on the impact of this improved modeling on the predicted spacecraft wall convective and radiative heat fluxes. Many more subtleties between molecular and atomic oxygen interactions with CO_2 might be found, and this could prove to be just the beginning of a very complex task. The eventual wider scale availability of more complex methods, such as QCT, applied to CO_2 would put an end to these inquiries. Such complex models, if done with the proper care, could potentially establish themselves as the *de-facto* golden standard for STS kinetic models for CO_2. But until that time, the FHO model will still have time to shine.

The next challenge for the CDSDv database would be the fitting against experimental data, to obtain gas parameters from matching experimental and simulated spectra. At higher-temperatures and in spectral regions other than the 4.3 μm, this might not be possible without adding in more data. This turns out to be a very intensive, mind-numbing task which should be automated whenever possible. Additionally, many rates were deemed unfitable, but may become fitable with the addition of an additional Herman–Wallis term. The most interesting cases of comparing CDSDv to experimental spectra is when the radiating gas is not a pure mixture and thus, the broadening coefficients of ro-vibrational databases is not accurate. As such it would be particularly stimulating to use the CDSDv method in these cases, providing a different way to simulate IR spectra, not only for CO_2 but towards other species as well. All this, depending on a way to automate the refitting process.

Bibliography

[1] L. S. Rothman and L. D. G Young. “Infrared energy levels and intensities of carbon dioxide-II”. In: *J. Quant. Spectrosc. Radiat. Transf.* 25.6 (1981), pp. 505–524.

[2] G. Amat and M. Pimbert. “On Fermi resonance in carbon dioxide”. In: *J. Mol. Spectrosc.* 16.2 (1965), pp. 278–290.

[3] T. Kozák and A. Bogaerts. “Evaluation of the energy efficiency of CO_2 conversion in microwave discharges using a reaction kinetics model”. In: *Plasma Sources Sci. Technol.* 24.1 (2015), p. 015024.

[4] W. A. Rosser, E. Hoag, and E. T. Gerry. “Relaxation of excess populations in the lower laser level $CO_2(100)$”. In: *J. Chem. Phys.* 57.10 (1972), pp. 4153–4164.

[5] A. M. Brodnikovskii et al. “Two-photon Raman excitation of molecular vibrations; a new approach to the study of vibrational relaxation in polyatomic gases”. In: *Zh. Eksp. Teor. Fiz* 84.October 1982 (1983), pp. 1664–1676.

[6] G. Millot and C. Roche. “State-to-state vibrational and rotational energy transfer in CO_2 gas from time-resolved raman–infrared double resonance experiments”. In: *J. Raman Spectrosc.* 29.4 (1998), pp. 313–320.

[7] S. A. Losev. “Kinetics of vibrational energy exchange in carbon dioxide gas and its mixtures with other gases”. In: *Combust. Explos. Shock Waves* 12.2 (1976), pp. 141–155.

[8] D C. Allen, T. Scragg, and C. J. S. M. Simpson. “Low temperature fluorescence studies of the deactivation of the bend—stretch manifold of CO_2”. In: *Chem. Phys.* 51.3 (1980), pp. 279–298.

[9] T. Urbanietz et al. “Non-equilibrium excitation of CO_2 in an atmospheric pressure helium plasma jet”. In: *J. Phys. D. Appl. Phys.* 51.34 (2018).

[10] C. Stewig et al. “Excitation and dissociation of CO_2 heavily diluted in noble gas atmospheric pressure plasma”. In: *J. Phys. D. Appl. Phys.* 53.12 (2020).

[11] T. Urbanietz. private communication. 2020.

[12] R. A. McClatchey et al. *Atmospheric Absorption Line Parameters Compilation.* Tech. rep. Air Force Cambridge Research Laboratories (AFCRL), 1973.

[13] S. A. Tashkun et al. “CDSD-1000, the high-temperature carbon dioxide spectroscopic databank”. In: *Journal of Quantitative Spectroscopy and Radiative Transfer* 82.1 (2003). The HITRAN Molecular Spectroscopic Database: Edition of 2000 Including Updates of 2001., pp. 165–196.

[14] S A. Tashkun and V. I. Perevalov. “CDSD-4000: High-resolution, high-temperature carbon dioxide spectroscopic databank”. In: *J. Quant. Spectrosc. Radiat. Transf.* 112.9 (2011), pp. 1403–1410.

[15] I. E. Gordon et al. “The HITRAN2016 molecular spectroscopic database”. In: *J. Quant. Spectrosc. Radiat. Transf.* 203 (2017), pp. 3–69.

[16] B. L. M. Klarenaar et al. “Time evolution of vibrational temperatures in a CO_2 glow discharge measured with infrared absorption spectroscopy”. In: *Plasma Sources Sci. Technol.* 26.11 (2017).

[17] T. Kozák and A. Bogaerts. “Splitting of CO_2 by vibrational excitation in non-equilibrium plasmas: a reaction kinetics model”. In: *Plasma Sources Sci. Technol.* 23 (2014), p. 045004.

[18] T. Silva et al. “Modelling the input and relaxation of vibrational energy in CO_2 plasmas”. In: *J. Phys. D. Appl. Phys.* 51.46 (Nov. 2018), p. 464001.

[19] M. Grufolović et al. “Kinetic study of CO\$_2\$ plasmas under non-equilibrium conditions. II. Input of vibrational energy”. In: *Plasma Sources Sci. Technol.* 27.11 (2018).

[20] A. A. Likal’ter. “Relaxation of the symmetric vibration mode of the CO2 molecule”. In: *Zhurnal Prikl. Mekhaniki i Tekhnicheskoi Fiz.* 3 (1975), pp. 8–17.

[21] T. A. Brabbs, F. E. Belles, and S. A. Zlatarich. “Shock-tube study of carbon dioxide dissociation rate”. In: *J. Chem. Phys.* 38.8 (1963), pp. 1939–1944.

[22] W. O. Davies. “Carbon dioxide dissociation at 3500° to 6000°K”. In: *J. Chem. Phys.* 41.6 (1964), pp. 1846–1852.

[23] W. O. Davies. “Carbon dioxide dissociation at 6000° to 11,000°K”. In: *J. Chem. Phys.* 43.8 (1965), pp. 2809–2818.

[24] K. W. Michel et al. “Untersuchung des thermischen Zerfalls von CO_2 in Stoßwellen”. In: *Zeitschrift fur Phys. Chemie Neue Folge* 44 (1965), pp. 160–172.

[25] E. S. Fishburne, K. R. Bilwakesh, and R. Edse. “Gaseous reaction rates at high temperature. I. The dissociation of carbon dioxide”. In: *J. Chem. Phys.* 45.1 (1966), pp. 160–166.

[26] A. M. Dean. “Dissociation of carbon dioxide behind reflected shock waves”. In: *J. Chem. Phys.* 5202.1973 (1973), pp. 5202–5208.

[27] N. A. Generalov and S. Losev. “Vibrational Excitation and Decomposition of Molecular Oxygen and Carbon Dioxide Behind Shock Waves”. In: *J. Quant. Spectrosc. Radiat. Transf.* 6.1 (1966), pp. 101–125.

[28] J. H. Kiefer. “Densitometric measurements of the rate of carbon dioxide dissociation in shock waves”. In: *J. Chem. Phys.* 61.1 (1974), pp. 244–248.

[29] W. A. Hardy et al. “Neuere Untersuchungen zum thermischen Zerfall von CO_2 1. Teil”. In: *Berichte der Bunsengesellschaft fur Phys. Chemie* 78 (1974), pp. 76–82.

[30] H. G. Wagner and F. Zabel. “Neuere Untersuchungen Zum Thermischen Zerfall von CO_2. Teil II”. In: *Berichte der Bunsengesellschaft fur Phys. Chemie* 78 (1974), pp. 705–712.

[31] N. A. Ebrahim and R. J. Sandeman. “Interferometric studies of carbon dioxide dissociation in a free-piston shock tube”. In: *J. Chem. Phys.* 65.9 (1976), pp. 3446–3453.

[32] T. C. Clark and G. B. Kistiakowsky. “Effect of organic impurities on the observed activation energy of CO_2 dissociation”. In: *J. Chem. Phys.* 54.4 (1971), pp. 1726–1727.

[33] I. E. Zabelinskii, S. A. Losev, and O. P. Shatalov. “Some Techniques for Physical Experiments in a Shock Tube With a Nozzle”. In: *J. Eng. Phys.* 48.3 (1985), pp. 249–255.

[34] T. C. Clark, S. H. Garnett, and G. B. Kistiakowsky. “Reaction of carbon dioxide with atomic oxygen and the dissociation of carbon dioxide in shock waves”. In: *J. Chem. Phys.* 51.7 (1969), pp. 2885–2891.

[35] S. Baber, S. Charles, and A. M. Dean. “Reaction of atomic oxygen with carbon dioxide behind reflected shock waves”. In: *J. Chem. Phys.* 60.1 (1974), pp. 307–313.

[36] T. C. Clark, S. H. Garnett, and G. B. Kistiakowsky. “ Exchange Reaction of 18 O Atoms with CO_2 and with SO_2 in Shock Waves ”. In: *J. Chem. Phys.* 52.9 (1970), pp. 4692–4698.

[37] N. Fujii et al. “Study of the Thermal Dissociation of Nitrous Oxide and Carbon Dioxide Using Oxygen (^{3}P) Atomic Resonance Absorption Spectroscopy”. In: *J. Chem. Phys.* 93.14 (1989), pp. 5474–5478.

[38] M. Burmeister and P. Roth. “Aras measurements on the thermal decomposition of co2 behind shock waves”. In: *AIAA J.* 28.3 (1990), pp. 402–405.

[39] A. V. Eremin and V. S. Ziborov. “Nonequilibrium radiation from the CO_2 band (1B2 -X1σg/+) in shock-heated flows”. In: *Shock Waves* 3.1 (1993), pp. 11–17.

[40] A. V. Eremin, D. Woiki, and P. Roth. “Measurement of O(1D) formation during thermal decomposition of CO_2 behind shock waves”. In: *Shock Waves* 6.2 (1996), pp. 79–83.

[41] C. Park et al. “Review of chemical-kinetic problems of future NASA missions, II: Mars entries”. In: *J. Thermophys. Heat Transf.* 8.1 (1994), pp. 9–23.

[42] L. B. Ibragimova et al. “Dissociation of CO_2 molecules in a wide temperature range”. In: *High Temp.* 38.1 (2000), pp. 33–36.

[43] S. Saxena, J. H. Kiefer, and R. S. Tranter. “Relaxation, incubation, and dissociation in CO_2”. In: *J. Phys. Chem. A* 111.19 (2007), pp. 3884–3890.

[44] R. L. Jaffe. “Vibrational and Rotational Excitation and Dissociation of CO_2 Reexamined”. In: *49th AIAA Aerosp. Sci. Meet.* January. 2011, pp. 1–14.

[45] L. T. Xu et al. “The effect of the spin-forbidden CO(1Σ+) + O(3P) → CO_2(1Σg+) recombination reaction on afterbody heating of mars entry vehicles”. In: *47th AIAA Thermophys. Conf. 2017* June (2017), pp. 1–21.

[46] D. Weaner, J. F. Roach, and W. R. Smith. “Vibrational relaxation times in carbon dioxide”. In: *J. Chem. Phys.* 47.8 (1967), pp. 3096–3097.

[47] C. J. S. M. Simpson and T. R. D. Chandler. “Shock Tube Study of Vibrational Relaxation in Pure CO_2 and Mixtures of CO_2 With the Inert Gases, Nitrogen, Deuterium and Hydrogen”. In: *Proc. R. Soc.* 317.1529 (1970), pp. 265–277.

[48] M. A. Oehlschlaeger et al. “Carbon dioxide thermal decomposition: Observation of incubation”. In: *Zeitschrift fur Phys. Chemie* 219.5 (2005), pp. 555–567.

[49] M. A. Oehlschlaeger. “Shock Tube Studies of Thermal Decomposition Reactions Using”. PhD thesis. 2005.

[50] C. K. N. Patel. “Continuous-wave laser action on vibrational-rotational transitions of CO_2”. In: *Phys. Rev.* 136.5A (1964).

[51] C. B. Moore et al. “Vibrational energy transfer in CO_2 lasers”. In: *J. Chem. Phys.* 46.11 (1967), pp. 4222–4231.

[52] N. N. Sobolev and V. V. Sokovikov. “A mechanism ensuring level population inversion in CO_2 lasers”. In: *JETP Lett.* 4 (1966). transl. from *ZhETF Pis. Red.*, Vol. 4, 1966, pp. 303.

[53] N. N. Sobolev and V. V. Sokovikov. “Influence of rate of disintegration of the lower laser level on the power of a CO_2 laser”. In: *JETP Lett.* 5 (1967). transl. from *ZhETF Pis. Red.*, Vol. 5, 1967, pp. 122.

[54] N. N. Sobolev and V. V. Sokovikov. “Reviews of topical problems: CO_2 lasers”. In: *JETP Lett.* 10 (1967). translated from *Sov. Phys. Usp.*, Vol. 10, 1967, pp. 153–170.

[55] B. F. Gordiets, N. N. Sobolev, and L. A. Shelepin. “Kinetics of physical processes in CO_2 lasers”. In: *Soviet Journal of Experimental and Theoretical Physics* 26 (May 1968), p. 1039.

[56] R. L. Taylor and S. Bitterman. “Survey of Vibrational Relaxation Data for Processes Important in the CO_2-N_2 Laser System”. In: *Rev. Mod. Phys.* 41.1 (1969), pp. 26–47.

[57] R. D. Sharma and C. A. Brau. “Energy Transfer in Near-Resonant Molecular Collisions due to Long-Range Forces with Application to Transfer of Vibrational Energy from $\nu 3$ Mode of CO_2 to N_2”. In: *J. Chem. Phys.* 50.2 (1969), pp. 924–930.

[58] W. A. Rosser, A. D. Wood, and E. T. Gerry. “Deactivation of Vibrationally Excited Carbon Dioxide (v_3) by Collisions with Carbon Dioxide or with Nitrogen”. In: *The Journal of Chemical Physics* 50.11 (1969), pp. 4996–5008.

[59] J. Blauer and G. Nickerson. “A survey of vibrational relaxation rate data for processes importantto CO_2-N_2-H_2O infrared plume radiation”. In: *7th Fluid Plasma-Dynamics Conf.* Vol. 1. 1974.

[60] G. D. Billing. “Semiclassical calculation of energy transfer in polyatomic molecules I. the N_2+CO_2 system”. In: *Chem. Phys.* 41 (1979), pp. 11–20.

[61] S. A. Losev. “Kinetics of vibrational energy exchange in carbon dioxide gas and its mixtures with other gases”. In: *Combust. Explos. Shock Waves* 12.2 (1976), pp. 141–155.

[62] S. W. Bougher and D. M. Hunten. “CO_2 cooling in terrestrial planet thermospheres”. In: *J. Geophys. Res.* 99.E7 (1994), pp. 14609–14622.

[63] M. López-Puertas and F. W. Taylor. *Non-LTE radiative transfer in the atmosphere.* World Scientific, 2001, p. 504.

[64] R. I. Azizov et al. “Nonequilibrium plasmachemical process of CO_2 decomposition in a supersonic microwave discharge”. In: *Akad. Nauk SSSR Dokl.* 271 (Aug. 1983), pp. 94–98.

[65] A. A. Fridman. *Plasma chemistry.* Cambridge University Press, 2008, pp. 1–978.

[66] A. Bogaerts et al. “Plasma-based conversion of CO_2: Current status and future challenges”. In: *Farady Discuss.* 183 (2015), pp. 217–232.

[67] M. Capitelli and R. Celiberto. *Fundamental aspects of plasma chemical physics: kinetics.* Vol. 85. New York, NY: Spinger, 2016.

[68] J. F. De La Fuente et al. “A new methodology for the reduction of vibrational kinetics in non-equilibrium microwave plasma: Application to CO_2 dissociation”. In: *React. Chem. Eng.* 1.5 (2016), pp. 540–554.

[69] A. Berthelot and A. Bogaerts. “Modeling of plasma-based CO_2 conversion: Lumping of the vibrational levels”. In: *Plasma Sources Sci. Technol.* 25.4 (2016), p. 45022.

[70] H. S. Kwak et al. “Disintegration of Carbon Dioxide Molecules in a Microwave Plasma Torch”. In: *Sci. Rep.* 5 (2015), pp. 1–13.

[71] S. Heijkers and A. Bogaerts. “CO_2 cnversion in a gliding arc plasmatron: Elucidating the chemistry through kinetic modeling”. In: *J. Phys. Chem. C* 121.41 (2017), pp. 22644–22655.

[72] I. Belov et al. “Carbon dioxide dissociation in a microwave plasma reactor operating in a wide pressure range and different gas inlet configurations”. In: *J. CO_2 Util.* 24.November 2017 (2018), pp. 386–397.

[73] G. J. Van Rooij et al. “Taming microwave plasma to beat thermodynamics in CO_2 dissociation”. In: *Faraday Discuss.* 183 (2015), pp. 233–248.

[74] C. O. Laux et al. “Rotational temperature measurements in air and nitrogen plasmas using the first negative system of N2+”. In: *J. Quant. Spectrosc. Radiat. Transf.* 68.4 (2001), pp. 473–482.

[75] C. O. Laux et al. “Optical diagnostics of atmospheric pressure air plasmas”. In: *Plasma Sources Sci. Technol.* 12 (2003), p. 125.

[76] C. O. Laux, L. Pierrot, and R. J. Gessman. “State-to-state modeling of a recombining nitrogen plasma experiment”. In: *Chem. Phys.* 398.1 (2012), pp. 46–55.

[77] V. D. Rusanov et al. *Vibrational kinetics and reactions of polyatomic molecules in non-equilibrium systems.* ”Kurchatov Institute of Atomic Energy, Moscow, vol. 4201/6.”. 1985.

[78] V. D. Rusanov, A. A. Fridman, and G. V. Sholin. “Vibrational kinetics and reactions of polyatomic molecules in nonequilibrium systems”. In: *Nonequilibrium Vib. Kinet.* Ed. by Mario Capitelli. Berlin, Heidelberg: Springer Berlin Heidelberg, 1986, pp. 295–314.

[79] A. A. Levitsky. “Kinetics and mechanisms of chemical reactions, investigated by means of mathematical modeling”. USSR Academy of Sciences, Moscow. PhD thesis. Institute of Petrochemical Synthesis, 1978.

[80] A. A. Levitsky. “Investigation of elementary reaction O + N_2 using method of classical trajectories”. In: *New Aspects of Petrochemical Synthesis* (1978). Institute of Petrochemical Synthesis of USSR Academy of Sciences, Moscow.

[81] Yu. P. Butylkin, L. S. Polak, and D. I. Slovetsky. *High Energy Chemistry (Khimia Vysokikh Energij).* Sov. Phys. vol. 12, p. 526. 1978.

[82] Yu. P. Butylkin, A. A. Grinenko, and Yu. S. Ermin. *High Energy Chemistry (Khimia Vysokikh Energij).* Sov. Phys., vol 13, p.545. 1979.

[83] L. S. Polak, D. I. Slovetsky, and Yu. P. Butylkin. *Carbon dioxide dissociation in electric discharges: Arc discharge.* Institute of Petrochemical Synthesis, USSR Academy of Sciences, Moscow. 1977.

[84] V. A. Legasov et al. 2nd World Hydrogen Energy Conference, Zurich, vol. 3, p. 1183. 1978.

[85] V. A. Legasov et al. *Doklady (Reports of USSR Academy of Sciences)*. Sov. Phys., vol. 238, p. 66. 1978.

[86] V. A. Legasov, V. D. Rusanov, and A. A. Fridman. *Plasma Chemistry, vol. 5.* Smirnov, B.M. (ed.), Atom-Izdat, Moscow. 1978.

[87] V. A. Legasov et al. *Doklady (Reports of USSR Academy of Sciences)*. Sov. Phys., vol. 243, p. 323. 1978.

[88] A. K. Vakar et al. *3rd USSR Symposium on High Current Electronics.* Tomsk, Russia, p. 31. 1978.

[89] A. K. Vakar et al. *3rd USSR Symposium on High Current Pulse Electronics.* Academy of Sciences of the USSR, Tomsk, Russia, p. 31. 1978.

[90] A. A. Ivanov and V. A. Nikiforov. *Plasma Chemistry, vol. 5.* Smirnov, B.M. (ed.), Atom-Izdat, Moscow. 1978.

[91] V. A. Nikiforov. "Experiments with plasma-beam discharge; Chemically active plasma". Moscow. PhD thesis. Kurchatov Institute of Atomic Energy, 1979.

[92] R. I. Asisov, V. K. Givotov, and V. D. Rusanov. *3rd International Symposium on Plasma Chemistry.* Limoges, France, vol. 1, p. 51. 1977.

[93] Yu. P. Butylkin et al. *Journal of Technical Physics.* Sov. Phys., vol. 51, p. 925. 1981.

[94] R. I. Asisov et al. *5th International Symposium on Plasma Chemistry.* Edinburgh, UK, vol. 1, p. 52. 1981.

[95] R. I. Asisov et al. *5th International Symposium on Plasma Chemistry.* Edinburgh, UK, vol. 2, p. 774. 1981.

[96] R. I. Asisov et al. *Sov. Phys.* Doklady, vol. 271, p. 94. 1983.

[97] A. Ozkan et al. "CO_2-CH_4 conversion and syngas formation at atmospheric pressure using a multi-electrode dielectric barrier discharge". In: *J. CO_2 Util.* 9 (2015), pp. 74–81.

[98] W. Bongers et al. "Plasma-driven dissociation of CO_2 for fuel synthesis". In: *Plasma Process. Polym.* 14.6 (2017), pp. 1–8.

[99] E. V. Kustova, E. A. Nagnibeda, and I. Armenise. "Vibrational-Chemical Kinetics in Mars Entry Problems". In: *Open Plasma Phys. J.* 7.1 (2014), pp. 76–87.

[100] O. Achasov and D. Ragosin. “Rate constants of V-V exchange for CO_2”. In: *GDL* (1986). Preprint 16. Minsk, Bielarus: Institute of Heat and Mass Transfer.

[101] V. Joly, C. Marmignon, and P. Jacquet. “Vibrational relaxation of CO_2(m,n^l, p) in a CO_2-N_2 mixture. Part 2: Application to a one-dimensional problem”. In: *Aerosp. Sci. Technol.* 3.5 (1999), pp. 313–322.

[102] I. Armenise and E. V. Kustova. “State-to-state models for CO_2 molecules: From the theory to an application to hypersonic boundary layers”. In: *Chem. Phys.* 415 (2013), pp. 269–281.

[103] I. Suzuki. “General anharmonic force constants of carbon dioxide”. In: *J. Mol. Spectrosc.* 25.4 (1968), pp. 479–500.

[104] M. Lino da Silva, V. Guerra, and J. Loureiro. “A review of non-equilibrium dissociation rates and models for atmospheric entry studies”. In: *Plasma Sources Sci. Technol.* 18.3 (2009), p. 034023.

[105] R. N. Schwartz, Z. I. Slawsky, and K. F. Herzfeld. “Calculation of Vibrational Relaxation Times in Gases”. In: *J. Chem. Phys.* 20.1952 (1952), p. 1591.

[106] D. Rapp and T. E. Sharp. “Vibrational energy transfer in molecular collisions involving large transition probabilities”. In: *J. Chem. Phys.* 38.11 (1963), pp. 2641–2648.

[107] C. E. Treanor. “Vibrational energy transfer in high-energy collisions”. In: *J. Chem. Phys.* 43.2 (1965), pp. 532–538.

[108] E. H. Kerner. “Note on the forced and damped oscillator in quantum mechanics”. In: *Can. J. Phys.* 36.3 (1958), pp. 371–377.

[109] A. Zelechow, D. Rapp, and T. E. Sharp. “Vibrational–Vibrational–Translational Energy Transfer between Two Diatomic Molecules”. In: *J. Chem. Phys.* 49.1 (1968), pp. 286–299.

[110] I. V. Adamovich et al. “Vibrational relaxation and dissociation behind shock waves part 1: Kinetic Rate Models”. In: *AIAA J.* 33.6 (1995), pp. 1064–1069.

[111] I. V. Adamovich et al. “Vibrational energy transfer rates using a forced harmonic oscillator model”. In: *J. Thermophys. Heat Transf.* 12.1 (1998), pp. 57–65.

[112] M. Lino da Silva et al. “Vibrational distributions in N_2 with an improved calculation of energy levels using the RKR method”. In: *Chem. Phys.* 348.1-3 (2008), pp. 187–194.

[113] I. V. Adamovich and J. William Rich. “Three-dimensional nonperturbative analytic model of vibrational energy transfer in atom-molecule collisions”. In: *J. Chem. Phys.* 109.18 (1998), pp. 7711–7724.

[114] I. V. Adamovich. “Three-dimensional nonperturbative analytic model of vibrational energy transfer in molecule-molecule collisions”. In: *AIAA J.* 39.10 (2001), pp. 1916–1925.

[115] S. O. Macheret and I. V. Adamovich. “Semiclassical modeling of state-specific dissociation rates in diatomic gases”. In: *J. Chem. Phys.* 113.17 (2000), pp. 7351–7361.

[116] M. Lino da Silva, V. Guerra, and J. Loureiro. “State-resolved dissociation rates for extremely nonequilibrium atmospheric entries”. In: *J. Thermophys. Heat Transf.* 21.1 (2007), pp. 40–49.

[117] M. Lino da Silva, V. Guerra, and J. Loureiro. “Nonequilibrium dissociation processes in hyperbolic atmospheric entries”. In: *J. Thermophys. Heat Transf.* 21.2 (2007), pp. 303–310.

[118] M. Lino da Silva, J. Loureiro, and V. Guerra. “A multiquantum dataset for vibrational excitation and dissociation in high-temperature O_2-O_2 collisions”. In: *Chem. Phys. Lett.* 531 (2012), pp. 28–33.

[119] B. Lopez et al. “Coupled Hydrodynamic / State-Specific Excitation and Dissociation”. In: (2013), pp. 24–27.

[120] B. Lopez and M. Lino da Silva. “Non-Boltzmann analysis of hypersonic air re-entry flows”. In: *AIAA Aviat. 2014 -11th AIAA/ASME Jt. Thermophys. Heat Transf. Conf.* June (2014), pp. 1–19.

[121] M. Lino da Silva et al. “A Multiquantum State-to-State Model For The Fundamental States Of Air And Application To The Modelling Of High-Speed Shock Flows”. In: *5th International Workshop on the Radiation High Temperature Gases in Atmospheric Entry*. publicly available at http://esther.ist.utl.pt/pages/stellar.html. Oct. 2012.

[122] J. Counil, R. Bonneville, and F. Rocard. “The french involvement in Mars Sample Return program”. In: *34th COSPAR Scientific Assembly.* Vol. 34. COSPAR Meeting. 2002, p. 3166.

[123] B. Harvey. *Europe’s Space Programme: To Ariane and Beyond.* Springer Praxis Books. Springer London, 2003.

[124] P. Messina and D. Vennemann. “The European Space exploration programme: Current status of ESA’s plans for Moon and Mars exploration”. In: *Acta astronautica* 57.2-8 (2005), pp. 156–160.

[125] P. Reynier. “Survey of aerodynamics and aerothermodynamics efforts carried out in the frame of Mars exploration projects”. In: *Progress in Aerospace Sciences* 70 (2014), pp. 1–27.

[126] R. C Blanchard and G. D. Walberg. “Determination of the hypersonic-continuum/rarefied-flow drag coefficient of the Viking lander capsule 1 aeroshell from flight data”. In: *NASA Technical Paper 1793* (1980).

[127] R. N. Ingoldby et al. “Entry data analysis for viking landers 1 and 2 final report”. In: *NASA CR-159388* (1976).

[128] J. Beck. *EXOMARS Aerodynamics and Aerothermodynamics: Viking Flowfield Calculations for Radiative Assessment.* Tech. rep. ESA, EXM-DM-AE-FGE-RAD01, 2010.

[129] M. Lino da Silva. *EXOMARS Aerodynamics and Aerothermodynamics Assesment of the Radiative Heat Fluxes on the VIKING Spacecraft Backcover.* Tech. rep. ESA, EXM-DM-TNO-IST-0001, 2011.

[130] R. N. Gupta, K. P. Lee, and C. D. Scott. “Aerothermal Study of Mars Pathfinder Aeroshell”. In: *Journal of Spacecraft and Rockets* 33.1 (1996), pp. 61–69.

[131] B. R. Hollis and J. N. Perkins. “Hypervelocity aeroheating measurements in wake of Mars mission entry vehicle”. In: *Fluid Dynamics Conference.* 1995.

[132] B. R. Hollis and J. N. Perkins. “High-Enthalpy Aerothermodynamics of a Mars Entry Vehicle Part 1: Experimental Results”. In: *Journal of Spacecraft and Rockets* 34.4 (1997), pp. 449–456.

[133] K. Edquist et al. “Aerothermodynamic Environments Definition for the Mars Science Laboratory Entry Capsule”. In: vol. 20. Jan. 2007.

[134] B. R. Hollis and S. Borrelli. *Aerothermodynamics of blunt body entry vehicles: Assessment of aerothermodynamic flight prediction tools through ground and flight experimentation.* Tech. rep. RTO - NATO Technical Report, 2011. Chap. 3.

[135] W. O'Neil and C. Cazaux. "Mars Sample Return Project". In: *Acta astronautica* 47 (July 2000), pp. 453–65.

[136] H. Fraysse et al. "CNES-NASA studies of the mars sample return orbiter aerocapture phase". In: *51st International Astronautical Congress* (2000).

[137] R. Bonneville, F. Rocard, and J.-L. Counil. "French involvement in Mars exploration". In: *Acta Astronautica* 51.1 (2002), pp. 329–335.

[138] E. Chabut. "Simulation aérothermodynamique en régime d'écoulement raréfié par méthode de Monte-Carlo". Thèse de doctorat Physique des gaz et des plasmas Orléans 2005. PhD thesis. Université d'Orléans, 2005, 1 vol. (318 p.)

[139] M. Lino da Silva. "Simulation des Propriétés Radiatives du Plasma Entourant un Véhicule Traversant une Atmosphère Planétaire à Vitesse Hypersonique: Application à La Planète Mars". PhD thesis. Université d'Orléans, 2004.

[140] B. Warmbein, ed. *Proceedings of the First International Workshop on Radiation of High Temperature Gases in Atmospheric Entry.* ESA Publications Division, Dec. 2003.

[141] K. Fletcher, ed. *Proceedings of the First International Workshop on Radiation of High Temperature Gases in Atmospheric Entry - Part II.* ESA Publications Division, May 2005.

[142] A. Wilson, ed. *Proceedings of the 2nd International Workshop on Radiation of High Temperature Gases in Atmospheric Entry.* ESA Publications Division, Nov. 2006.

[143] H. Lacoste and L. Ouwehand, eds. *Proceedings of the 3rd International Workshop on Radiation of High Temperature Gases in Atmospheric Entry.* ESA Publications Division, Jan. 2009.

[144] H. Lacoste-Francis, ed. *Proceedings of the 4th International Workshop on Radiation of High Temperature Gases in Atmospheric Entry.* ESA Publications Division, Feb. 2011.

[145] L. Ouwehand, ed. *Proceedings of the 5th International Workshop on Radiation of High Temperature Gases in Atmospheric Entry.* ESA Publications Division, Dec. 2012.

[146] *6th International Workshop on Radiation of High Temperature Gases in Atmospheric Entry.* Nov. 2014.

[147] *7th International Workshop on Radiation of High Temperature Gases in Atmospheric Entry.* Nov. 2016.

[148] *8th International Workshop on Radiation of High Temperature Gases in Atmospheric Entry.* Mar. 2019.

[149] J. M. Charbonnier et al. "Definition of an Axially Symmetric Testcase for High Temperature Gas Radiation Prediction in Mars Atmosphere Entry". In: *Rapport CNES NG104-07-TF-001-CNES* (2003).

[150] J. M. Charbonnier. "Analysis of the results for TC3 presented at the 1st International Workshop on Radiation of High Temperature Gas in Planetary Atmosphere Entry". In: *Radiation of High Temperature Gases in Atmospheric Entry.* Vol. 533. 2003, pp. 145–159.

[151] O. Rouzaud et al. "Numerical, analytical and experimental investigation of convective and radiative heating of a martian descent module". In: *Radiation of High Temperature Gases in Atmospheric Entry.* Ed. by K. Fletcher. Vol. 583. ESA Special Publication. May 2005, p. 93.

[152] I. Egorov, V. Borovoy, and V. Skuratov. "Afterbody Convective Heating of a Martian Descent Vehicle". In: *48th AIAA Aerospace Sciences Meeting Including the New Horizons Forum and Aerospace Exposition.*

[153] A. Soufiani and J. Taine. "High temperature gas radiative property parameters of statistical narrow-band model for H2O, CO_2 and CO, and correlated-K model for H_2O and CO_2". In: *International Journal of Heat and Mass Transfer* 40.4 (1997), pp. 987–991.

[154] M. B. E Aguir, M. Y Perrin, and J. Taine. "Variational Calculation of Energies of Highly Excited Rovibrational States of 12C16O2". In: *Journal of Molecular Spectroscopy* 215.2 (2002), pp. 234–243.

[155] D. Scutaru, L. Rosenmann, and J. Taine. “Approximate intensities of CO_2 hot bands at 2.7, 4.3, and 12μm for high temperature and medium resolution applications”. In: *Journal of Quantitative Spectroscopy and Radiative Transfer* 52.6 (1994), pp. 765–781.

[156] M. Y. Perrin, P. Rivière, and A. Soufiani. *Radiation Database for Earth and Mars Entry.* Tech. rep. RTO - NATO Technical Report, 2008.

[157] P. Rivière, A. Soufiani, and M. Y. Perrin. “Line by line and statistical narrowband calculations of radiative transfer in some atmospheric entry problems”. In: *European Space Agency, (Special Publication) ESA SP* 533 (Nov. 2003), pp. 189–196.

[158] V. Gromov and S. Surzhikov. “Convective and Radiative Heating of a Martian Space Vehicle Base Surface”. In: *Proceedings of the Fourth Symposium on Aerothermodynamics for Space Vehicles.* Ed. by R. A. Harris. Vol. 487. ESA Special Publication. Feb. 2002, p. 265.

[159] S. T. Surzhikov. “Numerical Simulation of Heat Radiation Generated by Entering Space Vehicle”. In: *37th AIAA Thermophysics Conference.*

[160] S. T. Surzhikov. “Radiative-gasdynamic model of a Martian descent space vehicle”. In: *42nd AIAA Aerospace Sciences Meeting and Exhibit.* 2004.

[161] S. T. Surzhikov. “TC3: Convective and radiative heating of MSRO for simplest kinetic models”. In: *Proceedings of the First International Workshop on Radiation of High Temperature Gases in Atmospheric Entry - Part II.* Ed. by K. Fletcher. Vol. 583. ESA Special Publication. May 2005, p. 55.

[162] D. Andrienko and S. T. Surzhikov. “Radiative heating of Martian space vehicle at crucial points of trajectory”. In: *49th AIAA Aerospace Sciences Meeting including the New Horizons Forum and Aerospace Exposition.* 2011, p. 246.

[163] S. T. Surzhikov. “Comparative analysis of radiative aerothermodynamics of Martian entry probes”. In: *43rd AIAA Thermophysics Conference.* 2012, p. 2867.

[164] C. Flament. “Écoulements de fluide visqueux de desequilibre chimique et vibrationnel modélisation, applications internes et externes”. Thèse Doctorat Physique Paris 6 1990. PhD thesis. Université Pierre et Marie Curie, 1990.

[165] J. William. “Etude des processus physico-chimiques dans les écoulements détendus à haute enthalpie application à la soufflerie à arc F4”. Thèse de doctorat Physique Aix-Marseille 1 1999. PhD thesis. Université de Provence, 1999, 2 vol., 622 f.

[166] L. Tessé. “Modélisation des transferts radiatifs dans les flammes turbulentes par une méthode de Monte Carlo”. Thèse de doctorat Energétique Châtenay-Malabry. PhD thesis. Ecole centrale de Paris, 2001, 1 vol. (158 p.)

[167] L. Tessé et al. “Radiative transfer in real gases using reciprocal and forward Monte Carlo methods and a correlated-k approach”. In: *International Journal of Heat and Mass Transfer* 45.13 (2002), pp. 2797–2814.

[168] L. Tessé, F. Dupoirieux, and J. Taine. “Monte Carlo modeling of radiative transfer in a turbulent sooty flame”. In: *International Journal of Heat and Mass Transfer* 47.3 (2004), pp. 555–572.

[169] O. Rouzaud et al. “Influence of Radiative Heating on a Martian Orbiter”. In: *Journal of Thermophysics and Heat Transfer* 22.1 (2008), pp. 10–19.

[170] M. Lino da Silva. “An adaptive line-by-line-statistical model for fast and accurate spectral simulations in low-pressure plasmas”. In: *J. Quant. Spectrosc. Radiat. Transf.* 108.1 (2007), pp. 106–125.

[171] M. Lino da Silva and B. Lopez. *SPARTAN 3.0 User Manual.* 2019.

[172] L. S. Rothman et al. “The HITRAN molecular database: Editions of 1991 and 1992”. In: *J. Quant. Spectrosc. Radiat. Transf.* 48.5-6 (1992), pp. 469–507.

[173] M. Lino da Silva. “A Contribution for the Simulation of VUV-IR Radiation Transfer in CO$_2$-N$_2$ Entry Flows Using a Line-By-Line Model”. In: *Proc. 4th Int. Work. Radiat. High Temp. Gases Atmos. Entry.* Vol. 689. 2011.

[174] O. Witasse et al. “Mars EXPRESS observation of the PHOENIX entry: simulations, planning, results and lessons learned”. In: *CEAS Space Journal* 6 (Feb. 2014).

[175] J. Beck et al. “Radiative Heating of the ExoMars Entry Demonstrator Module”. In: *Proceedings of the 7th European Symposium on Aerothermodynamics* (Aug. 2011), p. 9.

[176] M. Lino da Silva and J. Beck. “Contribution of CO_2 IR Radiation to Martian Entries Radiative Wall Fluxes”. In: *49th AIAA Aerospace Sciences Meeting Including the New Horizons Forum and Aerospace Exposition.* Jan. 2011.

[177] A. Gülhan et al. “Aerothermal Measurements from the ExoMars Schiaparelli Capsule Entry”. In: *Journal of Spacecraft and Rockets* 56.1 (2019), pp. 68–81.

[178] D. Bogdanoff. “Shock Tube Experiments for Earth and Mars Entry Conditions”. In: *Non-Equilibrium Gas Dynamics - From Physical Models to Hypersonic Flights, The Research and Technology Organisation (RTO) of NATO. Educational Notes, 2009* (Jan. 2009).

[179] B. Cruden, D. Prabhu, and R. Martinez. “Absolute Radiation Measurement in High Mass Venus and Mars Entry Conditions”. In: *Journal of Spacecraft and Rockets* 49 (Nov. 2012), pp. 1069–1079.

[180] R. L. Sundberg, J. W. Duff, and L. S. Bernstein. “Nonequilibrium infrared emission model for the wake flow of re-entry vehicles”. In: *Journal of Spacecraft and Rockets* 30.6 (1993), pp. 731–741.

[181] G. Palmer and B. Cruden. “Experimental Validation of CO_2 Radiation Simulations”. In: June 2012.

[182] B. Cruden, A. M. Brandis, and D. Prabhu. “Measurement and Characterization of Mid-wave Infrared Radiation in CO_2 Shocks”. In: June 2014.

[183] A. M. Brandis et al. “Radiative Heating on the After-Body of Martian Entry Vehicles”. In: *45th AIAA Thermophysics Conference.*

[184] B. Cruden et al. “Radiative Heating for MSL Entry: Verification of Simulations from Ground Test to Flight Data”. In: *53rd AIAA Aerospace Sciences Meeting.*

[185] A. M. Brandis et al. “Simulation of the Schiaparelli Entry and Comparison to Aerothermal Flight Data”. In: *AIAA Aviation 2019 Forum.* 2019.

[186] M. Born and R. Oppenheimer. “Zur Quantentheorie der Molekeln”. In: *Annalen der Physik* 389.20 (1927), pp. 457–484.

[187] M. Born and J. R. Oppenheimer. “On the Quantum Theory of Molecules”. In: *Ann. Phys.* 84.458 (1927). Translated by S. M. Blinder.

[188] D. Giordano. “Impact of the Born-Oppenheimer approximation on aerothermodynamics”. In: *J. Thermophys. Heat Transf.* 21.3 (2007), pp. 647–657.

[189] G.G. Chernyi et al. *Physical and Chemical Processes in Gas Dynamics: Cross Sections and Rate Constants for Physical and Chemical Processes Volume II.* Vol. 53. 9. 2002, pp. 1689–1699.

[190] Landau, L. and Teller, E. In: *Physik Zeitschrift der Sowjetunion* 10 (1936), pp. 34–38.

[191] J. Loureiro and J. Amorim. *Kinetics and Spectroscopy of Low Temperature Plasmas.* Springer International Publishing, 2016.

[192] H. W. Drawin and F. Emard. "Optical Escape Factors for Bound-bound and Free-bound Radiation from Plasmas. I. Constant Source Function". In: *Beiträge aus der Plasmaphys.* 13.3 (1973), pp. 143–168.

[193] R. L. Macdonald et al. "Construction of a coarse-grain quasi-classical trajectory method. I. Theory and application to N2-N2 system". In: *J. Chem. Phys.* 148.5 (2018).

[194] R. L. Macdonald et al. "Construction of a coarse-grain quasi-classical trajectory method. II. Comparison against the direct molecular simulation method". In: *J. Chem. Phys.* 148.5 (2018).

[195] A. Sahai. "Reduced-Order Modeling of Non-Boltzmann Thermochemistry and Radiation for Hypersonic Flows". PhD thesis. University of Illinois at Urbana-Champaign, 2019.

[196] J. Annaloro. "Modèles collisionels-radiatifs appliqués aux situations d'entrée atmosphérique martienne et terrestre". PhD thesis. University of Rouen, 2013.

[197] T. L. Cottrell and N Ream. "Transition probability in molecular encounters. Part 1. The evaluation of perturbation integrals". In: *Trans. Faraday Soc.* 51 (1955), pp. 159–171.

[198] E. E. Nikitin and A. I. Osipov. "Vibrational Relaxation in Gases". In: *Kinet. Catal.* 4.VINITI - All-Union Institute of Scientific and Technical Information (1977).

[199] I. V. Adamovich et al. "Vibrational Relaxation and Dissociation behind Shock Waves Part 2: Master Equation Modeling". In: *AIAA J.* 33.6 (1995), pp. 1070–1075.

[200] E. E. Nikitin. "Nonadiabatic transitions: what we learned from the old masters and how much we owe them". In: *Annu. Rev. Phys. Chem.* 50 (1999), pp. 1–21.

[201] M. Lino da Silva, J. Vargas, and J. Loureiro. *STELLAR CO_2 version 2: A database for vibrationally-specific excitation and dissociation rates for Carbon Dioxide*. Tech. rep. Available at http://esther.ist.utl.pt/stellar/STELLAR-CO2.pdf. Instituto Superior Técnico, 2018, pp. 1–30.

[202] D. Rapp and T. Kassal. “The theory of vibrational energy transfer between simple molecules in nonreactive collisions”. In: *Chem. Rev.* 69.1 (1969), pp. 61–102.

[203] J. T. Yardley, ed. *Introduction to Molecular Energy Transfer.* Academic Press, 1980.

[204] X. Huang et al. “An isotopic-independent highly accurate potential energy surface for CO 2 isotopologues and an initial 12C 16O 2 infrared line list”. In: *J. Chem. Phys.* 136.12 (2012).

[205] H. M. Hulburt and J. O. Hirschfelder. “Potential energy functions for diatomic molecules”. In: *J. Chem. Phys.* 9.1 (1941), pp. 61–69.

[206] W. Quapp and B. P. Winnewisser. “What you thought you already knew about the bending motion of triatomic molecules”. In: *J. Math. Chem.* 14.1 (1993), pp. 259–285.

[207] A. Chedin. “The carbon dioxide molecule. Potential, spectroscopic, and molecular constants from its infrared spectrum”. In: *J. Mol. Spectrosc.* 76.1-3 (1979), pp. 430–491.

[208] S. Y. Grebenshchikov. “Infrared Spectra of Neutral Bent Carbon Dioxide”. In: *J. Phys. Chem. A* 121.22 (2017), pp. 4296–4305.

[209] A. Spielfiedel et al. “Bent valence excited states of CO_2”. In: *J. Chem. Phys.* 97.11 (1992), pp. 8382–8388.

[210] D. Y. Hwang and A. M. Mebel. “Ab initio study of spin-forbidden unimolecular decomposition of carbon dioxide”. In: *Chem. Phys.* 256.2 (2000), pp. 169–176.

[211] T. Silva et al. “Kinetic study of low-temperature CO\$_2\$ plasmas under non-equilibrium conditions. I. Relaxation of vibrational energy”. In: *Plasma Sources Sci. Technol.* 27.1 (2018), pp. 0–12.

[212] B. A. Cruden, A. M. Brandis, and M. E. Macdonald. “Characterization of CO thermochemistry in incident shockwaves”. In: *2018 Jt. Thermophys. Heat Transf. Conf.* (2018), pp. 1–22.

[213] K. G. P. Sulzmann, B. F. Myers, and E. R. Bartle. “ CO Oxidation. I. Induction Period Preceding CO_2 Formation in Shock-Heated CO–O_2–Ar Mixtures ”. In: *J. Chem. Phys.* 42.11 (1965), pp. 3969–3979.

[214] K. Thielen and P. Roth. “Stoßtwellenuntersuchungen zum Start der Reaktion CO + O2”. In: *Berichte der Bunsengesellschaft für Phys. Chemie* 87.10 (1983), pp. 920–925.

[215] K. Schofield. “An evaluation of kinetic rate data for reactions of neutrals of atmospheric interest”. In: *Planet. Space Sci.* 15.4 (1967), pp. 643–664.

[216] L. B. Ibragimova. “Recommended rate constants of CO + O_2 reversible CO_2 + O reactions”. In: *Khim. Fiz.* 10 (1991), pp. 307–310.

[217] A. S. Sharipov and A. M. Starik. “Theoretical study of the reaction of carbon monoxide with oxygen molecules in the ground triplet and singlet delta states”. In: *J. Phys. Chem. A* 115.10 (2011), pp. 1795–1803.

[218] T. Varga. “Optimization and uncertainty quantification of hydrogen and syngas combustion models”. PhD thesis. Eötvös Loránd University, 2017.

[219] D. Husain and A. N. Young. “Kinetic investigation of ground state Carbon Atoms, C(2^3Pj)”. In: *J. Chem. Soc. Faraday Trans. 2 Mol. Chem. Phys.* 71.February (1975), pp. 525–531.

[220] J. L. Fox and A. B. Hać. “Escape of O(^{3}P), O(^{1}D), and O(^{1}S) from the Martian atmosphere”. In: *Icarus* 300 (2018), pp. 411–439.

[221] E. J. Dunlea and A. R. Ravishankara. “Kinetic studies of the reactions of O(^{1}D) with several atmospheric molecules”. In: *Phys. Chem. Chem. Phys.* 6.9 (2004), pp. 2152–2161.

[222] J. H. Yee, S. L. Guberman, and A. Dalgarno. “Collisional quenching of O(^{1}D) by O(^{3}P)”. In: *Planet. Space Sci.* 38.5 (1990), pp. 647–652.

[223] P. H. Wine and A. R. Ravishankara. “Kinetics of O(^{1}D) interactions with the atmospheric gases N_2, N_2O, H_2O, H_2, CO_2, and O_3”. In: *Chem. Phys. Lett.* 77.1 (1981), pp. 103–109.

[224] R. J. Donovan and D. Husain. “Recent advances in the chemistry of electronically excited atoms”. In: *Chem. Rev.* 70.4 (1970), pp. 489–516.

[225] J. A. Davidson et al. “Absolute rate constant determinations for the deactivation of O(^{1}D) by time resolved decay of O(^{1}D) - O(^{3}P) emission”. In: *J. Chem. Phys.* 64 (1976).

[226] R. K. Hanson. “Shock-tube study of carbon monoxide dissociation kinetics”. In: *J. Chem. Phys.* 4970.August 1973 (1974), pp. 4970–4976.

[227] A. R. Fairbairn. “The dissociation of carbon monoxide”. In: *Proc. R. Soc.* 312 (1969), pp. 207–227.

[228] J. Warnatz. “Rate Coefficients in the C/H/O System”. In: *Combust. Chem.* Ed. by William C Gardiner. New York, NY: Springer New York, 1984, pp. 197–360.

[229] Park, C. *Nonequilibrium Hypersonic Aerothermodynamics.* John Wiley & Sons, New York, 1989.

[230] Ph. Teulet et al. “One-dimensional hydro-kinetic modelling of the decaying arc in air-PA66-copper mixtures: II. Study of the interruption ability”. In: *J. Phys. D. Appl. Phys.* 42.18 (2009).

[231] C. Park. “Review of chemical-kinetic problems of future NASA missions, I: Earth entries”. In: *J. Thermophys. Heat Transf.* 7.3 (1993), pp. 385–398.

[232] G. D. Billing. “Semiclassical calculation of energy transfer in polyatomic molecules VI. On the theory for linear triatomic molecules”. In: *Chem. Phys.* 61 (1981), pp. 415–430.

[233] B. Lopez and M. Lino da Silva. “SPARK: A Software Package for Aerodynamics, Radiation and Kinetics”. In: *46th AIAA Thermophysics Conference.* 2016.

[234] L. Santos Fernandes, B. Lopez, and M. Lino da Silva. “Computational fluid radiative dynamics of the Galileo Jupiter entry”. In: *Physics of Fluids* 31.10 (2019), p. 106104.

[235] D. Gonçalves et al. “Adaptation of SPARK to Atmospheric-Pressure Micro-Plasma Jets flow conditions”. In: *ESCAMPIG XXV, Paris, France.* 2020.

[236] E. M. Anokhin. “Physical and Chemical Relaxation Behind Strong Shock Waves in CO_2–N_2 Mixtures”. PhD thesis. Moscow Institute of Physics and Technology (MIPT), 2005.

[237] A. Chikhaoui et al. *Support during the MIPT Shock Tube Calibration.* Tech. rep. European Space Agency, 2008, pp. 1–49.

[238] J. Beck. *CFD validation in a CO_2 environment: synthesis report.* Tech. rep. Emsworth, UK: Fluid Gravity Report CR012/08, 2008.

[239] P. Reynier, M. Bugel, and A. Smith. "Survey of European and major ISC facilities for supporting Mars and sample return mission aerothermodynamics and tests required for thermal protection system and dynamic stability". In: *Int. J. Aerosp. Eng.* 2011.i (2011).

[240] E. M. Anokhin et al. "Dynamics of radiation in a CO:N_2 mixture behind strong shock waves". In: *High Temp. (Teplofizika Vysokikh Temperatur)* 45.6 (2007), pp. 807–813.

[241] E. M. Anokhin, T. Yu Ivanova, and A. Yu Starikovskii. "Energy Spectral Distribution Behind Strong Shock Waves in CO:N_2 Mixture". In: *45th AIAA Aerosp. Sci. Meet. Exhib.* Jan. 2007.

[242] J. Vargas, B. Lopez, and M. Lino da Silva. "CDSDv: A compact database for the modeling of high-temperature CO_2 radiation". In: *J. Quant. Spectrosc. Radiat. Transf.* 245 (2020), p. 106848.

[243] J. Tennyson et al. "The ExoMol database: Molecular line lists for exoplanet and other hot atmospheres". In: *J. Mol. Spectrosc.* 327 (2016), pp. 73–94.

[244] L. S. Rothman et al. "HITEMP, the high-temperature molecular spectroscopic database". In: *J. Quant. Spectrosc. Radiat. Transf.* 111.15 (2010), pp. 2139–2150.

[245] P. Passarinho and M. Lino da Silva. "GPRD, a database for the spectral properties of diatomic molecules of atmospheric interest". In: *J. Mol. Spectrosc.* 236.1 (2006). available at: http://esther.ist.utl.pt/gaspar, pp. 148–149.

[246] O. K. Voitsekhovskaya, D. E. Kashirskii, and V. S. Korchikov. "Determination of dunham coefficients and calculation of the energies of highly excited vibrational-rotational levels of the carbon monoxide molecule in the electronic ground state". In: *Moscow Univ. Phys. Bull.* 65.5 (2010), pp. 386–391.

[247] P. F. Bernath. *Spectra of Atoms and Molecules.* Oxford University Press, 2016.

[248] V. M. Osipov. "Partition sums and dissociation energy for $^{12}C^{16}O_2$ at high temperatures". In: *Mol. Phys.* 102.16-17 (2004), pp. 1785–1792.

[249] J. Vargas et al. “Refitting of detailed CO_2 IR databases to vibrationally specific databases tailored for aerothermodynamic flows”. English (US). In: *2018 Joint Thermophysics and Heat Transfer Conference.* American Institute of Aeronautics and Astronautics Inc, AIAA, Nov. 2018.

[250] E. E. Whiting. “An empirical approximation to the Voigt profile”. In: *Journal of Quantitative Spectroscopy and Radiative Transfer* 8.6 (1968), pp. 1379–1384.

[251] J. J. Olivero and R. L. Longbothum. “Empirical fits to the Voigt line width: A brief review”. In: *Journal of Quantitative Spectroscopy and Radiative Transfer* 17.2 (1977), pp. 233–236.

[252] D. F. Potter. *Photaura User Guide.* 2013.

[253] X. Zhu. “An improved voigt line approximation for the calculations of equivalent width and transmission”. In: *J. Quant. Spectrosc. Radiat. Transf.* 39.6 (1988), pp. 421–427.

[254] Smith, A. J and Gogel, T and Vandevelde, P. *Plasma radiation database PARADE, Final Report.* Tech. rep. ESTEC Contract 11148/94/NL/FG, TR28/ 96, Apr. 1996.

[255] S. N. Mikhailenko, Yu. L. Babikov, and Golovko V. F. “Information-calculating system Spectroscopy of Atmospheric Gases. The structure and main functions.” In: *Atmospheric and oceanic optics* 18.9 (2005), pp. 685–695.

[256] A. Lemal et al. “Simulations of Carbon-Dioxide Equilibrium Infrared Radiation Measurements”. In: *Journal of Thermophysics and Heat Transfer* 32.1 (2018), pp. 184–195.

[257] H. Takayanagi et al. “Measurements of Carbon Dioxide Nonequilibrium Infrared Radiation in Shocked and Expanded Flows”. In: *Journal of Thermophysics and Heat Transfer* 32 (Apr. 2018), pp. 483–494.

[258] E. Pannier and C. O. Laux. “RADIS: A nonequilibrium line-by-line radiative code for CO_2 and HITRAN-like database species”. In: *J. Quant. Spectrosc. Radiat. Transf.* 222-223 (2019), pp. 12–25.

[259] E. Pannier and C. O. Laux. “Analysis of the JAXA Nonequilibrium Infrared Emission Spectra for Mars Entry Conditions”. In: *Journal of Thermophysics and Heat Transfer* (May 2019), pp. 1–5.

[260] B. A. Cruden et al. “Radiative heating during mars science laboratory entry: Simulation, ground test, and flight”. In: *J. Thermophys. Heat Transf.* 30.3 (2016), pp. 642–650.

[261] E. S. Lee, Chul Park, and K. S. Chang. “Shock-Tube Determination of CN Formation Rate in a CO-N_2 Mixture”. In: *Journal of Thermophysics and Heat Transfer* 21.1 (2007), pp. 50–56.

[262] Cruden, B. A. *Test-case for Mid-Infrared Radiation Prediction in MSL-Similar Shock Tube Test.* 2019.

[263] S. Depraz, M. Y. Perrin, and A. Soufiani. “Infrared emission spectroscopy of CO2 at high temperature. Part I: Experimental setup and source characterization”. In: *J. Quant. Spectrosc. Radiat. Transf.* 113.1 (2012), pp. 1–13.

[264] S. Depraz et al. “Infrared emission spectroscopy of CO2 at high temperature. Part II: Experimental results and comparisons with spectroscopic databases”. In: *J. Quant. Spectrosc. Radiat. Transf.* 113.1 (2012), pp. 14–25.

[265] A. S. Morillo-Candas et al. “Oxygen atom kinetics in CO2 plasmas ignited in a DC glow discharge”. In: *Plasma Sources Sci. Technol.* 28.7 (2019).

[266] A. S. Morillo-Candas. “Investigation of fundamental mechanisms of CO2 plasmas”. prepared at LPP. PhD thesis. École Polytechnique, 2019.

[267] L. Landau and E. Teller. *L. D. Landau. Collection of Papers [in Russian].* Vol. 1, Moscow, pp. 181–188. 1969.

[268] V. V. Nevdakh, L. N. Orlov, and N. S. Leshenyuk. “Temperature dependence of the vibrational relaxation rate constants of CO_2 (00^01) in binary mixtures”. In: *J. Appl. Spectrosc.* 70 (2003), pp. 276–284.

[269] Baulch, D. L. and Drysdale, D. D. and Duxbury, J. and Grant, S. J. *Evaluated Kinetic Data for High-Temperature Reactions Vol 3: Homogeneous Gas Phase Reactions of the O_2-O_3 system, CO-O_2-H_2 system and of Sulphur-containing species.* Buttersworth, Toronto, 1976.

[270] Y. Liu et al. “General multi-group macroscopic modeling for thermo-chemical non-equilibrium gas mixtures”. In: *J. Chem. Phys.* 142.13 (2015), pp. 1–18.

[271] A. Sahai et al. “Adaptive coarse graining method for energy transfer and dissociation kinetics of polyatomic species”. In: *J. Chem. Phys.* 147.5 (2017).

[272] A. Sahai et al. “Flow-radiation coupling in CO2 hypersonic wakes using reduced-order non-Boltzmann models”. In: *Phys. Rev. Fluids* 4.9 (2019), p. 93401.

[273] V. D. Rusanov, A A. Fridman, and G. V. Sholin. “Population of vibrationally excited states of diatomic molecules in a nonequilibrium plasma in the diffusion approximation”. In: *Sov. Phys. Tech. Phys* 24.3 (1979).

[274] V. D. Rusanov, A. A. Fridman, and G. V. Sholin. “The Physics of a Chemically Active Plasma With Nonequilibrium Vibrational Excitationc of Molecules”. In: *Sov. Phys. - Uspekhi* 24.6 (1981), pp. 447–474.

[275] P. Diomede, M. C. M. Van De Sanden, and S. Longo. “Insight into CO2 Dissociation in Plasma from Numerical Solution of a Vibrational Diffusion Equation”. In: *J. Phys. Chem. C* 121.36 (2017), pp. 19568–19576.

[276] P. Diomede, M. C. M. Van De Sanden, and S. Longo. “Vibrational Kinetics in Plasma as a Functional Problem: A Flux-Matching Approach”. In: *J. Phys. Chem. A* 122.39 (2018), pp. 7918–7923.

[277] S. Longo, M. C. M. van de Sanden, and P. Diomede. “Fokker–Planck equation for chemical reactions in plasmas”. In: *Rend. Lincei* 30.1 (2019), pp. 25–30.

[278] P. Viegas et al. “Validation of the Fokker-Planck Approach to Vibrational Kinetics in CO2 Plasma”. In: *J. Phys. Chem. C* 123.37 (2019), pp. 22823–22831.

[279] A. Chedin and J. L. Teffo. “The carbon dioxide molecule: A new derivation of the potential, spectroscopic, and molecular constants”. In: *J. Mol. Spectrosc.* 107.2 (1984), pp. 333–342.

[280] M. E. Kellman and E. D. Lynch. “Fermi resonance phase space structure from experimental spectra”. In: *J. Chem. Phys.* 85.12 (1986), pp. 7216–7223.

[281] M. Bermudez-Montaña et al. “Comprehensive vibrational analysis of CO2 based on a polyad-preserving model”. In: *Eur. Phys. J. D* 71.6 (2017), pp. 1–8.

[282] M. Bermúdez-Montaña et al. “An algebraic alternative for the accurate simulation of CO2 Raman spectra”. In: *J. Raman Spectrosc.* April 2019 (2020).

[283] M. Sánchez-Castellanos and R. Lemus. “A systematic polyad breaking approach to anharmonic systems”. In: *J. Phys. B At. Mol. Opt. Phys.* 41.17 (2008).

[284] M. E. Kellman and V. Tyng. “The dance of molecules: New dynamical perspectives on highly excited molecular vibrations”. In: *Acc. Chem. Res.* 40.4 (2007), pp. 243–250.

[285] J. P. Pique et al. “Spectroscopy, dynamics, and chaos of the CS2 molecule: Fourier transform and phase-space analysis”. In: *J. Chem. Phys.* 95.12 (1991), pp. 8744–8752.

[286] C. Zhou et al. “Quantum calculation of highly excited vibrational energy levels of CS_2(X) on a new empirical potential energy surface and semiclassical analysis of 1:2 Fermi resonance”. In: *Spectrochimica Acta Part A: Molecular and Biomolecular Spectroscopy* 58.4 (2002), pp. 727–746.

[287] A. J. Wolf et al. “CO_2 Conversion in Nonuniform Discharges: Disentangling Dissociation and Recombination Mechanisms”. In: *J. Phys. Chem. C* 124.31 (2020), pp. 16806–16819.

[288] D. Luis. “Mapping of the aerodynamic performance of the ESTHER shock-tube”. MA thesis. Lisbon, Portugal: Instituto Superior Técnico, Universidade de Lisboa, 2018.

[289] *ESA Contract No. 4000118059/16/NL/KML/fg, Standard kinetic models for CO_2 dissociating flows.* 2016.

[290] *SPARK Line-by-line code.* `http://esther.ist.utl.pt/sparklbl/`.

[291] H. Khun, H.-D. Försterling, and D. H. Waldeck. *Principles of Physical Chemistry, 2nd Edition.* Wiley, 2009.

[292] V. B. Leonas. “Studies of Short-range Intermolecular Forces”. In: *Soviet Phys. - Uspekhi* 15.3 (1973).

[293] S. Bock, E. Bich, and E. Vogel. “A new intermolecular potential energy surface for carbon dioxide from ab initio calculations”. In: *Chem. Phys.* 257.2-3 (2000), pp. 147–156.

[294] A. Biryukov et al. “Relaxation of the vibrational energy of the (00^01) level of the CO_2 molecule”. In: *Sov. J. Exp. Theor. Phys.* 39 (1974), pp. 1248–1257.

[295] George C. Schatz and M. J. Redmon. “A quasiclassical trajectory study of collisional excitation in $O(^3P)+CO_2$”. In: *Chem. Phys.* 58 (1981).

[296] D. C. Clary. “Quantum study of vibrational excitation in the three-dimensional collisions of CO2 with rare gas atoms”. In: *J. Chem. Phys.* 75.1 (1981), pp. 209–219.

[297] J. O. Chu, G. W. Flynn, and R. E. Weston. “Spectral distribution of CO_2 vibrational states produced by collisions with fast hydrogen atoms from laser photolysis of HBr”. In: *J. Chem. Phys.* 78.6 (1983), pp. 2990–2997.

[298] R. M. Siddles, G. J. Wilson, and C. J. S. M. Simpson. “Modes of CO_2 measured down to 140 K”. In: *Chem. Phys.* 189 (1994), pp. 779–791.

[299] N. M. Harvey. “A quantum mechanical investigation of vibrational energy transfer in $O(^3P) + CO_2$ Collisions”. In: *Chem. Phys. Lett.* 88.6 (1982), pp. 553–558.

[300] M. P. De Lara-Castells et al. “Vibrational quenching of $CO_2(010)$ by collisions with $O(^3P)$ at thermal energies: A quantum-mechanical study”. In: *J. Chem. Phys.* 124.16 (2006), pp. 1–10.

[301] K. J. Castle et al. “Vibrational relaxation of $CO_2(v_2)$ by $O(^3P)$ in the 142-490 K temperature range”. In: *J. Geophys. Res. Sp. Phys.* 117.4 (2012), pp. 1–6.

[302] R. E. Center. “Vibrational relaxation of CO_2 by O atoms”. In: *J. Chem. Phys.* 3523 (1973), pp. 3523–3527.

[303] I. Armenise and E. Kustova. “Mechanisms of Coupled Vibrational Relaxation and Dissociation in Carbon Dioxide”. In: *J. Phys. Chem. A* 122.23 (2018), pp. 5107–5120.

[304] T. G. Kreutz, J. A. O’Neill, and G. W. Flynn. “Diode laser absorption probe of vibration-vibration energy transfer in CO_2”. In: *J. Phys. Chem.* 91.22 (1987), pp. 5540–5543.

[305] M. D. Thomason. “PhD. Thesis”. LA9420-T. PhD thesis. University of Virginia, Los Alamos National Laboratory, 1982.

[306] N. S. Leshenyuk, V. V. Nevdakh, and L. N. Orlov. “Vibrational Relaxation in a CO_2-N_2 mixture”. In: *J. Appl. Spectrosc.* 34.6 (1981).

[307] D. J. Miller and R. C. Millikan. “Vibration-Vibration Energy Exchange Between Carbon Monoxide and Carbon Dioxide”. In: *Chem. Phys.* 6 (1974), pp. 317–324.

Appendix A

Fluid governing equations

A.1 Time and Space Marching governing equations

The mass, momentum and energy conservation equations are:

$$\frac{\partial \rho c_i}{\partial t} + \nabla \cdot (\rho \boldsymbol{v} c_i) = \dot{\omega}_i \tag{A.1}$$

$$\frac{\partial \rho \boldsymbol{v}}{\partial t} + \nabla \cdot (\rho \boldsymbol{v} \boldsymbol{v}) = -\nabla p \tag{A.2}$$

$$\frac{\partial \rho E}{\partial t} + \nabla \cdot (\rho H \boldsymbol{v}) = 0 \tag{A.3}$$

where ρ and p are the density and pressure of the gas, c_i and $\dot{\omega}_i$ are the mass fraction and the mass production rate of species i, $\boldsymbol{v}$ is the velocity of the gas and E and H are the total energy and enthalpy of the gas respectively. To obtain the system of equations corresponding to the time-marching solution of the flow, the spatial derivatives are set to zero and the following system is obtained:

$$\frac{\partial \rho c_i}{\partial t} = \dot{\omega}_i \tag{A.4}$$

$$\frac{\partial \rho \varepsilon}{\partial t} = 0 \tag{A.5}$$

where ε is the sum of the internal energies of the system. The total gas density of the system is fixed as the ideal gas relation must hold $p = \rho R_{spe} T$ where R_{spe} is not the universal gas constant but the specific gas constant which is equal to the ratio of the universal gas constant divided by the molar mass of the mixture R/M. Since the gas is ideal, the internal energy of the gas is given by:

$$\varepsilon = C_V^f T \tag{A.6}$$

where C_V^f is the mixtures heat capacity at volume constant is:

$$C_V^f = \sum_i c_i C_{V,i}. \tag{A.7}$$

The system of equations can then be written as

$$\frac{\partial c_i}{\partial t} = \frac{\dot{\omega}_i}{\rho}, \tag{A.8}$$

$$C_V^f \frac{\partial T}{\partial t} + T\frac{\partial C_V^f}{\partial t} = 0. \tag{A.9}$$

Replacing the definition of the heat capacity of the mixture and the first equation on the second the final system of equations is obtained in terms of primitive variables c_i and T,

$$\frac{\partial c_i}{\partial t} = \frac{\dot{\omega}_i}{\rho}, \tag{A.10}$$

$$\frac{\partial T}{\partial t} = -\frac{\sum\limits_i \dot{\omega}_i \varepsilon_i}{\rho C_V^f} \tag{A.11}$$

where ε_i is the internal energy of species i.

The spatial relaxation system of equations is obtained by setting the time derivatives of the conservation equations to zero and assuming a one dimension flow

$$\frac{\partial \rho v c_i}{\partial x} = \dot{\omega}_i \tag{A.12}$$

$$\frac{\partial \rho v^2}{\partial x} = -\frac{\partial p}{\partial x} \tag{A.13}$$

$$\frac{\partial \rho v H}{\partial x} = 0 \tag{A.14}$$

In this derivation it is more useful to go step by step on the derivation of each equation. As such, starting with the mass conservation equation it is obtained:

$$c_i\left[v\frac{\partial \rho}{\partial x} + \rho\frac{\partial v}{\partial x}\right] + \rho v\frac{\partial c_i}{\partial x} = \dot{\omega}_i \tag{A.15}$$

The first term on the LHS equates to zero. This is a consequence of the total mass of the system being conserved, meaning ρv is a constant and as such the term inside the square brackets must be zero. As such, this is reduced to simply:

$$\frac{\partial c_i}{\partial x} = \frac{\dot{\omega}_i}{\rho v}. \tag{A.16}$$

Next, in the energy conservation equation the total enthalpy is separated into the kinetic and thermodynamic contributions:

$$\rho v\left[\frac{\partial h}{\partial x} + v\frac{\partial v}{\partial x}\right] = 0 \tag{A.17}$$

where h is the "traditional" enthalpy equal to $e + pV$. The enthalpy in a perfect gas is also defined by $h = \sum_i c_i h_i = \sum_i c_i C_{P,i} T = C_P^f T$, where h_i is the enthalpy of species i. The partial derivative of the enthalpy can then be expanded thus:

$$\frac{\partial h}{\partial x} = \frac{\partial}{\partial x}\left[\sum_i c_i h_i\right] = C_P^f \frac{\partial T}{\partial x} + \sum_i h_i \frac{\dot{\omega}_i}{\rho v} \tag{A.18}$$

and substituting back to equation A.17 it is obtained:

$$v\frac{\partial v}{\partial x} + C_P^f \frac{\partial T}{\partial x} = -\sum_i h_i \frac{\dot{\omega}_i}{\rho v}. \tag{A.19}$$

The energy conservation equation is left aside for now and the derivation moves to the momentum conservation equation which can be expressed as:

$$\rho v \frac{\partial v}{\partial x} + \frac{\partial p}{\partial x} = 0 \tag{A.20}$$

by remembering that ρv is a flow constant. From the ideal gas state equation $p = \rho R_{spe} T$, the second term can be developed:

$$\frac{1}{p}\frac{\partial p}{\partial x} = \frac{1}{\rho}\frac{\partial \rho}{\partial x} + \frac{1}{R_{spe}}\frac{\partial R_{spe}}{\partial x} + \frac{1}{T}\frac{\partial T}{\partial x}. \tag{A.21}$$

From the conservation of total mass, the first term on the RHS can be defined as $-v^{-1}\partial_x v$. The specific gas constant R_{spe} can also be expressed in terms of the mixture as $\sum_i c_i r_i$ where $r_i = R/M_i$ where R is the unversal gas constant and M_i is the molar mass of species i. As such the equation becomes:

$$\frac{1}{p}\frac{\partial p}{\partial x} = -\frac{1}{v}\frac{\partial v}{\partial x} + \frac{1}{T}\frac{\partial T}{\partial x} + \left(\sum_i c_i \frac{R}{M_i}\right)^{-1} \sum_i \frac{R}{M_i}\frac{\partial c_i}{\partial x} \tag{A.22}$$

The last term on the RHS can be transformed into

$$\left(\sum_i c_i \frac{R}{M_i}\right)^{-1} \sum_i \frac{R}{M_i}\frac{\partial c_i}{\partial x} = \frac{M}{\rho v}\sum_i \frac{\dot{\omega}_i}{M_i} \tag{A.23}$$

by recognizing that the the molar mass of the mixture $M = (\sum_i c_i/M_i)^{-1}$ and substituting in equation A.16. Finally, the momentum continuity equation becomes:

$$\left(\rho v - \frac{p}{v}\right)\frac{\partial v}{\partial x} + \frac{p}{T}\frac{\partial T}{\partial x} = -\frac{M}{\rho v}\sum_i \frac{\dot{\omega}_i}{M_i}. \tag{A.24}$$

The momentum and energy conservation equations can then be written:

$$\left(\frac{\rho v^2}{p} - 1\right)\frac{\partial v}{\partial x} + \frac{v}{T}\frac{\partial T}{\partial x} = -\frac{M}{\rho p}\sum_i \frac{\dot{\omega}_i}{M_i} \tag{A.25}$$

$$v\frac{\partial v}{\partial x} + C_P^f \frac{\partial T}{\partial x} = -\sum_i h_i \frac{\dot{\omega}_i}{\rho v} \tag{A.26}$$

which can be seen as a system of linear equations:

$$\begin{bmatrix} a_1 & a_2 \\ b_1 & b_2 \end{bmatrix} \cdot \begin{bmatrix} \frac{\partial v}{\partial x} \\ \frac{\partial T}{\partial x} \end{bmatrix} = \begin{bmatrix} c_1 \\ c_2 \end{bmatrix} \tag{A.27}$$

where the a, b and c coefficients are the ones in chapter 3. The system above can be solved by Cramer's rule which leads to the solution:

$$\frac{\partial v}{\partial x} = \frac{c_1 b_2 - c_2 b_1}{a_1 b_2 - a_2 b_1} \tag{A.28}$$

$$\frac{\partial T}{\partial x} = \frac{c_1 a_2 - c_2 a_1}{a_1 b_2 - b_1 a_2}. \tag{A.29}$$

Appendix B

Reduced mass for each vibrational mode

Figure B.1 presents a schematic of the ground state of CO_2. The position of each atom in the molecule is labeled from left to right "1", "2" and "3". The bonds are modelled considering a system of spring and masses. This analysis can be found in [291].

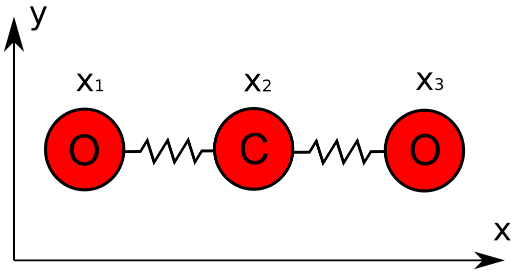

Figure B.1: Ground state CO_2 schematic representation.

B.1 Ground state

B.1.1 Symmetric stretch

To derive the reduced mass for the symmetric stretch movement one writes the center of mass equation where the origin of the coordinates is set

$$m_{\mathrm{O}} x_1 + m_{\mathrm{O}} x_3 + m_{\mathrm{C}} x_2 = 0. \tag{B.1}$$

With no external forces acting on the center of mass and considering the symmetric stretch motion where the C atom does not move,

$$x_3 = -x_1. \tag{B.2}$$

As such the force acting on a O atom depends only on x_1,

$$m_{\mathrm{O}} \frac{\partial^2 x_1}{\partial t^2} = -k x_1. \tag{B.3}$$

This equation is reduced to the well known harmonic oscillator equation where:

$$\frac{\partial^2 x_1}{\partial t^2} = -\omega x_1. \tag{B.4}$$

where the ω parameter is $\sqrt{k/\mu}$. As such, the reduced mass of the symmetric stretch motion is m_{O}.

B.1.2 Asymmetric stretch

The asymmetric stretch will have the O atoms moving in the the same direction and the C atom moving the opposite way to keep the center of the mass from moving. From the center of mass equation it is obtained:

$$(x_1 + x_3) = -\frac{m_{\mathrm{C}}}{m_{\mathrm{O}}} x_2 \tag{B.5}$$

The force applied on the C atom is written:

$$m_{\mathrm{C}} \frac{\partial^2 x_2}{\partial t^2} = -K \left(2x_2 - [x_1 + x_3]\right) \tag{B.6}$$

from the sum of two forces, $-k(x_2 - x_1)$ and $k(x_3 - x_2)$. Plugging in the parametrization obtained from the center of mass equation the following ODE is obtained:

$$\frac{\partial^2 x_2}{\partial t^2} = -\frac{k}{m_{\mathrm{C}}} \left(\frac{2m_{\mathrm{O}} + m_{\mathrm{C}}}{m_{\mathrm{O}}}\right) x_2 \tag{B.7}$$

and the reduced mass for the asymmetric stretch can be recognized as:

$$\mu = \frac{m_{\mathrm{C}} m_{\mathrm{O}}}{m_{\mathrm{C}} + 2m_{\mathrm{O}}} \tag{B.8}$$

B.1.3 Bending

In bending motion the bond length will remain constant d. The O atoms will move away from the horizontal and the C atom will go in the other direction to conserve the center of mass. Conserving the center of mass in the y axis requires:

$$2y_1 m_{\mathrm{O}} = y_2 m_{\mathrm{C}} \tag{B.9}$$

Furthermore the total sum of the y displacement is a function of the angle $(\alpha/2)$ between the C-O bonds and the horizontal

$$y_1 + y_2 = d \sin\left(\frac{\alpha}{2}\right) \approx \frac{d\alpha}{2} \tag{B.10}$$

where the last approximation is the small angle approximation $\sin\theta \approx \theta$ for small θ. Replacing the second equation on the first,

$$y_1 = d\frac{m_{\mathrm{C}}}{2(2m_{\mathrm{O}} + m_{\mathrm{C}})}\alpha. \tag{B.11}$$

The force acting on both O atoms is

$$m_{\mathrm{O}}\frac{\partial^2 y_1}{\partial t^2} = -k'\alpha d \tag{B.12}$$

where k' is the bending force constant. Replacing the definition x_1 in the equation above it is obtained:

$$\frac{\partial^2 \alpha}{\partial t^2} = -k'\alpha\left[\frac{2(m_{\mathrm{C}} + 2m_{\mathrm{O}})}{m_{\mathrm{O}}m_{\mathrm{C}}}\right] \tag{B.13}$$

and the bending reduced mass is recognized as:

$$\mu = \frac{m_{\mathrm{O}}m_{\mathrm{C}}}{2(m_{\mathrm{C}} + 2m_{\mathrm{O}})}. \tag{B.14}$$

Appendix C

Determination of FHO parameters

This appendix is dedicated to the methodology in determining the FHO parameters and obtaining calculated rates that are a good match for measured or high-fidelity references. The material laid out here can also be mostly found in STELLAR.

C.1 Morse Potential

The approach that has been followed in the past [118] is to consider the α and E_m parameters, discussed in section 3.2.1, as fully adjustable, iterating the values until a best fit with reference rates is achieved. With this said, a review of the available data on intermolecular potentials is always pertinent, since it allows establishing some boundaries allowing the verification of the iteratively determined isotropic Morse potential

$$V = E_m \left[1 - \exp\left(-\alpha[r - r_{eq}]\right)\right]^2 \tag{C.1}$$

It is also useful for determining the ratios of given state-specific potentials for different collisional pairs, allowing the extension of a calculated state-specific dataset to another one (for example, extending a dataset for CO_2–CO_2 collisions to CO_2–N_2 collisions).

Here, molecular beam experiments have been investigated, which allow the determination of short-range repulsive potentials, and "ab-initio" multidimensional intermolecular PES that are used in high-fidelity trajectory methods for the determination of synthetic transition rates (quasiclassical or full quantum methods).

Leonas [292] has carried out an extensive study of the repulsive intermolecular forces between a large number of atomic, diatomic and triatomic species pairs. The results for the chemical species relevant to CO_2–N_2 gas mixtures are summarized in table C.1.

Table C.1: Measured repulsive potentials from [292]

System	A (keV)	α (Å^{-1})	A (keV)	α (Å^{-1})
O - CO_2	1	4.06	7	3.89
N_2 - CO_2	1.17	4.06	30	3.78
O_2 - CO_2	0.49	3.58	8.72	3.33
CO - CO_2	0.897	3.81	19.2	3.55
CO_2 - CO_2	1.09	3.96	44.9	3.43

This analysis is complemented with a review of the PES from Bock [293] for CO_2–CO_2 collisions, which is easily reproducible based on the expressions published therein. Figure C.1 presents the intermolecular potential for the different molecular orientations.

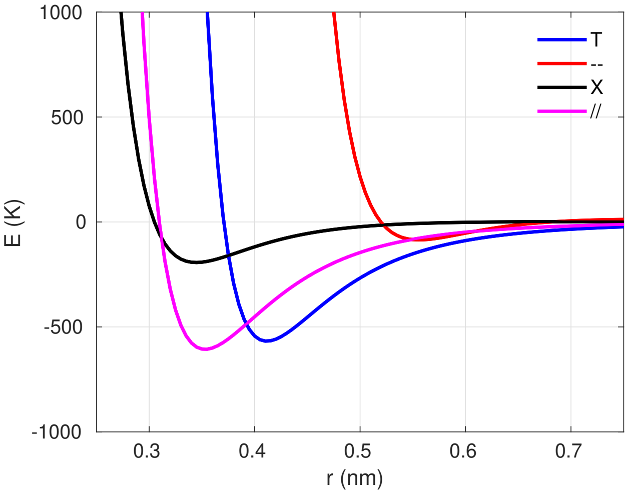

Figure C.1: Bock intermolecular potential [293] for different collision geometries

Each collision configuration has been fitted to a Morse potential. The corresponding repulsive and well depth parameters are reported in table C.2.

Table C.2: Morse fit to the Bock potential [293] for different collision configurations

Configuration	E (K)	α (Å^{-1})
T	616	4.87
Linear (– –)	75	5.46
X	193	4.89
Slip parallel (//)	642	4.56

These two sets of data may then be considered as a reference regarding intermolecular potentials. Any iteratively determined potential should be expected to remain close to these values.

C.2 Bending mode V–T rates determination

The procedure for the determination of a dataset of v_2 V–T rates is rather straightforward, since Blauer [59] proposed a set of rates

$$CO_2(0, v_2, 0) + CO_2 \rightarrow CO_2(0, v_2 - 1, 0) + CO_2 \tag{C.2}$$

for v_2=[5–1], from room temperature up to 3,000 K. A best fit between the FHO model and the Blauer data is found for the intermolecular parameters from table C.3. A comparison of Blauer's rates with the best-fit FHO rates is presented in figure C.2.

Table C.3: Best-fit intermolecular potential and steric factor parameter

$\alpha^{-1}(\text{Å}^{-1})$	E(K)	S_{VT}
4.3	650	6×10^{-4}

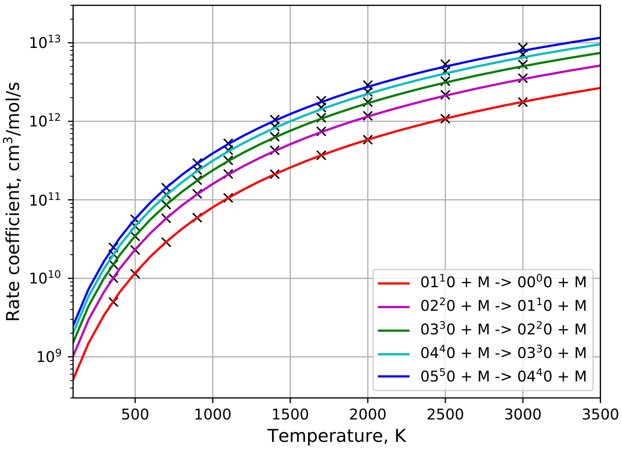

Figure C.2: Comparison of Blauer [59] rates (–x–) with rates from the FHO model (–)

C.2.1 Symmetric and Asymmetric V–T rates determination

The procedure for the calculation of v_1 and v_3 V–T rates is significantly more complex and requires a substantial number of underlying assumptions. These rates have to be considered as a "best-guess" estimation since pure V–T quenching rates are found to be too low to be accurately determined in experimental measurements [7], and since detailed PES-based simulations are lacking for these modes[1]. The measurements compiled by Byriukov [294] are first considered for the total quenching rate of CO(v_3):

$$CO_2(0,0,v_3) + CO_2 \rightarrow CO_2(n,m,0) + CO_2 \tag{C.3}$$

A best-fit of this rate is performed using the FHO model. The corresponding intermolecular parameters are presented in table C.4. A comparison of the experimental data with the best-fit FHO rate is presented in figure C.3.

Table C.4: Best-fit intermolecular potential and steric factor parameter

α (Å^{-1})	E(K)	S_{VT}
7	1700	1/3

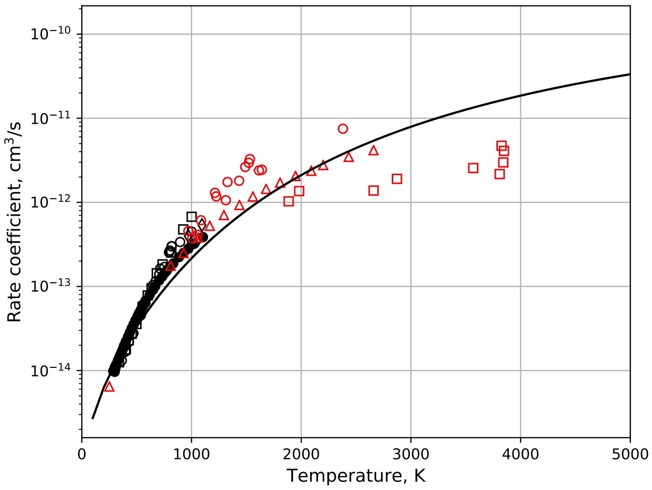

Figure C.3: Comparison of Byriukov [294] rates (points) with best-fit from the FHO model (–)

Note that the best-fit potential differs significantly from the boundaries recommended in section C.1. This is not surprising as the quenching rate is in fact a mix of different transitions to several intermode levels below the (001) level. Losev carried out a review [7] of the temperature-dependent branching ratios for the $CO_2(v_3)$ quenching rate. The global FHO quenching rate (figure C.3) is divided by the branching ratios proposed in the T=300–2000 K range and a set of Arrhenius rates is obtained[2], presented in table C.5.

---

[1] also since the pure V–T rates for modes v_1 and v_3 have low transition probabilities, they are difficult to determine with enough accuracy, unless an inordinate number of trajectories is sampled using PES models

[2] after performing a fit to an Arrhenius expression

The corresponding rates (original and fitted to an Arrhenius expression) are presented in figure C.4. The Arrhenius fit extrapolates well in the low-temperature range, and in the high-temperature range (remaining below the gas-kinetic rate up to 10,000 K and beyond).

Table C.5: Arrhenius – $AT^n \exp(-\theta_r/T)$ – rate expressions for v_3 quenching rates, T=[300–2,000] K.

Transition	A	n	θ_r
$00^01 \rightarrow 02^00 + 10^00$	7.93×10^{-19}	1.74	156
$00^01 \rightarrow 03^10 + 11^10$	1.82×10^{-21}	2.83	1788
$00^01 \rightarrow 04^00 + 12^00 + 20^00$	4.29×10^{-13}	-0.36	1469
$00^01 \rightarrow 01^10$	5.04×10^{-21}	2.54	4607

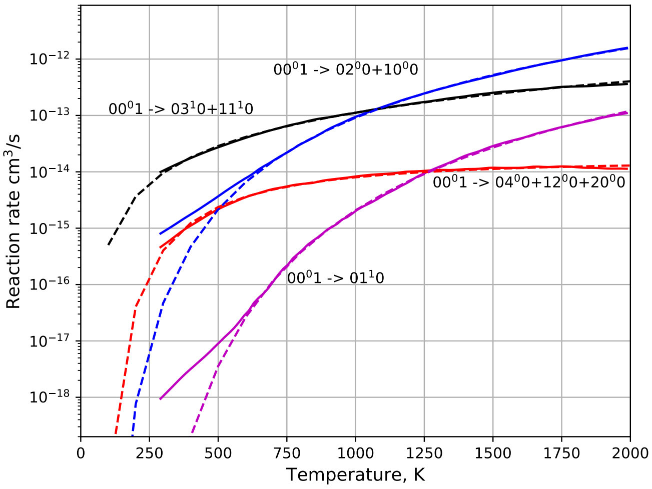

Figure C.4: Quenching rates in the 300–2000 K range, assuming the branching ratios proposed by Losev [7]. The corresponding Arrhenius fits are presented in dashed lines

The compilation above is insufficient to provide any estimate of the v_3 VT deactivation rate $CO_2(00^01) \rightarrow CO_2(00^00)$, and it is necessary to review other works in search for data that might complement these results. A bibliography research yields PES trajectory data from Billing [232], where the calculations, according to the vibrational cose-coupling rotational infinite order sudden method (VVC IOS), did not have enough trajectories sampled to yield a reliable rate. Schatz [295] reported a v_3 excitation cross-section below 2×10^{-18} cm^3 for CO_2–O collisions. Clary [296] carried out PES-based simulations (VVC IOS method) for collisions with noble gas atoms (He, Ne, Ar), however its results are limited in range (around 300 K), lack transitions to the v_3 state, and are difficult to transpose to CO_2–CO_2 collisions. Chu [297] presented an experimentally measured set of transition probabilities for CO_2–H collisions at two different temperatures (18,000 and 24,000 K). Again his results are difficult to transpose for the case of CO_2–CO_2 collisions. Nevertheless, these results may be summarized to present a clearer view on the influence of the mass of the colliding partner in the transfer rates for the different vibrational modes. This is done in table C.6. It is further noted that Siddles [298] reviewed the dependence on the collisional partner for the quenching ratios of the v_3 and v_2 levels. These are reported in table C.7

Table C.6: Probabilities for T–V excitation processes for CO_2–X collisions

	H(18–24 kK)[1]	He(300 K)[2]	Ne(300 K)[2]	Ne(300 K)[3]	Ar(300 K)[2]	O(2–6 eV)[4]
$P_{0\to v_1}$	12–16%	1.8e-5	1.6e-7	4.0e-7	4.9e-6	
$P_{0\to v_2}$	16–21%	0.93%	0.16%	0.16%	0.12%	
$P_{0\to v_3}$	1.1–1.7%	5.9e-9	4.4e-7	–	–	<0.05%

[1]: Chu 1983 [297]; [2]: Clary 1981 [296]; [3]: Billing 1981 [232]; [4]: Schatz 1981 [295]

Table C.7: Quenching ratio v_3/v_2 dependence on the collisional partner

	155 K	295 K
H_2	0.004	0.020
D_2	0.010	0.013
He	0.028	0.018
Ne	0.65	0.37
N_2	1.7	1.0
O_2	2.5	0.81
Ar	4.7	2.1
CO_2	4.0	1.8
Xe	5.7	7.2

Ultimately, the results of Harvey [299] are considered, who used a VCC IOS method to obtain energy-dependent transitions cross-sections for the excitation of the v_1, v_2, v_3 modes from the ground-state of CO_2, for an energy range of 1–6 eV, and considering a CO_2–O collision. This work has been carried out in relation of the investigation for the energy transfer process:

$$CO_2(01^10) + O \rightarrow CO_2(00^00) + O \tag{C.4}$$

which is known to be of paramount importance for upper-atmospheric processes [63]. The excitation cross-sections have been carefully extrapolated in the lower range and converted into de-excitation cross-sections using the detailed balance principle. A comparison has been carried out between these cross-sections, and the v_2 quenching cross-section calculated at low collision energy by Lara–Castells [300], which accounted for spin-orbit interactions of the 3 different electronic states for the O atom, something that is neglected in the calculations of Harvey. The obtained probabilities are presented in figure C.5

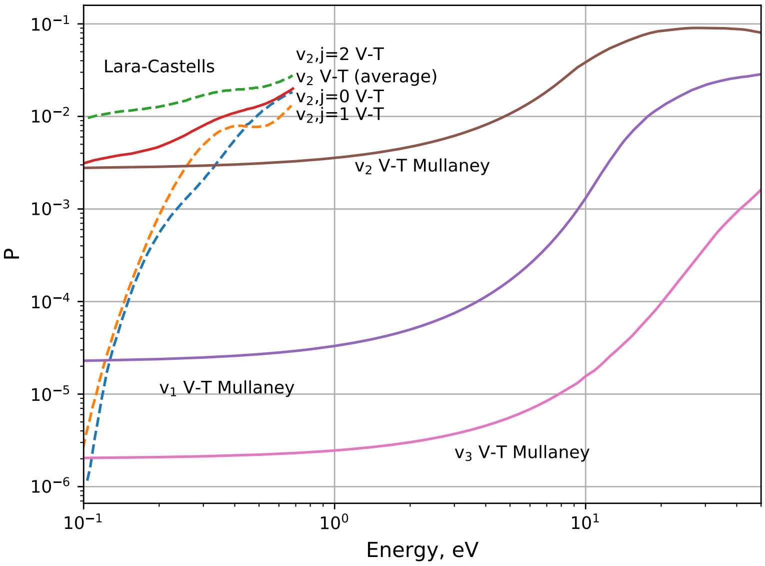

Figure C.5: Quenching (1–0) probabilities for the v_1, v_2, v_3 modes, as proposed by Harvey [299], and comparison with the probabilities obtained by Lara–Castells for the v_2 mode quenching

The cross-sections for the v_2 excitation process, as proposed by Harvey, are underestimated in the low-energy limit, likely due for the model not accounting for spin-orbit interactions. Lara–Castells shows that the collision CO_2+$O(^3P_2)$ has significantly higher probabilities, as a consequence of spin-orbit interactions, therefore yielding a much higher transition cross-section at low impact energies, which helps to explain the abnormally high transition rate for the process of equation C.4 at lower temperatures. Despite this, the results from Harvey and Lara–Castells are not significantly different, and the resulting de-excitation probabilities from Harvey may not be converted to yield the corresponding rates. A further comparison between the resulting rates with other v_2 de-excitation data is made and presented in figure C.6. The comparison with Castle [301] data in the low-temperature range (142–490 K), and with Center [302] in the high-temperature range (2,000–4,000 K) yields a satisfactory comparison in terms of orders of magnitude, despite that the low-temperature rates are one order of magnitude higher and show the well-known inverse temperature dependence [63], due to the CO_2+$O(^3P_2)$ spin-orbit interaction [300]. Further, the rate derived from Harvey's cross-sections appears to be relatively "flat" at higher temperatures, despite evidences of increase in the transition rates, as shown by Center's data. For reference, Blauer's proposed rate for $CO_2(v_2)$–CO_2 quenching is also reported. In conclusion, and despite the shortcomings from the rates that are derived from Harvey's extrapolated cross-sections, these are considered to be credible enough for the purposes of this work, which are not to directly deploy these in kinetic models, but instead to investigate the 0–1 quenching rates ratios between the v_1, v_2, v_3 modes, for a large temperature range. These are reported in figure C.7.

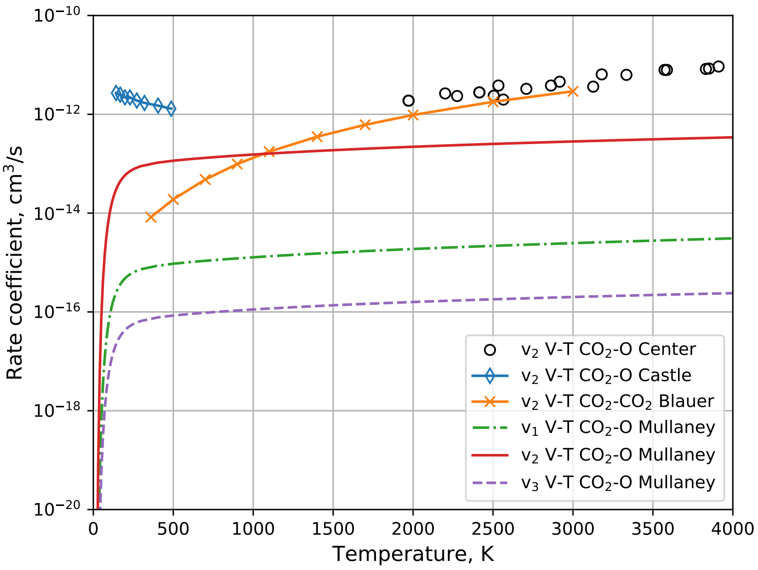

Figure C.6: Quenching (1–0) rates the v_1, v_2, v_3 modes, as proposed by Harvey [299], and comparison with other reported data for the v_2 mode

The ratios between the v_2 and v_3 1–0 de-excitation rates remain relatively insensitive to temperature, ranging from 7.4×10^{-4} at 2,000 K and 6.4×10^{-4} at 10,000 K respectively. A similar trend is found for the v_3/v_1 ratio, who varies from 0.09 to 0.06 in the same temperature range. This may be compared to the estimations proposed by different authors. Moore [51] cites a probability of 10^{-10} at room temperature, comparable to that for N_2

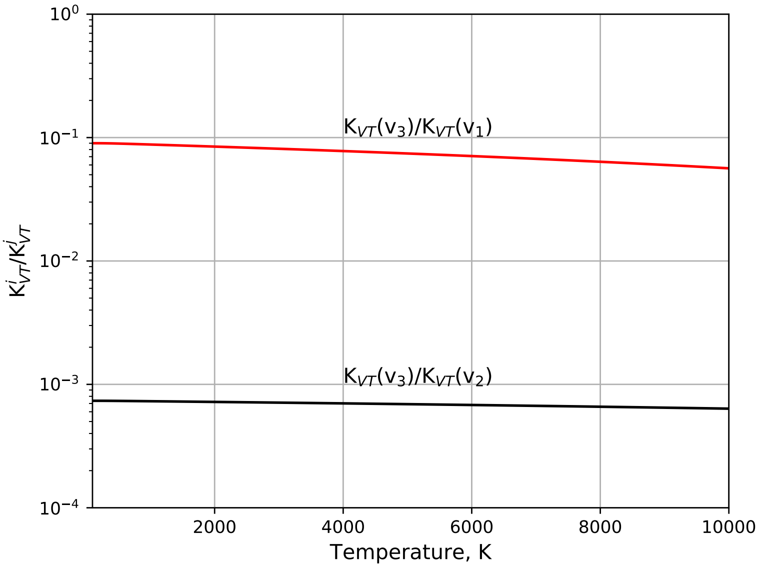

Figure C.7: Quenching (1–0) rate ratios between the v_1, v_2, v_3 modes, from the cross-sections proposed by Harvey [299]

or CO relaxation. Since the v_2 relaxation probability is 3×10^{-5}, this yields a v_2/v_3 ratio of 3×10^5. Fridman ([65], pp. 270, Fig. 5–13) proposes a v_3 1–0 rate of 10^{-17} at room temperature. This corresponds to a v_2/v_3 ratio of about 10^3, since the v_2 relaxation rate is about 10^{-14}. Kustova [99] and Armenise [303] present VT relaxation rates for v_1, v_2 and v_3. The v_3/v_2 ratio ranges from 10^{-8} at 700 K to 10^{-5} at 2,000 K [3] for the former, and from 10^{-8} at 1000 K to 10^{-4} at 4,000 K for the latter. Overall, the v_2/v_3 ratio obtained in this work appears quite reasonable given the scattering of the estimations from other authors.

The v_3/v_1 rate ratio may be simply compared to the one obtained by considering an identical intermolecular potential for both modes (a reasonable assumption, regarding the kinematic similarity between both symmetric and asymmetric stretch motions) and obtaining the corresponding 1–0 de-excitation rates, whose ratio will depend only from the respective energy spacings (the v_1 rate being higher due to the lower energy jumps). Using the intermolecular potential from C.4 the ratios of 0.07 at 2,000 K and 0.5 at 10,000 K are obtained. The latter value is one order of magnitude above the ratio from Harvey, which is not surprising since, as discussed before, this intermolecular potential is rather unrealistic. If a more reasonable potential is used, such as the one from C.3, the ratios become 0.005 at 2,000 K and 0.09 at 10,000 K. Here the ratio at lower temperature is

---

[3] and a v_1/v_2 ratio ranging from 10^{-4} to 10^{-2} in the same temperature range

one order of magnitude below the ratio from Harvey, but the high-temperature limit is relatively close to the value from the ratio of the rates based on Harvey's cross-sections.

The knowledge of the 1–0 rate ratios allows the determination of v_3 1–0 de-excitation rate. The fitted potential from table C.4 is not considered, in view of the aforementioned issues. Instead, the potential for v_2 de-excitation is used (table C.3), since it has good agreement with the review of section C.1 and since it is expected the the intermolecular potentials for the stretching and bending motion shouldn't be intrinsically different. Keeping the intermolecular potentials and steric factors of table C.3, the corresponding v_3 and v_1 rates are obtained, and compared to the ratios for the rates issued from Harvey in figure C.8.

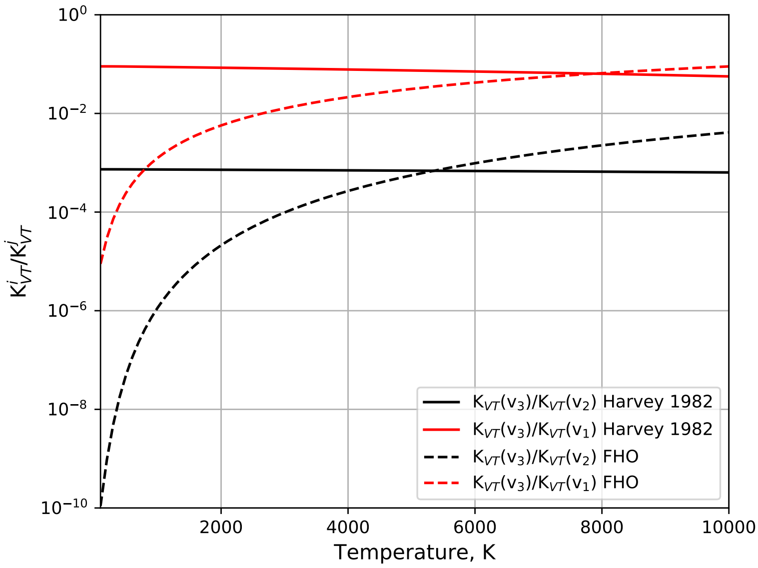

Figure C.8: Same as Fig. C.7, with the ratios for the V_1, v_2, v_3 FHO rates using the potential parameters of table C.3

Unlike Harvey's rate ratios, the FHO rate ratios evidence a significant variability over the temperature range, and are relatively consistent with the rate ratios proposed from different literature sources[4]. Nevertheless, the average values for the ratios are relatively consistent in terms of orders of magnitude, for the temperature ranges where V–T processes will be noticeable. When calculating v_1 and v_3 FHO rate coefficients, the exact same intermolecular potential than for v_2 V–T rates is considred (table C.3).

---

[4] although the SSH-based works will inevitably yield similar rate ratio dependences, since the SSH theory is a first-order approximation of the FHO theory

C.2.2 v_1, v_2, and v_3 V–V–T rates determination

Owing to the hypothesized importance of ladder-climbing V–V–T phenomena in CO_2 dissociation processes, an extension of the analysis to the modeling of these processes is presented. This focuses on the mono-quantum processes which are expected to be near resonant for a large range of the vibrational ladder

$$CO_2(v_k = i) + CO_2(v_k = i) \rightarrow CO_2(v_k = i + 1) + CO_2(v_k = i - 1) + \Delta E, \qquad \text{(C.5)}$$

where v_k is any of the vibrational modes v_1, v_2, or v_3. Firstly the degree of near-resonance for the processes above is examined. The energy defects between the levels determined from the extrapolated potentials determined in section 3.3.1 (full lines), with the ones obtained using Chedin's expression [207]. The results are reported in figure C.9.

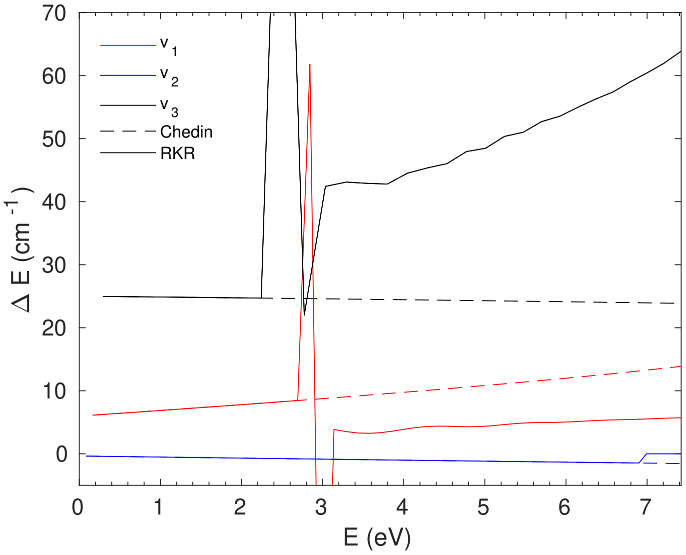

Figure C.9: Energy defects for the mono-quantum transition of equation C.5

To no surprise, the results from the NASA Ames potential [204] and Chedin's expression [207] coincide up to the limits where the AMES potential is considered to no longer be accurate and starts being extrapolated by an adequate near-dissociation potential. No special care is considered in maintaining the first and second order derivatives continuity when the switch from Chedin's expression and the radial Schrödinger equation solutions is performed. As such, there is a discontinuity at the quantum levels where this occurs. This might be revisited in future versions of the database if it is found to impact the modeling of CO_2 excitation and dissociation processes adversely. From further analysis of the calculated energy defects, all V–V–T rates will be near-resonant up to the 7.42 eV dissociation limit, with v_1 having a maximum energy defect up to about 10 cm^{-1}, v_2 an energy defect up to about 1–2 cm^{-1}, and v_3 an energy defect up to about 60 cm^{-1}. This means that the V–V–T transition rates for all the 3 vibrational modes are expected to be quite high.

Firstly the v_3 mode is examined. Experimental data is scarce and limited to the near-resonant (25 cm^{-1} energy defect) $CO_2(001)+CO_2(001)\to CO_2(000)+CO_2(002)$ [304, 305]. A fit to the FHO theory has proved to be unfeasible given the very high transition probabilities reported in these references. Actually, these exceed one for the rate at 700 K proposed by Thomason [305]. The comparison between the experimental rates, the closest FHO rate, and the gas-kinetic rate are presented in figure C.10. Given the puzzling and physically inconsistency between the measurements against the gas-kinetic rate, the decision was made not to use it for calibrating the FHO potentials for V–V–T transitions. Instead, the near-resonant CO_2–N_2 "laser" transition $CO_2(001)+N_2(0)\to CO_2(000)+N_2(1)$ for which an extensive amount of data exists [51, 56, 58, 306, 59, 60]. A best-fit for the FHO theory, including the near-resonant V–V–T trasitions correction, is presented in figure C.11.

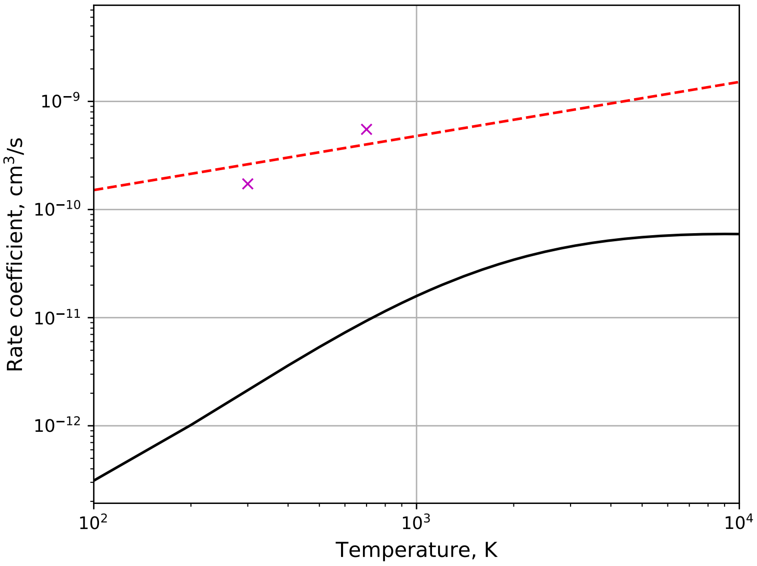

Figure C.10: Comparisons for the $CO_2(001)+CO_2(001)\to CO_2(000)+CO_2(002)$ V–V–T rate

The FHO theory, with the correction for near-resonant V–V–T transitions, is found to provide a good agreement with available experimental data in the high-temperature limit. For low temperatures, it is necessary to resort to the Sharma–Brau theory [57].

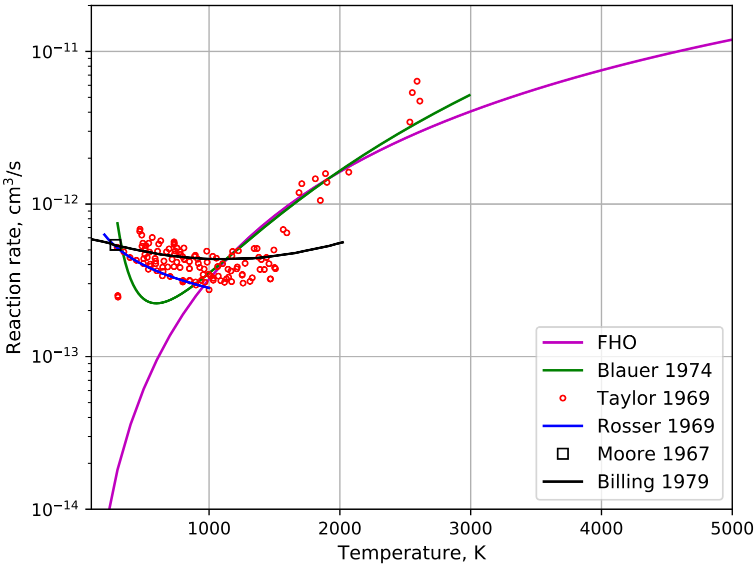

Figure C.11: Comparisons for the $CO_2(001)+N_2(0)\rightarrow CO_2(000)+N_2(1)$ V–V–T rate

The rates from both theories can be safely added together as they are mutually exclusive (Sharma-Blau theory gives a negligible rate at high temperatures, and the FHO theory at low temperatures). The steric factors for the best fit are presented in table C.8. The intermolecular potential parameter is kept at the same value than for the V–T transitions case (see table C.3).

Table C.8: Best-fit steric factor parameters for the $CO_2(001)+N_2(0)\rightarrow CO_2(000)+N_2(1)$ V–V–T rate

S_{VT}	S_{VVT}
6.5×10^{-5}	6.5×10^{-5}

An additional comparison is carried against a review of measured $CO_2(001)+CO(0) \longleftrightarrow CO_2(000)+CO(1)$ V–V–T rates, published by Miller [307]. This is presented in figure C.12. Again, a best-fit is obtained for the intermolecular potential of table C.3, with a slight adjustment of the V–T steric factor S_{VT}. The result for the “standard” $S_{VT} = 6 \times 10^{-4}$ is also reported, and it could be argued that this is also a reasonable fit, owing to the scattering for the experimental data. As for all the near-resonant V–V–T transitions, these are found to be insensitive to the V–V–T steric factor S_{VVT}, who is set by default equal to S_{VT}.

The analysis of V–V–T rates is concluded with a comparison against the CO_2–CO_2

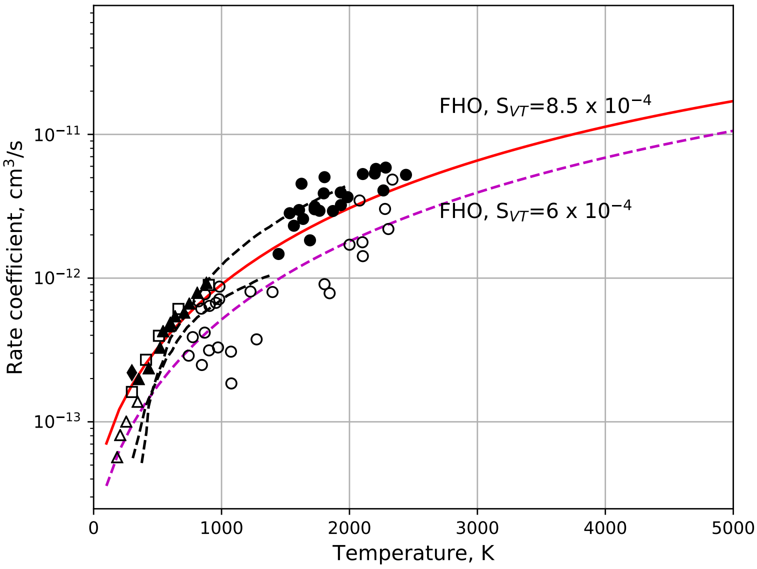

Figure C.12: Comparisons for the $CO_2(001)+CO(0)\rightarrow CO_2(000)+CO(1)$ V–V–T rate

v_2 bending rates published by Blauer [59]. A select number of published V–V–T rates is tested against the FHO model, but also the proposed Landau–Teller rate for CO_2–CO_2 near resonant rates:

$$K_{10} \sim \exp\left\{\left[-\frac{54\pi^2\mu x_0^2(\Delta E_v)^2}{h^2 k_B T}\right]^{1/3}\right\}. \tag{C.6}$$

The comparison for the $CO_2(03^30)+CO_2(01^10)\rightarrow CO_2(02^20)+CO_2(02^20)$ V–V–T rate is presented in figure C.13. The steric factor had to be adjusted to $S_{VT} = 1.7 \times 10^{-6}$, but other intermolecular parameters were kept the same as in table C.3. The comparison with the FHO theory provides a reasonable agreement with the published Blauer rates, while the Landau–Teller equation will only yield the correct order of magnitude, being flat over the whole temperature range. This is to be expected in the scope of equation C.6, since the energy defect for this transition is only ΔE =0.5 cm^{-1}.

A further set of v_2 V–V–T rates has been fitted in the same fashion, with the previous rate reproduced alongside two more. The considered transitions are then:

$$CO_2(03^30) + CO_2(01^10) \rightarrow CO_2(02^20) + CO_2(02^20) \tag{C.7}$$

$$CO_2(04^40) + CO_2(00^00) \rightarrow CO_2(03^30) + CO_2(01^10) \tag{C.8}$$

$$CO_2(04^40) + CO_2(02^20) \rightarrow CO_2(03^30) + CO_2(03^30) \tag{C.9}$$

The comparison with Blauer rates is presented in figure C.14. In this case, the intermolecular potential parameters are the same as in table C.3, however the V–T steric

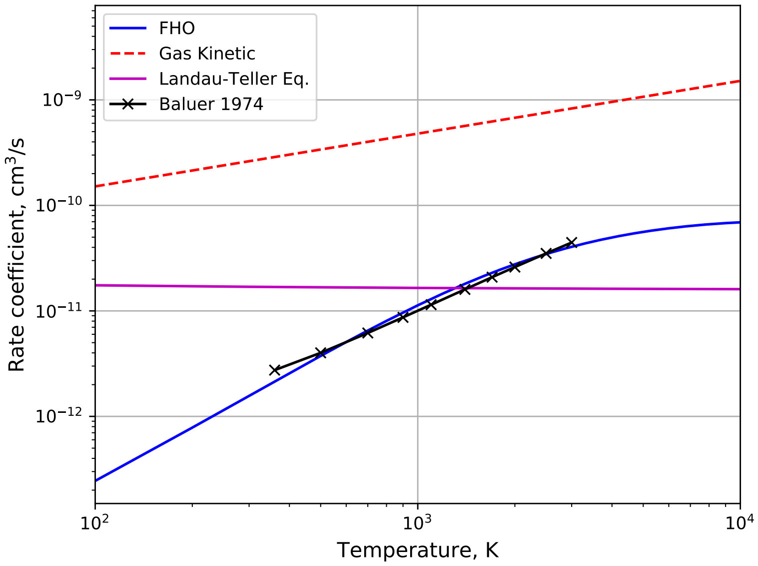

Figure C.13: Comparisons for the $CO_2(03^30)+CO_2(01^10) \rightarrow CO_2(02^20)+CO_2(02^20)$ V–V–T rate

factors S_{VT} had to be considerably adjusted. The best-fit were respectively $S_{VT} = 1.7 \times 10^{-6}$, 6.0×10^{-6}, and 0.1×10^{-6}. Again, the S_{VVT} steric factors were insensitive for this kind of almost resonant rates.

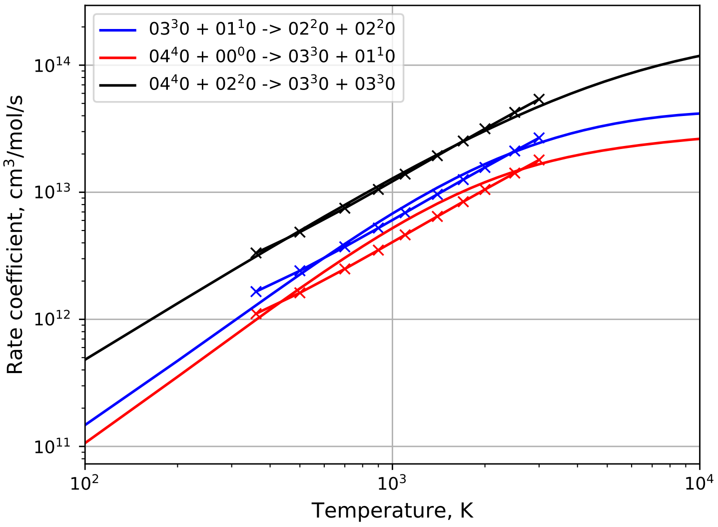

Figure C.14: Comparisons for the $CO_2(v_2)$ V–V–T rates from Eqs. C.7 to C.9